Multi-resonant Passive Components for Power Conversion

by

Joshua W. Phinney

B.A., Wheaton College (1995)
B.S., University of Ilinois at Chicago (1999)
S.M., Massachusetts Institue of Technology (2001)

Submitted to the Department of Electrical Engineering and Computer Science
in partial fulfillment of the requirements for the degree of

Doctor of Philosophy

at the

MASSACHUSETTS INSTITUTE OF TECHNOLOGY

May 2005
[June 2005]

© Massachusetts Institute of Technology, MMV. All rights reserved.

MASSACHUSETTS INSTITUTE OF TECHNOLOGY
OCT 2 1 2005
LIBRARIES

Author _____
Department of Electrical Engineering and Computer Science
May 23, 2005

Certified by _____
David J. Perreault
Associate Professor, Department of Electrical Engineering and Computer Science
Thesis Supervisor

Certified by _____
Jeffrey H. Lang
Professor, Department of Electrical Engineering and Computer Science
Thesis Supervisor

Accepted by _____
Arthur C. Smith
Chairman, Departmental Committee on Graduate Students

ARCHIVES

IPR2024-00706 EX. 2005

Multi-resonant Passive Components for Power Conversion

by
Joshua W. Phinney

Submitted to the Department of Electrical Engineering and Computer Science
on June 22, 2005, in partial fulfillment of the
requirements for the degree of
Doctor of Philosophy

Abstract

Semiconductor-device limitations to system miniaturization have receded, but exposed by their improvement numerous "ancillary" barriers which continue to preoccupy nearly every electronics industry. Prominent among these obstacles are package parasitics and heat, which have come to the fore as conventional circuits are applied in modern regimes of frequency and integration density. To an ever increasing extent, integration limits are symptoms of the fundamental frequency- and size-scaling limits of passive components. Power inductors and transformers, in particular, are challenging to miniaturize because of their poor performance when scaled down in size, and the difficulty of fabricating them with available planar processes.

A family of approximating networks for transmission lines, the focus of this work, enables miniaturization by internally circulating energy and exchanging delay fidelity for bulk energy storage. These multi-resonant components are substantially smaller than their lumped counterparts, in particular requiring less inductance, and enforce useful waveform symmetries that can be traded for higher power or higher efficiency. Lumped analogs of transmission lines, and delay-based means of processing energy in general, exploit rather than fight the parasitics which can restrict conventional designs to lower switching frequencies, and are compatible with RF power-conversion techniques.

Printed-circuit and wafer- or package-scale construction methods for multi-resonant structures are presented, along with power-converter topologies that exploit the waveform symmetries they enforce. A new soft-switched RF power converter is introduced, in particular, that demonstrates reductions in peak device stress and passive-component size. Taken together, the construction techniques, networks, and converter topologies presented here extend the power levels and applications for which passive components can be manufactured in an integrated fashion, within a printed circuit board or at the die/package scale alongside semiconductor switches and converter controls.

Thesis Supervisor: David J. Perreault
Title: Associate Professor, Department of Electrical Engineering and Computer Science

Thesis Supervisor: Jeffrey H. Lang
Title: Professor, Department of Electrical Engineering and Computer Science

IPR2024-00706 EX. 2005

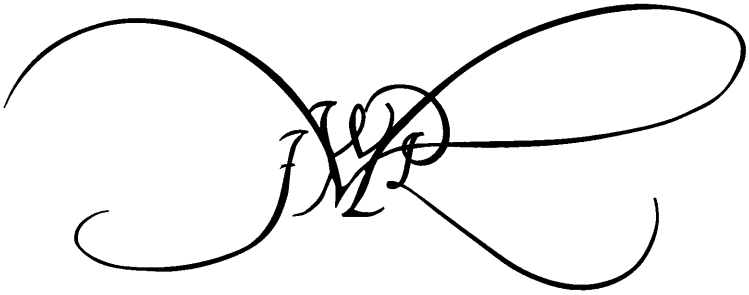

for Jennifer

Acknowledgements

My thanks are due to the US Office of Naval Research, National Science Foundation, and MIT Microengine Project for funding my assistantship at different times over the last four years. Our collaborators at the Georgia Institute of Technology provided much initial guidance for the fabrication component of this thesis, and I would like to thank Mark Allen, David Arnold, and Florent Cros for all their advice. To Juan Rivas, Pádraig Cantillon-Murphy, John Shafran, Dave Jackson, Lucy Rodd, Kurt Broderick, and Jim Warren, warmest thanks for helping with research and writing when I needed help most. The LEES faculty — Jeffrey Lang, Thomas Keim, David Perreault, and George Verghese — were models of creativity, assiduity, and judgement whose example will always stay with me. To Chris Laughman, Robert Cox, Ernst Scholtz, Matthew Mishrikey, Rob Jensen, Ivan Celanovic, Al Avestruz, Leandro Lorilla, and Jim Paris thank you for patient ears, help, and friendship (or even a quick beer). I would like to single out for special thanks Lodewyk Steyn, best man at my wedding, consummate squash instructor, and a great engineer.

IPR2024-00706 EX. 2005

Contents

1 Introduction **19**

1.1 Magnetic scaling limitations 21

1.2 Techniques for Reducing Passive-Component Values 23

1.2.1 Bulk reactive components 23

1.2.2 Resonant and delay networks 26

1.3 Contributions and Organization of the thesis 31

2 Resonators and transmission lines **35**

2.1 Networks with one resonance 37

2.2 Networks with multiple resonances 41

2.3 Lumped models for the terminated transmission line 45

2.3.1 Foster realizations of transmission-line impedance 48

2.3.2 Cauer-form realizations of transmission-line impedance 52

2.3.3 Cut-off frequency 53

2.3.4 Choosing total line inductance and capacitance 54

2.4 Critical-frequency alignment of lumped lines 55

2.4.1 Coupling and Pole-Zero Separation 55

2.4.2 Terminal Impedance and Zero Alignment 58

2.5 Chapter summary 59

3 Multi-resonant component design **61**

3.1 Tapped toroidal structures 62

3.2 Iterated-Network Impedance 63

3.2.1 Analytic expression for transmission-line critical frequencies 64

3.2.2 Inductance-matrix diagonalization 71

IPR2024-00706 EX. 2005

3.2.3 Iterated-network measurements 75
3.3 Iterated network with mutual coupling 78
3.3.1 Inductance cancellation 78
3.3.2 Measurements of the undiagonalized, iterated network 81
3.4 Cauer synthesis 82
3.4.1 Description of the synthesis method 82
3.4.1.1 A network explanation of synthesis 83
3.4.1.2 Algebraic explanation of synthesis 85
3.4.2 Approximation of the Cauer network with a tapped toroid 88
3.4.3 Measurements of the Cauer-synthesized toroid 92
3.4.4 Perturbations of Network Models 94
3.4.4.1 End-to-end coupling 94
3.4.4.2 Shielding 96
3.5 Chapter summary 98

4 Multi-resonant power converters 99
4.1 Cell topologies 101
4.1.1 Class E Inverter 101
4.1.1.1 Stresses in the Class E 102
4.1.1.2 Class E design 104
4.1.2 Class F Inverter 106
4.1.3 Class Φ converter 108
4.1.3.1 Stresses in the Class Φ 112
4.2 Analysis and design of the Class Φ inverter 113
4.2.1 Switched-mode state-space analysis of the Class Φ inverter 114
4.2.2 Improvements to the basic Class Φ design 117
4.3 Measurements of the Class Φ inverter 120
4.3.1 Low-power example 120
4.3.2 High-power example 122
4.3.2.1 Frequency and Switch Selection 122

IPR2024-00706 EX. 2005

4.3.2.2 Class E inverter 124
4.3.2.3 Distributed Class Φ implementation 126
4.3.2.4 Integrated Class Φ implementation 129

5 Fabrication **133**
5.1 Printed-Circuit Board Structures 135
5.1.1 Layout 136
5.1.2 Estimation of inner-layer thickness 137
5.2 Wafer-level Structures 137
5.2.1 SU-8 139
5.2.1.1 Pour application 140
5.2.1.2 Contrast Enhancement Lithography 142
5.2.1.3 Thick-film development 146
5.3 Electroplating 147
5.4 Process flow 148
5.5 Results 154

6 Summary and Conclusions **157**
6.1 Thesis summary 157
6.2 Thesis conclusions 159
6.3 Future work 159

A Layout scripts **163**
A.1 Eagle scripts 163
A.2 FastHenry model scripts 182
A.3 Cauer synthesis scripts 185
A.4 simulation scripts 190

B Pulse-reverse current source **195**

C Lithography Masks **197**

IPR2024-00706 EX. 2005

List of Figures

1.1 Limitations of magnetic scaling 22
1.2 Energy-transport components in power-converter circuits 24
1.3 Low impedance viewed as charge dilution 25
1.4 Mechanical analogies for bulk and resonant filters 26
1.5 Feedforward cancellation of periodic waveforms 28
1.6 Work cycles for half-cycle and full-cycle delays 29
1.7 Dimensions of EHPS power converter 33

2.1 Distributed and lumped resonators 36
2.2 A single power-stage resonance in a direct converter 37
2.6 Cascaded resonators in a direct converter 41
2.7 A uniform, lossless transmission line 42
2.8 Measured input impedance for RG-58/U coaxial line 43
2.9 Half-wave symmetric and half-wave repeating waveforms 44
2.10 An exemplary reactance function $X(j\omega)$ 46
2.11 Frequency pattern for a generalized reactance function 47
2.12 Foster realizations of transmission-line impedances 49
2.13 Iterated Cauer model for the transmission line 51
2.14 Input impedance of a semi-infinite ladder network 52
2.15 A simple example of coupling 56
2.16 Explanation of coupling in terms of pole/zero separation 57
2.17 Zero shifting from a series inductance is series with $X(j\omega)$ 58

3.1 Tapped toroidal structure 62
3.2 Input impedances of normalized, iterated L-networks 66
3.3 Analytical prediction of the pole and zero frequencies for iterated L-section networks 69

IPR2024-00706 EX. 2005

3.4 Ladder network with a fully populated inductance matrix 71
3.5 Contour of segment-to-segment mutual inductance for a toroid 72
3.6 computed inductance matrices: diagonalized and undiagonalized 73
3.7 Effect of tap inductances on L matrix 74
3.8 Measured input impedance of an iterated, coupled L-section network 76
3.9 Normalized critical-frequency alignment for the iterated network 77
3.10 Multi-tap inductance cancellation 78
3.11 Magnetically coupled windings 79
3.12 Measured input impedance of an undiagonalized toroid 80
3.13 Graphical depiction of Cauer synthesis 84
3.14 Cauer-synthesized L and C values for transmission-line behavior 87
3.15 Series port connection in the inductance matrix 89
3.16 FastHenry models and the computed inductance matrix: Cauer case 90
3.17 Iterative method for determining tap locations along toroid 91
3.18 Measured input impedance of a Cauer-derived toroid 93
3.19 Frequency alignment for Cauer-derived toroid, compared to model 94
3.20 Shifting of zero frequencies for end-to-end mutual inductance 95
3.21 Shift of critical frequencies for shielding 97

4.1 Block diagram of an RF dc-dc converter 99
4.2 New architectures for high-frequency dc-dc converters 100
4.3 Schematic of a Class E inverter 102
4.5 Class F converter 105
4.6 Idealized drain waveforms of the Class F inverter. 106
4.7 Schematic for stresses in the Class F converter 107
4.8 Switch stress in the Class F inverter. 108
4.9 Schematic of the Class Φ converter 109
4.10 Idealized waveforms of the Class Φ inverter 110
4.11 Reflection diagram 111
4.12 Class E design with a small switch relative its to passive components 113
4.13 States of LC ladder network 114

IPR2024-00706 EX. 2005

4.14 Simulated waveforms of the Class Φ inverter 118
4.15 Two methods of compensating for switch reactances in the Class Φ 119
4.16 The multi-resonant structure used in the low-power Class Φ inverter 120
4.17 Comparison of drain-voltage waveforms for the Class E and Class Φ 121
4.18 Power and efficiency curves used for switch and frequency selection 123
4.19 Schematic (with parastics) of the Class E converter of Section 4.3.2.2. . . . 125
4.20 Measured drain and load voltages for a Class E inverter 126
4.21 Multi-resonant converter constructed with a length of RG-58/U coaxial line. 127
4.22 Measured drain and load voltages for the Class Φ inverter with transmission line 128
4.23 Copper layers of the Class Φ converter with integrated 20 Ω multi-resonant structure. 130
4.24 Schematic (with parastics) of the Class Φ converter of Section 4.3.2.4. . . . 131
4.25 Measured drain and load voltages for the Class Φ inverter with transmission line analog 131

5.1 Compatibility of epoxy resins for fabrication at different scales 134
5.2 layup for a 4-layer PCB 135
5.3 Views of fabricated toroidal inductors 138
5.4 Photograph of levelled hotplate 140
5.5 SU-8 pre-bake temperature profiles 141
5.6 Transmittance of CEM-388S Contrast Enhancement Material 143
5.7 Contrast Enhancement Material applied to SU-8 lithography 144
5.8 Effect of Contrast Enhancement Material on the exposure of an underlying film 145
5.9 results of SU-8 lithography with contrast enhancement material 146
5.10 Electroformation process with etched seed layer 149
5.11 Electroformation process with etchback 150
5.12 SU-8 process 151
5.13 Top-layer interconnects 152
5.14 Measured impedance magnitude of a wafer-level toroid 155
5.15 DC and periodic pulse-reverse palting 155

IPR2024-00706 EX. 2005

6.1 Inverter networks incorporating multi-resonant structures 160
6.2 An example of a multi-resonant network incorporated in a load network . . 161
6.3 Transformers incorporating multiple resonances 162

IPR2024-00706 EX. 2005

List of Tables

3.1 Tabular arrangement of impedance-function coefficients 65
3.2 Fibonacci polynomials and Pascal's triangle 66
3.3 Chebyshev polynomials and Fibonacci polynomials 68

4.1 Parameters of the candidate MOSFETs for a high-power inverter 124

IPR2024-00706 EX. 2005

Chapter 1

Introduction

NOTHING is so productive of problems as a good solution. Semiconductor devices, in particular, have improved by every measure of performance in past decades to drive miniaturization in digital, RF, and power electronics. Device limitations to system miniaturization have receded, but exposed by their improvement numerous "ancillary" barriers which continue to preoccupy nearly every electronics industry. Prominent among these obstacles are package parasitics and heat,[1] which have come to the fore as old solutions are applied in modern regimes of frequency and integration density. For instance, though digital designers might dispute the contention, the cooling and packaging of modern CPUs (with package-scale passives integration, point-of-load power conversion, and elaborate material and thermal design), has demanded more attention and *de novo* design effort than the CPU circuitry itself. The 1 MW phased-array radar from Raytheon's THAAD missile-defense system is a modern example of a highly integrated, loss-limited system from RF electronics; the dominant design, manufacturing, and maintenance expense of the radar installation is, significantly, the glycol-refrigeration *trailer.*

In the design of miniaturized power electronics, parasitics and the interrelated concerns of heat and efficiency are pitfalls facing a designer on either hand. Given the excellent performance of modern switches, these pitfalls are to an ever greater extent symptoms of the fundamental frequency- and size-scaling limits of *passive components.* The trend of inverse-frequency scaling of passive-component values, by which decreased cycle-to-cycle flux linkage and charge corresponds to a decrease in bulk, has reached a practical loss limit for conventional materials. Moreover, reduction of passive-component size at a constant

[1] I am using "heat" here as a catch-all phrase for the trade-offs between heat-management and the decidedly *non*-ancillary concern of efficiency. Given a commitment to integrated manufacture on all hands, and the fact that many components are loss-limited rather than energy-storage-limited at frequencies of interest, excess heat has become more and more a "given," and heat management — rather than bulkier but efficient design — the solution.

IPR2024-00706 EX. 2005

switching frequency (where such reduction is even *possible* from energy-density considerations) is attended by losses incompatible with typical converter efficiency and thermal requirements. Power passive components are often constrained, therefore, to sizes impractically large for integrated manufacture, and system designers must tolerate the associated parasitics. These parasitics — e.g., interconnect inductance in series with a load, or ground-lead inductance in ripple-current shunt paths — erode the ripple performance of a power circuit and slow its response to changing output conditions. Such power-delivery and packaging issues are a significant bottleneck in the development of future microprocessors, for instance, where extremely tight and localized control of power delivery will be necessary.

This thesis explores techniques for reducing the volume and values of passive components, techniques which are compatible with a shift to HF and VHF switching frequencies, air-core magnetics, and planar magnetic geometries. These techniques can increase converter efficiency or power density, and have substantial manufacturing and cost advantages over power converters with comparable specifications. At the core of these improvements are multi-resonant components, structures which *exploit* rather than fight the parasitics which plague conventional designs. These components reduce frequency-dependent losses and the cut into the bulk of low-Q reactive energy storage, promising to extend the energy- and loss-limited frontiers of miniaturization. Multi-resonant structures are not simple drop-in replacements for passive components, notably, but alter converter operation in a manner that can *further* benefit efficiency. The prize to be won for circumventing the conventional limitations considered above is a galvanizing trend of size and cost reduction in power electronics. Depending on the power level of application, reduced-volume passive elements can be constructed on die or board scale, fabricated alongside semiconductor devices and controls, or effectively *printed* within the thickness of PCB laminates. Both types of manufacture exploit the mask-based, batch-fabrication techniques that are central to the cost and size benefits of integrated circuits, and can reduce or control the packaging and interconnect parasitics that can otherwise limit power-circuit performance.[2]

[2] "Integration," it should be noted, has two senses, referring to wafer-level fabrication and to miniaturization techniques which reuse volume for multiple modes of energy storage. Notable within the "integrated passives" field are techniques for manufacture of magnetic structures directly within PCB laminates, with a degree of care in layout which is normally reserved for integrated circuits [1, 2].

IPR2024-00706 EX. 2005

1.1 Magnetic scaling limitations

Power inductors and transformers are challenging to miniaturize — especially by available planar processes — and suffer from chronically low Q at high frequencies and small scales. Multi-resonant structures bypass the relevant energy- and loss-limited mechanisms, and are moreover well-suited to the laminate form-factors which constrain integrated magnetics to undesirable geometries.

Frequency-dependent losses place a lower bound on magnetic-component volume, volume which would otherwise dwindle at higher switching frequencies and lower applied volt-seconds. At high frequencies, loss (rather than energy storage) is the dominant consideration in sizing magnetics. The core-loss densities of most power ferrite materials rise rapidly with frequency in the megahertz range, necessitating flux de-rating as frequency is increased.[3] As a result, magnetic component size does not always decrease with higher frequencies, but can actually *increase* [3, section 15.3.1]. Air-core magnetics do not suffer this limitation, but must be operated at still higher frequencies to compensate for reduced inductance and the lack of a permeable core material. The multi-resonant structures constructed as a part of this thesis contain no permeable materials, and are complemented by power-conversion architectures capable of operating at tens to hundreds of megahertz, frequencies well-matched to air-core inductors and the impedances of comparably sized capacitors.

For a fixed frequency, inductor Q decreases with smaller dimensions because of fundamental scaling relationships between linear dimensions and flux- or current-carrying area. Consider the inductor of Fig. 1.1a when all linear dimensions in the core and winding decrease together by a factor $\alpha < 1$ (e.g., ℓ_c is reduced to $\alpha\ell_c$). Winding resistance can be expressed as $R = N\rho\ell_w/A_w$ for N turns with resistivity ρ. The geometrical factor ℓ_w/A_w, and hence resistance, increases by $1/\alpha$. Inductance, conversely, scales as an area over a length:

$$L = \frac{\mu N^2 A_c}{\ell_c}$$

so that $Q = X/R$ decreases as α^2 without compensated winding build. Microfabricated windings are often patterned with large dimensions relative to the core (when magnetic

[3]Core loss considerations are of particular importance in magnetic elements with significant ac flux components, such as transformers and resonant inductors.

IPR2024-00706 EX. 2005

(a) area and length scaling in magnetics

(b) Inductor geometries compatible with planar manufacturing

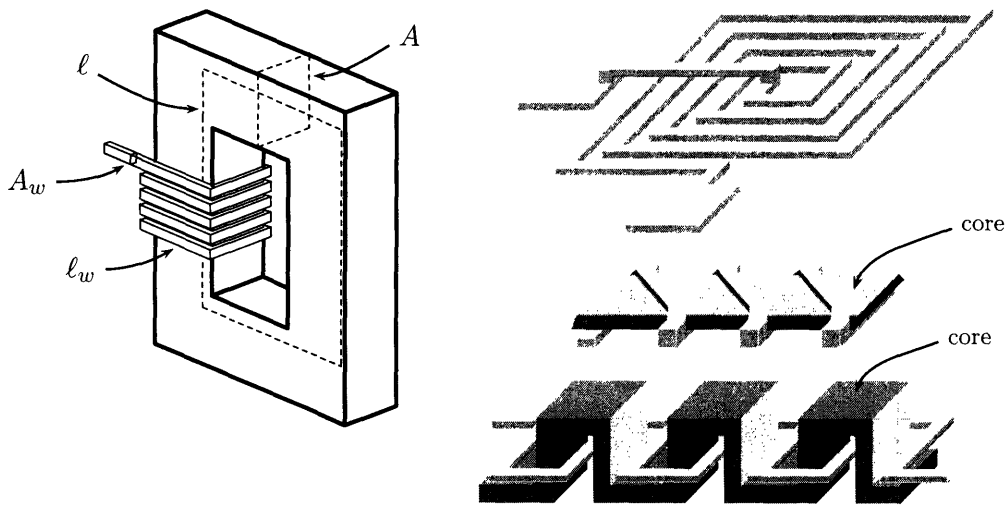

Figure 1.1: **(a) Limitations of magnetic scaling, considered as a fundamental relationship between flux- and current-carrying areas to lengths. (b) Magnetic geometries fabricated with planar processes**

materials are employed at all) precisely to reduce winding loss.[4] Similar scaling laws are found for other inductor geometries [4, 5], including the planar spirals (see Fig. 1.1b) favored for micro-scale fabrication [6, 7, 8]. Planar construction techniques introduce a host of further restrictions — on assembly, winding layers, laminations, and form factor — which can prevent the designer from even achieving the inductance and Q that might be anticipated from the scaling of a board-level component.

Multi-resonant components do not rely on lossy inductive reactances exclusively, but exchange energy internally between electric and magnetic modes of energy storage. Because high-Q capacitive reactances can be constructed with in relatively small volumes, higher-order structures can circulate energy with less overall loss for a fixed volume. I.e., by exchanging for higher Q the volume reduction that might otherwise attend decreased inductance, multi-resonant structures can push back the loss limits of miniaturization. Also unlike their fully magnetic counterparts, multi-resonant structures actually *benefit* from laminar form-factors because of the leakage inductances peculiar to planar geometries, a

[4]Inasmuch as N is decreased by attempts to construct windings with larger conduction area, however, Q can still suffer. As N decreases, flux linkage λ decreases as N^2, outstripping an approximately linear decrease in winding resistance with N.

IPR2024-00706 EX. 2005

claim which will be supported by measurements in Chapter 3,

1.2 Techniques for Reducing Passive-Component Values

Because passive components can be so troublesome to converter efficiency, bulk, and manufacturability, the task of doing more with less — of converting power with less capacitance and inductance — is of major practical concern. Reduction of passive values has largely been driven by increases in switching frequency. Rising from tens of kilohertz in the early 1970's into the megahertz range today, this converter "blue shift" has been enabled, in turn, by new devices and materials better suited to high-frequency operation (e.g., power MOSFETs and new ferrite magnetic materials) and by circuits and components that reduce the losses associated with high-frequency switching [9, 10]. Cellular conversion schemes, significantly for manufacturability, reduce passive-component values on a cell-by-cell basis, requiring that paralleled converters be rated for only fraction of the overall system power [11]. Though such schemes can outperform their bulk counterparts through interleaved operation, preferable from a standpoint of system miniaturization is an aggressive decrease, rather than a subdivision, of bulk passives.

Multi-resonant components reduce passive volume at roughly constant efficiency, compared to bulk passive elements, by circulating energy among internal modes of energy storage. As we've seen, this reduction is especially significant for reducing the size of magnetics, and can be exploited to increase efficiency at constant volume. To understand how multi-resonant networks achieve these trade-offs, let us first consider in general terms the components they replace.

1.2.1 Bulk reactive components

The standard distinction between direct and indirect converters developed in [12] and [13] can be generalized to distinguish converters which modulate a direct connection between source and load, and those which exchange energy with source and load during alternate portions of a switching cycle. We can classify, on this basis, the class-E inverter of Fig. 1.2d with the indirect converters of Fig. 1.2b and c, because it rings the energy in its drain-

IPR2024-00706 EX. 2005

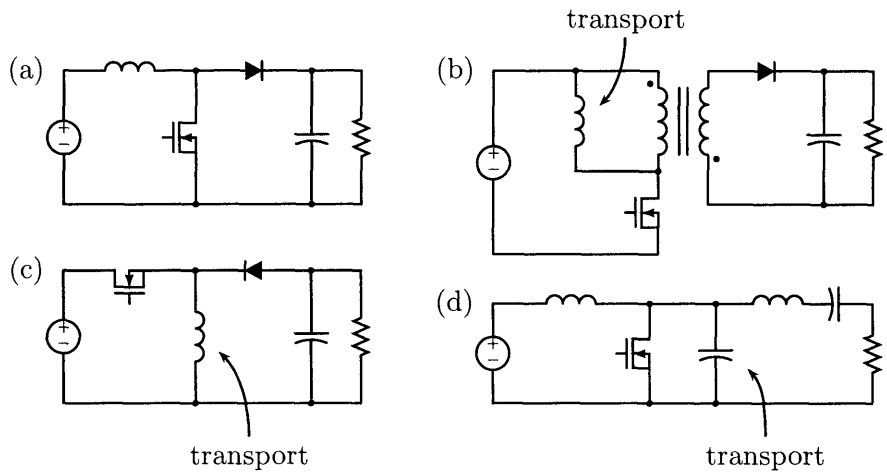

Figure 1.2: **Energy-transport components in power-converter circuits**

source capacitance toward the load once every switching cycle. Bringing the division to the component level, we can distinguish between reactive elements with an energy-storage and transport function — i.e., which pass energy *between* ports — and those which reflect energy to the *same* port over a cycle to develop a reactive impedance. Components of the first type are labelled Fig. 1.2, where the boost converter contains no "transport" elements, notably, because it is a direct converter. Let us focus for a moment on components which develop reactive impedance at the driving port.

Single-pole reactive elements develop large immitance by *dispersing* injected charge or *overwhelming* applied volt-seconds over the course of a cycle, and we refer to such elements as "bulk" capacitors and inductors for precisely this reason. The reaction impedance for the capacitive case is depicted in Fig. 1.3a. The parallel-plate structure has a low impedance when the plates are brought closer together, as the electric field between them is integrated over a shorter distance (i.e., the geometry has less terminal voltage V for a given plate charge Q). For practical film capacitors of comparable voltage rating, however, larger *area* is the principal means of scaling reactance. Developing admittance is a problem of reducing the integrated electric field; of *diluting* charge across a wide area to decrease surface-charge density at the inner plate faces.

The pressure vessel of Fig. 1.3b illustrates this notion by a fluid analogy. The vessel contains a compliant gas volume above a liquid phase, and is the hydraulic analog of the capacitor

IPR2024-00706 EX. 2005

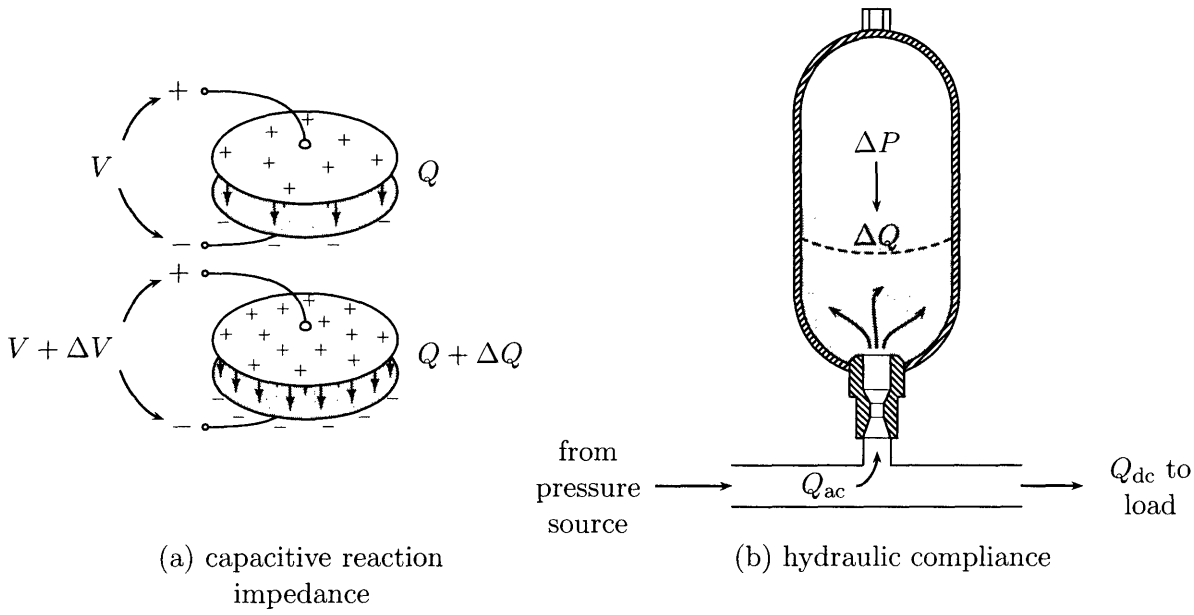

Figure 1.3: **Low impedance viewed as charge dilution**

on a force-voltage basis[5] (see the discussions of lumped-parameter electromechanics in [14], Chapter 3, and [15], section 4.4). The plenum has large ac compliance inasmuch as the incremental back-pressure ΔP is small for an incremental flow ΔQ. Compliance is thus analogous to capacitance — a ratio of charge to effort — and a large fluid compliance (a large capacity) is again precisely a matter of dilution. An ideal reservoir can accommodate arbitrary ΔQ at any frequency with no back-pressure; like a capacitor of infinite extent, it accumulates no incremental charge density for *any* input current, and has zero incremental impedance.

Inductance, continuing the force-voltage analogy, is analogous to inertia. Large inertia corresponds to large bucking flux-linkage and many inductor turns. In both the mechanical or electrical domains, a leading reaction impedance bears a clear relation to the volume of the corresponding component.

[5] i.e., in which force or pressure is analogous to voltage, and flow or velocity to current. The pressure vessel is incidentally an *accumulator*, most often employed to mitigate pressure ripple on hydraulic lines. It is placed, for instance, close to the pressure port of the oil pump in most automotive power-steering systems.

IPR2024-00706 EX. 2005

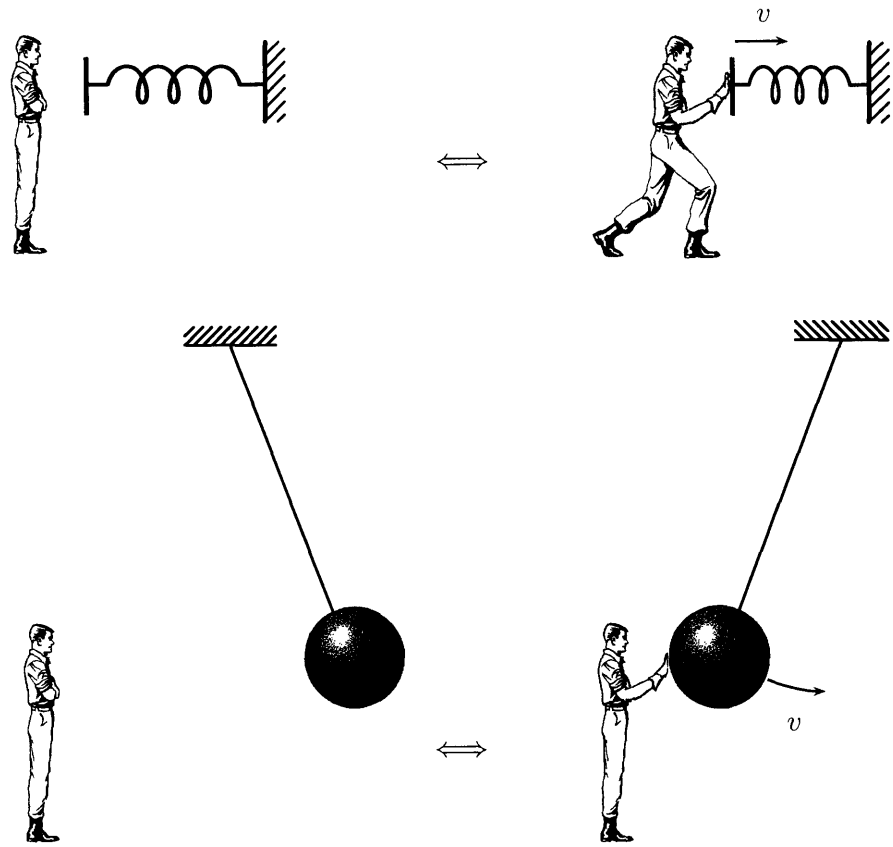

Figure 1.4: **Mechanical analogies for bulk and resonant filters**

1.2.2 Resonant and delay networks

The basic technique behind the structures of this thesis is a replacement of bulk energy storage by resonance, as illustrated in Fig. 1.4. The action of a switch during converter operation is represented schematically by the periodic application of effort, alternating on the left and right of Fig. 1.4. The illustrations with the spring represent the case of a bulk compliance; some effort is needed to effect the velocity v, and the reaction impedance of the spring is available at any point during the switching cycle. In the case of the pendulum, however, a small incremental mechanical impedance (like that of a large compliance or large capacitor) is subject to a *phase condition* between the pendulum velocity and applied effort. If the effort source has excited the pendulum at its eigenfrequency over previous cycles, this phase condition is met for continued periodic effort. When the peak excursion is *fixed* — which could correspond, for instance, to some steady-state application of a constant force or voltage through a source impedance — the pendulum's potential energy aids in developing

IPR2024-00706 EX. 2005

the velocity that would otherwise result from the application of force. The incremental impedance F/v is nulled, not in the sense that pendulum has no inertia, but in the sense that once excited, it requires no force to maintain a fixed peak excursion. That the impedance is non-reactive in this case is insignificant. Effort and velocity (or voltage and current) are in phase, but the source is not required to do any work inasmuch as the pendulum and its suspension are lossless.[6] We will see shortly how the resonant impedance condition is compatible with the delivery of power from the effort source through the structure, but first let us extend the treatment from the sinusoidal case to periodic waveforms in general.

Just as a pendulum's states, once excited, encode the fundamental phase and amplitude of applied effort, so the states of a higher-order system can store converter waveforms with many degrees of freedom, and again use terminal behavior from previous cycles to manipulate impedances. Fig. 1.5 depicts the feedforward cancellation of a periodic waveform by a delay, in illustration of this principle. Two types of cancellation are shown, the general periodic case in Fig. 1.5a, and the half-wave symmetric case in Fig. 1.5b.[7] The delay act as record of applied input, and begins with nulled internal states to produce the output shown. As with the pendulum, the delay must be "charged" by the input, during which time the output is not cancelled, analogous to the manner in which work must be done on the pendulum to excite it. Unlike the pendulum — the single conjugate mode of which has two degrees of freedom with which to encode the amplitude and phase of its steady-state response — the delays have an infinite number of states and can encode (and cancel) arbitrary periodic inputs. In the case of Fig. 1.5b, which is of special importance in later chapters, the record of applied input need only be one-half period long to effect cancellation at the quiet port (note the change in sign at the summing junctions, corresponding to the half-wave symmetry between the feedforward and delayed wave).

Fig. 1.6 builds upon feedforward cancellation, presenting in schematic form the effect of stored, reflected waveforms at a driving port. The forward delay has been replaced by a *ring delay* of the same overall record-length (half- and full-period) as the corresponding cases

[6] I am being cavalier in blurring distinctions between sinusoidal steady state and what appears to be, from the position of the force source, and impulsive excitation. The basic fact remains, however, that once excited to some fixed peak excursion, a lossless pendulum requires no additional work impulse to continue swinging to the same height.

[7] For the half-wave symmetric waveform, $x(t) = -x(t \pm T/2)$ for all t. I.e., the input in any given half-period is the inverse of its value in adjacent half-periods (or more generally, it assumes a value symmetric about its dc level).

IPR2024-00706 EX. 2005

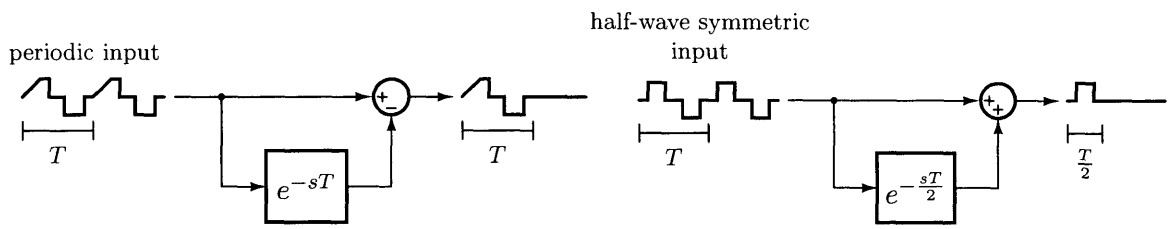

(a) Full-wave delay (b) Half-wave delay

Figure 1.5: **Feedforward cancellation of periodic waveforms**

of Fig. 1.5. The circulating and terminal signals have the units of work, and cancellation of the input signal (or more specifically, the ac input work) proceeds as before. For nulled initial states, the input signal passes through half of the overall ring delay, is offset by some constant value, and returns to the source. At the source, the return wave cancels the input at the first summing junction (labelled "cancel") to whatever degree the overall transport delay has faithfully preserved the input signal. The portion of the return energy which cancels the input work is not destroyed, but *reflected* back around the ring, augmented from the source by some incremental Δ (the result of imperfect cancellation) which compensates for ring losses. After a startup transient, during which the ring delay is "charged," the system is in periodic steady state and net ac work from the source is minimized.

The delay-cancellation effect shown in Fig. 1.6 is an ac phenomenon, and does not affect the dc power delivered across the transport delay. For both of the depicted cases, the input delivers constant power through the delay once periodic steady state is reached. This power is absorbed by the offset term on the right of Figs. 1.6a and 1.6b (which in the depicted simulations has a constant *negative* value equal to the average value of the input). Note that there is nothing fundamental about this choice of source and sink, for purposes of minimizing Δ. The half-wave symmetric "input" might as well represent the drain node of a power converter, drawing energy through the ring delay from a dc *source* on the right.

Also not fundamental to the energy formulation in Fig. 1.6 are specific boundary conditions at the input and output ports, corresponding to some particular relationship between effort and flow variables. As we will see in the next chapter, the delays of Fig. 1.6 are implemented with propagating waves which require cross-coupled modes of energy storage to subsist. The effort and flow quantities comprising these waves require different sorts of termination to circulate around the transport delay, entailing different terminal impedances at the ports. The minimization condition for Δ, for instance, might correspond to a returning voltage

IPR2024-00706 EX. 2005

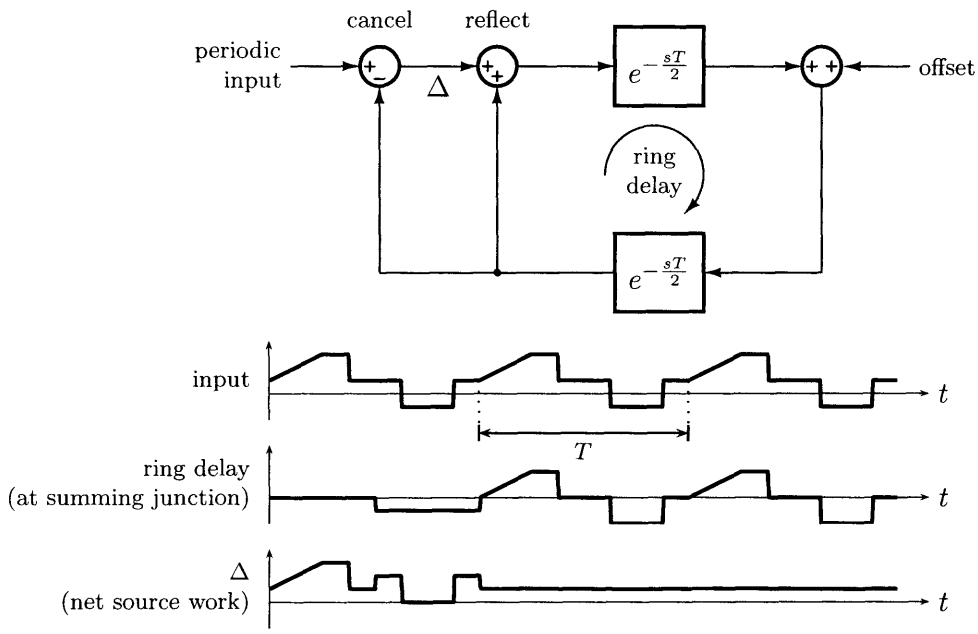

(a) Full-wave delay ring

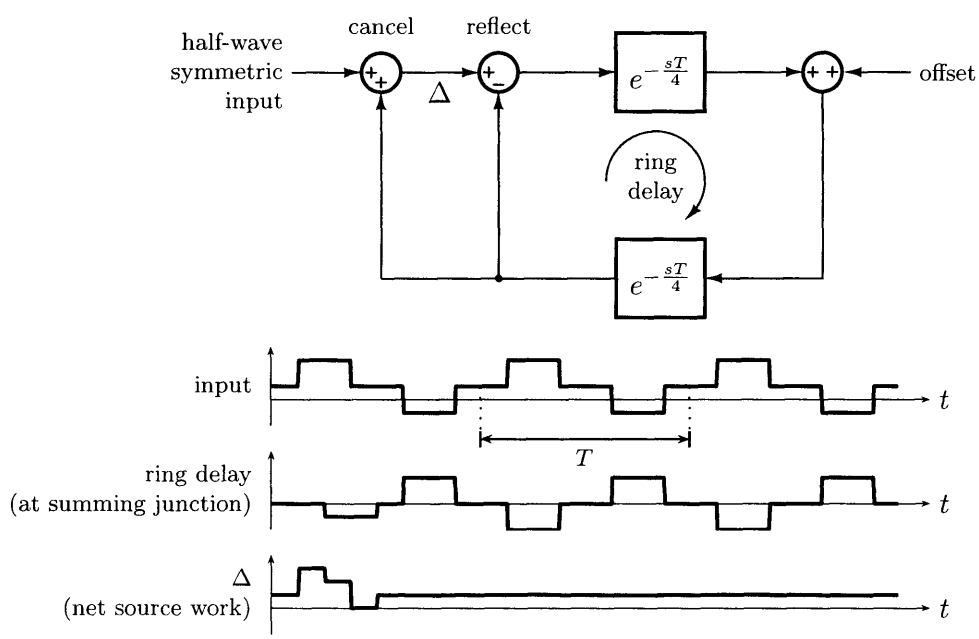

(b) Half-wave delay ring

Figure 1.6: **Work cycles for half-cycle and full-cycle delays**

IPR2024-00706 EX. 2005

wave in phase with an applied source voltage, in which case the cancellation condition corresponds to an impedance maximum at which no current (ideally) is required from the source. The treatment on an admittance or impedance basis will be developed further — in relation to delay times, symmetries, and terminations — in Chapters 2 to 4

An important consideration worth mentioning here is that while the treatment began impedance generation at the driving port, the delay ring of Fig. 1.6 can function as *transport element* in the sense of Fig. 1.2. I.e., the energy stored in travelling waves can replace lumped transport elements of the type shown in the indirect converters of Figs. 1.2b and c. For the buck-boost converter of Fig. 1.2c, in particular, we can imagine a converter in which the bulk inductance is replaced by a transmission delay. When switched in, the source can launch a travelling wave along the delay, which returns to deliver its energy to the load during the switch-off portion of the conversion cycle.

Reflected waves, significantly, are able to do work on the port which launched or sustained them initially. Referring to Fig. 1.4, we can readily appreciate that the source may not always command (on the mechanical analogy) velocity or displacement in the pendulum; the pendulum is thoroughly capable of enforcing velocity with its inertia. For converter systems of the half-wave type in Figs. 1.5b and 1.6b, this insight has an important consequence. Given enough circulating energy and the proper timing of applied effort or flow, the transport delay does not require a half-wave symmetric input to function, but can *enforce* symmetry conditions at its ports. This important circuit-design concept can enable efficient (i.e., soft) switching at very high frequencies, and will be explored further in Chapter 4.

The energy stored in travelling waves around the ring delay highlights one last point worth mentioning, regarding the hidden cost of implementing delay-based power conversion schemes. Fig. 1.6 glibly shows a constant "offset" on the right of both delay rings. The dc condition at the offset terminal is equivalent to an ideal termination of the transport delay at switching frequencies, one which enforces an ac energy-reflection condition while sourcing or sinking dc power. Given the dynamic impedance of practical sources and sinks, this dc port may be difficult to implement.[8]

[8]In the converters considered in Chapter 4, for instance, this termination is a broadband ac short-circuit at the source, required to sink several amps at 13-65 MHz. This termination is expensive, relative to the small component values in the power stage.

IPR2024-00706 EX. 2005

1.3 Contributions and Organization of the thesis

Multi-resonant components, and delay-based power electronics in general, is a conception of energy conversion that dissolves inherited problems in power electronics, and is the fundamental contribution of this thesis. Whereas reduction of high-frequency parasitics is a major preoccupation of circuit and component design, multi-resonant devices can *incorporate* parasitics to accomplish their function. Tolerance for irreducible parasitics encourages a shift to much higher switching frequencies, as does the eschewal of lossy permeable materials and the imposition of waveform symmetries compatible with soft-switching. These same symmetries can be leveraged to increase efficiency, should a designer choose increased efficiency over increased power. Subject to some loss, the size of a network which implements a delay bears a precise relationship to the size of a corresponding lumped filter, allowing accurate comparisons between conventional and resonant design on a constant-performance or constant-volume basis. The glorious fact is that multi-resonant structures can be *much smaller* than conventional reactive networks for constant ripple performance.[9] Circuit models for lumped approximations of transmission delays, as compared to lower-order lumped networks with the same total inductance and capacitance, are presented in Chapter 2 alongside background material for subsequent chapters.

It is worthwhile reiterating that a avoiding a straight energy-impedance or volume-impedance tradeoff requires a gross departure from single-pole dynamics. Though the delays we will consider are on the order of 10–100 nanoseconds, multi-resonant structures must still provide several cycles of phase shift at switching-frequency harmonics, all subject (for ideal performance) to the same excitation condition depicted schematically in Fig. 1.4 (i.e., the higher-order modes must still be excited at the proper point during a switching period). Large phase shift implies that our networks must necessarily contain many poles, and hence many inductors and capacitors. The phase conditions placed on these harmonic modes highlights the need for an accurate understanding of high-order modal-frequency alignment, the subject of Chapter 3. This chapter presents a new clarification, in particular, of the otherwise fuzzy boundary between lumped and distributed systems.

A new class of soft-switching HF/VHF power inverters incorporating multi-resonant net-

[9] Magnetic-volume reduction of three times was demonstrated using the single-resonant method for developing impedance at the switching fundamental, by electrical analogy to Fig. 1.4 [16, 17].

IPR2024-00706 EX. 2005

works as delay elements is presented in Chapter 4. This converter is one of numerous examples that could have been chosen to demonstrate the principles of Chapters 2 and 3. The control context of this thesis will be considered in more detail here, in particular the topology, tuning, and regulation issues which are perhaps the greatest barriers to operating at dramatically increased switching frequencies.

Chapter 5 presents methods for fabricating structures which approximate delays, at both the wafer/package and PCB scales. A 3-D copper electroformation process that extends the practical dimensions of on-die magnetics is the central contribution of this chapter. Air-core magnetic structures — suitable for switching frequencies higher than in the PCB case — can be electrodeposited by this technique on finished die using additive, low-temperature processes.

Memory- or delay-based power electronics in general, and multi-resonant components in particular, are an effective means of reducing the values and bulk of passive components required to implement a power-conversion function. Multi-resonant passive networks enforce converter waveform symmetries that can be exploited to increase efficiency or output power with smaller reactive-component values, as will be seen in comparisons with conventional power-electronics circuits. The components, converters, and manufacturing techniques presented in this thesis provide, moreover, a viable means for *printing* all converter passives elements, including those normally considered too large for laminate construction.

As a final note, it should be mentioned that though we've introduced delay components in a context of miniaturization and board- and die-level integration, there is no reason that multi-resonant techniques cannot be applied to conventional discrete designs. As exemplified by the 1 kW converter for the automotive electro-hydraulic power-steering system in Fig. 1.7 (shown alongside the component dimensions for its second-order, conducted-EMI filter), passive sizes for discrete designs can dominate converter volume and contribute significantly to material and assembly cost. Even without dramatic shifts in manufacturing technique, reduction of parts count is of considerable value in a cost-sensitive designs for the automotive industry.

IPR2024-00706 EX. 2005

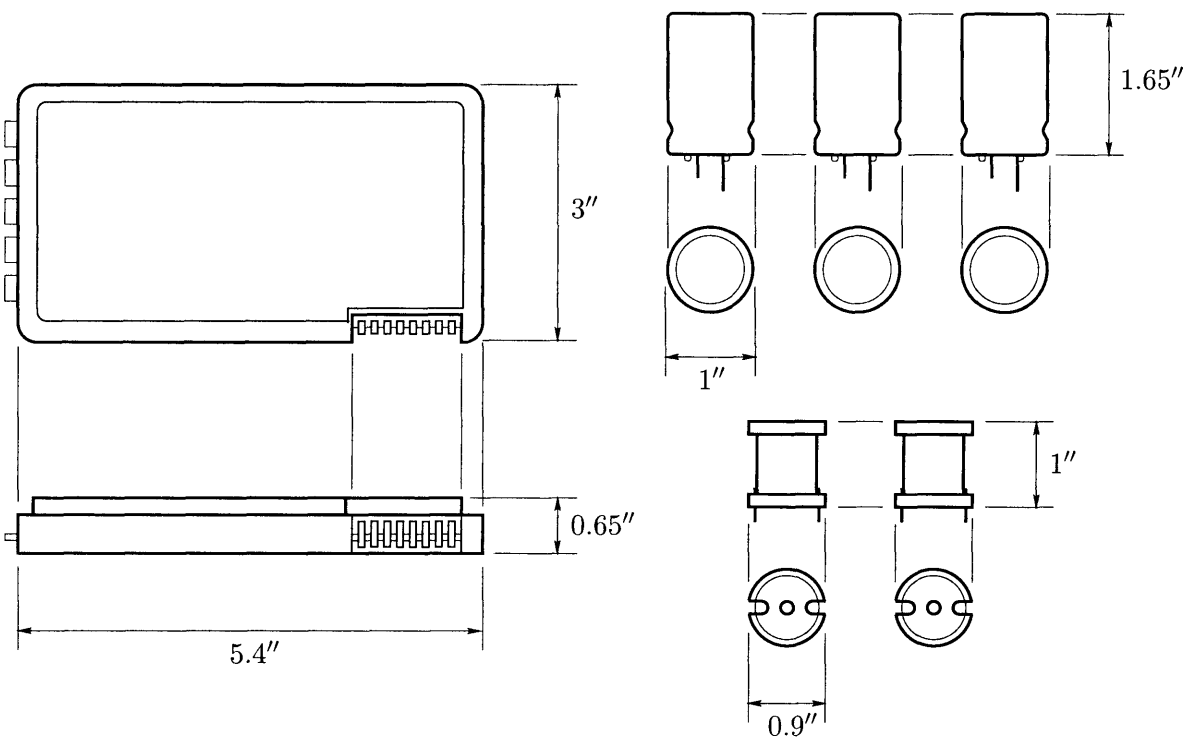

Figure 1.7: **Physical dimensions the power converter module and EMI-filter components for an Automotive EHPS (Electro-Hydraulic Power Steering) system. The converter module is mounted in the hydraulic fluid reservoir, so little extra volume is required for heatsinking. The volume of the 5 principle EMI filter elements (3 capacitors and 2 inductors) is 5.65 in^3, compared to about 6 in^3 converter volume (control and power devices) within the depicted enclosure.**

IPR2024-00706 EX. 2005

Chapter 2

Resonators and transmission lines

THERE are two important regimes of operating frequency, distinguished by whether one may treat a network as lumped or distributed. In the distributed regime, resonance assumes its proper significance, namely — at "re-sonance" — reflected waves return through a transport delay precisely in phase or out of phase with the sinusoidal drive depending on the properties of the reflecting interface. On an impedance basis[1], any frequency at which a returning wave is in phase with applied effort is an impedance pole, and the generator source impedance is bootstrapped insofar as the transport delay preserves the energy stored in the travelling wave (*cf.* the electrical analog of Fig. 2.1a, top). With perfect fidelity, the returning wave develops infinite input impedance at the driven port, requiring no flow from the source. An inverted reflected wave, on the other hand, cancels source effort at an impedance-zero frequency. The input port demands a large flow limited by the source impedance R_s, completely collapsing source effort in the case of perfect return-wave fidelity.

Focusing on the electrical case, when a transmission line is longer than a some fraction of a signal wavelength, the finite speed of signal propagation is significant (referring to Fig. 2.1a, "some fraction" is often set somewhat arbitrarily as the lower bound $\ell > \lambda/10$). Near the lower bound, the schematic twin-lead lines of Fig. 2.1a store less and less energy in travelling waves, Kirchhoff's laws become less approximate when applied to the lines' port variables, and partitioning of energy-storage volume becomes less ambiguous. Finally, when $\ell \ll \lambda$, the impedance of the short-circuited twin-lead of Fig. 2.1a closely approximates that of the loop inductance L_0. The transmission-line conductors link flux in a quasistatic sense, and the stored magnetic energy is accurately measured by the line's port variables (by loop current, in this case). Likewise for the open-circuit termination, as $\ell \ll \lambda$ the line impedance approaches that of the low-frequency line capacitance C_0, and the unloaded source voltage

[1]according to typical impedance analogies between electric and mechanical system, "effort" is a voltage or a force, and "flow," "current," and "velocity" are interchangeable.

IPR2024-00706 EX. 2005

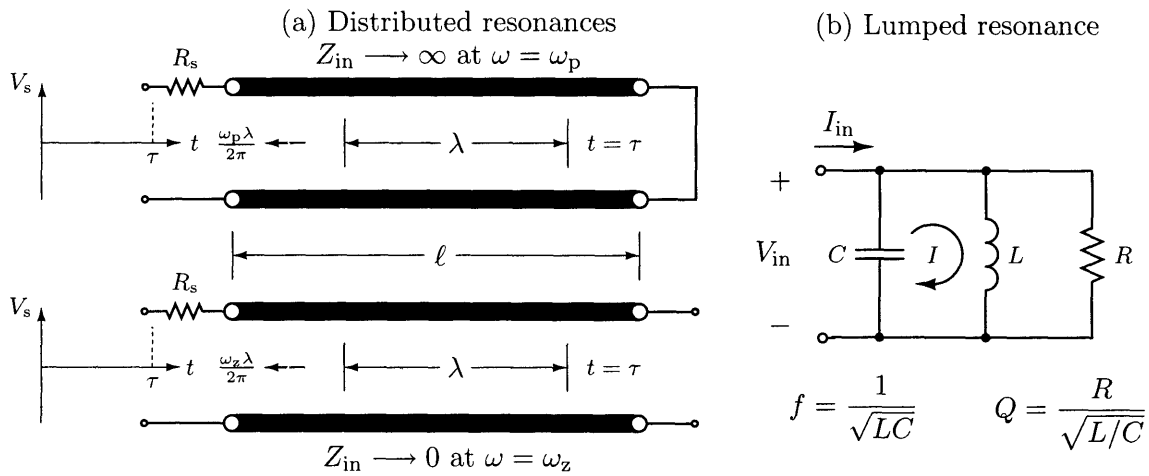

Figure 2.1: **Distributed and lumped resonators, demonstrating how stored waveforms can develop impedance extrema**

accurately measures the electrical energy stored in the structure.

In this lumped regime, so-called because of the partitioning of energy storage elements, resonance is perhaps not immediately recognizable as a case of waveform storage or delay in the sense of Chapter 1. Consider, however, the circulating current in the tank of Fig. 2.1b. At resonance, the voltage across the network is $V_{in} = I_{in}R$. Since the inductive and capacitive reactances are equal in magnitude at resonance, the inductor and capacitor branch currents are also equal in magnitude:

$$|I_L| = |I_C| = \frac{|V|}{Z} = \frac{|I_{in}|\,R}{\omega_0 L} = \frac{|I_{in}|\,R\sqrt{LC}}{L} = |I_{in}|\,\frac{R}{\sqrt{L/C}} = Q\,|I_{in}|$$

Though the current flowing in the inductive and capacitive branches is Q times higher than the net terminal current, the network impedance is also Q times as higher than either reactance at resonance. The tank circulating current, therefore, is the current that would have been provided from by external network had it driven either reactance with the same voltage magnitude V_{in} at the resonator terminals. In the parallel-tuned case, we can think of the capacitor as storing — at one frequency $\omega_0 = 1/\sqrt{LC}$ — the current that would have been supplied in its absence. Once energized, and with perfect cycle-to-cycle energy fidelity (infinite tank Q), the tank capacitance supplies *all* of the current necessary to maintain V_{in} across L, and the input impedance is infinitely large.

As introduced in Chapter 1, the waveform-storage properties of resonances (in both the

IPR2024-00706 EX. 2005

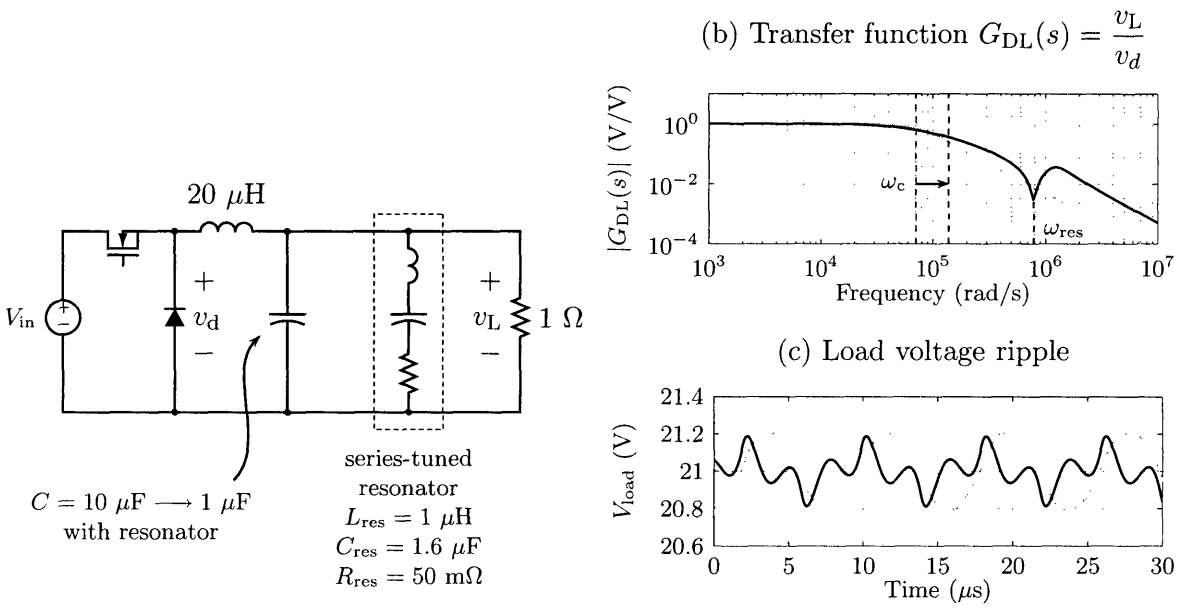

Figure 2.2: **(a) Buck converter demonstrating the reduction in output-network component values by the introduction of a series-tuned resonance. As shown in (b), the output-network presents a low impedance at the converter switching frequency f_{sw}.**

distributed and lumped regimes) can supplant bulk energy-storage in power converters. Though electrical resonances are considered in this chapter, the same framework — Q, characteristic impedance, and coupling — applies to the electromechanical analogs of Chapter 6. We will extend the present discussion to multi-resonant structures in Section 2.2, after considering their single-resonant counterparts in more detail.

2.1 Networks with one resonance

Networks incorporating a single resonance are a convenient means of reducing the volume of the passive components in a power converter, and for increasing converter control bandwidth. Resonant ripple filters with active tuning control [16]–[19] use the immitance peaking of series- and parallel-tuned networks to provide extra attenuation at discrete frequencies, reducing the requirements on accompanying low-pass networks. A series-tuned resonator in parallel with the load in Fig. 2.2a), for instance, diverts power-stage ripple currents away from the load at the switching frequency when properly tuned ($\omega_{res} = 2\pi f_{sw}$). With deep

IPR2024-00706 EX. 2005

resonant attenuation of the fundamental, higher switching harmonics need not be attenuated as effectively to maintain peak-to-peak ripple performance (Fig. 2.2c), so that the corner frequency of an accompanying low-pass filter (comprising the 20 μH buck inductor and output capacitor C) can increase nearly two times. Though the resonator introduces more passive components into the output network, the total value of the passives components (as well as their bulk) can typically be reduced three times or more [16, 18, 17].

Along with smaller passive components — i.e., less capacitance and inductance — comes faster closed-loop response. Consider the buck converter and resonant-filter buck converter in Fig. 2.3 operating under average current-mode control, where instead of a series-tuned network, a parallel-tuned resonator has been introduced into the switching cell. In this dual of Fig. 2.2a, the increase in low-pass corner frequency is due to a decrease in the buck inductance, which diminishes more than 4.9 times (from 59 μH to 12 μH) while maintaining constant peak-to-peak current ripple. The average inductor current in the converter with the resonant filter can slew more than twice as fast as the regular buck converter, for the same current-loop phase margin and ripple performance (at $D = 0.5$). The power-cell resonance is closed within the current loop, so the outer voltage-loop has no special complications; the controller commands inductor current into the same load and output capacitor, but with higher bandwidth in the resonant case.

The smaller passive values in resonant networks can also reduce manufacturing and material costs. The magnetizing inductance L_μ of air-core transformers and inductors, for instance, are typically too low for many practical power-conversion applications. A capacitor in parallel with a low L_μ (Fig. 2.4), however, decreases the current supplied by the driving network — at the resonant frequency — by ringing the magnetizing current i_μ from an internal mode of energy storage. Such single-resonant techniques have made printed-magnetic implementations of gate drives and isolated converters practical [20].

To take advantage of high-Q resonant filters, a designer must ensure that the converter switching frequency remains aligned with the filter resonance across component variations and operating conditions. Excitation of a resonance is equivalent to maintaining a resistive phase relationship (0°) between resonator voltage and current, a phase shift which increases or decreases monotonically around the 0° tuning point (*viz.* the grey phase curve of Fig. 2.4b). Whether a network's impedance transitions from capacitive to inductive phase or vice versa past resonance, the $I - V$ phase difference can be used as an error signal

IPR2024-00706 EX. 2005

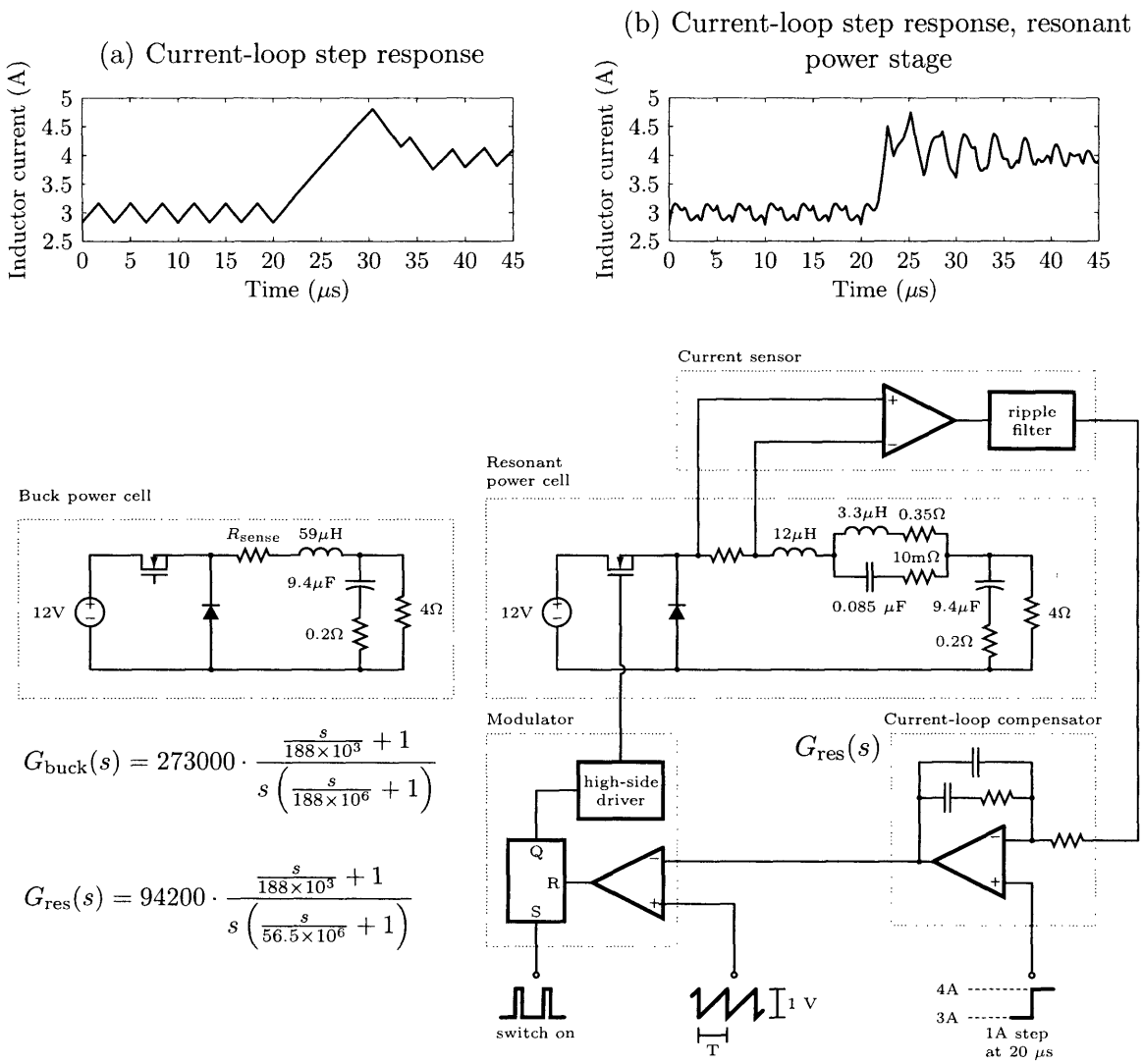

$$G_{buck}(s) = 273000 \cdot \frac{\frac{s}{188\times10^3}+1}{s\left(\frac{s}{188\times10^6}+1\right)}$$

$$G_{res}(s) = 94200 \cdot \frac{\frac{s}{188\times10^3}+1}{s\left(\frac{s}{56.5\times10^6}+1\right)}$$

Figure 2.3: **Simulated step responses of current-control loops for a (a) buck converter and (b) a buck converter with a power-stage resonance, demonstrating an increase in control bandwidth accompanying a reduction in power-stage inductance. Both converters are 300-kHz, 36 W buck converters under average current-mode control, and the magnetics are designed for ferrite cores using manufacturer's loss models. That the resonant filter behaves like a smaller inductor across the regulation bandwidth is plausible: the resonator Q is high enough that impedance variations are appreciable only above half the switching frequency, yet not so high that earlier crossover is necessary to maintain acceptable gain margin in the current-command loop.**

IPR2024-00706 EX. 2005

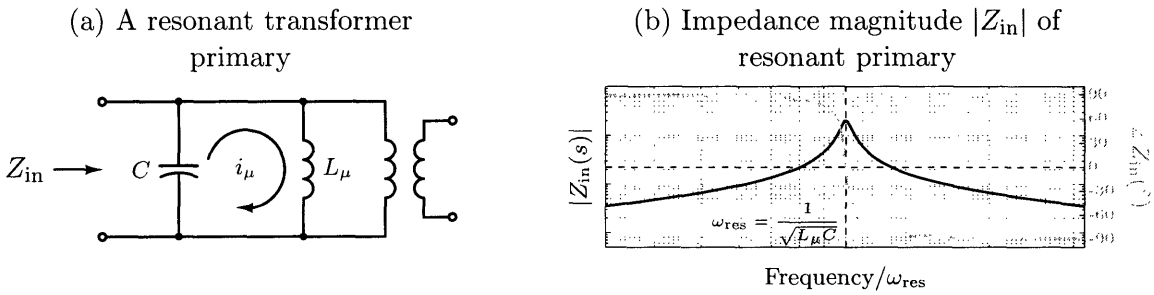

Figure 2.4: **A resonant transformer primary, illustrating how magnetizing current i_μ can be supplied by the capacitance C, increasing the impedance Z_{in} seen from the primary terminals at a discrete frequency.**

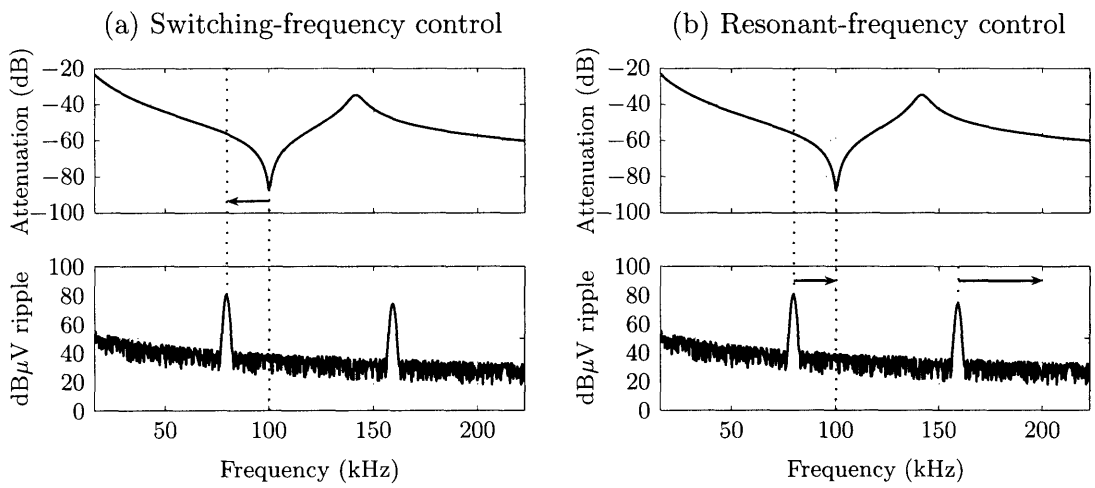

Figure 2.5: **Two tuning methods which assure resonant attenuation over a range of component values and operating conditions**

to tune an excitation to the frequency of maximum immitance or attenuation, as shown schematically in Fig. 2.5a. The phase-lock tuning systems presented in [16, 18, 17] employ this method precisely, feeding back impedance phase to drive a voltage-controlled oscillator (VCO) toward a series- or parallel-tuned frequency.

Phase-sensing control can be applied to tune a filter resonant frequency (as in Fig. 2.5b) rather than a converter switching frequency. An electrically controlled reactance implemented, for instance, with a cross-field reactor [21]–[24] can shift a filter transmission null as currents are applied to a control winding. An advantage of the resonance-tuning approach is that it can support tuned attenuation of multiple harmonic frequencies.

IPR2024-00706 EX. 2005

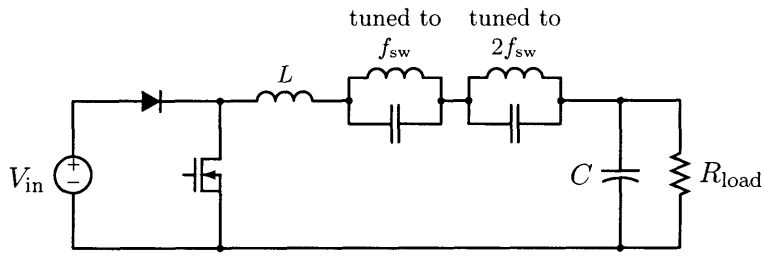

Figure 2.6: **Cascaded, parallel-tuned resonators in the power-stage of a buck converter, an extension of the network in Fig. 2.3**

2.2 Networks with multiple resonances

Multi-resonant extensions of filters like those in Section 2.1 could realize even greater attenuation than their single-resonant counterparts. Discrete resonators might be cascaded as in Fig. 2.6, with branch or mesh resonances tuned to a fundamental frequency and select harmonics. Such networks could present impedance extrema to a general class of periodic waveforms, rather than just one frequency-component of a switching waveform, as in Fig. 2.2b. In the PWM converters of Figs. 2.2 and 2.3b, a single resonance is aligned to $\omega_{\text{res}} = 2\pi f_{\text{sw}}$ so that switching ripple is mitigated most effectively at a duty ratio $D = 0.5$. Harmonic resonances at the second or third multiple of f_{sw} could effectively limit peak-to-peak load-voltage ripple over a broader range of duty ratios.

The performance promise of multiple, discrete resonators is undermined by practical considerations of tolerance and volume. The alignment of multiple modal frequencies, whether by careful manufacture or closed-loop control (along the lines of Fig 2.5), grows so rapidly in complexity as to be impractical for mass-manufactured power electronics.[2] The cascaded approach to synthesis, moreover, is volume-inefficient beyond two or three resonances, as will be demonstrated in Section 2.3.

A transmission-line resonator (*cf.* Fig. 2.7) circumvents the problems of large size and imprecise alignment of critical-frequencies quite naturally. Whether terminated in an open or short, the line and its boundary conditions develop many extrema in Z_{in} — an *infinite* number in the lossless case — by a corresponding number of modeshapes superposed along a single arrangement of conductors and dielectric. The material of the line is effectively

[2]In large power-electronics systems the effort may be cost-effective. The 2 GW, 12-pulse inverter at Sandy Pond in Massachusetts, for instance, has 100-yard long banks of carefully aligned harmonic traps on its AC side.

IPR2024-00706 EX. 2005

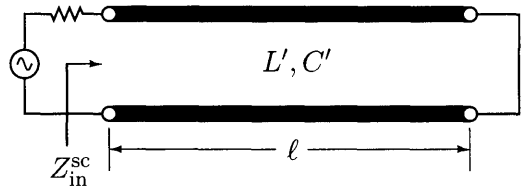

Figure 2.7: **A uniform, lossless transmission line used to introduce the frequency relationships of impedance nulls and peaks.**

reused, and such a distributed structure is much smaller than a cascaded realization of the same impedance extrema (with one resonator per mode, as in Fig. 2.6). The impedance pole and zero frequencies, corresponding to standing-wave constraints enforced by the the line's termination and propagation properties, are precisely related among themselves inasmuch as the line and its terminations are predictable.

Expressions for the critical frequencies of the terminated line can be derived by reference to Fig. 2.7, which illustrates a line of length ℓ short-circuited at the far end. Z_{in} might represent the impedance seen from a drain node in a power converter — looking back to the source or toward the load — in which the terminal short is approximated in practice by a small AC reactance (a large capacitance). If L' and C' are the distributed inductance and capacitance per unit length, the input impedance is a transcendental function with an infinite number of j-axis poles [25]:

$$Z_{\text{in}}^{\text{sc}} = j\sqrt{\frac{L'}{C'}}\tan\left(\omega\ell\sqrt{L'C'}\right) \tag{2.1}$$

The zeros of $Z_{\text{in}}^{\text{sc}}$ are seen to lie at $s = j\omega_\nu$, where

$$\omega_\nu = \frac{\nu\pi}{2\ell\sqrt{L'C'}} \quad \text{for } \nu = 0, 2, 4, \ldots \tag{2.2}$$

The admittance, likewise, is

$$Y_{\text{in}}^{\text{sc}} = -j\sqrt{\frac{C'}{L'}}\cot\left(\omega\ell\sqrt{L'C'}\right) \tag{2.3}$$

so that the poles of $Z_{\text{in}}^{\text{sc}}$ are described by Eqn. 2.2 for *odd integral* ν. By a similar development for an open-circuit termination, $Z_{\text{in}}^{\text{oc}}$ is maximum at DC and all even integral multiples of the first null frequency. In a converter whose switching frequency f_{sw} is aligned to the first impedance maximum of a open-circuited transmission line, therefore, the line presents

IPR2024-00706 EX. 2005

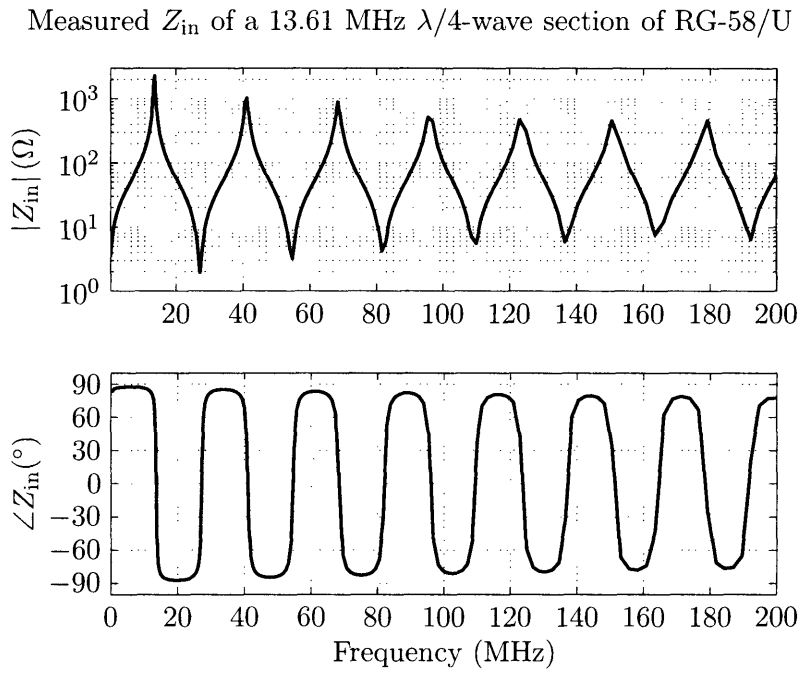

Figure 2.8: **Measured input impedance of a 13.61 MHz $\lambda/4$-wave section of RG-58/U coaxial line, terminated in a short circuit**

high impedance to dc and *all integral multiples* of the switching fundamental, i.e., a high impedance to any waveform periodic in $T = 1/f_{\text{sw}}$.

The measured input impedance of a 136" length of RG-58 coaxial line terminated in a short is shown in Fig. 2.2. The principal quarter-wave resonance at $\omega_1/2\pi = 13.61$ MHz is followed by zeros and poles at even and odd multiples of ω_1, respectively, as just described. For a voltage excitation with period $T = 2\pi/\omega_1$ from a finite source impedance, the low even-harmonic impedance will effectively short out the corresponding harmonics (ω_2, ω_4, ω_6, ...). Because the line will not collapse odd-harmonic voltages,[3] the voltage waveform at the input port will be *half-wave symmetric*, as depicted in Fig. 2.9a. At even multiples of ω_1, the line will draw large currents by collapsing the effort applied by the source. The input-port current will have enriched even-harmonic content or, equivalently, one-half the period $T = 2\pi/\omega_1$ of the source. The current in this case is *half-wave repeating*, a sum of even harmonics as shown in Fig. 2.9b.

[3]The line is a quarter-wave transformer of the short-circuit termination at $\omega = \omega_1$, with a large impedance at that frequency and all its odd multiples. Recall that for every additional $\lambda/4$ length of line the driving-point impedance is inverted. In the lossless case the line transforms the termination from a short → open → short → ··· for successive zero → pole → zero → ··· , at each of which, successively, the line is electrically one quarter-wavelength longer.

IPR2024-00706 EX. 2005

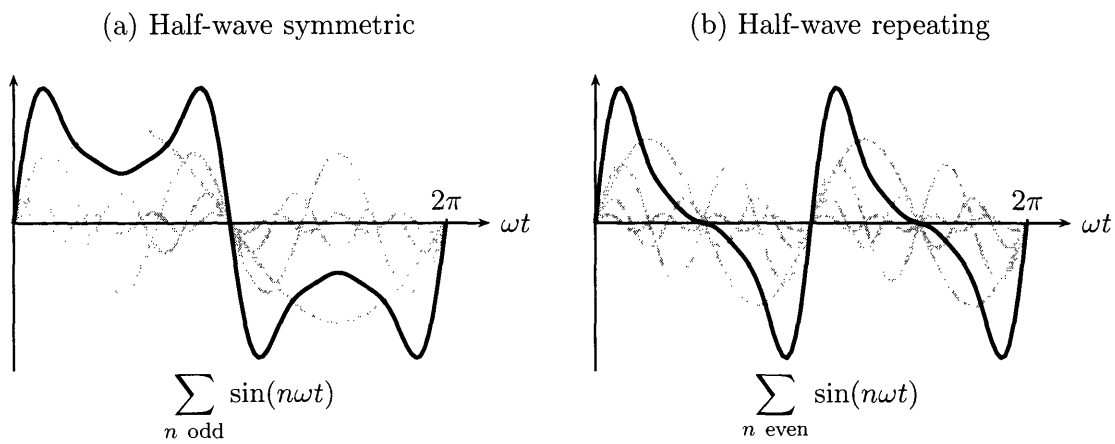

Figure 2.9: **The sum of odd harmonics is a half-wave symmetric waveform, and the sum of even harmonics is a half-wave repeating waveform.**

Note that the V–I symmetry relations are the result of the line's infinite-dimensional dynamics, and obtain even for a half-period of effort by the source. If the external circuit imposes a voltage waveform during the first half of a cycle, the transmission line will become energized so as to impose a half-wave symmetric voltage during the other half, even if the source is removed. The line stores the voltage waveform in a travelling wave along its length, which returns delayed by one-half fundamental period and inverted, because of the power-reflection condition at the short-circuit termination. The applied current wave also returns, delayed π/ω_1 seconds but erect, so that the line attempts to do the same work on the network at its input port that was done on the line in the first half of the cycle.

Multi-resonant networks, as exemplified by the transmission line, are much more than a means of generating large impedance extremes, by analogy to the single-resonant case. The control of *zero and pole frequencies* is key to enforcing symmetries in voltage and current waveforms, and is a ready means of not only reducing the volume of passive components in a power converter, but of limiting device stresses, increasing efficiency, creating soft-switching opportunities, or altogether eliminating switches in certain cases. Applications of transmission lines and their approximating networks will be considered further in Chapter 4.

IPR2024-00706 EX. 2005

2.3 Lumped models for the terminated transmission line

Chapter 3 treats in detail the problem of constructing compact structures which mimic the driving-point impedance of a transmission line over a range of frequencies. These designs are based upon lumped models of the line, so it is of some interest to discuss possible ways of synthesizing finite-dimensional networks simulating a full, infinite-dimensional transmission delay.

The transcendental functions describing the input immitance of a transmission line (Eqns. 2.1 and 2.3) have an infinite number of ordinary poles, and can at best only be approximated by a finite network. However, since the poles are all simple and lie on the $j\omega$-axis, and the residues are all real and positive, it is reasonable that a lumped, finite network can be constructed which simulates the impedance Z_{sc} over a finite range of frequencies [26]. Such a simulating network has several possible forms, though the so-called Foster form (considered further in Section 2.3.1) is easiest to derive because of its explicit relationship to modal frequencies.

A generic expression for the input impedance $Z_{\text{in}}(s)$ of the line of Fig. 2.7 has a finite number of simple zeros at $s = 0$, $\pm s_2$, $\pm s_4, \ldots$, and simple poles at the points $\pm s_1$, $\pm s_3, \ldots$. As a quotient of factored polynomials $Z_{\text{in}}(s)$ has the form

$$Z(s) = G \cdot \frac{s(s^2 - {s_2}^2)(s^2 - {s_4}^2)(s^2 - {s_6}^2)\cdots}{(s^2 - {s_1}^2)(s^2 - {s_3}^2)(s^2 - {s_5}^2)\cdots} \tag{2.4}$$

where G is a constant impedance-level factor, and each factor $(s^2 - s_\nu^2) = (s + j\omega_\nu)(s - j\omega_\nu)$ represents a pair of conjugate, imaginary critical frequencies. For $\omega \ll \omega_\nu$, $Z(s)$ is dominated by the factor $s = j\omega$ in the numerator, and is evidently an impedance function describing the short-circuit case. Evaluated at any $s = j\omega$, the impedance will have a real and imaginary component $Z(j\omega) = R(j\omega) + jX(j\omega)$, but because the singularities of the transmission-line impedance Z_{sc} lie along the $j\omega$-axis, $Z(s)$ cannot consume any average power in sinusoidal steady state, and is represented fully by its lossless reactance function $Z(j\omega) = X(j\omega)$.

The reactance function $X(j\omega)$ has several properties worth mentioning because of the insight they offer into the network synthesis problem. $X(j\omega)$, first of all, has a positive nonzero

IPR2024-00706 EX. 2005

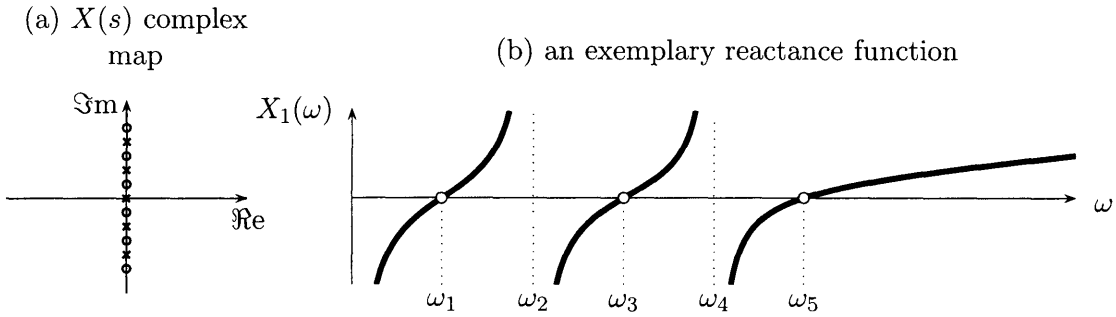

Figure 2.10: **An exemplary reactance function** $X(j\omega)$

slope at all j-axis frequencies, i.e.,

$$\left[\frac{dX(s)}{d\omega}\right]_{s=j\omega} > 0$$

In the context of a Lagrangian formulation for network equilibrium in terms of associated energy functions [27, Chapter 10], this constraint on reactance slope follows from the Cauchy-Riemann equations [28, Chapter 6] and is of a fundamental character. From an intuitive point of view in the complex plane (*viz.* Fig. 2.10a), $Z(j\omega)$ will assume completely inductive or capacitive phase when evaluated along the positive $j\omega$ axis. For either $\pm 90°$, the reactances ωL and $-1/\omega C$ *increase* with increasing ω.

The $dX/d\omega > 0$ condition shows in the first place, and in agreement with the assumed formulation of Eqn. 2.4, that all of the zeros must be simple. Referring to Fig. 2.10b, $X(j\omega)$ clearly has one intersection with the ω-axis for each capacitive-to-inductive traverse, and since the corresponding analysis on an admittance basis shows the slope of the susceptance function $Y(j\omega) = jB(j\omega)$ to be strictly positive, the zeros of $Y(s)$ and the poles of $Z(s)$ are likewise simple. The positive-slope condition requires, secondly, that poles and zeros must alternate since $X(j\omega)$ is constrained to the general appearance of Fig. 2.10b. I.e.,

$$0 < \omega_1 < \omega_2 < \omega_3 < \omega_4 < \cdots$$

Two zeros cannot follow in succession because reactance always increases with ω, nor can two poles, since the reciprocal $B(j\omega)$ has the same character. The customary interpretation of the complex Z-plane as the surface of a sphere is important to keep in mind here, on the surface of which the imaginary axis is a great circle passing through the south pole at $Z = 0$

IPR2024-00706 EX. 2005

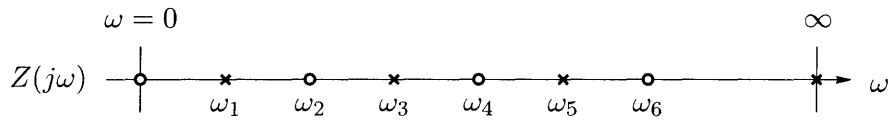

Figure 2.11: **Frequency pattern depicting all the information necessary to specify a reactance or susceptance function. For this particular arrangement of ω_1–ω_6, the alternation property of poles and zeros requires that $Z(s)$ have a zero at $s = 0$ and a pole $s = \infty$, because the lowest and highest non-zero critical frequencies are pole and zero, respectively.**

and through the north pole at $Z = \infty$. Passage through $X = \infty$ results in the behavior shown in Fig. 2.10b where, after reaching $+\infty$, the function emerges out of $-\infty$ without violating the condition that it must continuously increase.[4]

$X(s)$ has further structure which determines its asymptotic high- and low-frequency behavior. If the highest-index factor $(s - s_\nu)$ in Eqn. 2.4 is in the numerator, then its degree is evidently larger by one than the degree of the denominator, and the function $Z(s)$ has a simple pole at $s = \infty$. If the last factor is in the denominator, then the denominator degree exceeds that of the numerator by one, and $Z(s)$ has a zero at $s = \infty$. The former case corresponds to a inductance dominating the high-frequency dynamics of $Z(j\omega)$ for $\omega \gg \omega_\nu$, and the latter case to asymptotic capacitive impedance. This limiting high-frequency behavior is a property of the finite-order approximation for the transmission-line impedance; the line itself has no asymptotic behavior at $s = \infty$ in the lossless case. The zero at $s = 0$ results from the factor s in the numerator (the numerator must incidentally be odd), corresponding to low-frequency inductive reactive and a short-circuit termination. If instead $Z(s)$ is an even-over-odd quotient, then the point $s = 0$ is a pole, corresponding to an open-circuit termination.[5] Whether the point $s = 0$ is a zero or pole is independent of whether the point $s = \infty$ is a zero or pole.

Because of the alternation property of the zeros and poles explained above, a specification of the finite nonzero critical frequencies of $X(j\omega)$ determines the behavior at the points $s = 0$ and $s = \infty$. A frequency pattern such as that in Fig. 2.11 is sufficient to specify $X(s)$ up to its impedance-level factor G. Though this development started with an odd-over-even reactance function, a pole at $s = 0$ shifts the conventional indices of critical frequencies —

[4]this behavior is reminiscent of the Nyquist D-contour, encircling the complex right half-plane by a similar passage through $s = \infty$.

[5]Note that, along with the odd/even-order property of the polynomials as a whole, the conjugate pole-pairs in numerator in denominator ensure that the degrees of their respective summands are odd/even interleaved.

IPR2024-00706 EX. 2005

the poles and zeros, numbered with increasing ω — so that the poles have *even-numbered*, and the zeros *odd-numbered* indices.

2.3.1 Foster realizations of transmission-line impedance

Though we will make much use later of the insights gained from the rational form of $X(s)$, a partial-fraction expansion for $X(s)$ is useful for the line-impedance synthesis problem at hand. $X(s)$ may be written in terms of the residues k_1, k_3, k_5, ... k_∞ in its poles at $s = \pm j\omega_1$, $\pm j\omega_3$, $\pm j\omega_5$,... and $s = \infty$ respectively [26, Sections 2.1 and 3.2]:

$$X(s) = \frac{2k_1 s}{s^2 + {\omega_1}^2} + \frac{2k_3 s}{s^2 + {\omega_3}^2} + \frac{2k_5 s}{s^2 + {\omega_5}^2} + ... + k_\infty s \tag{2.5}$$

Here we've assumed that the high-frequency reactance is asymptotically inductive by the inclusion of the k_∞ term, which will vanish for a zero at $s = \infty$. These residues may be evaluated by several methods [28], including the well-known Heaviside "cover-up" method, *viz.*

$$k_n = \left[(s - s_\nu)X(s)\right]_{s=s_\nu} \tag{2.6}$$

In the form of Eqn. 2.4 with unity impedance-level factor, and setting the highest finite critical frequency arbitrarily at $\omega = \omega_4$, the residue in the pole at ω_1 is

$$(s - j\omega_1)Z(s) = \frac{s(s^2 + {\omega_2}^2)(s^2 + {\omega_4}^2)}{(s + j\omega_1)(s^2 + {\omega_3}^2)}$$

and since $s = j\omega_1$

$$k_1 = \frac{({\omega_2}^2 - {\omega_1}^2)({\omega_4}^2 - {\omega_1}^2)}{2({\omega_3}^2 - {\omega_1}^2)}$$

More useful in the case of a transcendental impedance function, with an infinite number of poles, is an expression for the residues in terms of the slope of the susceptance $B(s) = X(s)^{-1}$:

$$k_\nu = \left[\frac{dB(s)}{ds}\right]^{-1}_{s=s_\nu} \tag{2.7}$$

A thorough development of this expression is found in [28, Chapter 6, Art. 15], but a brief example here will show the equivalence to more familiar means of partial-fraction expansion.

IPR2024-00706 EX. 2005

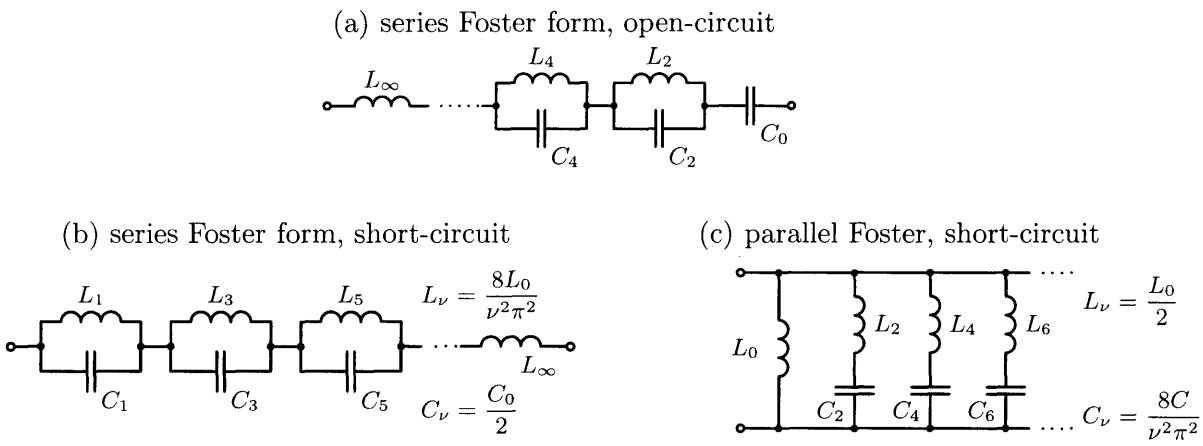

Figure 2.12: **A canonical Foster form (a) for network synthesis in the case of an open-circuited line, and series (b) and parallel (c) Foster realizations of the impedance of a transmission line with short-circuit termination**

For the same residue considered above, the admittance function is

$$Y(s) = \frac{(s^2 - {s_1}^2)(s^2 - {s_3}^2)}{s(s^2 - {s_2}^2)(s^2 - {s_4}^2)} = \frac{Q(s)}{P(s)}$$

and since $Q(s_1) = 0$,

$$\left[\frac{dY(s)}{ds}\right]_{s=s_1} = \left[\frac{P(s)Q'(s) - Q(s)P'(s)}{P^2(s)}\right]_{s=s_1} = \frac{Q'(s_1)}{P(s_1)} \tag{2.8}$$

If we now write $Q(s) = (s^2 + {\omega_1}^2)q(s)$, then

$$Q'(s_1) = \left[(s^2 + \omega_1^2)q'(s) + 2sq(s)\right]_{s=s_1} = 2s_1 q(s_1)$$

Substitution of this expression into Eqn. 2.8 and the result into Eqn. 2.7 yields, on an impedance basis

$$k_1 = \frac{P(s_1)}{2s_1 q(s_1)} = \left[\frac{(s^2 + {\omega_2}^2)(s^2 + {\omega_4}^2)}{2(s^2 + {\omega_3}^2)}\right]_{s^2 = -{\omega_1}^2}$$

In agreement with the earlier result.

The admittance-slope expression provides a ready means of synthesizing a reactance or susceptance function when its zeros and slope are easily determined, even if the function itself is not algebraic and subject to the development of Eqn. 2.6. For the transmission-line impedance of Eqn. 2.1, for instance, component values in the so-called series Foster form

IPR2024-00706 EX. 2005

(Fig. 2.12b [29, Chapter 4]) can be determined by a term-by-term comparison of the Foster impedance to Eqn. 2.5:

$$Z_{\text{Foster}} = \frac{\frac{1}{C_1}s}{s^2 + \frac{1}{L_1C_1}} + \frac{\frac{1}{C_3}s}{s^2 + \frac{1}{L_3C_3}} + \cdots + sL_\infty$$

from which

$$\omega_\nu{}^2 = \frac{1}{L_\nu C_\nu} \quad \text{and} \quad 2k_\nu = \frac{1}{C_\nu} \quad \text{for } \nu = 1, 3, 5, \ldots$$

where the $L_\infty = k_\infty$ term will vanish in the case of a zero at $s = \infty$. Rewriting in terms of the susceptance slope:

$$C_\nu = \frac{1}{2}\left[\frac{dB(s)}{ds}\right]^{-1}_{s=s_\nu} \quad \text{and} \quad L_\nu = \frac{1}{C_\nu \omega_\nu{}^2}$$

for $\nu = 1, 3, 5, \ldots$. Referring back to the short-circuit admittance Y_{sc} of the transmission line in Eqn. 2.3, the zero admittance frequencies are

$$\omega_\nu = \frac{\nu\pi}{2\ell\sqrt{L'C'}} \quad \text{for } \nu = 1, 3, 5, \ldots$$

from which the Foster capacitances can be found:

$$\left[\frac{dY_{\text{in}}^{\text{sc}}}{ds}\right]_{\omega=\omega_\nu} = \sqrt{\frac{C'}{L'}}\frac{\ell\sqrt{L'C'}}{\sin^2\theta_\nu} = C'\ell = C_0 \tag{2.9}$$

I.e., $C_\nu = C_0/2$, where C_0 is the total open-circuit, low-frequency line capacitance. The corresponding modal inductances L_ν decrease as the square of the mode-number:

$$L_\nu = \frac{8L_0}{\nu^2\pi^2} \quad \text{where} \quad L_0 = L'\ell \tag{2.10}$$

For the parallel Foster form (Fig. 2.12c), a dual development from a partial-fraction expansion for susceptance is straightforward:

$$L_\nu = \frac{1}{2}\left[\frac{dX(s)}{ds}\right]^{-1}_{s=s_\nu} \quad \text{and} \quad C_\nu = \frac{1}{L_\nu \omega_\nu{}^2}$$

for $\nu = 1, 3, 5, \ldots$, in which $s_\nu = j\omega_\nu$ are the poles of $Y(s)$ and the zeros of $Z(s)$. In the transmission-line case, again noting a shift in the numbering of critical frequencies, the

IPR2024-00706 EX. 2005

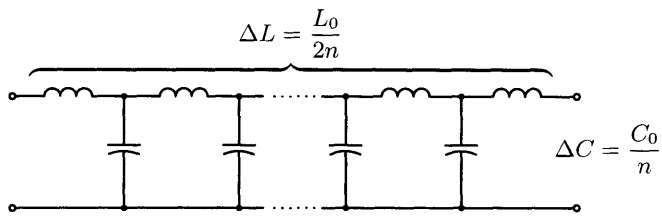

Figure 2.13: **Iterated Cauer model for the transmission line. n iterated T-sections are shown, though L and Π sections could be used. The total open-circuit line capacitance C_0 is divided into n equal ΔC, and the short-circuit line inductance L_0 is divided into $2n$ equal ΔL (the left and right crossbars of each T-section). The ΔL of adjacent T-sections add to L_0/n along the line, with half-sections at either end. Such an arrangement has a higher cutoff frequency than the network with uniform inductances (see Section 2.3.3)**

derivative of $Z_{\text{in}}^{\text{sc}}$ (Eqn. 2.1) yields series-tuned inductances and capacitances:

$$L_\nu = \frac{L_0}{2} \qquad C_\nu = \frac{8C_0}{\nu^2\pi^2} \tag{2.11}$$

These expressions for line modes — in terms of modal inductance and capacitance — are useful for design comparisons because they are expressed in terms of C_0 and L_0, the total low-frequency open-circuit line capacitance and short-circuit line inductance. The relative merits of distributed resonators, lumped resonators, and bulk filters can now be treated on a common basis. E.g., for a given total C_0 and L_0, the first impedance maximum on a shorted line has an index $\nu = 1$ (with $\nu = 0$ for the DC zero). From Eqn. 2.10 and the modal capacitance $C_\nu = C_0/2$, the first quarter-wave resonance is at

$$\frac{1}{2\pi\sqrt{L_1C_1}} = \frac{1}{4\sqrt{L_0C_0}} \text{ Hz}$$

This resonant frequency is $\pi/2$ times higher than the knee frequency of a 2nd-order low-pass filter, should L_0 and C_0 be used in such a manner. Assuming a switching frequency of $\left(2\pi\sqrt{L_1C_1}\right)^{-1}$ Hz, a designer can compare the $-40\log_{10}(\pi/2)$ dB attenuation in low-pass case to the attenuation expected from the resonator (this attenuation depends, in turn, on Q and the impedance mismatch the resonator sees).

IPR2024-00706 EX. 2005

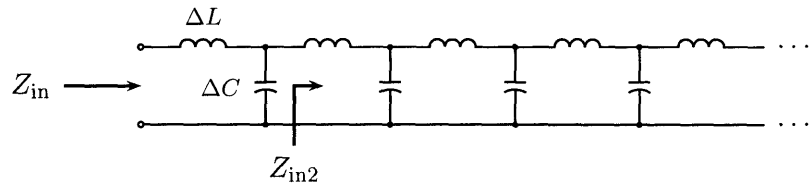

Figure 2.14: **Input impedance of a semi-infinite ladder network**

2.3.2 Cauer-form realizations of transmission-line impedance

Though the Foster realization yields a precise match to the impedance-maxima frequencies of the transmission line, an iterated network of the so-called Cauer form[6] (Fig. 2.13) exhibits an *approximate* harmonic alignment of peaks and nulls. Indeed, the network is a physical analog of a transmission line, comprising iterated L- or T- or Π-sections, with section inductance and capacitance ΔL and ΔC approximating the continuously varying magnetic and electrical quantities along the line. A semi-infinite ladder network of infinitesimally small inductors and capacitors (*cf.* Fig 2.3.2, with $\Delta L, \Delta C \longrightarrow 0$), has a purely real input impedance over an infinite bandwidth — like a lossless line — and can store infinite energy in waves propagating down its length. When terminated in its characteristic impedance $\sqrt{\Delta L/\Delta C}$, the infinitesimally sectioned ladder simulates the distributed line over an arbitrarily large bandwidth.

In RF design, uniform, lumped Cauer networks are used to realize delays with smaller overall volume than sections of transmission line. These lumped analogs offer greater control over line constants (e.g., characteristic impedance) than is readily achieved with distributed lines [30, Chapter 5]. The finite number of poles of the artificial line, however, bounds the high-frequency phase shift of the network; exactly like the algebraic expression of Eqn. 2.4, a coarse Cauer network approximates the unbounded high-frequency phase-shift of the infinite-dimensional delay. Of practical importance to an RF designer is a measure of the bandwidth over which the lumped analog is useful.

[6]Note that Cauer form, in which L and C series and shunt branches alternate along a ladder network, is distinct from Cauer synthesis, a technique for pole-zero placement in a network of Cauer structure (see Section 3.4). That a network is in "Cauer form" does not imply that its L and C values have been selected using Cauer synthesis.

IPR2024-00706 EX. 2005

2.3.3 Cut-off frequency

The useful approximation bandwidth for an iterated ladder network is usually expressed as a fraction of the cutoff frequency ω_h, the frequency below which the input impedance of the artificial line — when terminated in its characteristic impedance — has a real component [30, Section 5.7]. The cutoff frequency can be derived by assuming that input impedance of the artificial line is constant after the removal of one iterated section, an approximation which holds true for a large number of sections. Considering again the network of Fig. 2.3.2, the input impedance can be expressed as:

$$Z_{\text{in}} = s\Delta L + \frac{1}{s\Delta C} \Big\| Z_{\text{in2}}$$

Because $Z_{\text{in}} = Z_{\text{in2}}$ in the semi-infinite case:

$$Z_{\text{in}} = s\Delta L + \frac{\frac{Z_{\text{in}}}{s\Delta C}}{\frac{1}{s\Delta C} + Z_{\text{in}}} \qquad (Z_{\text{in}} - s\Delta L)\left(\frac{1}{s\Delta C} + Z_{\text{in}}\right) = \frac{Z_{\text{in}}}{s\Delta C}$$

From which

$$Z_{\text{in}} = \frac{s\Delta L \pm \sqrt{s^2\Delta L^2 + 4\Delta L/\Delta C}}{2} = \frac{s\Delta L}{2}\left(1 \pm \sqrt{1 + \frac{4}{s^2\Delta L\Delta C}}\right) \tag{2.12}$$

Substituting $s = j\omega$, the rightmost radical in Eqn. 2.12 is the only term in the bracketed expression that contributes to a real component of the input impedance. At low frequencies, for a given choice of $\Delta L\Delta C$, the term $-4/(\omega^2\Delta L\Delta C)$ is large with respect to unity, and Z_{in} has a real component. At the cutoff frequency $\omega = \omega_h$, Z_{in} becomes purely reactive. I.e.,

$$1 - \frac{4}{(\omega_h^2\Delta L\Delta C)} = 0 \qquad \omega_h = \frac{2}{\sqrt{\Delta L\Delta C}}$$

No power can be delivered through the line above ω_h, since the input impedance is dominated by the input-section inductance ΔL, effectively shorted across the input terminals by the first lumped capacitance ΔC. Given no restrictions on the fineness of discretization, transmission-line behavior can be simulated with arbitrary precision by the choice of a sufficiently small section delay $\sqrt{\Delta L\Delta C}$.

Z_{in} for a finite, lumped network deviates far from the distributed-system input impedance well below the cutoff frequency, a discrepancy which is usually expressed in terms of phase

IPR2024-00706 EX. 2005

error or input-impedance variation for a matched, lumped ladder. No good expressions for the frequency deviation of coarsely discretized artificial lines seem to be published, with most authors relying on *ad hoc* guidelines, e.g., that electrical lengths be more than 10 times less the shortest wavelength of interest.

2.3.4 Choosing total line inductance and capacitance

Building upon the derivation of modal inductance and capacitance in Section 2.3.1, we can approximate the first few non-zero critical frequencies of an iterated network in terms of the total inductance and capacitance along the line. For alignment with some switching frequency f_{sw}, we simply choose $L_0 = n\Delta L$ and $C_0 = n\Delta C$ (for n iterated sections) to have the correct product, and rely on the fine discretization of the Cauer network to align higher-order poles and zeros with switching harmonics. The characteristic impedance $\sqrt{L_0/C_0}$ of the iterated network can be set from manufacturing considerations, or to match impedance levels in a circuit. A design with larger inductances and smaller capacitances, for instance, will ring up to higher impedances for the same Q, with smaller capacitor-plate areas that may be less expensive to fabricate.

To demonstrate selection of L_0 and C_0, suppose we wish to align the zeros of a short-circuited transmission-line analog to even harmonics of a switching frequency. Impedance zeros in a short-circuited line are described by the series-tuned network from Fig. 2.12c

$$L_\nu = \frac{L_{\text{tot}}}{2} \qquad C_\nu = \frac{8C_{\text{tot}}}{\nu^2\pi^2}$$

The first nonzero null has an index $\nu = 2$ (i.e., $\nu = 0$ for the DC zero, $\nu = 1$ for the first peak). We would choose L_2 and C_2[7] to resonate at $2f_{\text{sw}}$ in this case, from which the relation between the switching fundamental and total line values L_0 and C_0 is:

$$2f_{\text{sw}} = \frac{1}{2\pi}\left[\sqrt{\frac{L_0}{2}\cdot\frac{2C_0}{\pi^2}}\right]^{-1} = \frac{1}{2\sqrt{L_0C_0}} \tag{2.13}$$

Alternately, we might wish to align the first non-zero eigenvalue of an open-circuited network to a switching frequency. The impedance peaks in this case are described by parallel-tuned

[7]Note that we are not *constructing* these components, just using them to model the desired line mode.

IPR2024-00706 EX. 2005

simulating networks with values:

$$L_\nu = \frac{8L_0}{\nu^2\pi^2} \qquad C_\nu = \frac{C_0}{2}$$

The mode of interest again has an index $\nu = 2$, so our alignment condition expressed in terms of total capacitance and inductance becomes:

$$2\pi f_{\text{sw}} = \left[\sqrt{\frac{2L_0}{\pi^2} \cdot \frac{C_0}{2}}\right]^{-1} = \frac{\pi}{\sqrt{L_0 C_0}} \tag{2.14}$$

Note that an iterated approximation of a transmission-line impedance is particularly volume-efficient because modal inductances and capacitances arise from different modeshapes on the *same structure.* The Foster forms, by comparison, are bulkier than the Cauer network beyond two or three resonances: they require, for each peak or null, one component which is half as large as the corresponding total-line value (L_0 or C_0).

2.4 Critical-frequency alignment of lumped lines

Chapter 3 presents impedance measurements for lumped transmission-line analogs; in light of the useful waveform symmetries arising from odd- and even-harmonic relationships among poles and zeros, is worthwhile considering how these measured critical frequencies can differ from the integrally related frequencies of a distributed line.

2.4.1 Coupling and Pole-Zero Separation

Whenever driving effort excites some mode, whether native to the energy-domain of excitation or not, the coupling coefficient k represents the extent of energy conversion, and is defined over a cycle as

$$k^2 = \frac{\text{energy delivered to load} + \text{energy stored and recovered from load}}{\text{total energy delivered}}$$

Consider a simple case of energy storage shown in Fig. 2.15a: a mass slides on a frictionless plane, and is tied to a mechanical ground through a spring k_1. A force with infinite authority

IPR2024-00706 EX. 2005

— i.e., no source impedance — stretches k_1 and stores energy in it. All of the energy delivered from the source stretches the spring, and the drive is perfectly coupled to k_1. For this case of zero source impedance, the coupling coefficient $k \equiv 1$.

Mode excitation is rarely as simple as the case pictured in Fig. 2.15a. Usually, energy stored in k_1 requires that some energy be delivered to the exciting structure, as shown in Fig. 2.15b. At frequencies far below resonance, the oscillator is compliance-dominated (i.e., the energy stored in m is negligible) and F stores energy in k_1 by stretching k_2. If k_2 is stiff, F is strongly coupled to k_1; if k_2 is compliant, it is stretched considerably, k_1 is relatively undisturbed, and the coupling is weak. k^2 in this case can be expressed as the fraction of total energy delivered to k_1:

$$k^2 = \frac{\text{energy stored in } k_1}{\text{energy stored in } k_1 + \text{energy stored in } k_2}$$

In laboratory practice, the frequency separation between resonance and antiresonance (i.e., between a modal resonance and the zero introduced by exciting it) is a measure of the degree of energy coupling. To understand this useful relationship, consider the impedance of Fig. 2.16a for the network in Fig. 2.16b:

$$Z = j\omega L_0 - \frac{j}{\omega C - \frac{1}{\omega L}} = j\omega\left[L_o - \frac{L}{\omega^2 LC - 1}\right] = j\omega \cdot \frac{\omega^2 L_0 LC - L_0 - L}{\omega^2 LC - 1}$$

ω_p and ω_z from Fig. 2.16a are found by setting numerator and denominator to zero and solving for frequency, from which:

$$\omega_\mathrm{p} = \sqrt{\frac{1}{LC}} \quad \text{and} \quad \omega_\mathrm{z} = \sqrt{\frac{1}{L_0 \| L \cdot C}} = \sqrt{\frac{1}{LC} + \frac{1}{L_0 C}}$$

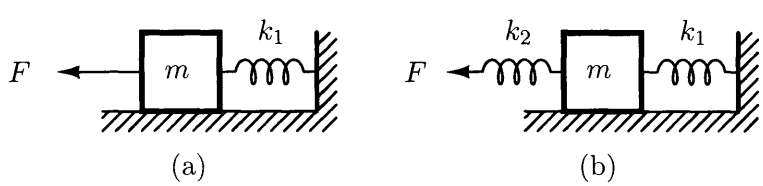

Figure 2.15: **A simple example of coupling**

IPR2024-00706 EX. 2005

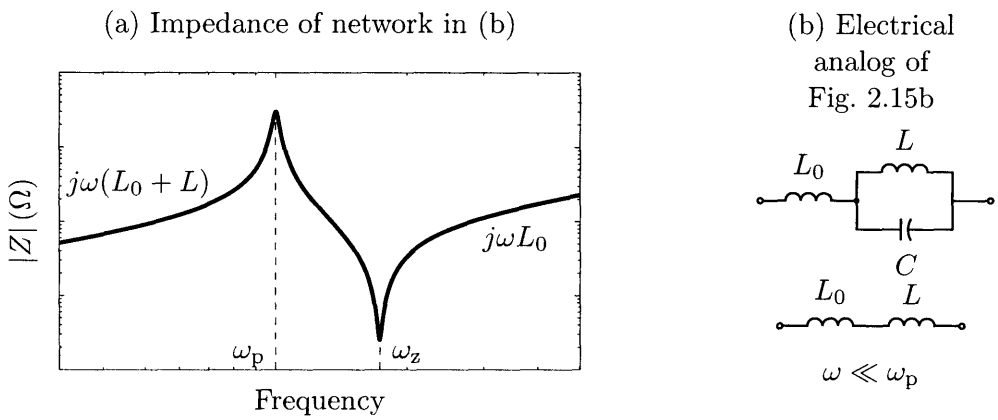

Figure 2.16: **Explanation of coupling in terms of pole/zero separation**

The ratio ω_z^2/ω_p^2 bears a useful relationship to k^2, and can be expressed as

$$\frac{\omega_z^2}{\omega_p^2} = \frac{L + L_0}{L_0} \qquad \text{since} \qquad \frac{\omega_z^2}{\omega_p^2} - 1 = \frac{L}{L_0}$$

By the energy definition of coupling coefficient, and for some applied current i in the low-frequency, inductance-dominated regime,

$$k^2 = \frac{\frac{1}{2}Li^2}{\frac{1}{2}Li^2 + \frac{1}{2}L_0 i^2} = \frac{L}{L_0 + L}$$

which can in turn be related to the ratio ω_z^2/ω_p^2:

$$1 - k^2 = \frac{L_0}{L + L_0} \qquad \Longrightarrow \qquad k^2 = 1 - \frac{\omega_p^2}{\omega_z^2} \tag{2.15}$$

Using the gross pole-zero coincidence approximation $\omega_z + \omega_p \approx 2\omega_z$,

$$k^2 = \frac{(\omega_z + \omega_p)(\omega_z - \omega_p)}{\omega_z^2} \approx 2 \cdot \frac{\omega_z - \omega_p}{\omega_z} \tag{2.16}$$

While Eqn. 2.15 precisely determines k from measured ω_z and ω_p, Eqn. 2.16 affords the insight that pole-zero spacing increases linearly with increasing k, to a better approximation as $\omega_z - \omega_p$ is small with respect to either critical frequency. We can apply this single-resonant treatment of coupling to cascaded oscillators, as long as we can ignore the impedances of neighboring intertia- or compliance-dominated resonators, excited away from their tuned

IPR2024-00706 EX. 2005

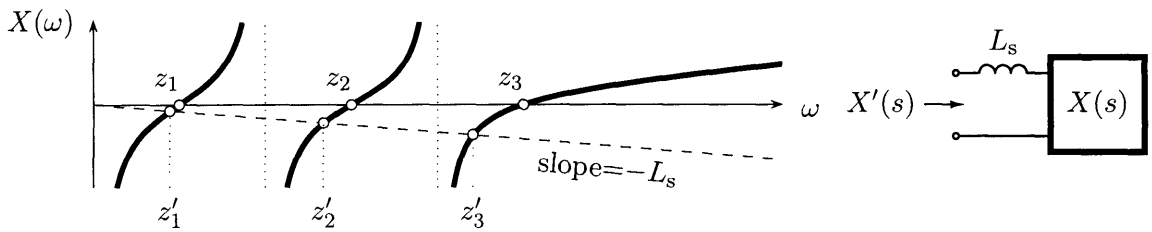

Figure 2.17: **Zero shifting from a series inductance is series with** $X(j\omega)$

frequencies. This approximation, and the others of this section, are common practice within the transducer field [15, Section 4.8], and are a convenient means of comparing the alignment of adjacent poles and zeros.

2.4.2 Terminal Impedance and Zero Alignment

The critical frequencies of a lossless network described by a reactance function $X(s)$ may be shifted up or down, in unison, by a common factor applied to the network's L and C values. Impedance zeros can be shifted down in frequency without disturbing pole locations, however, by exciting $X(s)$ through a terminal inductance. Fig. 2.17 shows an exemplary $X(s)$ in series with a inductance L_s, where the original zeros z_1–z_3 of $X(s)$ move closer toward their associated poles — to the new frequencies z_1'–z_3' — when L_s is introduced. Intersections between the reactance $-\omega L_s$ and $X(\omega)$ specify the new zero locations, because subtracting the series impedance $-sL_s$ from $X(s)$ is equivalent to adding sL_s to $X(s)$. Clearly, the pole locations are not affected by this finite impedance offset. The zero frequencies can often not be shifted to appreciably higher frequencies by *removing* series inductance inside $X(s)$, simply because the network realizations considered in Chapter 3 have very small input-section inductances. I.e., mode coupling cannot be improved for the class of transmission-line analogs considered; if zeros fall below a desired even-harmonic alignment, the shortfall can only be made worse by parasitics.

The dual phenomenon of pole-shifting with shunt capacitance cannot be readily exploited to compensate for a zero misalignment, or to correct systematic misalignment in pole frequencies. This constraint is again due to the particular application at hand. The exciting network at the port of $X(s)$ is, for the cases in Chapters 3 and 4, the drain of a FET, and

IPR2024-00706 EX. 2005

we are typically not at liberty to add or subtract capacitance from the driven node.

2.5 Chapter summary

This chapter considers second-order electrical networks and transmission lines as storage elements in the sense of Chapter 1. Foundations for later chapters have been introduced here, including lumped realizations of transmission-line impedances (Foster and Cauer forms) and methods for comparing the size and critical-frequency alignment of such networks. The importance of frequency alignment of poles and zeros is considered with respect to waveform symmetries, symmetries which enable the soft-switching converter operation discussed in Chapter 4. These higher-order systems take advantage of periodic switching to develop impedance extremes by energy *fidelity* rather than bulk energy storage. By storing and internally circulating periodic applied voltages or currents, high-order networks can develop impedance extremes by decreasing the instantaneous work delivered through driving terminals. Such resonant and delay networks, moreover, can be substantially smaller than their bulk counterparts.

IPR2024-00706 EX. 2005

Chapter 3

Multi-resonant component design

FOR the cases of short or open (non-reactive) termination, the boundary conditions of a lossless transmission line enforce a precise integral alignment of impedance-maximum and -minimum frequencies. As explored in Chapter 2, such harmonic relationships can enforce useful waveform symmetries and present large impedance extrema to periodic waveforms. A uniform-cross-section line which supports resonances at power switching frequencies, however, may be inconveniently long. Though telecom applications at gigahertz frequencies routinely exploit the cavity modes of miniaturized, high-Q dielectric resonators, structures with electromagnetic modes in the vicinity of 10 MHz would be orders of magnitude larger.[1] A transmission-line analog which mimics — in a smaller volume — the impedance of a distributed line would be eminently useful, especially if it could be electromagnetically shielded and manufactured directly alongside other components.

This chapter treats in detail the critical-frequency alignment of a family of transmission-line analogs formed by tapping a planar inductor along its length with capacitors. Analytic and synthetic means of designing such structures are considered, corresponding to iterated networks and ladder structures with individually selected inductors and capacitors. The impedances of the different types of approximating networks are confirmed by experiment, as are means of compensating for the mutual inductances that arise from compact construction methods.

[1] To give some a sense of scale, a length of RG-58/U coax with a $\lambda/4$-wave resonance at 13.56 MHz (in the ISM band) is 136″ long. In a design example presented in Chapter 4 this line is a somewhat bulky replacement for a 10 μH inductor (*cf.* Sec. 4.3.2 and the converter of Fig. 4.21).

IPR2024-00706 EX. 2005

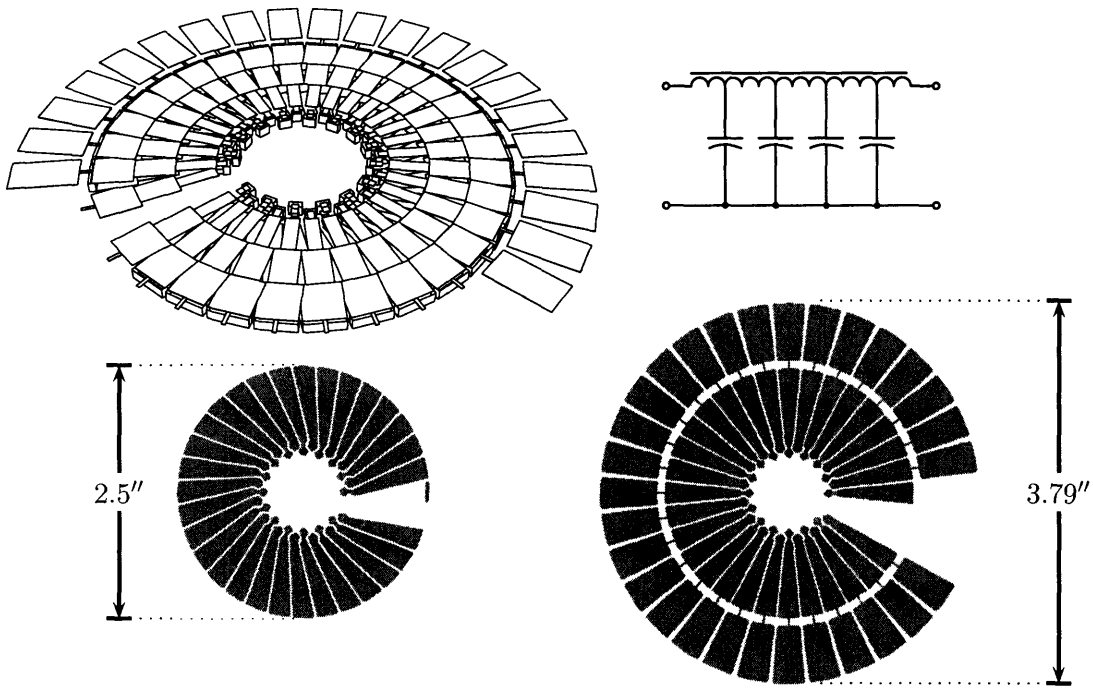

(a) Bottom copper (b) Top copper

Figure 3.1: **Schematic rendering of the tapped toroidal inductors considered in this chapter, alongside a circuit model. The air-core inductors can be manufactured in a printed-circuit board, with the principal flux path in the board thickness. Full information on this structure is provided in Section 3.2.3.**

3.1 Tapped toroidal structures

The family of simulating networks considered in this chapter is rendered schematically in Fig. 3.1. A base inductance, in this case an air-core toroid with 30 turns, is tapped uniformly along its length with capacitors. The lower plate of these capacitors is shown in the rendered model, with plates in front removed for clarity. In the full structure, a dielectric layer separates the top metal layer from a ground plane, which overlies just the capacitor taps or — preferably, for shielding — the toroid and taps (see Section 3.4.4.2). The air-core toroid can be manufactured in a laminate printed-circuit process, and exemplary top and bottom metal layers are reproduced in Figs. 3.1a and 3.1b (PCB fabrication is elaborated further in Chapter 5). The staggered radial traces on the bottom layer connect successive turns around the toroid, so that with the principal flux path is in the board thickness. The structure relies on leakage flux to mimic transmission-line behavior, as we will see shortly, so

IPR2024-00706 EX. 2005

shielding of some sort is a practical necessity. Just as a dielectric resonator is miniaturized at microwave frequencies by the high relative permittivity of its cavity material, so the tapped toroid, by linking more flux per unit length than a coaxial geometry, is smaller than its transmission-line counterpart.

Though one equal capacitor per turn is shown in Fig. 3.1, different arrangements of tap locations, tap capacitances, and tap-capacitance leads will be explored in this chapter. Variations of the basic tapped-toroidal structure have different merits as transmission-line simulating networks, and will be considered in turn.

Iterated network	A network in the Cauer form as presented in 2.3.2, with uniform L/C and no mutual inductance between sections
Non-diagonalized network	As above, but with mutual inductance coupling adjacent inter-tap segments along the toroid. This form is most similar to the network shown in the top right of Fig. 3.1
Cauer-synthesized network	The same base toroid as in the above cases, tapped at selected points around its periphery with nonuniform capacitors (no longer with an even tap spacing or uniform tap capacitance, necessarily)

We will analyze these structures on a *network basis*, though full-field simulations should be useful for predicting the effect of distributed capacitance on driving-point impedance (see Section 3.4.4.2). Rather than translating the opacity of multi-resonant design to a computer, a network approach readily suggests techniques for aligning impedance peaks and nulls.

3.2 Iterated-Network Impedance

In this section we focus on identifying the critical frequencies of uniform, iterated L/C networks with short- or open-circuit terminations. In the discussion of Cauer-form networks

IPR2024-00706 EX. 2005

in Section 2.3.2, the useful approximation range of an artificial line was expressed in terms of the cutoff frequency ω_h. A great deal of ingenuity has been demonstrated in techniques for increasing ω_h (e.g., half-sections and m-derived sections, see [30, Chapter 5] and [31, Chapter 9]) or otherwise maximizing the real part of Z_{in} in lumped, artificial lines (e.g., by synthesizing non-coincident critical frequencies, deliberately shifted away from those of a transmission line [31, Chapter 7]). All of these techniques are concerned with power delivery, and express their results in terms of input-impedance variation for a matched, lumped ladder. No authors seem to treat systematically perturbations of critical frequencies in consideration of the *reactive* properties of an artificial line with an open or short termination.

3.2.1 Analytic expression for transmission-line critical frequencies

To understand how minima and maxima in Z_{in} shift for a given degree of discretization in an iterated network, first consider the impedances of the normalized networks of Fig. 3.2. As shown in the topmost T-section, all inductors have a value of 1 H, and all capacitors a value of 1 F. The impedance levels and critical frequencies of the cascaded sections can be denormalized without affecting the relative frequency relationships among poles and zeros.[2] The input impedance functions Z_{in} are a ratio of a numerator n_k, an odd polynomial in s, and a denominator d_k, an even polynomial in s, with indices equal to the number of inductors in the network they describe. Not shown is the untapped network comprising a single 1 Henry inductor with impedance $n_1/d_1 = s$.

If the *non-zero* coefficients of the d_k and n_k polynomials are written from highest order to lowest order in a tabular arrangement, the interesting pattern shown in Table 3.1 emerges, in which the entries along descending diagonals are evidently rows of Pascal's triangle. The diagonals $n = 2$ to $n = 5$ are labelled in Table 3.1, where n corresponds to the $C(n, k)$ notation for the binomial coefficient. Note that the arrangement in Table 3.1 does not take into account the staggered odd-even order of the terms in d_k and n_k, which we will re-introduce later (see the discussion of reactance functions, Section 2.3).

The diagonal sequences from the table of numerator and denominator coefficients are them-

[2]The impedance can be shifted up or down by reciprocal scaling of L and C values, i.e., $L' = \alpha L$, and $C' = C/\alpha$, which will leave the critical frequencies unchanged. A common factor β in L and C values will likewise shift critical frequencies by a factor $1/\beta$ while leaving the impedance unchanged.

IPR2024-00706 EX. 2005

Table 3.1: **Tabular arrangement of impedance-function coefficients**

												row sum
d_1			1								$m=1$	$\sum_{i=1}^{1} d_{0i} = 1$
n_1	$n=2$		1								$m=2$	$\sum_{i=1}^{1} n_{0i} = 1$
		$\searrow$										
d_2	$n=3$		1		1							
		$\searrow$		$\ddots$								
n_2	$n=4$		1		2						$\vdots$	$\vdots$
		$\searrow$		$\ddots$		$\ddots$						
d_3	$n=5$		1		3		1					
		$\searrow$		$\ddots$		$\ddots$						
n_3			1		4		3				$m=6$	$\sum_{i=1}^{3} n_{2i} = 8$
				$\ddots$		$\ddots$		$\ddots$				
d_4			1		5		6		1			
						$\ddots$		$\ddots$				
n_4			1		6		10		4		$\vdots$	$\vdots$
								$\ddots$		$\ddots$		
d_5			1		7		15		10		1	
										$\ddots$		
n_5			1		8		21		20		5	$m=10$	$\sum_{i=1}^{5} n_{4i} = 55$
			highest order						lowest order			

IPR2024-00706 EX. 2005

$$Z_{\text{in}} = \frac{n_2}{d_2} = \frac{s^3 + 2s}{s^2 + 1} \longrightarrow$$

$$Z_{\text{in}} = \frac{n_3}{d_3} = \frac{s^5 + 4s^3 + 3s}{s^4 + 3s^2 + 1} \longrightarrow$$

$$Z_{\text{in}} = \frac{n_4}{d_4} = \frac{s^7 + 6s^5 + 10s^3 + 4s}{s^6 + 5s^4 + 6s^2 + 1} \longrightarrow$$

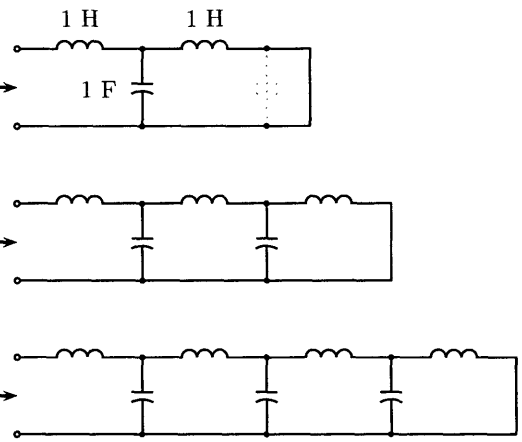

Figure 3.2: **Input impedances of the normalized, iterated L-networks, in which the k subscript of numerator and denominator polynomials corresponds to the number of iterated L-sections. Note that the termination of each of the networks in shorts across a terminal L-section capacitor (hence the dashed capacitor at the right of the topmost network). This detail is significant when comparing open- and short-circuit impedances, since the open-circuit network gains a capacitor rather than losing an inductor.**

					1					
				1		1				
			1		2		1			
		1		3		3		1		
	1		4		6		4		1	
1		5		10		10		5		1

1						
1	1					
1	2	1				
1	3	3	1			
1	4	6	4	1		
1	5	10	10	5	$\boxed{1}$	
1	6	15	20	$\boxed{15}$	6	1
1	7	21	$\boxed{35}$	35	21	
1	8	$\boxed{28}$	56	70		
1	$\boxed{9}$	36	84			
$\boxed{1}$	10	45				
1	11					
1						

$$\binom{0}{0}$$

$$\binom{1}{0} \quad \binom{1}{1}$$

$$\binom{2}{0} \quad \binom{2}{1} \quad \binom{2}{2}$$

$$\binom{n}{0} \quad \cdots \quad \binom{n}{n-1} \quad \binom{n}{n}$$

$$\binom{n}{k} = \frac{n!}{k!(n-k)!}$$

Table 3.2: **The numerator and denominator coefficients from Table 3.1 are taken from alternating rows of Pascal's triangle.**

IPR2024-00706 EX. 2005

selves diagonal sequences from Pascal's triangle, as demonstrated by the left-justified triangle on the right of Table 3.2. The ascending diagonals of this tabular arrangement are numbered by increasing m, beginning with $m = 1$, and corresponding to the m numbering shown on the right of the Table 3.1.

The polynomials whose coefficients are taken from diagonals of Pascal's triangle, when expressed in the staggered-order form of our n_k and d_k, are the Fibonacci polynomials F_m. $F_m(x)$ evaluated at $x = 1$ yields the corresponding Fibonacci number, as defined by the recurrence relation $F_n \equiv F_{n-2} + F_{n-1}$, where $n = 3, 4, \ldots$ and $F_1 = F_2 = 1$ (*cf.* the right column of Table 3.1). Möbius expresses the roots of collapsed-order versions of the Fibonacci polynomials in deriving a periodicity condition for Möbius transforms [32]. The boxed coefficients from the $m = 11$ diagonal in Table 3.2, for instance, correspond to the polynomial:

$$\sigma^5 + 9\sigma^4 + 28\sigma^3 + 35\sigma^2 + 15\sigma + 1 = 0$$

which has five roots given by

$$\sigma = -4\cos^2\left(\frac{k\pi}{m}\right) = 4\cos^2\left(\frac{k\pi}{11}\right) \qquad \text{for } k = 1, 2, \ldots, 5$$

These roots can also be expressed in terms of the roots of unity. I.e., if r denotes any m^{th} root of 1, then:

$$\sigma = -\frac{(1+r)^2}{r} \qquad \text{E.g.,} \quad 4\cos\left(\frac{\pi}{11}\right)^2 = \frac{[1 + 1\angle(180/11)^\circ]^2}{1\angle(180/11)^\circ} \approx 3.6825$$

The original polynomial ratios describing the iterated network impedances were odd-over-even reactance functions, with a zero at $s = 0$ (That is, the numerator had non-zero coefficients for odd powers of s, and the denominator had non-zero coefficients for even powers of s). By tabulating nonzero numerator and denominator coefficients without regard for the staggering of order in the terms, the analytic roots for the Fibonacci polynomials no longer have the units of frequency. Z_{in} maxima from the denominator polynomial in σ, however, are easily recovered by the substitution $\sigma = s^2 = -\omega^2$, from which the peak frequencies ω_{p} are:

$$\omega_{\text{p}} = \sqrt{4\cos^2\left(\frac{k\pi}{m_{\text{p}}}\right)} = 2\cos\left(\frac{k\pi}{m_{\text{p}}}\right) \qquad \text{for } m_{\text{p}} \text{ odd and } k = 1, \ldots, \left\lfloor \frac{m_{\text{p}}}{2} \right\rfloor$$

IPR2024-00706 EX. 2005

Chebyshev polynomials of the 1st kind	Chebyshev polynomials of the 2nd kind	Fibonacci polynomials
$T_0(x) = 1$	$U_0(x) = 1$	$F_1(s) = 1$
$T_1(x) = x$	$U_1(x) = 2x$	$F_2(s) = s$
$T_2(x) = 2x^2 - 1$	$U_2(x) = 4x^2 - 1$	$F_3(s) = s^2 + 1$
$T_3(x) = 4x^3 - 3x$	$U_3(x) = 8x^3 - 4x$	$F_4(s) = s^3 + 2s$
$T_4(x) = 8x^4 - 8x^2 + 1$	$U_4(x) = 16x^4 - 12x^2 + 1$	$F_5(s) = s^4 + 3s^2 + 1$
$T_5(x) = 16x^5 - 20x^3 + 5x$	$U_5(x) = 32x^5 - 32x^3 + 6x$	$F_6(s) = s^5 + 4s^3 + 3s$
$T_{n+1}(x) = 2xT_n - T_{n-1}$	$U_{n+1}(x) = 2xU_n - U_{n-1}$	$F_{m+1}(s) = sF_m + F_{m-1}$

Table 3.3: **Chebyshev polynomials and Fibonacci polynomials, with their recurrence relationships**

Where $\lfloor\cdot\rfloor$ is the floor function. The same substitution $\sigma = s^2 = -\omega^2$ in the diagonal polynomial with $m = m_\mathrm{z} = m_\mathrm{p} + 1$, yields the original numerator polynomial with its zero at $s = 0$ factored away. The non-zero roots of this polynomial, the zeros of Z_in, are given by:

$$\omega_\mathrm{z} = \sqrt{4\cos^2\left(\frac{k\pi}{m_\mathrm{z}}\right)} = 2\cos\left(\frac{k\pi}{m_\mathrm{z}}\right) \qquad \text{for } m_\mathrm{z} \text{ even and } k = 1, \ldots, \left\lfloor\tfrac{m_\mathrm{z}-1}{2}\right\rfloor = \left\lfloor\tfrac{m_\mathrm{p}}{2}\right\rfloor$$

Note that because of the initial arrangement of numerator and denominator polynomials and their corresponding m-indices in Table 3.1, m_z is always one greater than m_p.

When the staggered order of the diagonal polynomials is re-introduced, the successive d_k and n_k have a generating function similar to that of Chebyshev polynomials. Listed in Table 3.3 are Chebyshev polynomials of the first (T_n) and second (U_n) kind, followed by their recurrence relationships. The Fibonacci polynomials F_m, corresponding to the m rows of the tabulated numerator and denominator coefficients, are listed in the right column, with their slightly different recurrence relation. The roots of T_n are given by

$$x = \cos\left[\frac{\pi\left(k - \frac{1}{2}\right)}{n}\right] \qquad \text{for } k = 1, 2, \ldots, n$$

which motivated a search for similar roots of F_m.[3]

[3]Also similar to Chebyshev polynomials of the first kind, F_m satisfy a curious determinant equation, effectively a recasting of the recurrence relation:

IPR2024-00706 EX. 2005

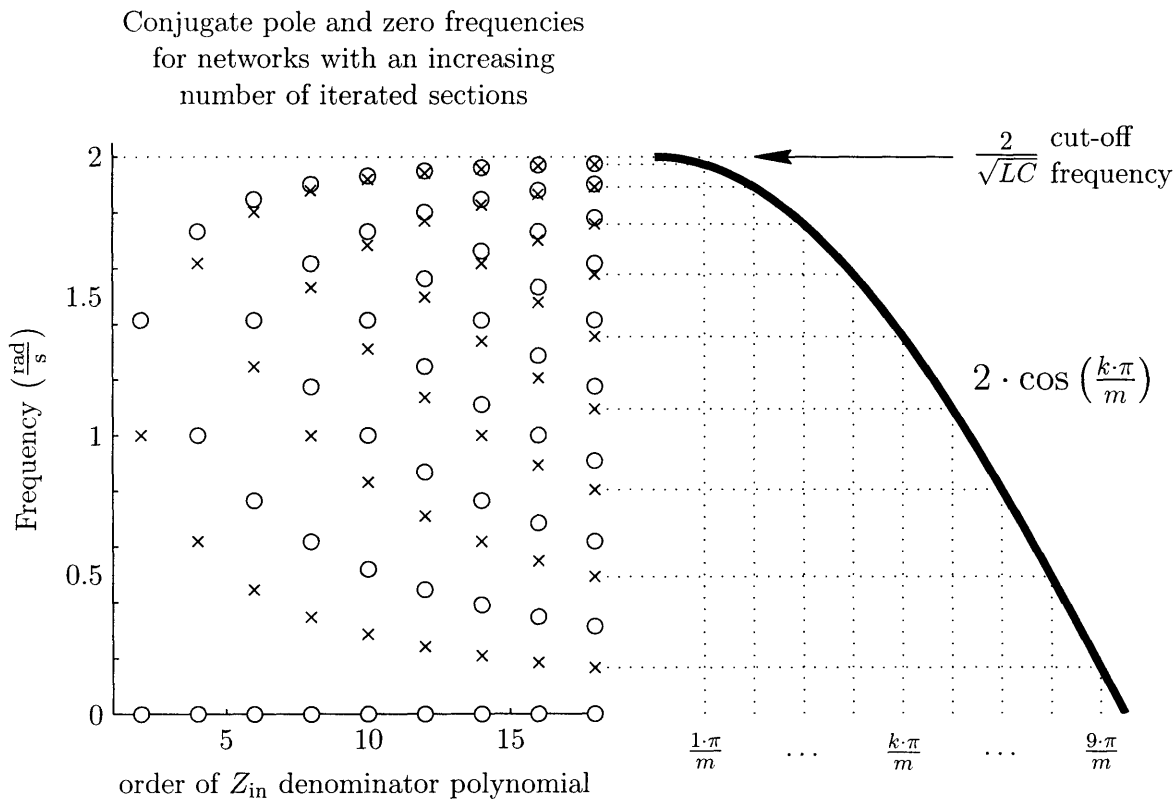

Figure 3.3: **Analytical prediction of the pole and zero frequencies for iterated L-section networks**

Many features of the critical-frequency alignment for Z_{in} become apparent from an explicit expression for the impedance-polynomial roots. Shown in Fig. 3.3 are peak and null frequencies for increasing numbers of cascaded L-sections (along the lines of Fig. 3.2), demonstrating the alignment of conjugate impedance poles with the range of $2\cos(k\pi/m)$ over $k = 1, \ldots, \lfloor m/2 \rfloor$. From the plot, it appears that impedance nulls are closer to their neighboring low-frequency pole, and never equidistant between adjacent peak frequencies as in an ideal, lossless transmission line. This non-coincident behavior can be explained by

$$\begin{vmatrix} s & -1 \\ 1 & s \end{vmatrix} = F_3(s) \qquad \begin{vmatrix} s & -1 & 0 \\ 1 & s & -1 \\ 0 & 1 & s \end{vmatrix} = sF_3 + 1 \cdot \begin{vmatrix} s & -1 \\ 0 & 1 \end{vmatrix} = F_4(s)$$

$$\begin{vmatrix} s & -1 & 0 & 0 \\ 1 & s & -1 & 0 \\ 0 & 1 & s & -1 \\ 0 & 0 & 1 & s \end{vmatrix} = sF_4 + F_3 = F_5(s)$$

The tri-diagonal matrix structure in is suggestive of the tableau-form of mesh equations written for the iterated ladder network.

IPR2024-00706 EX. 2005

considering the alignment of the lowest-frequency peak and the lowest-frequency AC null. For any desired iterate network and the corresponding denominator polynomial with m_p odd, the first conjugate-pole frequency can be computed from the largest allowable index k:

$$\omega_\mathrm{p} = 2\cos\left(\frac{k\pi}{m_\mathrm{p}}\right) = 2\cos\left(\frac{\lfloor \frac{m_\mathrm{p}}{2} \rfloor \pi}{m_\mathrm{p}}\right)$$

In consideration of the near linearity of the cosine function near $\pi/2$, a metric of the frequency ω_p can be approximated by the separation of the cosine argument from $\pi/2$. Discarding the common factors of π and performing a similar approximation for the lowest null frequency, the differences

$$\frac{1}{2} - \frac{\lfloor \frac{m_\mathrm{p}}{2} \rfloor}{m_\mathrm{p}} \qquad \text{and} \qquad \frac{1}{2} - \frac{\lfloor \frac{m_\mathrm{p}}{2} \rfloor}{m_\mathrm{z}}$$

are suitable measures for the lowest-frequency ω_p and ω_z. Note that given the inflection of the cosine function and because $\omega_\mathrm{p} < \omega_\mathrm{z}$, the approximation $\cos(\pi/2 - \epsilon) = \epsilon$ places an upper bound on ω_z as compared to ω_p. I.e., the cosine function shifts ω_z further down in frequency than ω_p, only worsening the lack of alignment being demonstrated.

Because m_p is always odd and m_z even, the product $m_\mathrm{p}m_\mathrm{z}$ is even, and the frequency metrics can be expressed with common denominators:

$$\frac{1}{m_\mathrm{p}m_\mathrm{z}}\left[\frac{m_\mathrm{p}m_\mathrm{z}}{2} - \left\lfloor\frac{m_\mathrm{p}}{2}\right\rfloor(m_\mathrm{p}+1)\right] \quad \text{for } \omega_\mathrm{p}, \text{ and} \quad \frac{1}{m_\mathrm{p}m_\mathrm{z}}\left[\frac{m_\mathrm{p}m_\mathrm{z}}{2} - \left\lfloor\frac{m_\mathrm{p}}{2}\right\rfloor m_\mathrm{p}\right] \quad \text{for } \omega_\mathrm{z}$$

discarding the common divisor $m_\mathrm{p}m_\mathrm{z}$ and remembering that $m_\mathrm{p} = m_\mathrm{z} - 1$ is odd, the frequency metric for ω_p can be simplified:

$$\frac{m_\mathrm{p}m_\mathrm{z}}{2} - \frac{(m_\mathrm{p}-1)(m_\mathrm{z})}{2} = \frac{m_\mathrm{z}}{2} = \frac{m_\mathrm{p}+1}{2}$$

Again discarding $m_\mathrm{p}m_\mathrm{z}$, the metric for the separation between the first peak and AC null is:

$$\left\lfloor\frac{m_\mathrm{p}}{2}\right\rfloor(m_\mathrm{p}+1) - \left\lfloor\frac{m_\mathrm{p}}{2}\right\rfloor m_\mathrm{p} = \left\lfloor\frac{m_\mathrm{p}}{2}\right\rfloor = \frac{m_\mathrm{p}-1}{2}$$

Therefore, for a finite, iterated network of the type in Fig. 3.2, the first null in Z_in can *never* reach twice the the frequency of the lowest-frequency peak, even with assumptions favoring a high zero frequency.

IPR2024-00706 EX. 2005

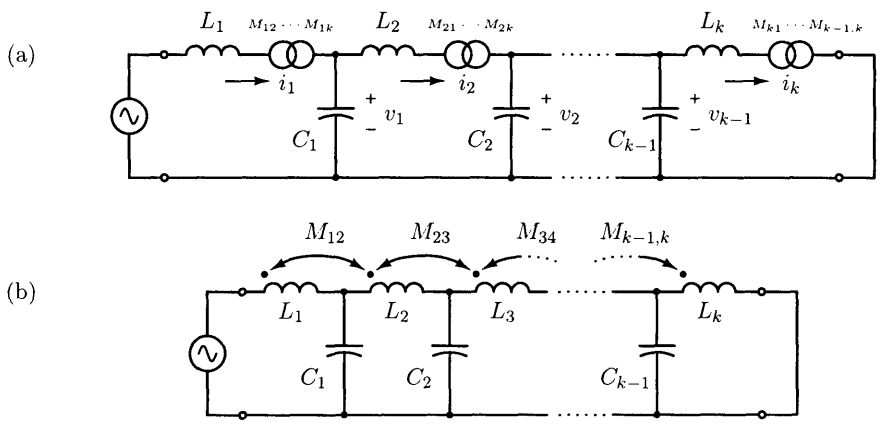

Figure 3.4: **A circuit model (a) for a toroid with a fully populated inductance matrix, and an approximating network (b) with only adjacent mutual inductances preserved.**

This non-coincident arrangement of poles and zeros in Z_{in} is exacerbated at higher frequencies. For the higher-order modes, the zeros approach — and nearly cancel — the adjacent low-frequency conjugate pole as is clearly visible in Fig. 3.3. This approximate cancellation follows from the greater proximity of k/m_{p} and $k/(m_{\text{p}}+1)$ for lower values of k, and from the higher inflection of $\cos(x)$ about $x = 0$.

3.2.2 Inductance-matrix diagonalization

Printed-circuit structures like those in Fig. 3.1 were constructed and measured, and verify the pole-zero structure derived in the previous section. An immediate discrepancy is apparent between the decoupled ladder networks — like those of Fig. 3.2 — and a capacitively tapped toroid. By linking more flux per unit length than the uniform cross-section transmission line, the toroid's meandering DC current path couples its component sections together magnetically. A section inductance no longer *exclusively* exchanges energy with the network through conduction currents at its terminals; its flux links every other portion of the toroid, as represented schematically in Fig. 3.4a.

Though a fully populated inductance matrix would seem to complicate the analysis hopelessly, in the case of air-core, planar magnetics the problem is tractable. Because of the large flux leakage in a structure like that of Fig. 3.1, the mutual inductances between any two ports (where a port is two adjacent tap terminals) falls off rapidly around the toroid.

IPR2024-00706 EX. 2005

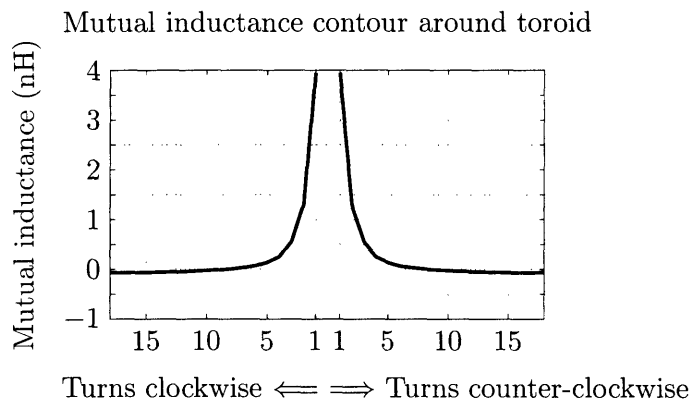

Figure 3.5: **Segment-to-segment mutual inductances around a full toroid, where ports are taken to be two adjacent tap terminals. The mutual inductance becomes small and negative when section coils have antiparallel axes on opposite ends of the toroid.**

Fig. 3.5 shows the computed decrease in mutual inductance for ports around a 38-turn toroid with 973 nH total self inductance. The model was 124 mil thick, with a 3-inch outer diameter, 0.93-inch inner diameter, and single-turn self-inductance of 15.4 nH.[4] The mutual inductances decrease rapidly, from 3.94 nH to the immediately adjacent turn, then 1.30 nH, 0.55 nH, ... moving clockwise or counterclockwise along the toroid. Mutual values eventually become small and negative when winding-sections have antiparallel axes, approaching opposite ends of the toroid. If possible, we would like to thoroughly diagonalize the inductance matrix, cancelling all mutual inductance entries.

Because the main-diagonal and adjacent-mutual entries are substantially higher than all the other entries in L, the section-to-section inductance matrix has an approximately tri-diagonal structure, as represented by the couplings of Fig. 3.4b and by the matrix view in Fig. 3.6a. Considering the adjacent-section M with reference to Fig. 3.7, for the sense of the windings shown (in which i_1 bucks i_2) there is a negative mutual induction $-M$ between the left and right mesh. The branch inductances in the equivalent T-model of Fig. 3.7 can be quickly verified by considering the open-circuit impedance of any pair of terminals in the three-terminal network. With the tap branch open, significantly, the total inductance

[4]There are actually two types of turn, which extend different amounts toward the toroid's center and have slightly different self inductances. These different turns were designed for efficient packing of vias in the center rosette of the structure, so that each turn was able to accommodate 3 vias in parallel for each traverse of the board. This construction technique lowers DC and AC resistance, and can easily be included in the analysis.

IPR2024-00706 EX. 2005

(a) Inductance matrix for ungapped toroid with no tap extensions

(b) Gapped toroid with tap extensions

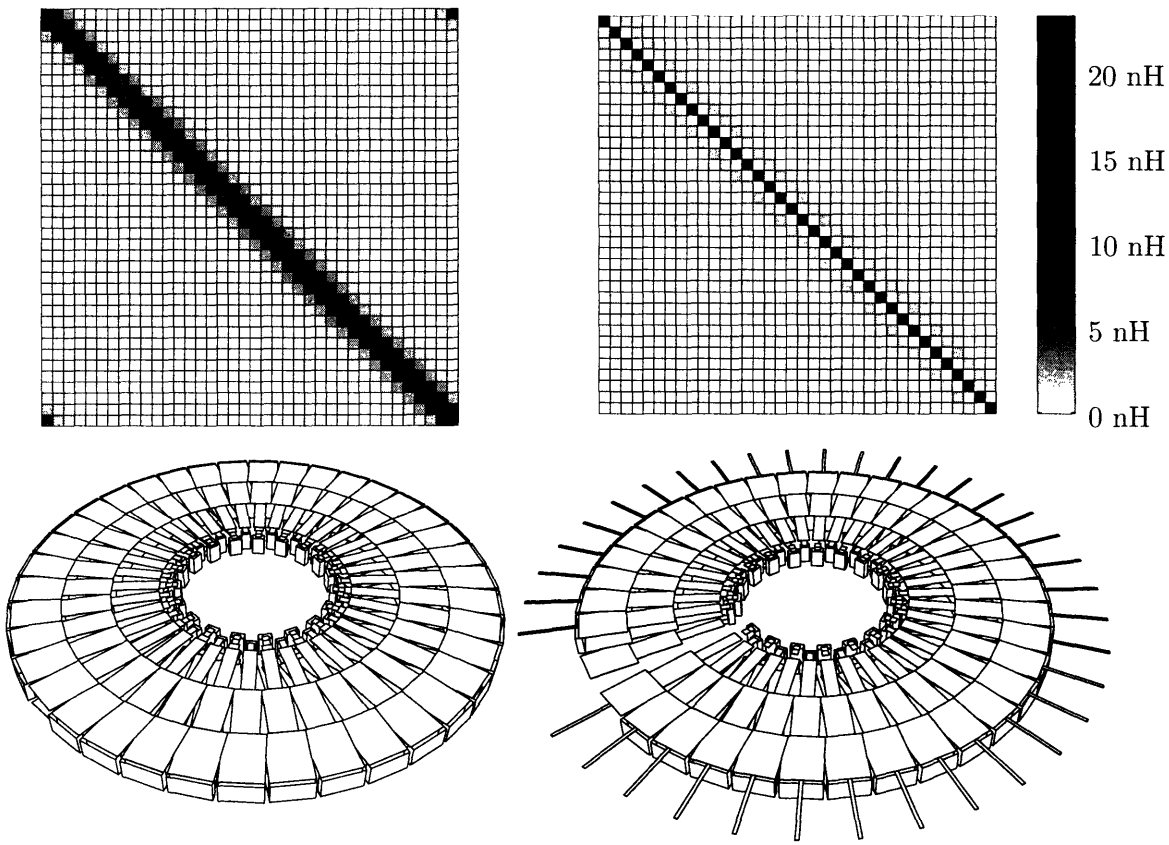

Figure 3.6: **FastHenry toroid models and their computed inductance matrices. Two nodes at the upper periphery of adjacent turns form a port. The L matrix for the toroid on the left shows substantial off-diagonal mutual terms, whereas the inductive tap extensions and eleminated turns in the right toroid effectively diagonalize its inductance matrix.**

IPR2024-00706 EX. 2005

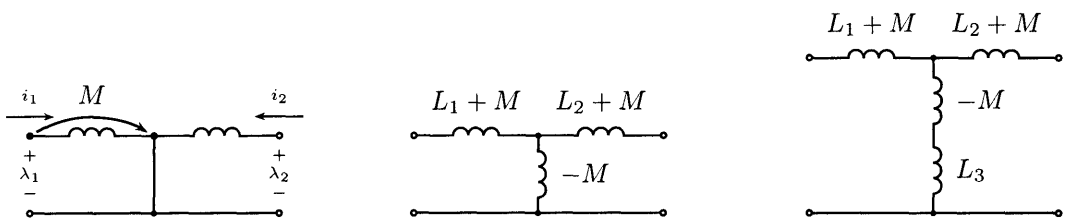

$$\begin{pmatrix} \lambda_1 \\ \lambda_2 \end{pmatrix} = \begin{pmatrix} L_1 & M \\ M & L_2 \end{pmatrix} \begin{pmatrix} i_1 \\ i_2 \end{pmatrix} \qquad \begin{pmatrix} L_1 + L_3 & M - L_3 \\ M - L_3 & L_2 + L_3 \end{pmatrix}$$

Figure 3.7: **A Δ-Y transformation of a mutual inductance provides intuition for how added tap-branch inductance affects the L matrix. Notice that the block sum is unchanged by L_3, i.e., the top-branch Δ impedance, with the L_3 branch open, is still $L_1 + L_2 + 2M$.**

of the coupled sections is the block sum of the inductance matrix (i.e., $L_1 + L_2 + 2M$, an observation which we will extend later).

Returning to the problem of diagonalization, note that a tap-path inductance L_3, shown in the rightmost network of Fig. 3.7, increases the mutual induction between the meshes. L_3 *cancels* $-M$, without affecting the total inductance of the sections in series (i.e., with the tap path open), or altering the block sum of the inductance matrix. Fig. 3.6b depicts the magnitude of L-matrix entries for the case of added tap-branch inductance. Both matrices in Fig. 3.6 were computed by FastHenry [33], a program for the efficient extraction of inductances and resistances of 3-dimensional conductor geometries on a quasistatic basis. Note that Fig. 3.6a has two more turns than the approximately diagonalized version with tap extensions on the right. The left structure is the 38-turn, 973 nH toroid whose mutual-inductance contour is plotted in Fig. 3.5. With turns packed all along its periphery, the 38-turn structure has significant end-to-end mutual inductances ($\approx$ 4 nH; the effect of this coupling term will be considered in Section 3.4.4.1). Removing two turns leaves the gapped toroid rendered on the right of Fig. 3.6, with an effectively diagonalized inductance matrix.

The planar aspect ratio and non-magnetic core of the toroids considered in this chapter are more than a manufacturing conveniences, as seen from this discussion of diagonalization. The ability to construct ladder networks in a small volume arises precisely from the low mutual inductance between turns far apart on the toroid, and the ability to compensate for adjacent-section mutual entries. Were the flux to be guided within the toroid completely,

IPR2024-00706 EX. 2005

the toroidal structure would have only one mode, and be unable to enforce the waveform symmetries discussed in Section 2.2.

3.2.3 Iterated-network measurements

The impedance data (shown in Fig. 3.8a) were taken from an iterated, coupled ladder network of 30 L-sections terminated in a short-circuit, with a total capacitance of 915 pF and a total inductance of 355 nH divided among the sections. The structure is exactly the one for which the top- and bottom-copper masks are reproduced in Fig. 3.1, and was built into a 62 mil printed circuit board. A mylar film was applied over the tap-capacitor plates, with 1-mil adhesive copper foil forming the common node for the taps (a capacitance-per-area of $C' = 157.6$ pF/in^2 was measured for this method of construction). The structures was designed for a characteristic impedance of 20 Ω and a $\lambda/4$ mode at 13.56 MHz. $Z_0 = 19.7\ \Omega$ was measured, with a principal peak at 13.41 MHz. Though the inductors in the ladder were coupled with small adjacent-section mutual terms, these mutual inductances were cancelled with 20×80-mil long inductor-traces in series with the capacitor branches (see Section 3.2.2).

Two measures are applied to the critical-frequency data from Fig. 3.8a. The first is the alignment measure of Fig. 3.8b, comparing measured pole and zero frequencies to the analytical predictions from Section 3.2.1 (dashed line), and to the desired harmonic alignment (solid line). The reflection conditions of the transmission line enforce a constant ratio between critical frequency and critical-frequency index, *viz.* $\left(4\sqrt{LC}\right)^{-1}$ for the line with a short termination (compare to the extrema Fig. 2.2, uniformly separated by one quarter wave). By normalizing all critical frequencies to this transmission-line slope, as in Fig. 3.9, it is easier to appreciate the slight crowding of critical frequencies below cutoff in the iterated case. Note that the dashed theoretical curve is the contour of denominator-polynomial roots according to the development in Section 3.2.1, and the corresponding measured impedance maxima are shown as $\times$'s. Though the zeros are non-coincident with the transmission-line locus, we could easily excite the network to exploit their alignment to a slightly lower base frequency, in this case 4% lower than the impedance-maximum frequency. The *relative* pole-zero alignment cannot be improved, however, because of the considerations of Sections 3.2.1 and 2.4. The zero shortfall (or equivalently, the pole elevation) is not due to

IPR2024-00706 EX. 2005

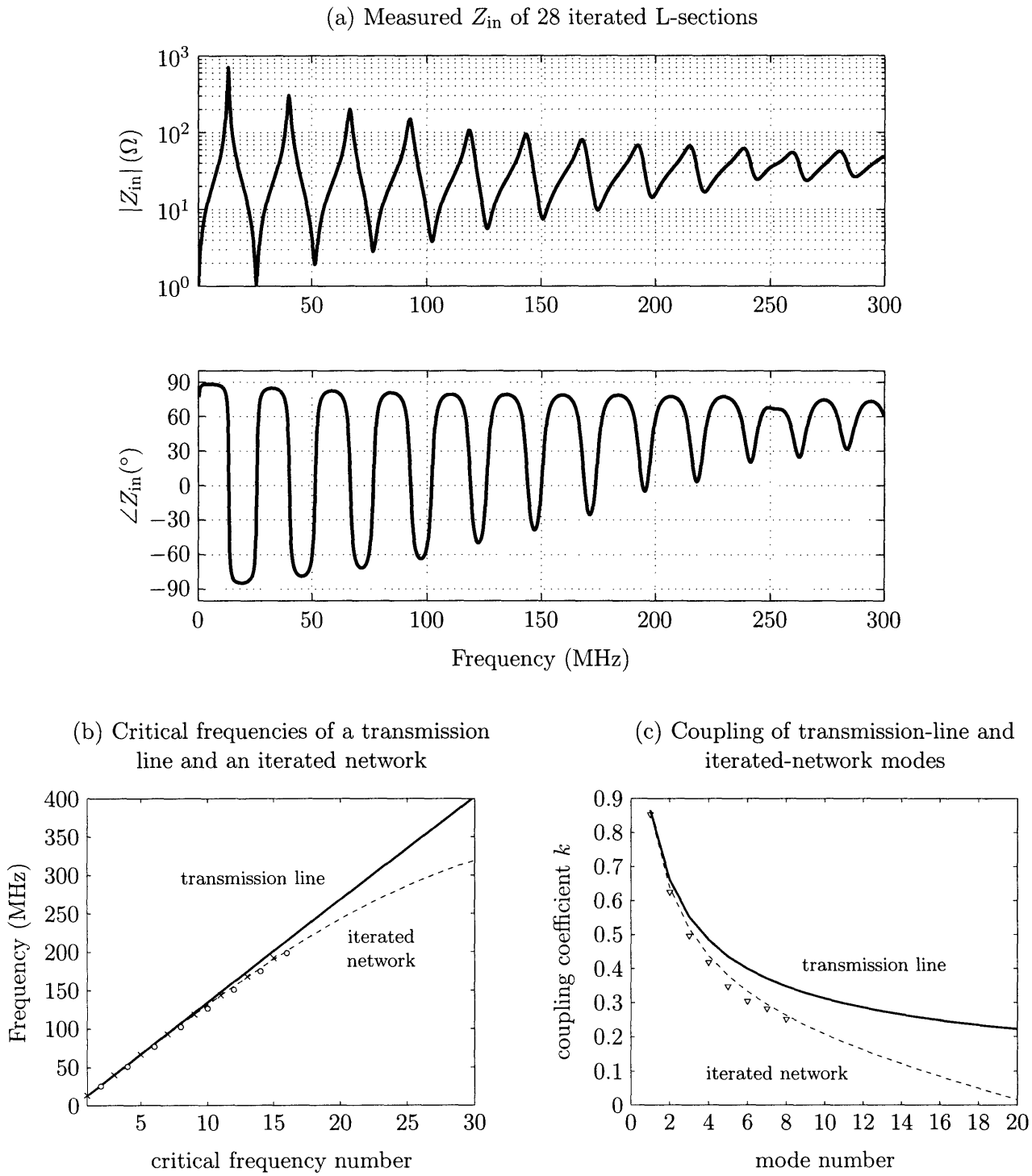

Figure 3.8: **Measured input impedance of 28 iterated, coupled L-sections, showing the trend in mode coupling and the trends in pole and zero frequencies. The data are for the design illustrated in Fig. 3.1 and described in Section 3.2.3 and Appendiz A.1.**

IPR2024-00706 EX. 2005

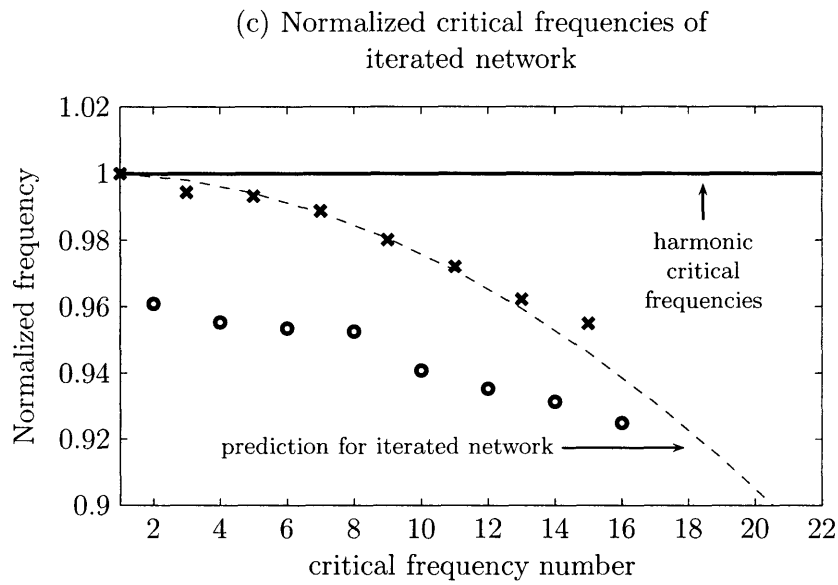

Figure 3.9: **Normalized critical-frequency alignment for the iterated network, from data in Fig. 3.8c.**

measurement parasitics, but the *low coupling* of the iterated modes, as described below.

The second metric for the impedance of Fig. 3.8a is the coupling measure plotted in Fig. 3.8c. Fig. 3.8a shows approximate pole-zero cancellations at high frequencies. I.e., zeros follow adjacent, low-frequency poles more and more closely, a phenomenon which can be quantified by the modal coupling coefficients for the iterated network. Coupling coefficients k, recall from Section 2.4, are a measure of the separation between modal frequencies and the zeros introduced by exciting them, as developed in [15, Section 4.8]. The measured values of k are computed from adjacent pole and zero frequencies using the relationship

$$k = \sqrt{1 - \frac{\omega_{\mathrm{p}}^2}{\omega_{\mathrm{z}}^2}} \tag{3.1}$$

derived in the last chapter. The measured k closely follow the trend (dashed curve) expected from the application of Eqn. 3.1 to the theoretical pole and zero frequencies from Section 3.2.1. Whereas a transmission line terminated in an open or short is capacitive and inductive over equally broad ranges of frequency (cf. Fig. 2.2), the iterated-network Z_{in} is capacitive over an increasingly narrow band following each conjugate pole, so that the phase envelope of Fig. 3.8a has an inductive bias at higher frequencies.

IPR2024-00706 EX. 2005

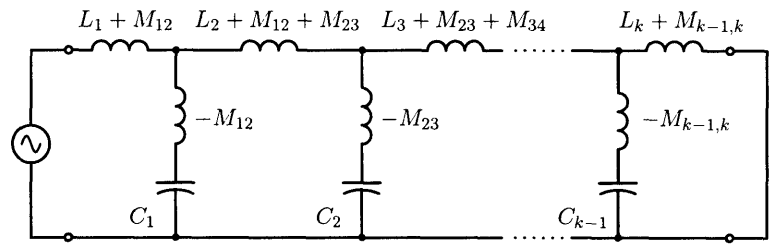

Figure 3.10: **For an a network with adjacent-section mutual coupling as in Fig. 3.4b, Δ-Y circuit transformations reflect the mutual terms as negative inductances in the tap paths.**

3.3 Iterated network with mutual coupling

Without compensating for adjacent-section mutual terms with tap inductance as in Section 3.2.2, off-diagonal mutual entries are diminished only by the low parasitic inductance in the capacitor/ground path. In such a case, after introducing a gap to eliminate end-to-end to coupling as in Fig. 3.6, the L matrix has an approximately tri-diagonal structure.

3.3.1 Inductance cancellation

In the tridiagonal case, a Δ-Y transformation for adjacent pairs of coupled inductors introduces a *negative inductance* in the intervening capacitive-tap branch. In an extension of the T-model shown in Fig. 3.7 with all section inductors wound in the same sense, the self-inductances are increased by an amount equal to the adjacent mutuals communicating with the section. Fig. 3.10 summarizes these network models for the banded L-matrix.

A negative inductance behaves like a reactance with capacitive phase but an impedance magnitude which *increases* with frequency. Though such a component would develop energy if isolated between terminals, it appears as an entry in a passive inductance matrix which is, from energy considerations, positive semidefinite. Consider the physical model in Fig. 3.11 of the transformer with parasitics in the upper left. The model includes inductance L_μ, reflecting finite permeability in the mutual flux path (with reluctance $\Re_M$), and the leakage inductances $L_{\ell 1}$ and $L_{\ell 2}$ modelling the imperfect coupling between transformer windings (with associated leakage reluctances $\Re_{\ell 1}$ and $\Re_{\ell 2}$). $L_{\ell 1}$ and $L_{\ell 2}$ are large insofar as flux

IPR2024-00706 EX. 2005

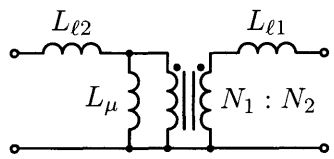

$$\begin{bmatrix} \lambda_1 \\ \lambda_2 \end{bmatrix} = \begin{bmatrix} \frac{N_1^2}{\Re_{\ell 1}} + \frac{N_1^2}{\Re_M} & \frac{N_1 N_2}{\Re_M} \\ \frac{N_1 N_2}{\Re_M} & \frac{N_2^2}{\Re_{\ell 2}} + \frac{N_2^2}{\Re_M} \end{bmatrix} \begin{bmatrix} i_1 \\ i_2 \end{bmatrix}$$

$$\begin{bmatrix} \lambda_1 \\ \lambda_2 \end{bmatrix} = \begin{bmatrix} L_{11} & L_M \\ L_M & L_{22} \end{bmatrix} \begin{bmatrix} i_1 \\ i_2 \end{bmatrix}$$

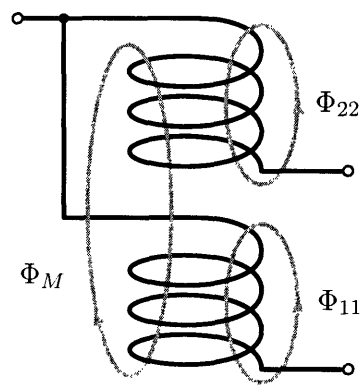

Figure 3.11: **Coupled windings, showing the paths of mutual flux Φ_M and leakage fluxes Φ_{11} and Φ_{22}. The inductance matrix which relates flux linkages to coil currents can have a "physical" form which reflects the actual paths seen by the magnetic flux, or a "phenomenonological" form like that shown on the lower left. In this inductance matrix, L_{11} and L_{22} are the self-inductances measured from either winding, and L_M is the windings' mutual inductance. Without further information about the magnetic coupling (e.g., the turns ratio), such terminal measurements do not determine a unique physical model of the magnetic circuit.**

from one winding does not link turns on the other winding (*cf.* Φ_{11} and Φ_{22} on the right of Fig. 3.11) The leakage and magnetizing inductances are "physical" — hence positive — because they correspond to energy storage within the magnetic structure. Note, however, that the physical model has four parameters (the turns ratio and the three inductances already mentioned) but can be modelled by a two-port network characterized by *three* impedances. As suggested by the equivalent inductance matrix formulation in Fig. 3.11, other "non-physical" inductances can preserve the terminal V-I (λ-I) relationships of a magnetic structure. An inaccessible internal node in the transformer model (resulting, for instance, from a Δ-Y transformation as in Fig. 3.7), can introduce a negative branch inductance while preserving the positive inductances seen from each port. We can treat the negative tap inductance like a regular circuit element, in other words, using it to cancel physical inductances or offset capacitances with a capacitive reactance that increases with frequency [16, 34, 35].

IPR2024-00706 EX. 2005

(a) Measured Z_{in} of 28 iterated L-sections with no diagonalization

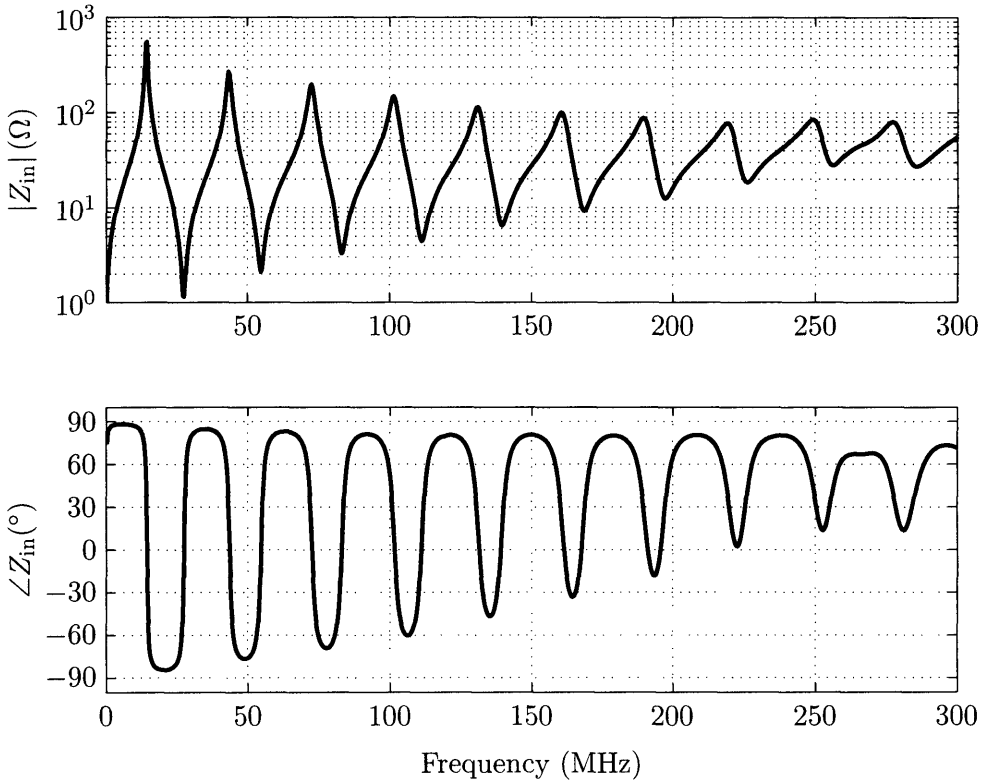

(b) Normalized critical frequencies of an undiagonalized iterated network

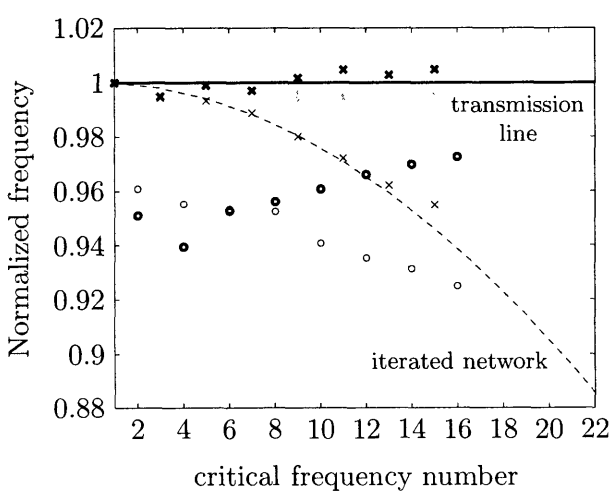

(c) Normalized coupling of undiagonalized iterated-network modes

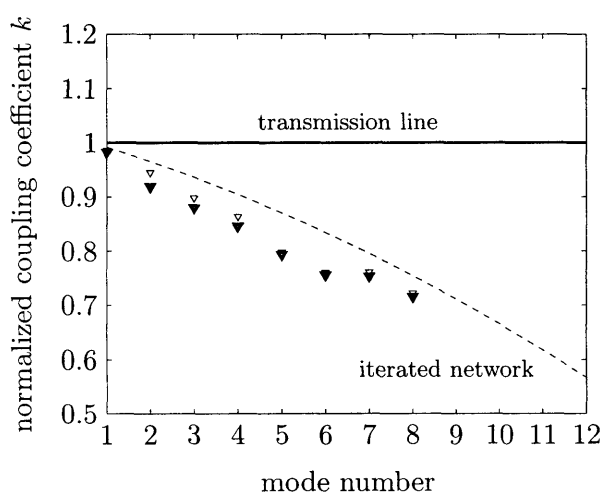

Figure 3.12: **Measured input impedance of 28 iterated L-sections, with no tap extensions and a roughly tri-diagonal inductance matrix. A full description of the experimental structure, almost identical to that described in Section 3.2.3 and Fig. 3.1, is provided in Appendix A.1.**

IPR2024-00706 EX. 2005

3.3.2 Measurements of the undiagonalized, iterated network

The measured impedance of the tapped toroid with no tap extensions, but otherwise identical the toroid of Section 3.2.3, is plotted in Fig. 3.12a. Though the mode coupling (Fig. 3.12c) is nearly identical to that of Fig. 3.8c (shown in light grey for comparison), the frequency alignment has become harmonic-coincident over a broader range of frequencies. The negative tap-path inductance cancels more and more loading capacitance at higher frequencies, just compensating for the decrease in harmonic alignment expected from the iterated network.

For the 20 Ω toroid shown here, the negative inductance in each tap L_t is about -1.5 nH, in series with $C_t = 30$ pF. An equivalent, frequency-dependent capacitance C' for both elements is given by the series combination

$$-\frac{1}{\omega C'} = -\omega L_t - \frac{1}{\omega C_t} \qquad \Longrightarrow \qquad C' = \frac{C_t}{\omega^2 L_t C_t + 1}$$

I.e., the effective loading capacitance has a knee frequency at $(L_t C_t)^{-1/2}$ rad/s, beyond which it drops at 40 dB/decade. The given L_t and C_t resonate at 750 MHz, but still affect the critical frequencies by a percent or more a decade below the LC corner. The 13th critical frequency, for instance, is a pole whose modal capacitance is decreased by the factor

$$\frac{1}{1 + \left(\frac{176}{750}\right)^2} = 0.947$$

corresponding to a 2.7% increase in frequency (a 3.8% change was observed).

Though capacitance offset improves harmonic alignment of higher frequencies, the effect is not that significant in a practical design. The alignment of the first few critical frequencies is of the greatest significance for enforcing waveform symmetries, and these poles and zeros are hardly moved at all. Moreover, as pointed out with the diagonalized structure of Section 3.2.3, poles and zeros are precluded from simultaneous coincident alignment because mode coupling in the iterated network falls below transmission-line values.

Inductance cancellation may prove important for miniaturizing line-simulating networks with low characteristic impedance and large tap capacitors, or miniaturizing analog networks for very long lines. In such cases, large capacitors with low self-resonant frequencies

IPR2024-00706 EX. 2005

might be appropriate. The base inductor in such a case could be designed such that its negative branch inductances approximately cancel the equivalent series inductance of the tap capacitors [35]. Inductance cancellation would prevent the order of the overall structure from collapsing beyond the self-resonant frequency of the capacitors.

3.4 Cauer synthesis

From the measurements presented in Sections 3.2.3 and 3.3.2, a salient problem of iterated networks is low mode coupling. In terms of impedance phase for a short-circuited termination, while the transmission line is capacitive and inductive over equally broad bands of frequency (Fig. 2.2), the iterated designs show approximate pole-zero cancellation and a pronounced inductive bias at high frequencies (*cf.* Figs. 3.8a and Fig. 3.12a). When considered separately, the poles and zeros of iterated networks have good harmonic alignment for little design effort, less than $\pm 1\%$ for the first 4 critical frequencies. Harmonic incidence, however, is much poorer (about $\pm 3\%$ of frequency) for poles and zeros considered together. Periodic waveforms can be accurately aligned to impedance minima or maxima, with half-wave repetition in current or half-wave symmetry in voltage, for instance, enforced by the network. The iterated structure cannot enforce *both symmetries simultaneously*, however, as well as it able. What we require, evidently, is a means of synthesizing a network with arbitrary modal frequencies and coupling (or, equivalently, arbitrary conjugate poles and zeros).

3.4.1 Description of the synthesis method

Cauer synthesis is a means of realizing a reactance function in a network of the Cauer form (i.e., in a ladder of series inductances and shunt capacitances, as introduced in Section 2.3.2 [26, Chapter 3]). A desired reactance or susceptance is first written in factored form, along the lines Eqn. 2.4, with a zero or pole at $s = 0$ as required:

$$X(s) = G \cdot \frac{s(s^2 - {s_1}^2)(s^2 - {s_3}^2)(s^2 - {s_5}^2)\cdots}{(s^2 - {s_2}^2)(s^2 - {s_4}^2)(s^2 - {s_6}^2)\cdots}$$

IPR2024-00706 EX. 2005

For a power-converter application with switching frequency f_{sw}, one might choose nulls at $s = 0$ and all even multiples of f_{sw}, with poles at odd multiples of f_{sw}. Residues at $s = \infty$ are now successively subtracted in the reactance or susceptance domains, corresponding to the removal of the L or C which dominates — at very high frequencies — the impedance of successive remainder networks. E.g., For the Cauer form of Fig. 3.2, the high-frequency impedance seen from the input ports are dominated by end-section inductors; the adjacent capacitors are effectively short-circuits.

3.4.1.1 A network explanation of synthesis

Removal of a residues at $s = \infty$ is illustrated graphically in Fig. 3.13. Suppose the given positive real $X_1(s)$ has a pole at at $s = \infty$. Removal of this pole in the form of a series inductance leaves a remainder that must be positive real and LC realizable, with a zero at $s = 0$ (because a reactance function must have a pole or zero at $s = \infty$, and a pole has just been removed). The inverted remainder — a susceptance function $B_2(s)$ — must therefore have a pole at $s = \infty$, and its removal yields a shunt capacitance. The remaining susceptance is again positive real and LC realizable, and has a zero at $s = \infty$, so that its reciprocal has a pole there. At this stage the original state of affairs again obtains, namely, we have a positive real and LC-realizable reactance function with a pole at $s = \infty$. The same cycle of manipulations as just carried out yields another series inductance followed by a shunt capacitance, and another reactance function with a pole at $s = \infty$. After each cycle, the remaining reactance function has one less finite nonzero pole and zero (two finite nonzero critical frequencies less than at the beginning of the cycle). When all the poles and zeros are exhausted, the process ends, and the given function is developed into an ladder network in which all series branches are inductances and all shunt branches are capacitances (cf. the networks of Fig. 3.2)

It is useful to note that the first and last elements in each of these ladder networks determines the behavior of the function at $s = 0$ and $s = \infty$. Specifically in the networks of Fig. 3.13, if $Z(s)$ has a pole at $s = \infty$, then $L_1 \neq 0$, and if $s = \infty$ is a zero, then evidently $L_1 = 0$. If $s = 0$ is a pole, then $C_n \neq \infty$, and if it has a zero, $C_n = \infty$ (a short circuit). When the given $Z(s)$ does not have a pole at $s = \infty$, therefore, the first step in the synthesis procedure is to consider its reciprocal admittance $Y(s) = 1/Z(s)$, which has a pole at $s = \infty$ that can

IPR2024-00706 EX. 2005

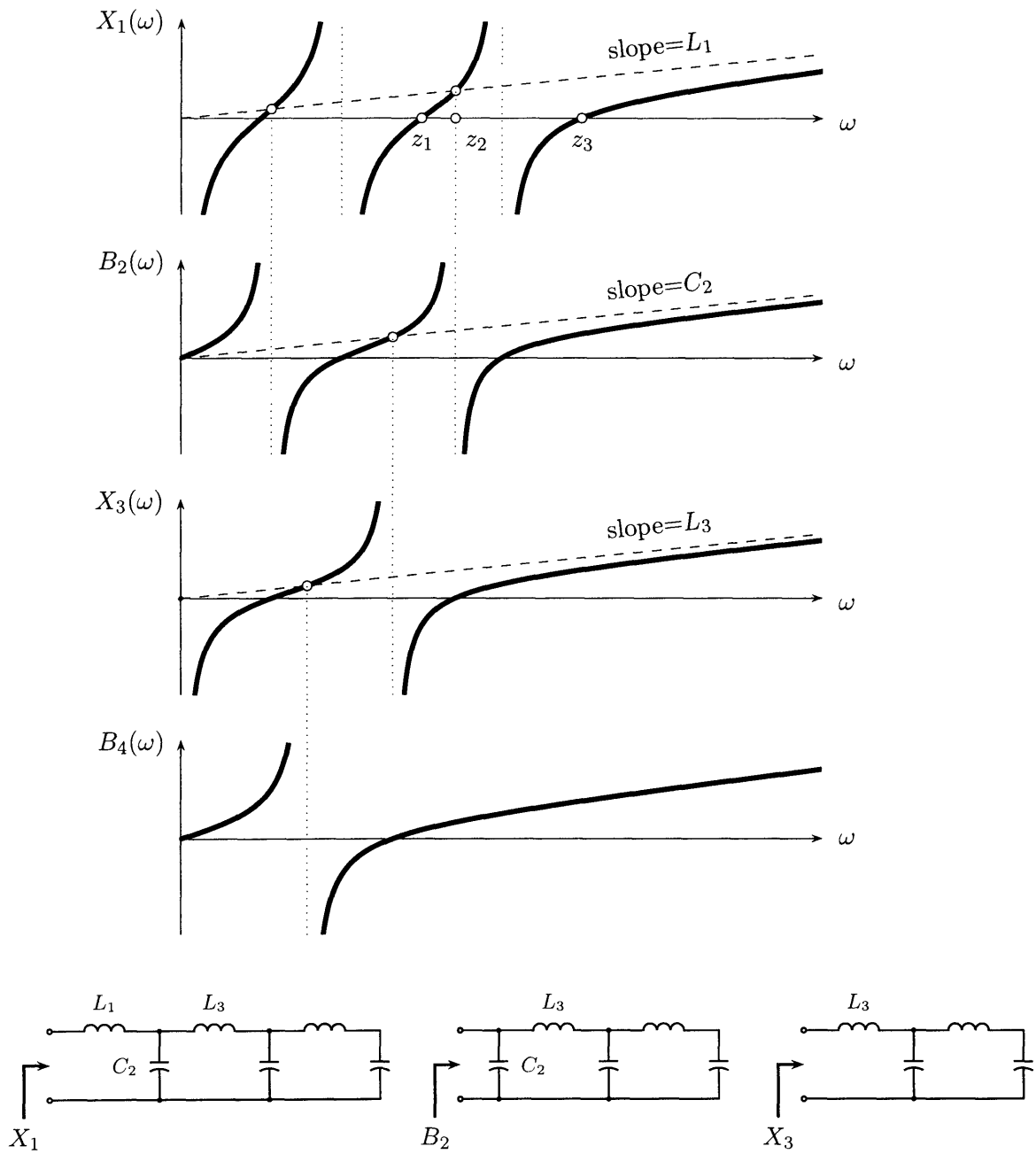

Figure 3.13: **Two cycles of Cauer synthesis, depicting the successive removal of residues in poles at $s = \infty$. Each step corresponds to a ladder-network development, i.e., the removal of the series or shunt element which dominates high-frequency reactance or susceptance, respectively.**

IPR2024-00706 EX. 2005

be subtracted as the shunt capacitance C_2.

A better appreciation of the process of successive pole removal is gained by observing graphically the details involved in some typical cycle of network reductions, as illustrated in Fig. 3.13. In the top part of this figure is a plot of the reactance $X_1(\omega)$ having a pole at $s = \infty$ which is to be removed as a series inductance L_1. Shown dashed is the asymptote of of the function $X_1(\omega)$, a straight line with a slope equal to the residue in the pole at $s = \infty$. This slope equals the value of the series inductance L_1, because its impedance dominates $X_1(\omega)$ at high frequencies . Removal of this pole at $s = \infty$ from $X_1(\omega)$ amounts to the subtraction of its linear asymptote. This process leaves the positions of the remaining poles unchanged, but shifts the zero at z_1, for instance, to z_2, located vertically below a point of intersection between the $X_1(\omega)$ curve and its linear asymptote. For the zero at z_3, the asymptotic intersection lies at infinity, and so this zero is shifted to $s = \infty$.

The inverted remainder function $B_2(\omega)$ is shown below the curve for $X_1(\omega)$ in Fig. 3.13. $B_2(\omega)$ has a pole at $s = \infty$ as explained above, and the residue in this pole is again equal to the slope of the linear asymptote, *viz.*, the value C_2 of the capacitance in the next shunt branch of the ladder. Removal of this pole from $B_1(\omega)$ shifts its highest zero to the point $s = \infty$, so that the next inverted remainder again has a pole at infinity. It is thus clear that each step in the process reduces number of finite nonzero critical frequencies by one. Eventually, there remains a function with critical frequencies only at the points $s = 0$ ans $s = \infty$, which is simply and inductance or a capacitance. The total number of elements in the complete ladder development is equal to the number of finite nonzero critical frequencies plus one, which exactly equals the number of parameters characterizing the given reactance or susceptance function as pointed out in Section 2.3.

3.4.1.2 Algebraic explanation of synthesis

In order to discuss this method of ladder development from an algebraic point of view, the reactance function is best written with the polynomials in unfactored form:

$$Z(s) = \frac{a_n s^n + a_{n-2} s^{n-2} + \cdots + a_2 s^2 + a_0}{b_{n-1} s^{n-1} + b_{n-3} s^{n-3} + \cdots + b_3 s^3 + b_1 s} \tag{3.2}$$

IPR2024-00706 EX. 2005

Removal of the pole at $s = \infty$ is accomplished by dividing the denominator polynomial into the numerator polynomial and obtaining a quotient $a_n s/b_{n-1}$ and a remainder function which is the ratio of an $(n-2)$-degree to an $(n-1)$-degree polynomial, as indicated below

$$Z(s) = L_1 s + \frac{a'_{n-2}s^{n-2} + a'_{n-4}s^{n-4} + \cdots + a'_2 s^2 + a'_0}{b_{n-1}s^{n-1} + b_{n-3}s^{n-3} + \cdots + b_3 s^3 + b_1 s}$$

where $L_1 = a_n/b_{n-1}$ is the value of the first series inductance. Inverting the remainder and repeating the process yields

$$Z(s) = L_1 s + \cfrac{1}{C_2 s + \cfrac{b'_{n-3}s^{n-3} + \cdots + b'_1 s}{a'_{n-2}s^{n-2} + \cdots + a'_2 s^2 + a'_o}}$$

in which C_2 is the value of the succeeding shunt capacitance, and the second remainder function is the ratio of an $(n-3)$-degree to an $(n-2)$-degree polynomial. Continuation of this process yields a continued-fraction development of the specified reactance or susceptance

$$Z(s) = L_1 s + \cfrac{1}{C_2 s + \cfrac{1}{L_3 s + \cfrac{1}{C_4 s + \cfrac{1}{L_5 s + \cfrac{1}{C_6 s + \cfrac{1}{\cdots}}}}}}$$

It should be noted that the expression 3.2 for $Z(s)$ assumes that n is even. If it is odd, then $Z(s)$ is an odd-over-even rational function and the final term in an inductive reactance $L_n s$.

When the reactance function $X(s)$ approximating a short-circuited line is synthesized using a Cauer development, section inductances and capacitances increase in a horn-like manner along the ladder (*cf.* Fig. 3.14, and the Cauer-synthesis code from Appendix A.3). Along the majority of the artificial line's length, the L and C values approximate those of an iterated ladder with the same number of meshes, and with the same fundamental resonance. The first section inductance, however, approaches a value 1/2 times as large as the second section, in the limit of many meshes. This initial half-section has a higher cutoff frequency than the full LC of the corresponding iterated line[5] (see Section 2.3.3). The end-section L

[5]Half-sections are used in more *ad-hoc* approximations of transmission-line impedance, *cf.* [30, Section 5.7.3]

IPR2024-00706 EX. 2005

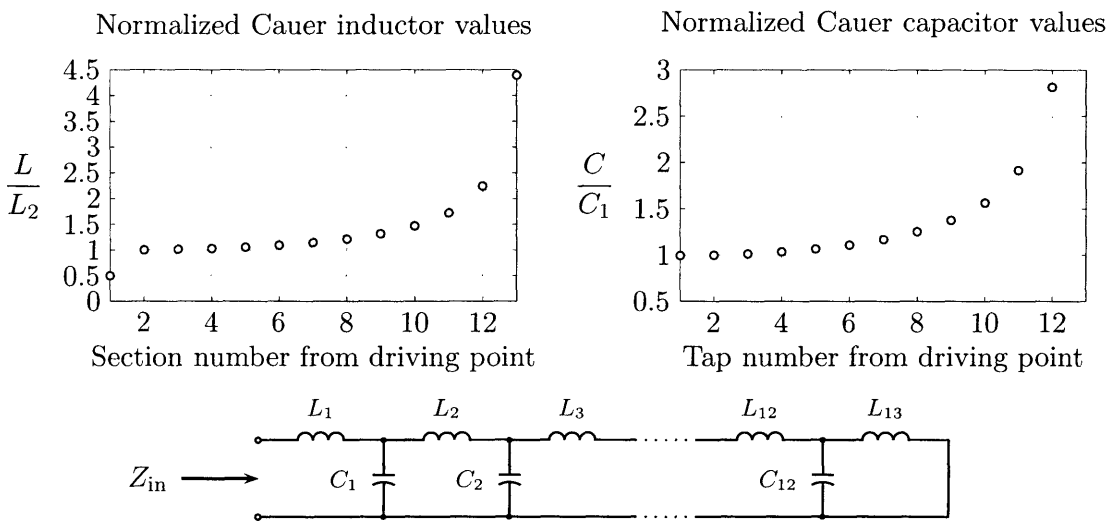

Inductors				Capacitors			
L_1	0.4983	L_8	1.2140	C_1	1.0000	C_8	1.2630
L_2	1.0000	L_9	1.3152	C_2	1.0067	C_9	1.3863
L_3	1.0102	L_{10}	1.4673	C_3	1.0206	C_{10}	1.5797
L_4	1.0279	L_{11}	1.7207	C_4	1.0426	C_{11}	1.9307
L_5	1.0544	L_{12}	2.2444	C_5	1.0742	C_{12}	2.8345
L_6	1.0916	L_{13}	4.3953	C_6	1.1180		
L_7	1.1429			C_7	1.1784		

Figure 3.14: **Cauer-synthesized L and C values for a 13-section ladder designed to match 25 transmission-line non-zero critical frequencies. The code used to generate these values can be found in Appendix A.3**

and C in Fig. 3.14 are 4.4 and 2.8 times larger than the iterated values, respectively, for 13 sections. This relative increase in end-section inductance and capacitance becomes even more pronounced for a large number of sections.

Recall that in the Foster realizations of the transmission-line impedance (Section 2.3.1), modal capacitance or modal inductance decrease as the mode-number ν squared. The total value of these tapering values roughly equals the total corresponding value in the Cauer network, taking account of the increase of values toward the end of the Cauer-synthesis procedure. The total *constant* modal L or C in the Foster form ($C_{\text{tot}}/2$ or $L_{\text{tot}}/2$), however, is much larger than the corresponding Cauer value beyond two or three modelled resonances.

IPR2024-00706 EX. 2005

The Cauer network, as asserted in Section 2.3.4 for the case of uniform L and C, is still a volume-efficient realization of $X(s)$ or $B(s)$.

3.4.2 Approximation of the Cauer network with a tapped toroid

The LC ladder values computed from Cauer synthesis can be realized with the same family laminar toroids in Fig. 3.1. By tapping a toroid nonuniformly along its length, the tap-to-tap section inductances can be chosen to approximate the Cauer-synthesized values. The self-inductance of a group of n turns in a series connection between taps is just the appropriate $n \times n$ block sum of the turn-to-turn inductance matrix.[6]

The process of condensing the full inductance matrix by progressive block sums is illustrated in Eqn. 3.3.

$$\left[\begin{array}{cc:ccc:ccc} L'_{11} & L'_{12} & L'_{13} & L'_{14} & L'_{15} & L'_{16} & L'_{17} & L'_{18} \\ L'_{21} & L'_{22} & L'_{23} & L'_{24} & L'_{25} & L'_{26} & L'_{27} & L'_{28} \\ \hdashline L'_{31} & L'_{32} & L_{33} & L_{34} & L_{35} & L_{36} & L_{37} & L_{38} \\ L'_{41} & L'_{42} & L_{43} & L_{44} & L_{45} & L_{46} & L_{47} & L_{48} \\ L'_{51} & L'_{52} & L_{53} & L_{54} & L_{55} & L_{56} & L_{57} & L_{58} \\ \hdashline L'_{61} & L'_{62} & L_{63} & L_{64} & L_{65} & L_{66} & L_{67} & L_{68} \\ L'_{71} & L'_{72} & L_{73} & L_{74} & L_{75} & L_{76} & L_{77} & L_{78} \\ L'_{81} & L'_{82} & L_{83} & L_{84} & L_{85} & L_{86} & L_{87} & L_{88} \end{array}\right] \Longrightarrow \left[\begin{array}{cc:c:ccc} L'_{11} & L'_{12} & L''_{13} & L'_{16} & L'_{17} & L'_{18} \\ L'_{21} & L'_{22} & L''_{23} & L'_{26} & L'_{27} & L'_{28} \\ \hdashline L''_{31} & L''_{32} & L'_{33} & L'_{36} & L'_{37} & L'_{38} \\ \hdashline L'_{61} & L'_{62} & L'_{63} & L_{66} & L_{67} & L_{68} \\ L'_{71} & L'_{72} & L'_{73} & L_{76} & L_{77} & L_{78} \\ L'_{81} & L'_{82} & L'_{83} & L_{86} & L_{87} & L_{88} \end{array}\right] \tag{3.3}$$

The primed values are self and mutual terms already condensed by summing, and the three next turns along the toroid — for this example of ladder development — are to be combined

[6]The interested reader can verify this fact by considering the inductance matrix on the left of Fig 3.7. With the $-M$ mutual-path open, the inductors appear in series with a total self-inductance is $L_1 + L_2 + 2M$. Extension of this case to a 3×3 example demonstrates how mutual terms of the condensed inductance matrix are formed by the row and column sums given in Eqn. 3.4.

IPR2024-00706 EX. 2005

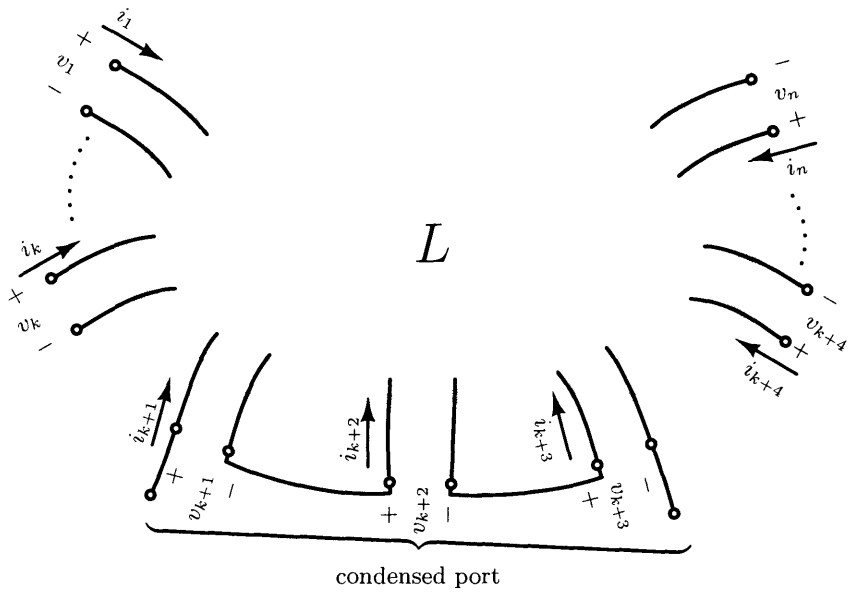

Figure 3.15: **Series port connection in the inductance matrix**

into one section inductance. The condensed self-inductance and mutual terms are

$$\text{where} \quad L'_{33} = \sum_{i=3}^{5}\sum_{j=3}^{5} L_{ij} \quad \text{and} \quad L''_{j3} = L''_{3j} = \sum_{i=3}^{5} L'_{ij} \quad \text{for } j < 3 \tag{3.4}$$

$$L'_{j3} = L'_{3j} = \sum_{i=3}^{5} L_{ij} \quad \text{for } j > 5$$

where the lower-right submatrix remains undisturbed.

A more powerful method of constructing the condensed inductance matrix is illustrated by Fig. 3.15 and Eqn. 3.5. A series connection of three ports is shown, such that the gathered turns have a total voltage drop equal to the sum of three individual port voltages. This series connection can be expressed algebraically as a transformation M between the n original port voltages v, and a new set of $n-2$ port voltages v':

IPR2024-00706 EX. 2005

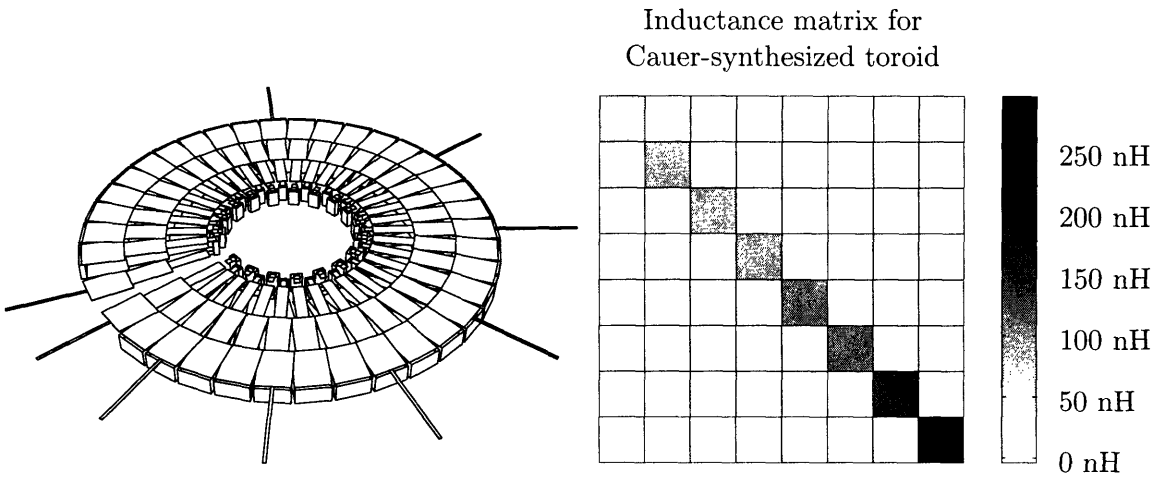

Figure 3.16: **FastHenry models and the computed inductance matrix for a 8-section Cauer-derived network. Pairs of adjacent tap extensions are ports for the L matrix, where the two extensions below the toroid gap correspond to the smallest self-inductance in the upper-left entry of the matrix. Design details for this structure, along with scripts for generating the corresponding FastHenry model, can be found in Appendix A.2.**

$$v' = Mv = \left[\begin{array}{c:c:c} I_k & 0 & 0 \\ \hdashline 0 & 1\ 1\ 1 & 0 \\ \hdashline 0 & 0 & I_{n-k-3} \end{array}\right] \begin{bmatrix} v_1 \\ \vdots \\ v_{k+1} \\ v_{k+2} \\ v_{k+3} \\ \vdots \\ v_n \end{bmatrix} \tag{3.5}$$

The correponding current transformation imposes an equality condition between connected terminals, so that $i = M^{\mathrm{T}} i'$, where i' the vector of new port currents. The new inductance matrix, under this transformation, is found by substitution:

$$v = sLi \qquad \Longrightarrow \qquad v' = sMLM^{\mathrm{T}} i' = sL'i'$$

Though adjacent ports are shown in this example, with only one gathering of turns, the basic structure of M can be extended to any set of simultaneous connections.

A rendering of a Cauer network synthesized from a 36-turn base toroid of 953 nH is shown in Fig. 3.16, full design details of which can be found in Appendix A.2. The taps start off closely spaced at the input node on the lower left, with turns per section n_k increasing

IPR2024-00706 EX. 2005

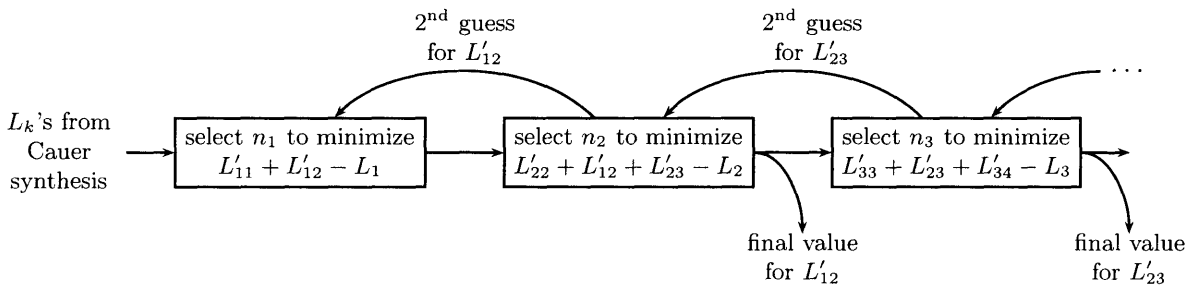

Figure 3.17: **Iterative method for determining tap locations along a toroid. The n_k are the number of turns in each Cauer-synthesized section with self-inductance L'_{kk}. Code implementing this strategy can be found in Appendix A.3**

counter clockwise toward the termination:

$$n_k = 2,\ 3\ ,3\ ,3\ ,4\ ,4\ ,6\ ,11 \text{ turns per section}$$

The self inductances L_k of the condensed network likewise increase as the block-sums for the 8 $n_k \times n_k$ L-matrix submatrices:

$$L_k = 37.7,\ 63.9,\ 62.6,\ 63.9,\ 89.9,\ 89.9,\ 144.5,\ 282.0 \text{ nH}$$

The discrepancy between the sum of these self inductance (834 nH) and the total toroidal self inductance is due to adjacent-section mutual entries. As one would expect form the turn-gathering procedure, the block sum of the condensed inductance matrix is identical to that of the original 36×36 L matrix.

As in the case of section-to-section coupling discussed in Sec. 3.3, mutual inductances M in an immediate off-diagonal add to the self-inductances of the sections they couple, and appear as an impedance $-sM$ in the tap between coupled sections. These mutual terms are of the order of 10% of the tap-to-tap self-inductances, and must be taken into account for accurate pole-zero placement in the Cauer-derived toroid. Assuming that the condensed L matrix is diagonalized with tap extensions (as depicted before in Fig. 3.6) we have only to consider the contribution of mutual inductances $L_{k-1,k}$ and $L_{k,k+1}$ to the section L_k of the Cauer network. The progressive grouping of turns along the toroid represented by Eqn. 3.3, however, cannot explicitly account for the mutual inductance of condensed sections yet to be designed. The iterated method summarized in Fig. 3.17 circumvents this difficulty by regrouping turns for each section k once the section $k+1$ is designed, refining the estimate of

IPR2024-00706 EX. 2005

condensed section-inductance L_k with a better approximation for $L_{k,k+1}$. The initial guess for L_k is based upon the forward mutual inductance to a block with an identical number of turns n_k. The Cauer structure of Fig. 3.16 was designed using this method.

3.4.3 Measurements of the Cauer-synthesized toroid

Fig. 3.18a shows the measured impedance of a Cauer-synthesized toroid based upon the 20 Ω layout of Figure 3.1 (see figure for dimensions), with diagonalizing tap inductances and 11 condensed sections. The phase envelope in Fig. 3.18a is more capacitive than in the iterated cases of Figs. 3.8a and 3.12a. As further evidenced by the close approximation to transmission-line coupling coefficients (Fig. 3.18c), Cauer synthesis can effectively raise zero frequencies and increase coupling of lumped-line modes. The critical-frequency alignment of Fig. 3.18b is mediocre compared to the iterated cases, however. Though poles and zeros are both in the vicinity of harmonic coincidence, their location seems much more uncertain (±3%) than in the iterated networks. The alignment of the lowest frequency poles and zeros is especially poor, compared to the readily achieved pole or zero alignment in Figs. 3.8b and 3.12b. Note that overall harmonic alignment (i.e., considering poles and zeros together) is not appreciably worse than in the iterated cases.

Critical-frequency alignment improves dramatically when we compare poles and zeros, not to harmonically aligned values, but to the values expected after the process of turns gathering outlined in Section 3.4.2. Because of the discrete choices for section-inductance available at any given point in the network realization, the smoothly flared L and C values (typified by Fig. 3.14) can at best be approximated. Normalizing measured poles and zeros to the frequencies computed from the approximated Cauer network yields the alignment depicted in Fig 3.19. Here we have ±1% alignment of poles and zeros over a broad frequency range, with tighter coincidence when the first 5 or 6 critical frequencies are considered alone. This result is a strong endorsement for the accuracy of the inductance matrix computed with FastHenry. Note that fringing capacitance and lead inductance were considered when predicting the critical frequencies for Fig 3.19 (see caption). While lead inductance was considered in the examples from Sections 3.2.3 and 3.3.2, capacitor uncertainty affected each section uniformly in the iterated cases, appearing as a frequency and characteristic-impedance discrepancy.

IPR2024-00706 EX. 2005

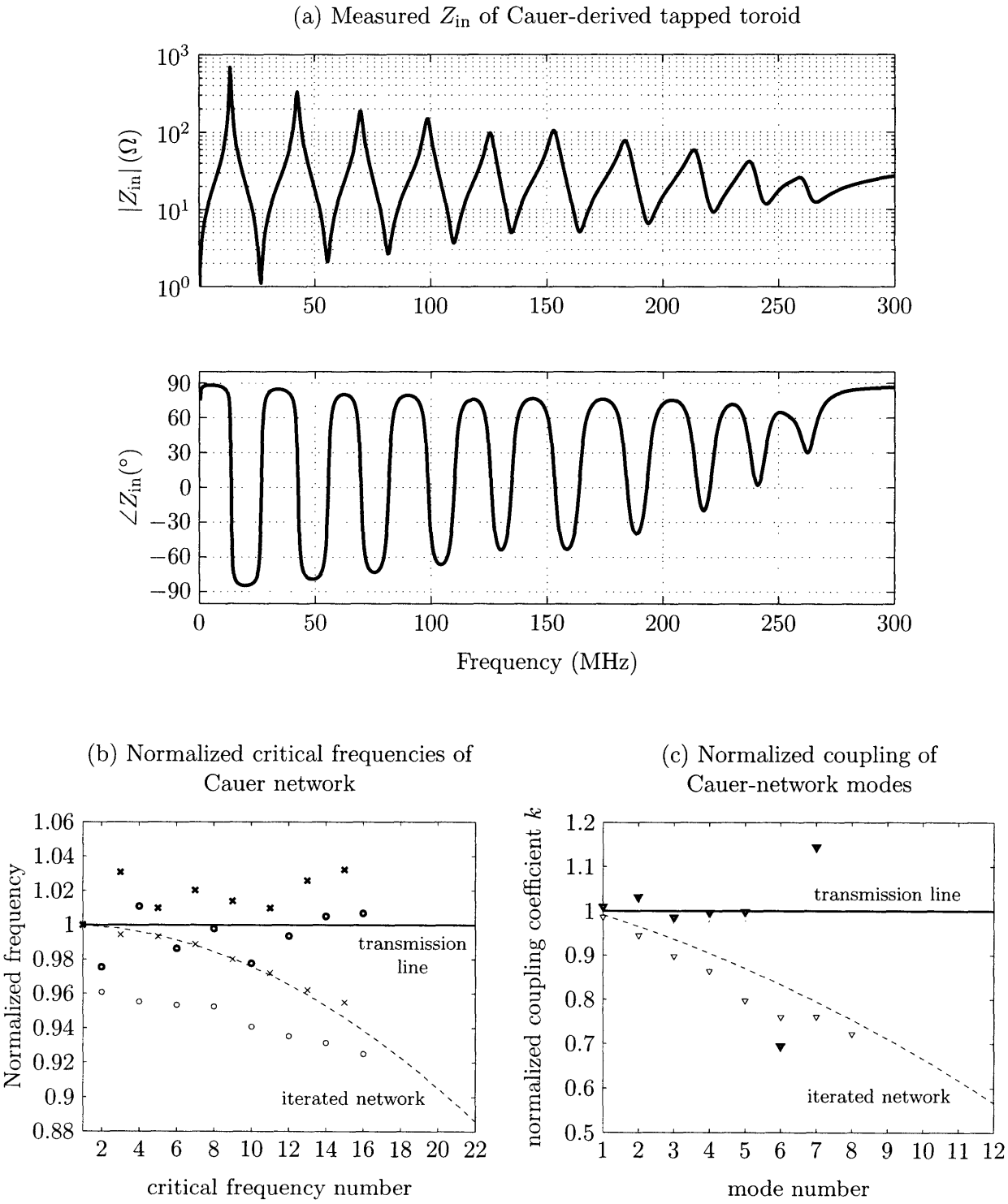

Figure 3.18: **Measured input impedance of a Cauer-derived toroid. Full details of this design can be found in Appendix A.1.**

IPR2024-00706 EX. 2005

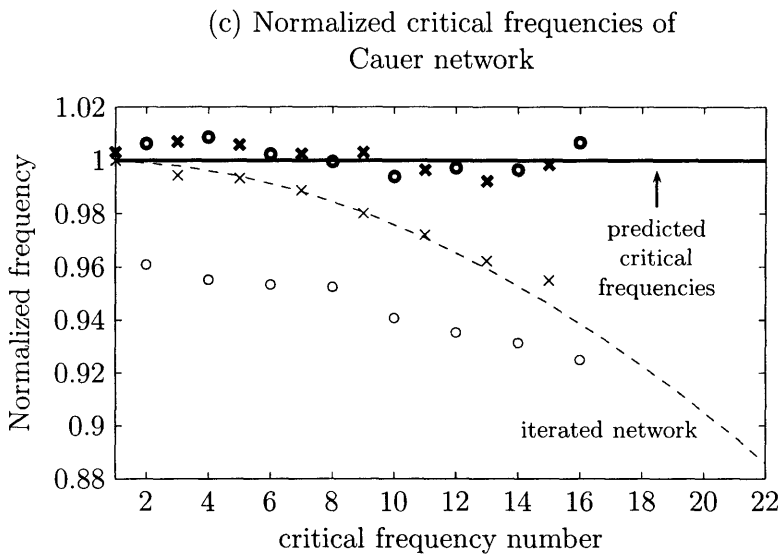

Figure 3.19: **Improved frequency alignment for the Cauer-derived toroid, compared to model prediction rather than a transmission line. 12.2 nH lead inductance were added to first section, and 5 pF stray capacitance added to each tap.**

3.4.4 Perturbations of Network Models

Our effort to model tapped toroids on a network basis has been fruitful. Methods for L-matrix diagonalization, compensation for non-coincident critical frequencies, and placement of impedance extrema have been considered in turn. This section introduces two departures from the results of network analysis that are difficult to analyze, because they require eigenanalysis of a non-diagonal matrix or abandonment of lumped models altogether. Note that because Cauer synthesis has enough degrees of freedom to place each pole and zero independently, the turns-condensation method — or some other means of varying inductance and capacitance along a structure — could compensate for the frequency perturbations mentioned here.

3.4.4.1 End-to-end coupling

Two turns were taken off the full PCB toroids constructed for Sections 3.2.3, 3.3.2, and 3.4.3 in order to elimate end-coupling entries in their inductance matrices. Small mutual inductances in the anti-diagonal extremes perturb the zeros of the tapped toroidal structures in the manner shown in Fig. 3.20a (where zeros shift from an original frequency ω_k to ω'_k).

IPR2024-00706 EX. 2005

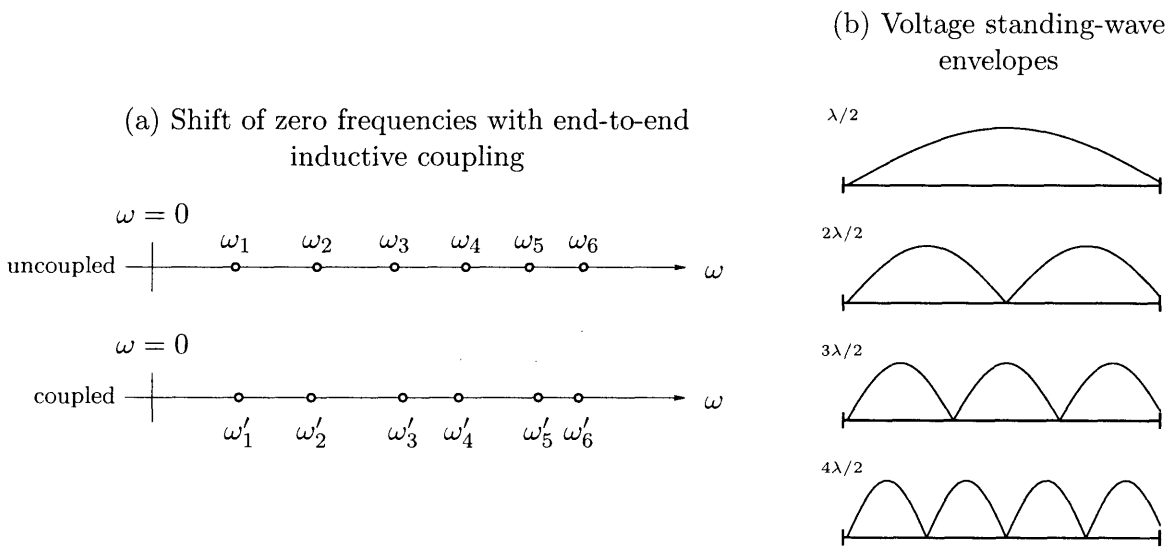

Figure 3.20: **Shifting of zero frequencies for end-to-end mutual inductance**

A network with 10 uniform inductors was considered for this example, with 9 uniform tap capacitances placed at internal nodes between inductors. Mutual terms 20% as large as the main-diagonal L-matrix entries were introduced to couple the terminal inductors. From eigenanalysis of a state-space model incorporating this non-diagonal inductance matrix and simulating a short termination (*cf.* Section 4.2.1), we conclude that odd-numbered zeros *increase* in frequency and even-numbered zeros *decrease.*

This zero "clustering" phenomenon can be explained with reference to voltage standing-wave envelopes along a distributed line, shown in Fig. 3.20b.[7] In the distributed line, the $\lambda/2$-mode corresponds to the first zero, with integral half-wavelengths added for each successive zero $\omega_2 < \omega_3 < \ldots$. The $\lambda/2$-mode is shorted at either and, and corresponds to a current modeshape with one internal node. The number of current inflections increases by one for each subsequent zero, from which we see that odd zeros have *anti-symmetric* end-section flux, and the even-numbered zeros *symmetric.* Even-numbered zeros are effectively "weighed down" by higher flux linkage, and move down in frequency to meet the approach of their odd, lower-flux neighbor.

[7] i.e., we are considering the transmission line approximated by our lumped network. The standing waves were plotted, incidentally, from the eigenvectors of a 120th-order version of the same state-space model we are analyzing.

IPR2024-00706 EX. 2005

3.4.4.2 Shielding

Multi-resonant structures of the type we've considered, and air-inductors more generally, can operate at much higher frequencies than magnetic elements incorporating lossy, permeable materials. Air-core structures have large leakage flux, however, and require shielding to decrease the sensitivity of their impedance to surrounding conductors and mitigate radiated EMI. Figure 3.21 depicts the measured shift in critical frequencies for a multi-resonant structure (the 20 Ω PCB element from 3.3.2) as a 1-mil copper ground plane is brought closer to both its faces. The dielectric for the 62 mil separation was FR4 ($\epsilon_r = 3.5$, 0.127 pF/in^2) and for the 5- and 10-mil separation was mylar adhesive tape ($\epsilon_r = 1.75$ including adhesive, with 78.8 pF/in^2 and 39.4 pF/in^2 capacitance, respectively).

The critical frequency alignment starts off for the 62 mil separation with roughly the expected alignment until the 4th zero. Upon a closer approach of the ground shield, two effects are observed. At 10 mil separation, the ground shield bucks leakage flux from the toroid; the device stores less magnetic energy and its critical frequencies increase.[8] The harmonic alignment of poles and zeros is perhaps tolerable until the second null frequency, though a judgment of this sort will depend on the increased eddy-current losses and harmonics that can be tolerated in a particular application. At a 5-mil shield separation, an increase in distributed capacitance eventually overwhelms the decrease in inductance. The structure is now loaded by much more electrical energy that out the outset and its critical frequencies decrease. It should be noted that the frequency shifts depicted in Fig. 3.21 appear complicated aside from general trends, especially at higher frequencies. The problem of designing a self-shielded transmission-line analog may therefore be intractable with the network methods developed in this chapter, and could possibly benefit from full-field simulations of the desired geometry. The design of successive pole/zero-placement experiments — using Cauer approximations of the type presented in Section 3.4.2 to counteract perturbations introduced by dual ground planes — may be the best alternative.

[8]It is precisely the leakage flux, incidentally, that is responsible for the harmonic alignment of critical frequencies we seek. A toroid with perfect section-to-section coupling along its length has only *one mode*.

IPR2024-00706 EX. 2005

(a) Shift of zero frequencies with shielding

(b) Shift of pole frequencies with shielding

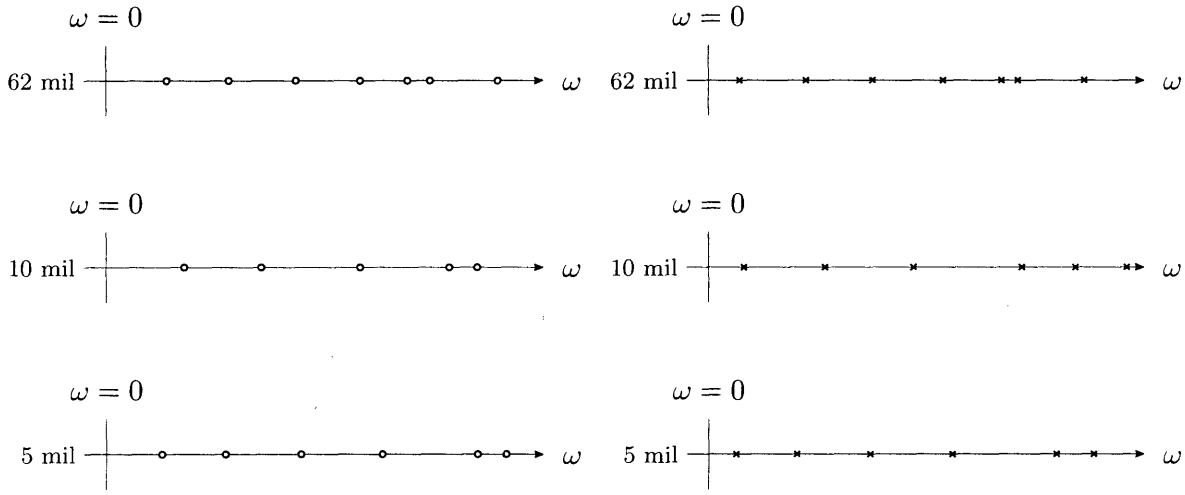

	Zero Frequencies (MHz)				**Pole Frequencies (MHz)**		
	62 mil	10 mil	5 mil		62 mil	10 mil	5 mil
z_1	27.7	35.6	25.4	p_1	14.4	16.4	12.7
z_2	55.8	70.6	54.3	p_2	45.0	53.9	40.8
z_3	86.4	116	88.7	p_3	75.6	94.4	74.4
z_4	116	157	126	p_4	108	144	112
z_5	138	170	170	p_5	134	168	160
z_6	148	206	206	p_6	142	192	177

Figure 3.21: **Shift of critical frequencies for three ground-shield separations**

IPR2024-00706 EX. 2005

3.5 Chapter summary

This chapter has considered critical-frequency alignment of iterated and Cauer-derived transmission-line analogs with planar, air-core magnetic geometries. For the iterated network, a relation between the critical frequencies of cascaded LC sections and the roots of Fibonacci polynomials has been presented. This result is an analytic means of treating the transition between a distributed line and its lumped analogs, and appears to be new in the literature. The Cauer type of line-simulating network, with non-uniform placement of taps in approximation of the L and C values from Cauer synthesis, was seen to have precise but inaccurate coincidence. Because such a network realizes a *specified* driving-point reactance, however, harmonic alignment can be improved.

Structure	**Harmonic alignment**	**Coupling**	**Tolerance**
Iterated	pole and zero frequencies decrease as $\cos\left(\frac{2k}{m}\right)$	lower at high frequencies	$\pm 1\%$ to the 10th critical frequency
Tri-diagonal	harmonic pole alignment	same as diagonalized case	$\pm 1\%$ to the 10th critical frequency
Cauer	harmonic pole and zero alignment	more even pole-zero spacing	$\pm 3\%$, or $\pm 1\%$ within prediction

IPR2024-00706 EX. 2005

Chapter 4

Multi-resonant power converters

THE multiresonant structures developed in Chapters 2 and 3 can be used as drop-in replacements for large passive elements in power converters. The application of *single*-resonant networks to switching cells and filters was considered in Section 2.1, and the impedance- and volume-enhancing techniques presented there will now be extended to multiple harmonics. Like their single-resonant counterparts, transmission-line analogs can exchange Q for bulk or efficiency and improve closed-loop bandwidth. Unlike the single-tuned case, significantly, multiple resonances can approximate delays which enforce waveform symmetries and can increase power or efficiency.

Consistent with the reduced losses but low magnetizing of the air-core structures we've considered, tolerable component volumes are only possible at high switching frequencies.[1] The greatest practical challenge to power conversion in HF and VHF regimes has scarcely been mentioned; namely, the problem of control and regulation at high frequencies. Shown in Fig. 4 is a block diagram of an *uncontrolled* dc-dc converter operating at radio-frequencies, comprising a high-frequency inverter with its output matched into a rectifier. In a practical dc-dc application, such a converter is usually required to operate efficiently over a wide load range (often in excess of 100:1) from a variable input voltage, and must regulate the

[1]The high- and low-power examples considered in this chapter, for instance, switch at 13.56 and 82 MHz, respectively.

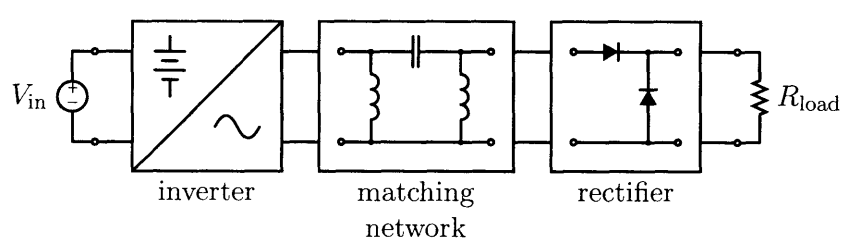

Figure 4.1: **Block diagram of an RF dc-dc converter**

IPR2024-00706 EX. 2005

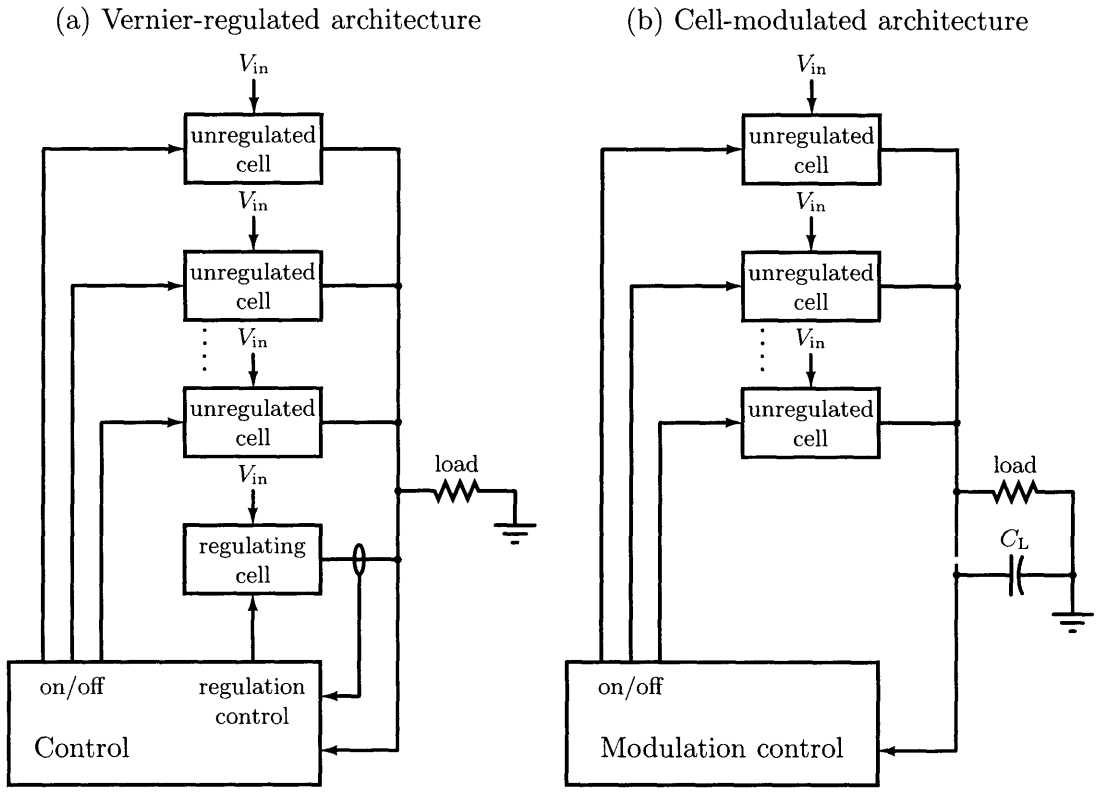

Figure 4.2: **Vernier-regulated architecture and cell-modulated architecture which provide on-off control for high-frequency dc-dc converters [36].**

output in the face of rapid and unpredictable load and input variations. RF power circuits, however, are particularly unsuited to these operational requirements, if they are to operate in the frequency ranges necessary for the passive scaling we seek. In the first place, inverters and rectifiers operate with tolerable efficiency only over a relatively narrow load range; load impedance greatly affects the tuned networks and waveforms internal to the stage. The controllability of these designs (e.g., to compensate for load or input variations) is also very limited, in large part because of the requirement that they operate at a fixed frequency. I.e., we are not able to regulate power by frequency-control techniques, in the manner of resonant converters, nor is it practical to modulate gating waveforms at the power levels and efficiencies we require.[2]

[2]The high-efficiency inverters we will consider are called *constant-envelope* designs. Their output level is not proportional to the drive, nor subject in any obvious way to control of the switch.

IPR2024-00706 EX. 2005

To overcome the unsuitability of traditional RF power amplifiers in a power setting, new cellular converter architectures of the types depicted in Fig. 4.2 have been proposed [36]. Cellular regulation schemes provide on-off commands to individual cells, each of which must only be rated for a fraction of the system load, and which are designed to deliver constant power (i.e., to function as switchable current sources into a constant load voltage). Cells can be turned on and off in a thermometer code, as suggested by Fig. 4.2a, with a small variable-output regulator (the so-called Vernier cell) controlling the output voltage with continuously variable current. With an energy buffer at the output, alternatively, individual cells can be turned on and off rapidly enough to control average power without a vernier cell[3] (*cf.* Fig. 4.2b).

The principal contribution of this chapter, a soft-switching inverter incorporating a multi-resonant input network, should be considered within the larger context of RF dc-dc converters presented in this section. Numerous ancillary issues that are not elaborated here — notably self-oscillating gate drives and active methods of tuning a switching frequency to excite a multi-resonant structure — are treated elsewhere [16, 17, 18, 36, 37].

4.1 Cell topologies

Several high-efficiency inverter topologies are usually considered for use in unregulated cells like those of Fig. 4.2. The operation of these inverters (and the size of their passive elements in particular) provides a backdrop for a new inverter topology incorporating multi-resonant structures, presented later in Section 4.1.3.

4.1.1 Class E Inverter

A Class E inverter, used in the cellular converters of [36] and [37], is depicted in Fig. 4.3. The input inductor L_{choke} provides a dc path to the source and approximates an open circuit at radio frequencies. The difference between the roughly constant I_{choke} and i_{load} (*cf.* the

[3]In an implementation comprising cells switching at 100 MHz, for instance, 75 kHz modulation of the converter was demonstrated [36], and modulation frequencies ten times higher are anticipated in the next generation.

IPR2024-00706 EX. 2005

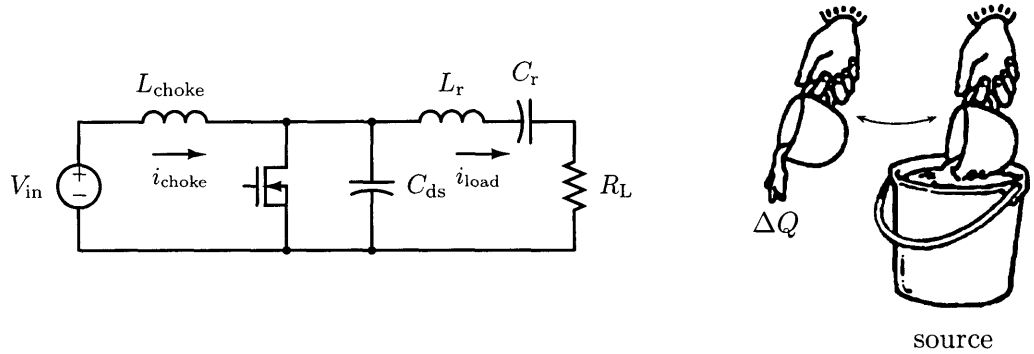

Figure 4.3: **Schematic of a Class E inverter, and a cup-and-bucket analogy for the relation between its switching frequency and power delivery.**

bottom plot of Fig. 4.1.1) is a sinusoidal current with dc offset which enters the FET channel and parallel capacitance C_{ds}[4] as conduction or displacement current (Fig. 4.1.1, middle plot). There are enough degrees of freedom in the output network (comprising C_{ds}, C_r, and L_r) such that the drain waveform can be shaped to have zero voltage and zero slope simultaneously. The resulting drain waveform (Fig. 4.1.1, top waveform) offers a broader opportunity for zero-voltage switching, and suffers less efficiency degradation for finite switching times than converters which do not enforce zero drain current at turn-on [38, 39].

4.1.1.1 Stresses in the Class E

Class E waveforms are treated in detail in [38, 39]. Analytical design equations assume that the current through L_r and C_r is sinusoidal, which is strictly true only for infinite loaded Q (Q_L, defined as $2\pi\omega_s L_r/R$, where R is a measure of the total average loss in the drain-source-load mesh, and ω_s is the switching frequency). To treat the more general case of finite Q, the authors cited above tabulate various dimensionless design parameters as functions of Q_L. A detailed analysis of Class-E waveforms highlights the dramatic peak-to-average ratio of switch voltage and current, indicative of the high switch stresses in this design. The peak drain voltage $v_{ds,pk}$ is approximately $3.56V_{in}$ (even larger when the non-linear drain-source capacitance of the FET is taken into account) and the peak conduction current is roughly

[4] C_{ds} may be external and/or internal capacitance.

IPR2024-00706 EX. 2005

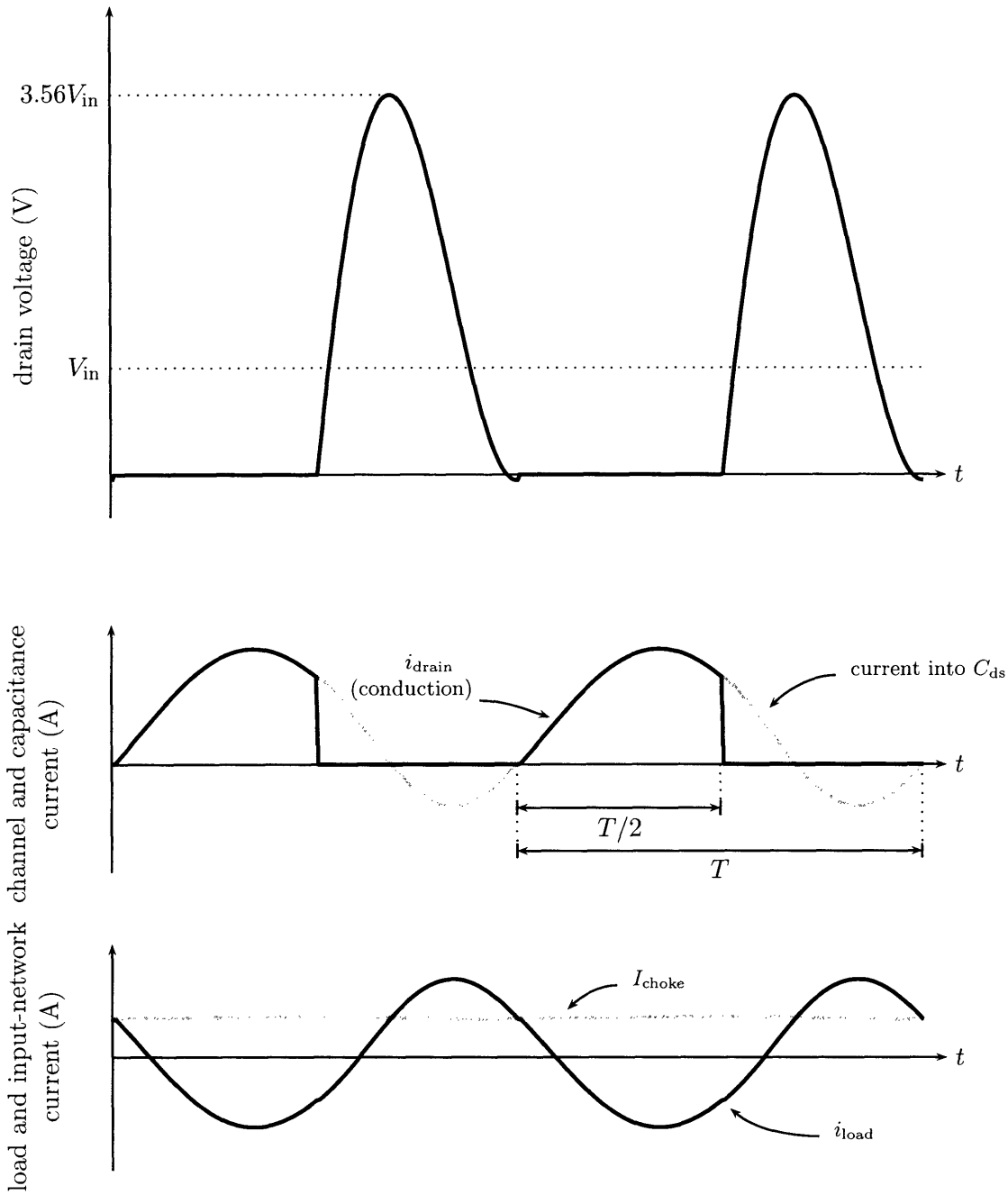

Figure 4.4: **Simulated waveforms of Class E inverter.**

IPR2024-00706 EX. 2005

$1.7V_{\text{in}}/R$. As a function of Q_{L}, the output power is described by a fit of simulation results:

$$P = \left(\frac{V_{\text{in}}^2}{R}\right)\left(\frac{2}{\frac{\pi^2}{4}+1}\right)\left(1.001245 - \frac{0.451759}{Q_{\text{L}}} - \frac{0.402444}{Q_{\text{L}}^2}\right)$$

where R is the total tank loss, including reactive-component ESR, switch conduction loss, and the load:

$$R = R_{\text{load}} + \text{ESR}_{L_{\text{r}}} + \text{ESR}_{C_{\text{r}}} - 1.365R_{\text{on}} - 0.2116\text{ESR}_{C_{\text{ds}}}$$

The normalized power output capability P_{N} is a dimensionless figure of merit quantifying device stress, with lower values corresponding to poorer switch utilization. For the Class E, we compute a P_{N} of

$$P_{\text{N}} \equiv \frac{P}{v_{\text{ds,pk}} \cdot i_{\text{d,pk}}} \approx 0.095$$

which is demanding on the switch, 40% lower than the Class F (see Section 4.1.2) and 70% lower than the Class D [30, Section 13.4]. Practical implementation of the Class E do not exhibit significantly improved efficiency over well-executed designs of other types [30, Section 13.5], in part because the switch turn-off occurs near maximum current. Dissipation for non-instantaneous switching at high frequencies can offset much of the efficiency improvement achieved by robust ZVS turn-on.

4.1.1.2 Class E design

The design equations used for inverter comparisons in this chapter (see the discussion of switch and frequency selection in Section 4.3.2.1) assume a $Q_{\text{L}} = 10$ and set the peak drain voltage v_{d} to 80% of the switch drain-source standoff (V_{dss}). The native C_{ds} of switches under consideration is used in simulation, approximated by linearized C_{ds} biased at V_{in}:[5]

$$C_{\text{ds}} = \frac{C_{\text{ds0}}}{\left(1 + \frac{V_{\text{in}}}{\psi}\right)^n}$$

[5] the parameters n and ψ were fit for each switch from drain-source impedance measurements under swept dc bias.

IPR2024-00706 EX. 2005

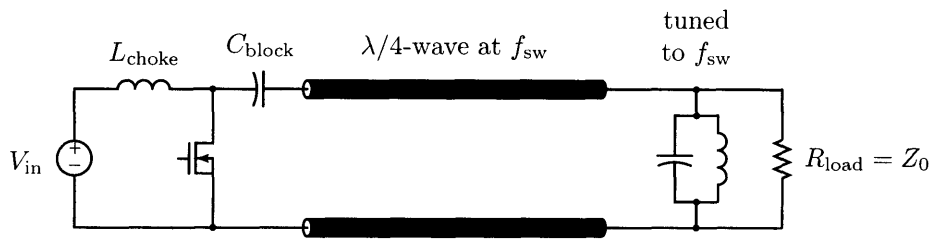

(a) Class F converter incorporating a transmission line

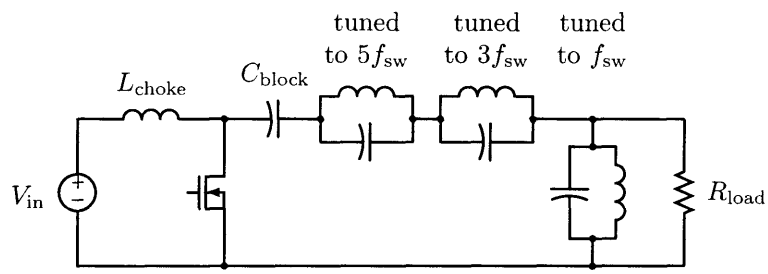

(b) Class F converter with Foster approximation of the line impedance

Figure 4.5: **A Class F inverter incorporating a transmission line, and an alternative realization approximating the line with two parallel-tuned resonators.**

The native device C_{ds} is often not augmented by external capacitance in order to limit the power processed by the switch. As represented by the cup-and-bucket analogy in Fig. 4.3, the Class E delivers drain-source charge ΔQ toward the load once per cycle. Thus, output power is proportional to drain-source capacitance in a Class E design. At the high frequencies (10-40 MHz) considered for some of the designs of this chapter, the delivered power can exceed 1 *kilowatt* for 40 MHz switching, an embarrassment of power which is impractical from passive- and thermal-design considerations (see Section 4.3.2.1). For some f_{sw} and fixed C_{ds}, then, the total tank resistance is set by another fit function reported in [39]:

$$R = \frac{1}{34.2219 f_{\text{sw}} C_{\text{ds}}} \left(0.99866 + \frac{0.91424}{Q_{\text{L}}} - \frac{1.03175}{Q_{\text{L}}^2} \right)$$

The design equations presented by the same author can now be applied in a straightforward manner:

$$C_{\text{r}} = \frac{1}{2\pi f_{\text{sw}} R} \left(\frac{1}{Q_{\text{L}} - 0.104823} \right) \left(1.00121 + \frac{1.01468}{Q_{\text{L}} - 1.7879} \right) \qquad \text{and} \qquad L_{\text{r}} = \frac{Q_{\text{L}} R}{2\pi f_{\text{sw}}}$$

Where L_{choke} can be conservatively selected 10 times larger L_{r}, and reduced later based on simulation of acceptable waveform distortions.

IPR2024-00706 EX. 2005

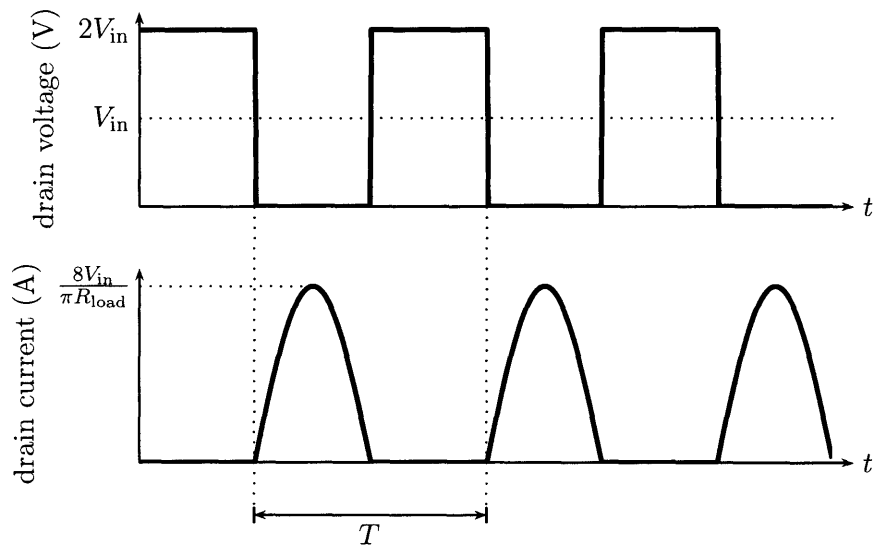

Figure 4.6: **Idealized drain waveforms of the Class F inverter.**

4.1.2 Class F Inverter

Fig. 4.5 depicts two examples of the Class F topology [40], [41, Chapter 5], one with a $\lambda/4$-wave length of line, and one with two parallel-tuned tanks approximating a transmission-line impedance (a Foster-form network, see Section. 2.3). A multi-resonant structure of a Cauer form, like those presented in Chapter 3 could also be incorporated into a Class F design, printed directly into a PCB, for instance, with the methods described in Chapter 5. The input inductor L_{choke}, as in the Class E, has a large value and is effectively an open circuit at radio frequencies. The capacitor C_{block} is likewise a large value, chosen to approximate an RF short. The switching fundamental sees a pure resistance $R_{\text{L}} = Z_0$ because the output tank (tuned to f_{sw}) is an open circuit and the line is terminated in its characteristic impedance. Away from f_{sw} the tank is capacitance-dominated, and terminates the line in a short (relative to other impedances seen at the load) for high tank Q. The situation of a shorted line now obtains (*cf.* Fig. 2.2), namely, the even v_{ds} harmonics see an even number of $\lambda/4$-wave transformations of the short termination and are collapsed, while odd multiples of f_{sw} see an open circuit. The drain waveform is therefore half-wave symmetric about its dc value (V_{in}) by the $\lambda/4$-wave action of the line, and reaches a peak value of $2V_{\text{in}}$ as shown

IPR2024-00706 EX. 2005

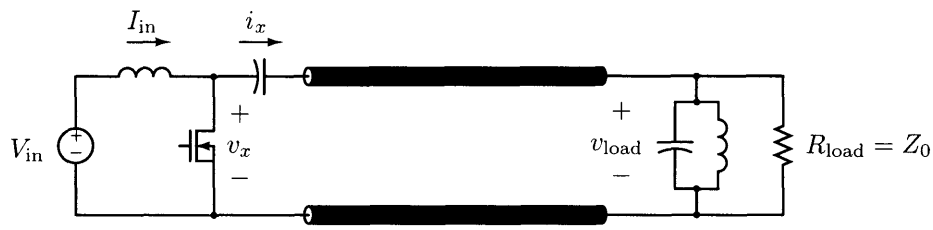

Figure 4.7: **Schematic for computation of stresses in the Class F converter**

in Fig. 4.6.[6]

Expressed in other terms with reference to Fig. 4.7, because v_x is at ground potential when the switch is on and has only odd-harmonic content, it is a square wave with a fundamental component equal to the inverter output:

$$v_{\text{load}} = v_{x,1} = \frac{4}{\pi} V_{\text{in}}$$

i_x can only deliver power to the load at the fundamental frequency because it has even harmonic content at higher frequencies. The load current and power are therefore determined:

$$i_{x,1} = \frac{4}{\pi} \cdot \frac{V_{\text{in}}}{R_{\text{load}}} \qquad P_{\text{out}} = \frac{8}{\pi^2} \cdot \frac{V_{\text{in}}^2}{R_{\text{load}}}$$

By conservation of energy,

$$I_{\text{in}} = \frac{P_{\text{in}}}{V_{\text{in}}} = \frac{P_{\text{out}}}{V_{\text{in}}} = \frac{8}{\pi^2} \cdot \frac{V_{\text{in}}}{R_{\text{load}}}$$

Referring to Fig. 4.8, i_x has no dc content and, except at the fundamental, no odd-harmonic components. Decomposing i_x into a sum of its fundamental and even harmonics as shown, the odd and even parts must exactly match the dc input current I_{in} when the switch is off. i_x is constrained to the form shown, with a lowest value

$$i_x = I_{\text{in}} - \frac{8}{\pi} \cdot \frac{V_{\text{in}}}{R_{\text{load}}}$$

[6]this assumption of quick drain transitions is standard when comparing power-amplifier stages [30, Section 13.6]. It is suitable for gross comparison, but simulation is required to check stresses and waveforms for the high switching frequencies we're considering, in which duty ratios are typically in the vicinity of 0.35. The risetime of v_{ds} will be given more detailed consideration in the next section.

IPR2024-00706 EX. 2005

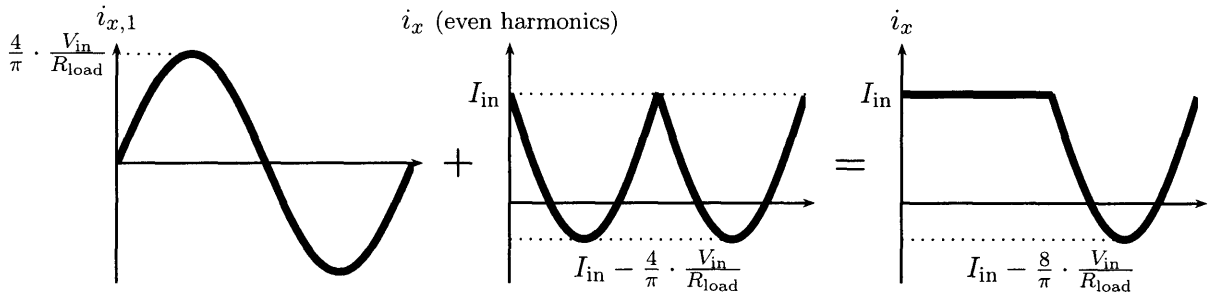

Figure 4.8: **Switch stress in the Class F inverter.**

Since the drain current $i_{\text{d}} = I_{\text{in}} - i_x$, the drain current has the peak value

$$\frac{8}{\pi} \cdot \frac{V_{\text{in}}}{R_{\text{load}}}$$

We therefore compute for the Class F a normalized power output capability of

$$P_{\text{N}} = \frac{\left(\frac{4}{\pi} V_{\text{in}}\right)^2 \cdot \frac{1}{2R_{\text{load}}}}{2V_{\text{in}} \cdot \left(\frac{8}{\pi} \cdot \frac{V_{\text{in}}}{R_{\text{load}}}\right)} = \frac{1}{2\pi} \approx 0.16$$

which is 68% higher than the Class E. Practical implementations can moreover, achieve efficiencies superior to Class E [30, Section 13.6], in part because the Class F has zero current at turn off.[7] Foster-type implementations of the Class F (Fig. 4.5b) perform nearly as well as their transmission-line exemplars, and frequently do not exhibit increased efficiencies for more than two resonator, as depicted in the schematic [loc. cit.].

4.1.3 Class Φ converter

We have chosen to term "Class Φ" the topology which results by replacing the input inductor in the Class E inverter (i.e., L_{choke} Figs. 4.3 and 4.5) with a $\lambda/4$ transmission line or one of its simulating networks.[8] As developed in Section 2.2 and reiterated on a frequency basis in Section 4.1.2, if a circuit periodically imposes a voltage waveform on a $\lambda/4$-wave delay

[7]The approximation of zero-current at turn-off holds inasmuch as the net device output capacitance is small.

[8]The name Class Φ was chosen because of it similarity to "Class F" while avoiding confusions with its variants (Class F inverse, Class EF, ...). The converters have fundamentally similar drain waveforms.

IPR2024-00706 EX. 2005

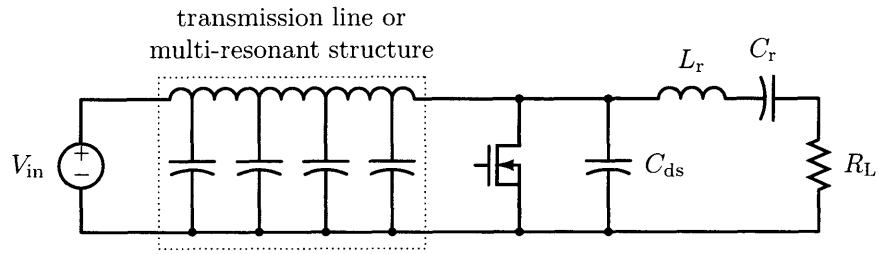

Figure 4.9: **Schematic of the Class Φ converter**

during one half of the switching cycle, the network (in periodic steady state) will become energized so as to impose half-wave symmetry in voltage during the other half-period.[9] The line current, conversely, will be half-wave repeating for the same line termination.

Consider the steady-state operation of the Class Φ for a switch duty cycle less than 50%, depicted in Fig. 4.10. The switch imposes a constant voltage (V_{in}) across the multi-resonant inductor during the first portion of the switching cycle (when the switch is on). At turn-off, the differential current between the line and the load flows into the C_{ds}, as depicted by the shaded region over the interval δ in the bottom and middle plots of Fig. 4.10. The half-wave symmetries enforced by the line ensure that the drain voltage is symmetric about the V_{in}; V_{in} was applied across the line when the switch was on and there is now a $-V_{in}$ drop along its length. v_{ds} therefore assumes a value of $2V_{in}$ for a time equal to the switch on time, until the line modes ring the drain back down to zero. At this point, the switch may be turned on with zero-voltage switching and zero drain current, and the cycle repeats.

The reflection diagram of Figure. 4.1.3 explains drain-voltage symmetries by the *delay* property of a transmission line or transmission-line analog. The time axis, showing the drain voltage during one switching period, is at the front of the figure. Capacitor voltages – in this case along a network model of the distributed line — extend from the front of the plot back along the length axis, so that cross-sections parallel to the time axis show the time evolution of voltage at specific points along the line. The $2V_{in}$ step in drain voltage launches a travelling wave down the line, which is reflected by the ac short at V_{in} and returns to the drain in time for a ZVS opportunity. The plot highlights the subsidiary turn-on waves, which can reflect and return to complicate the v_{ds} rise at turn-off. The line-simulating network was synthesized by the Cauer method (Section 3.4) to have 24 critical frequencies

[9]This property is analogous to the manner in which an inductor becomes energized such that it imposes zero average voltage across its terminals during periodic-steady-state operation.

IPR2024-00706 EX. 2005

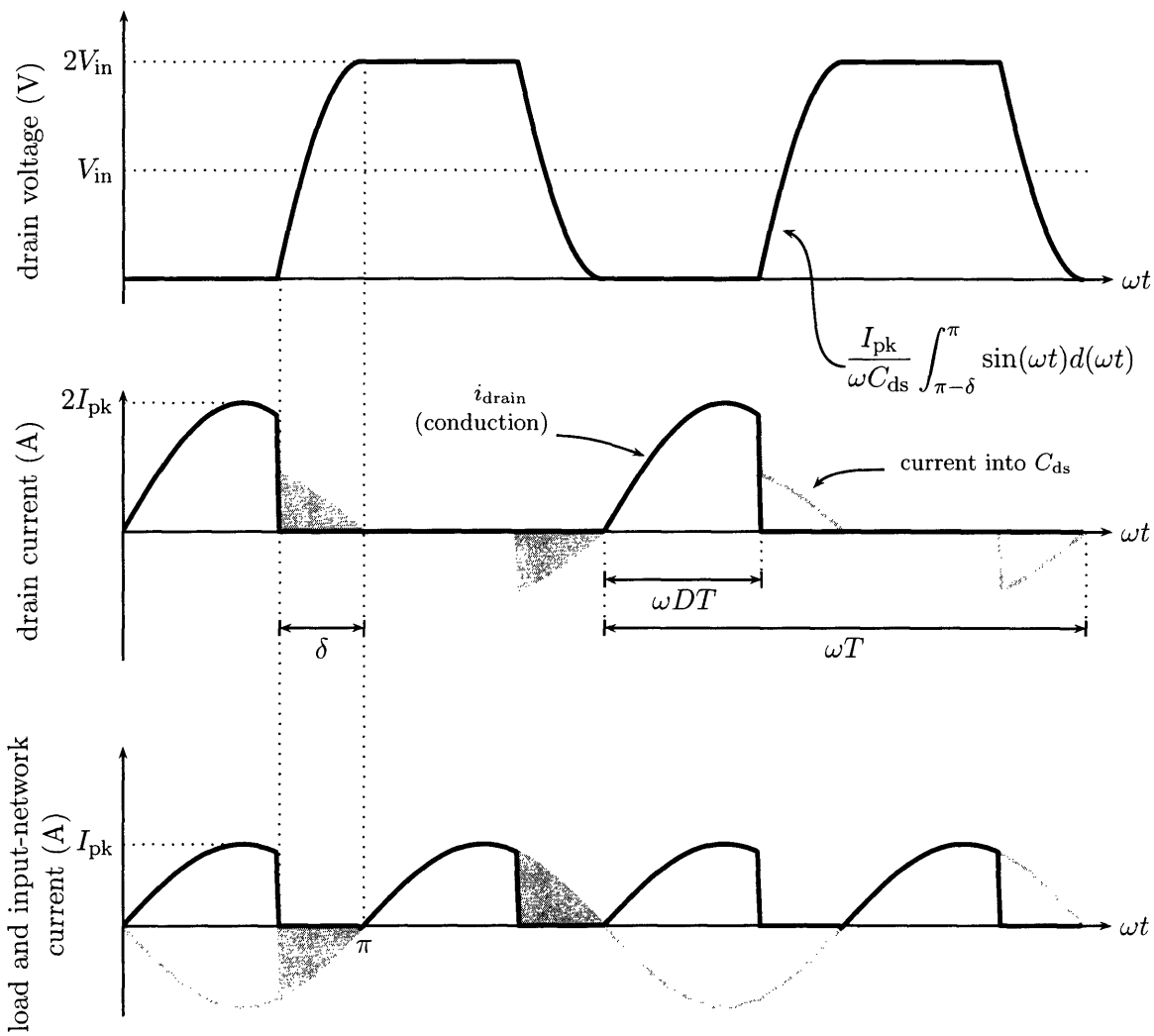

Figure 4.10: **Idealized waveforms of the Class Φ inverter**

IPR2024-00706 EX. 2005

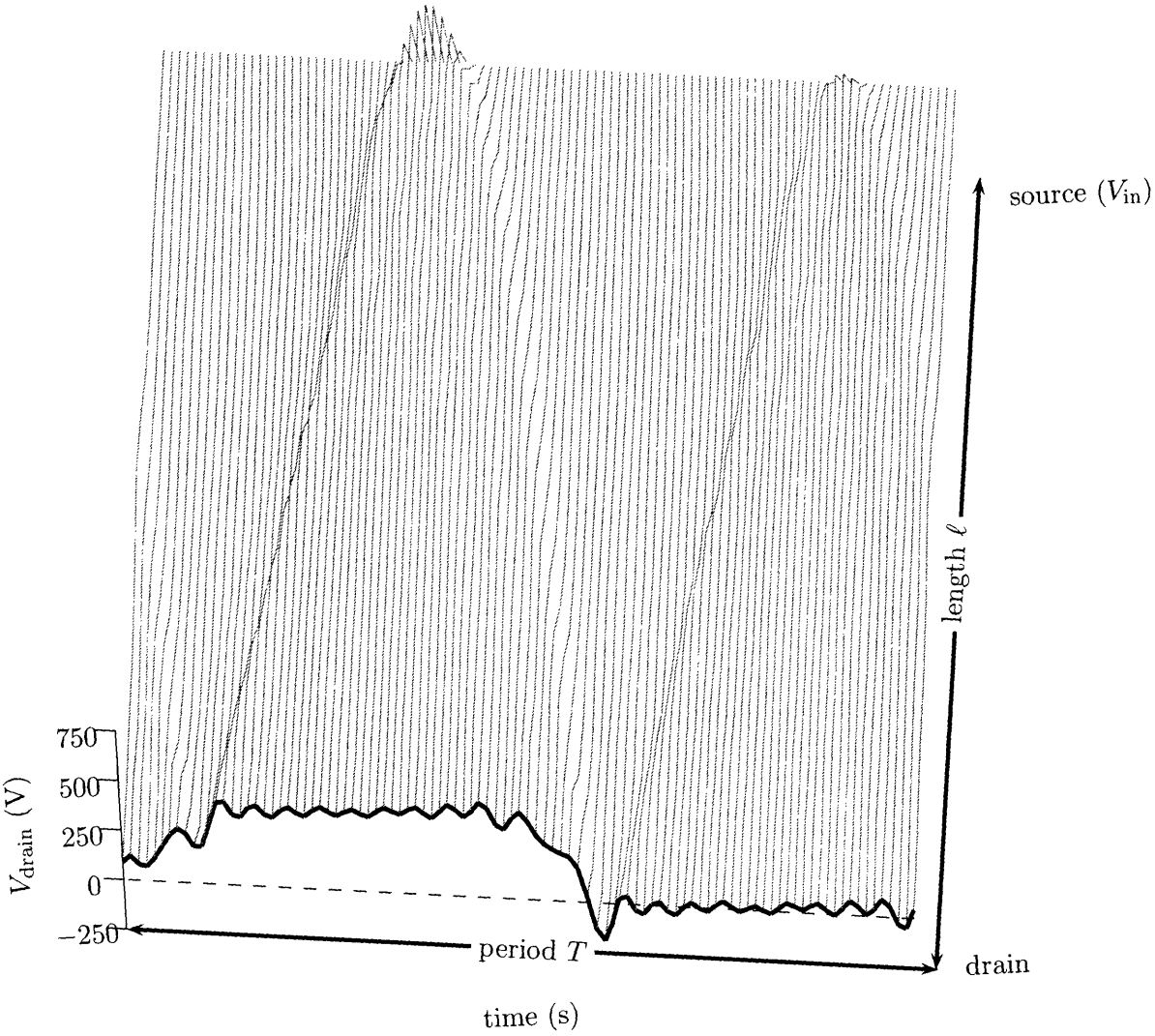

Figure 4.11: **Reflection diagram showing the propagation of drain-voltage edges along the transmission line. The returning turn-off edge creates a zero-voltage switching opportunity for turn-on.**

IPR2024-00706 EX. 2005

coincident with the full transmission line, and comprised 13 inductors tapped at internal node by 12 capacitors (these are the section values given in Fig. 3.14). The inverter used in this simulation is the high-power example which will be presented in Section 4.3.2.

If we *assume* a square-wave drain waveform like that shown in Figs. 4.10 and 4.1.3, details of the current waveform become clear upon consideration its half-wave repetition. In the switch on state, and with v_{ds} settled, the line current must equal the load current, and will repeat this sinusoidal behavior during switch-on time. Because the differential current between load and line must drive half-wave symmetric edges in v_{ds}, this drain displacement current must be half-wave symmetric (*cf.* the shaded areas of Figs. 4.10). The alternating sign in i_{d} can *only* come from i_{load}, because it is half-wave symmetric; the line current, with its half-wave repeating content, must necessarily fall to zero during drain-voltage edges. This condition places some practical upper limits on the characteristic impedance of the line, which should be compliant enough to allow the switch to divert the entire load current quickly. To ensure turn-on with zero drain current, note that the load network must appear slightly inductive to the drain so that the load current lags the applied effort by δ radians, corresponding to the rise and fall times in v_{ds}.

4.1.3.1 Stresses in the Class Φ

For heavy-load conditions, for which the drain-transition interval δ becomes smaller with respect to a switching period, the normalized power output capability of the Class Φ is simple to derive, and follows the development of Section 4.1.2. The output power P and peak values of v_{ds} and switch current are identical to the Class F, since the peak load current is

$$i_{\mathrm{load,pk}} = \frac{4}{\pi} \cdot \frac{V_{\mathrm{in}}}{R_{\mathrm{load}}}$$

The input line reflects load-current pulses such that a sinusoidal current from the line converges with the load current at the drain, doubling the switch conduction with respect to either incident current. We compute for the Class Φ, therefore, a normalized power output capability of

$$P_{\mathrm{N}} = \frac{\left(\frac{4}{\pi} V_{\mathrm{in}}\right)^2 \cdot \frac{1}{2R_{\mathrm{load}}}}{2V_{\mathrm{in}} \cdot \left(\frac{8}{\pi} \cdot \frac{V_{\mathrm{in}}}{R_{\mathrm{load}}}\right)} = \frac{1}{2\pi} \approx 0.16$$

IPR2024-00706 EX. 2005

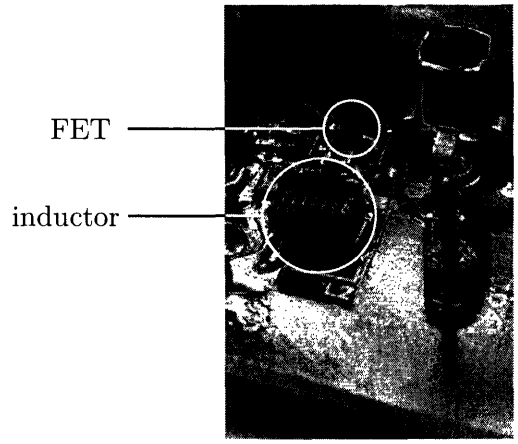

Figure 4.12: **An 8 W Class E dc-dc converter (3.3 to 7 V) highlighting a disproportionately small switch package, compared to neighboring reactive elements.**

68% less demanding on the switch than the Class E, exactly like the Class F (see Section 4.1.2).

The switch stress of all of these amplifier topologies is not as significant as one might suspect, from a point of view of miniaturization. As pointed out in Chapter 1, the excellent performance of modern switches has shifted many frequency- and size-scaling limits to *passive components*. Consider the Class E inverter/rectifier of Fig. 4.12 [42]. The switch is dwarfed by the neighboring inductors, especially the dc input choke, highlighting the advantage of techniques which exchange the switch stress of this Class E inverter — with its disproportionately small switch package — for reduced passive volume. The Class Φ is precisely suited to such a miniaturization trade-off (over against the Class E) because of its ability to operate at higher power without additional components, and because of the the smaller size and superior manufacturability of its multi-resonant replacement for a bulk input inductor. Considered against the Class F, the Class Φ eliminates reactive elements entirely (*viz.*, blocking elements like C_{block} and L_{choke}, and both output-tank elements).

4.2 Analysis and design of the Class Φ inverter

The quasi-static analyses in Chapter 3 yielded fully populated inductance matrices describing the magnetic coupling between turns and groups of turns around the periphery

IPR2024-00706 EX. 2005

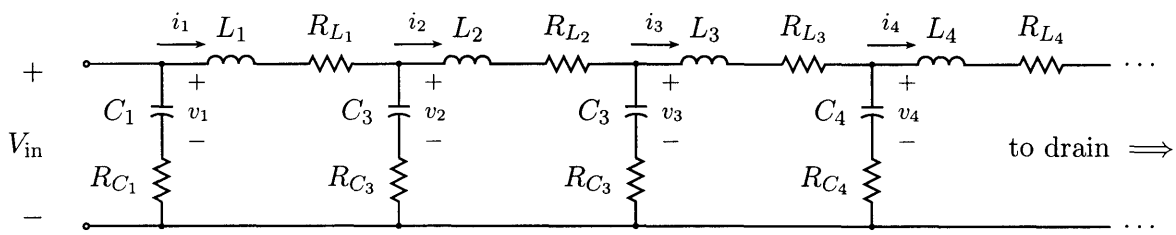

Figure 4.13: **States of LC ladder network**

of planar toroids. While the off-diagonal entries fell off rapidly for the modelled air-core structures, the measurements of Sections 3.2.3 and 3.3.2 highlighted the fact that small mutual inductance entries could affect harmonic coincidence of poles and zeros. Shifts of a few percent in critical frequencies are significant, especially as zero misalignment spoils the symmetry conditions for ZVS.[10] The switched-mode method described below can simulate the Class Φ converter with inclusion of these mutual effects, directly incorporating the results of FastHenry simulations.

4.2.1 Switched-mode state-space analysis of the Class Φ inverter

First consider the states of the multi-resonant component itself, with reference to Fig. 4.13. Note that because we will drive the structure with a switch on its right terminal (*cf.* Fig. 4.9, the line-section L and C are now numbered with increasing indices as we move across the schematic from left to right, *from* the termination and *toward* the load. In a practical implementation, V_{in} is bypassed to act as the RF *termination* for the lumped line, which has been flipped end to end compared to the development in Chapter 3.[11]

The state equations for the ladder network are:

[10]Moreover, phase changes rapidly (away from 0° and coincident alignment) for conjugate poles close to the $j\omega$-axis. These phase shifts are readily detectable in converter drain waveforms, for instance, as the gate-drive frequency is tuned past the modes of a high-order network. Square-wave topping changes in a complicated manner, and can overshoot its expected half-wave-symmetric rise.

[11]The largest Cauer-synthesis section of Fig. 3.16, for instance, is adjacent to the dc source.

IPR2024-00706 EX. 2005

$$\frac{dv_1}{dt} = \frac{1}{C_1}(-i_1) \qquad \frac{di_1}{dt} = \frac{1}{L_1}\left[\, v_1 - i_1 R_{C_1} - v_2 - (i_1 - i_2)R_{C_3} - i_1 R_{L_1}\right]$$

$$\frac{dv_2}{dt} = \frac{1}{C_2}(i_1 - 1_2) \qquad \frac{di_1}{dt} = \frac{1}{L_1}\left[\, v_1 - i_1 R_{C_1} - v_2 - (i_1 - i_2)R_{C_3} - i_1 R_{L_1}\right] \qquad x_{\text{in}} = \begin{bmatrix} i_1 \\ i_2 \\ i_3 \\ \vdots \\ v_1 \\ v_2 \\ v_3 \\ \vdots \end{bmatrix}$$

$$\frac{v_3}{dt} = \frac{1}{C_3}(i_2 - i_3) \qquad \frac{di_1}{dt} = \frac{1}{L_1}\left[\, v_1 - i_1 R_{C_1} - v_2 - (i_1 - i_2)R_{C_3} - i_1 R_{L_1}\right]$$

Where x_{in} is the state vector with an an equal number of voltages and currents. C_1 is chosen to be very large, and can be given an initial condition to simulate both the dc source and the ac short termination. The state equations can be summarized in a matrix A_{in} and generalized to the case of a fully populated L as shown below.

$$\mathcal{A}_{\text{in}} = \begin{bmatrix} 0 & \mathcal{C}^{-1}\begin{bmatrix} -1 & 0 & 0 & 0 & \\ 1 & -1 & 0 & 0 & \cdots \\ 0 & 1 & -1 & 0 & \\ 0 & 0 & 1 & -1 & \\ & \vdots & & & \ddots \end{bmatrix} \\ \mathcal{L}^{-1}\begin{bmatrix} 1 & -1 & 0 & 0 & \\ 0 & 1 & -1 & 0 & \cdots \\ 0 & 0 & 1 & -1 & \\ 0 & 0 & 0 & 1 & \\ & \vdots & & & \ddots \end{bmatrix} & \mathcal{L}^{-1}\mathcal{R} \end{bmatrix}$$

IPR2024-00706 EX. 2005

$$\mathcal{R} = \begin{bmatrix} -R_{C_1} - R_{C_2} - R_{L_1} & R_{C_2} & 0 & 0 & \\ R_{C_2} & -R_{C_2} - R_{C_3} - R_{L_2} & R_{C_3} & 0 & \cdots \\ 0 & R_{C_3} & -R_{C_3} - R_{C_4} - R_{L_3} & R_{C_4} & \\ 0 & 0 & R_{C_4} & -R_{C_4} - R_{C_5} - R_{L_4} & \\ & \vdots & & & \ddots \end{bmatrix}$$

$$\mathcal{C}^{-1} = \begin{bmatrix} 1/C_1 & 0 & 0 & \\ 0 & 1/C_2 & 0 & \cdots \\ 0 & 0 & 1/C_3 & \\ & \vdots & & \ddots \end{bmatrix}$$

This method includes only the conduction losses specified in R. R can be constructed from the calculated or measured Q of the self-inductances along a toroid, and the Q of capacitor taps along its periphery. To model the incorporation of his network into an inverter, the on-state resistance of a FET can be subtracted from the lower-left entry of R.

Referring to Fig. 4.9, the output tank (comprising L_r and C_r) has two states, the tank-capacitor voltage and tank-inductor current. It is modelled by the 2×2 state-transition matrix A_out:

$$A_\mathrm{out} = \begin{bmatrix} 0 & -\frac{1}{C_\mathrm{r}} \\ \frac{1}{L_\mathrm{r}} & -\left(\frac{R_\mathrm{L}}{L_\mathrm{r}} + \frac{r_\mathrm{ds,on}}{L_\mathrm{r}}\right) \end{bmatrix} \quad \text{where} \quad \frac{d}{dt}\begin{bmatrix} i_{C_\mathrm{r}} \\ v_{L_\mathrm{r}} \end{bmatrix} = A_\mathrm{out}\begin{bmatrix} i_{C_\mathrm{r}} \\ v_{L_\mathrm{r}} \end{bmatrix} = A_\mathrm{out} x_\mathrm{out}$$

The multi-resonant input network and second-order output network are coupled through the drain node and device capacitance when the switch is off. The dynamics of this coupled system are described by a new state vector x and a new matrix A, expressed and terms of

IPR2024-00706 EX. 2005

A_{in} and A_{out}, with cross-coupling entries between the appropriate current states:

$$A = \left[\begin{array}{c:c:c} A_{\text{out}} & \begin{matrix} 0 \\ \frac{1}{L_{\text{r}}} \end{matrix} & 0 \\ \hdashline 0 \quad -\frac{1}{C_{\text{ds}}} & 0 & 0 \quad \cdots \quad \frac{1}{C_{\text{ds}}} \\ \hdashline 0 & \begin{matrix} 0 \\ \vdots \\ 0 \end{matrix} & A_{\text{in}} \end{array}\right] \quad \text{and} \quad x = \left[\begin{array}{c} x_{\text{out}} \\ \hdashline v_{C_{\text{ds}}} \\ \hdashline x_{\text{in}} \end{array}\right]$$

Switched-mode simulation proceeds by alternately simulating the undriven dynamics of A (switch off), then the undriven dynamics of A_{in} and A_{out} (switch on). New state vectors are assembled at the switching interfaces, with the most recent states transferred to the next step in the cycle as initial conditions (but with the voltage on C_{ds} nulled, notably, at turn on, and the voltage across C_1 replenished). The coupling of A_{in} and A_{out} through the on-state resistance of the FET was ignored, and drain inductance can be considered by introducing a negative mutual term coupling the inductors which communicate with the drain node (see Section 4.2.2). Class Φ waveforms simulated by this method are shown in Fig. 4.14 (see caption for details of the simulation).

Code implementing this scheme, with further elaborations to account for gating and DC loss, is presented in Appendix A.4.[12] This code was used as a design tool for selecting the characteristic impedance of the lumped line relative to the load, and exploring effect of various misalignments in the input-network impedance on Class Φ efficiency. Diagonal, Cauer-synthesized L matrices can easily be constructed with a misaligned first null, for instance, to account for observed distortions in Class Φ waveforms.

4.2.2 Improvements to the basic Class Φ design

Two techniques for enhancing the basic Class Φ design by altering its effective switch reactances are shown in Fig. 4.15. Fig. 4.15a shows a means of compensating for the package inductance of the FET. Recall from the previous section that this parasitic can

[12]Note, incidentally, that the same code can be used to simulate a Class E inverter with the choice of a second-order A_{in} (the choke state plus the capacitor C_1 mimicking the DC input over a cycle). The simulation of Fig. 4.1.1 was performed by this means precisely.

IPR2024-00706 EX. 2005

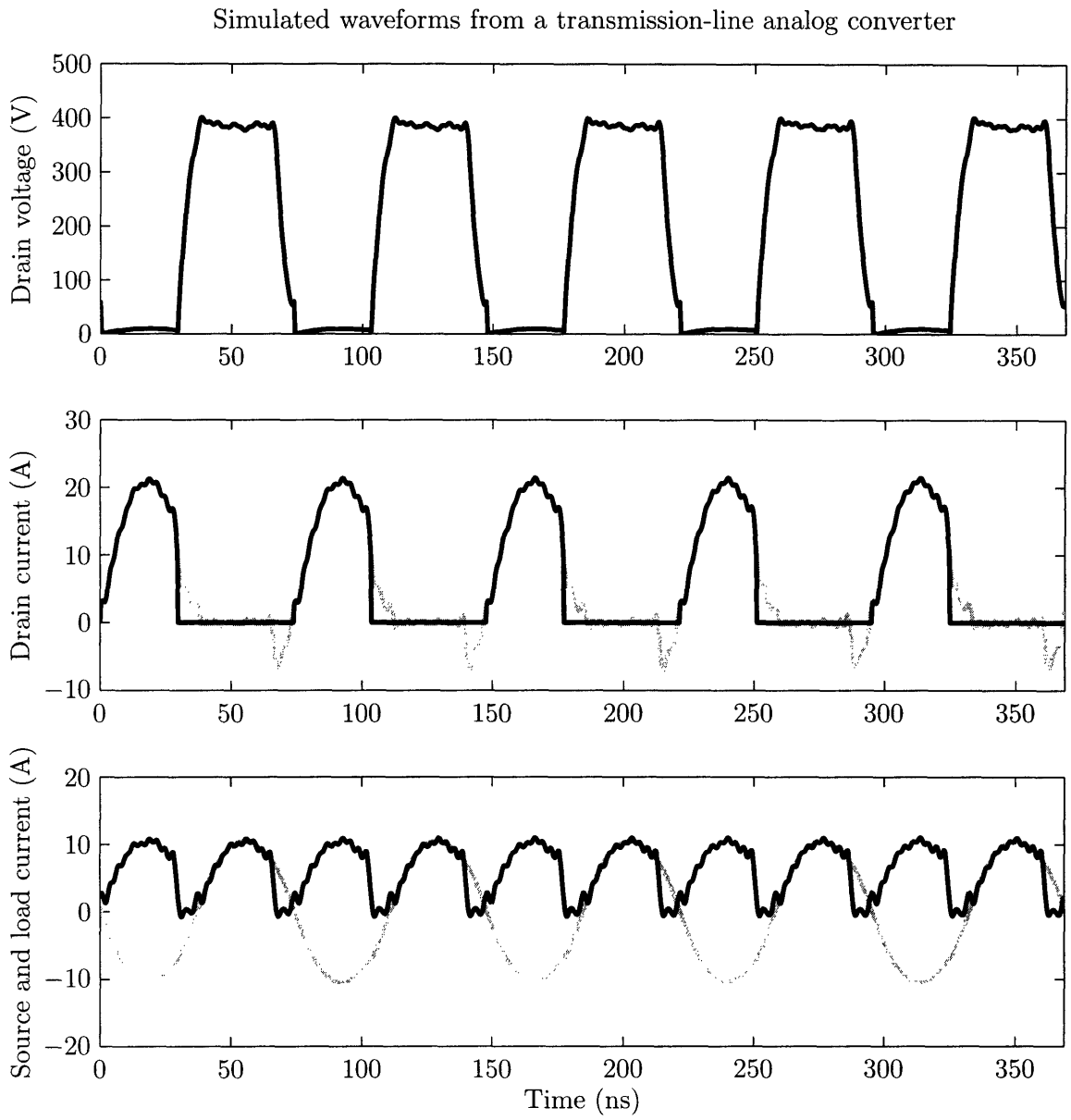

Figure 4.14: **Waveforms of the Class Φ inverter of Fig. 4.9 simulated with the state-space method described in Section 4.2.1.** $f_{sw} = 13.56$ **MHz,** $D = 0.4$, $V_{in} =$ 200 **V, IXFT21N50F switch** ($C_{ds,on} = 90.3$ **pF at** V_{in}, $r_{ds} = 0.45\ \Omega$), $C_r =$ 318 **pF,** $L_r = 533$ **nH,** $R_{load} = 20\ \Omega$. **The input network had a Cauer-synthesized values with 24 harmonic-coincident critical frequencies (13 inductors and 12 capacitors at internal tap nodes with the normalized values of shown in Fig. 3.14). The first section inductance was 40 nH first-section inductance (next to the drain node) and a high inductor** Q **of 300 was used to yield waveforms similar to those in Fig. 4.10.**

IPR2024-00706 EX. 2005

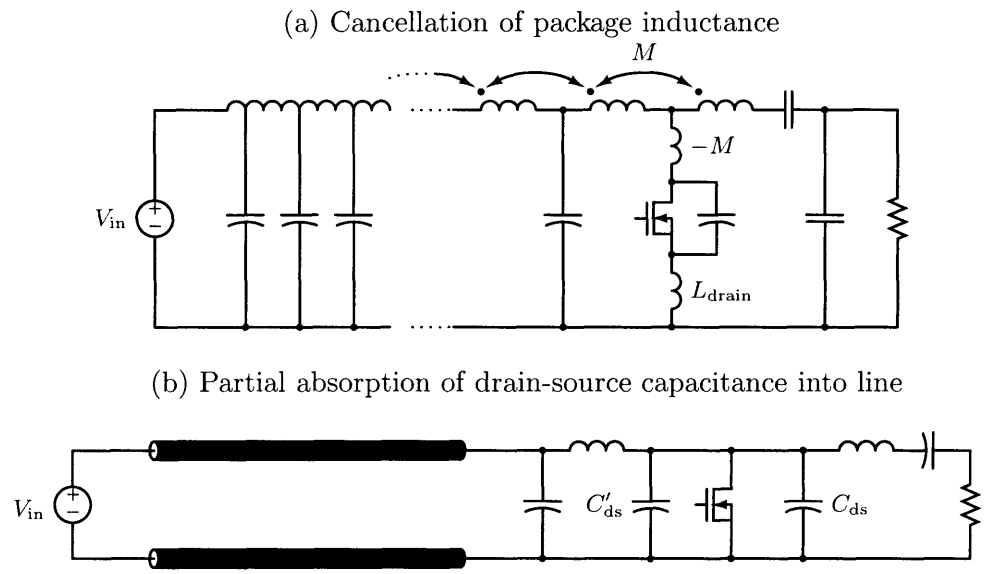

Figure 4.15: **Two methods of compensating for switch reactances in the Class Φ inverter**

be modelled as a negative mutual entry between the inductors communicating with the drain node (L_r and the first section-inductance of the artificial line) because it appears as a mutual induction between the corresponding meshes. Added coupling (M) in the sense shown in Fig. 4.15a offsets this parasitic package inductance by $-M$, as explained in Section 3.2.2. Note that this technique is an extension of our ability to make a compact *lumped* transmission line as in Chapter 3, and cannot be implemented with a transmission line alone.

The second technique, shown in Fig. 4.15b, is sometimes implemented with distributed lines in the Class F amplifiers which employ [40]. Recall from the cup-and-bucket analogy of Fig. 4.3 that power delivery and frequency necessarily scale in the Class E architecture, with no apparent means of reducing C_{ds} and delivered power. Even if a switch is capable of operating at tens or hundreds of megahertz, a design may be limited by the power-handling ability of its switch and reactive elements.[13] The Class Φ can offset this frequency/power scaling by absorbing part of the switch drain-source capacitance (C'_{ds}) into the line, either by shortening its electrical length for constant f_{sw}, or shifting to a lower f_{sw}. Further passive

[13]This limitation will become clear for a practical design in Section 4.3.2.1. The achievable efficiency of a Class E converter ultimately declines with frequency for this reason.

IPR2024-00706 EX. 2005

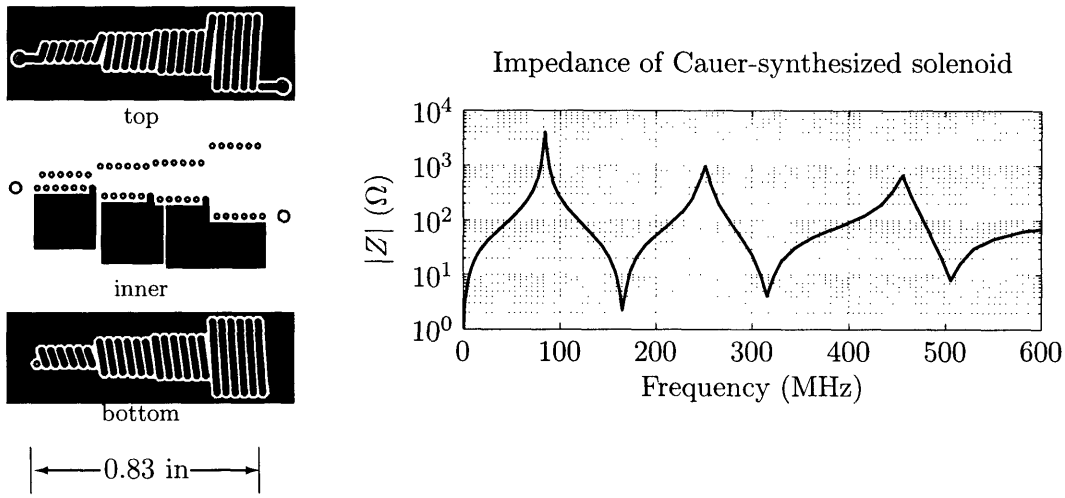

Figure 4.16: **The multi-resonant structure used in the low-power Class Φ inverter of Fig. 4.17. The structure shown was constructed within the layup presented in Fig. 5.2.**

miniaturization and higher inductor Q can be expected by a move to faster switching.

4.3 Measurements of the Class Φ inverter

Low-power and high-power prototypes of the Class Φ converter were constructed, incorporating both PCB-scale structures and transmission lines.

4.3.1 Low-power example

A drop-in, multi-resonant replacement of for the input choke of a Class E cell (Fig. 4.16) was constructed to demonstrate Class Φ operation at power levels of several watts. The inverter depicted in Fig. 4.17 was used in a cellular architecture in conjunction with matching and rectifier stages as depicted in Fig. 4 [36]. The 569 nH input choke of the original inverter was replaced by a 238 nH solenoid (62 mΩ DC resistance) built into the thickness of a 4-layer PCB. Cross-sections of the tapped inductor are shown in Fig. 4.16, with three internal taps loading the structure along its length with capacitances to outer-layer ground floods. The L and C section values — 4 inductances and 3 capacitances — were computed by Cauer synthesis (see Section 3.4). The inductor geometries were then designed by a

IPR2024-00706 EX. 2005

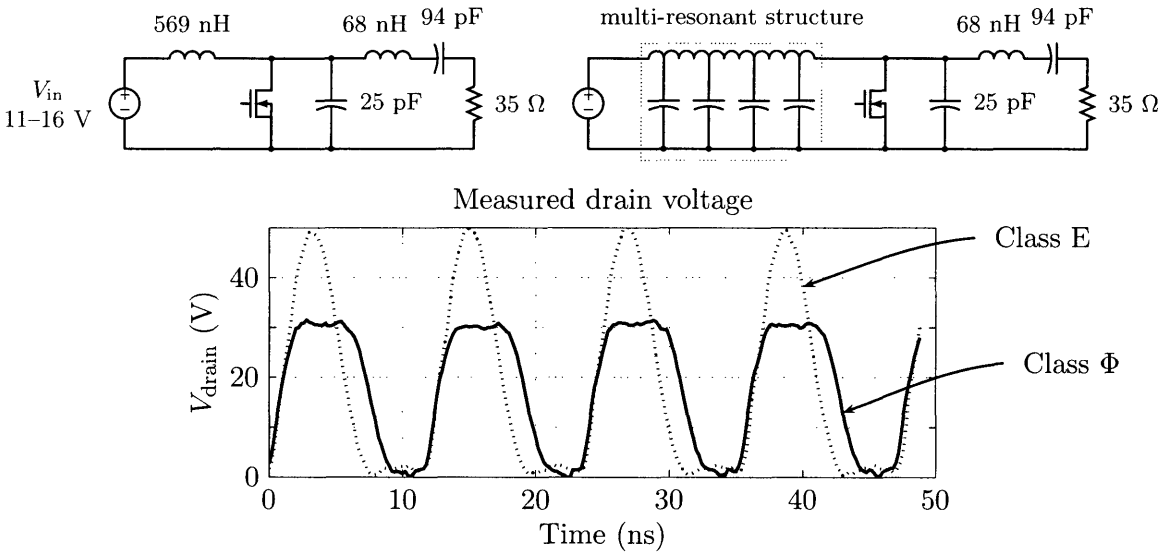

Figure 4.17: **Comparison of drain-voltage waveforms for a 82 MHz class-E inverter (a) and an inverter in which input inductor L_{in} has been replaced by the multi-resonant PCB structure of Fig. 4.16. An STMicroelectronics PD57018 65 V FET was used in both converters, though the lower drain voltage in the multi-resonant case is compatible with a lower-voltage switch.**

rectangular current-sheet approximation for the inductance of a rectangular cross-section solenoid, reported by Grover ([5, Chapter 10]) in cgs units. With fixed pitch, board thickness, and 6 turns per section, the inductances were approximated by varying their width. Mutual inductances were neglected in the design, and the resulting harmonic incidence was mediocre, as seen from the impedance (Fig. 4.16) measured from the narrower (drain) end of the solenoid.

Even with the poor assumptions mentioned above, peak transistor voltage in this Class Φ was significantly reduced compared to the Class E converter (*cf.* Fig. 4.17) measured for V_{in}=16 V). Both inverters maintained soft-switching at 82 Mhz: the broader, approximately square-wave drain voltage (31 V peak) of the multi-resonant inverter delivered 1.49 A p-p into the 13.5 Ω load through the $Q = 10$ output filter; the class-E design, for 50 V peak drain voltage, delivered 1.98 A p-p into the same load. The lower switch stress in the multi-resonant case would allow the 65 V PD57018 FET of the class-E inverter to be replaced with a 40 V member of the same family, the PD55025, with an $r_{ds,on}$ 2.7 times smaller than the higher-voltage FET. The efficiency of both inverters was between 80 and 84%, without considering gate-drive losses. Notably for miniaturization, the multi-resonant structure in this example was 42% of the Class E bulk value, though inductance reduction of 5 to 6

IPR2024-00706 EX. 2005

times is possible with better alignment of impedance peaks and nulls, as we will see in the next section.

4.3.2 High-power example

To begin investigating design issues for higher power levels, a board-level implementation of the Class Φ inverter for hundreds of watts was designed, tested, and compared to the Class E.

4.3.2.1 Frequency and Switch Selection

Metal-gate vertical MOSFET devices from IXYS and Advanced Power Technology were compared in simulations of the Class E and Class Φ to select a combination of device, power level, and switching frequency for the proposed inverter comparison. Metal gate device were chosen because of their high-frequency gate pole $(R_g C_g)^{-1}$ and consequent low gating losses. Parameters of the candidate devices are summarized in Table 4.1. The values of C_{ds0}, ψ, and n were obtained from drain-source impedance measurements with gate and source shorted, under three bias conditions. The parameters were fit by minimizing the deviation of the non-linear capacitance expression

$$C_{ds} = \frac{C_{ds0}}{\left(1 + \frac{V_{ds}}{\psi}\right)^n} \tag{4.1}$$

to the measured capacitances. This capacitance was linearized for simulation by replacing it with Eqn. 4.1 evaluated at $V_{ds} = V_{in}$.

Plots of anticipated power output and efficiency for various switching frequencies, considering each device from Table 4.1 in turn, are shown in Fig. 4.18. The design equations presented in Section 4.1.1.2 were used to obtain the trends shown, and simulation confirmed the results at several points along the curves.[14] From the plots, the IXFT21N50F

[14]The simulations included more detailed switch and reactive-component losses and predicted lower efficiency (typically 2%) and lower power ($\approx$ 10%), but still exhibited the same relationships between devices presented in Fig. 4.18.

IPR2024-00706 EX. 2005

(a) Power vs. switching frequency for the Class E

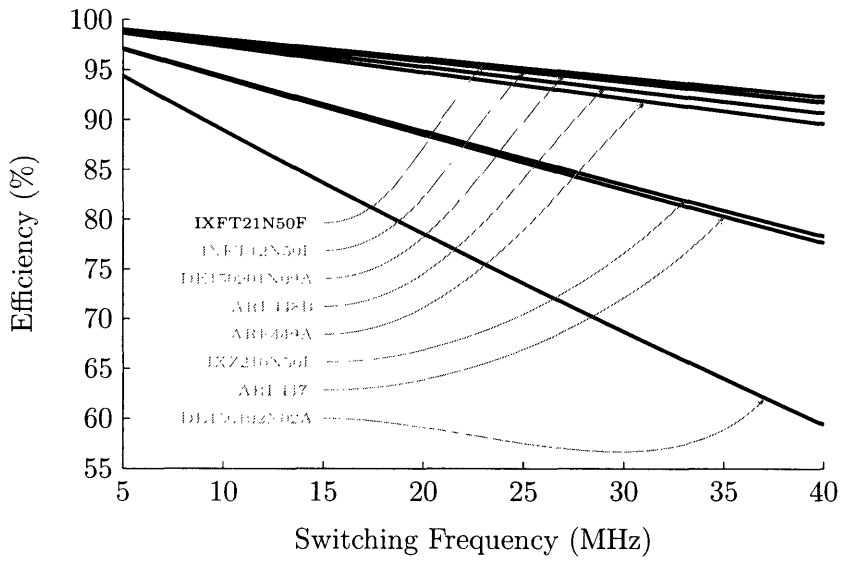

(b) Efficiency vs. switching frequency for the Class E

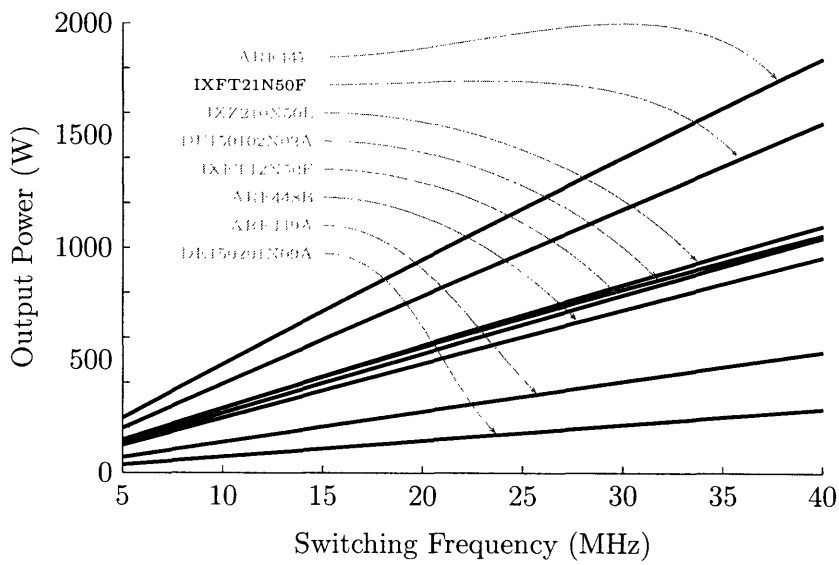

Figure 4.18: **Power and efficiency curves used for switch and switching-frequency selection in the high-power inverter example of Section 4.3.2. A dc input voltage 80% of the rated breakdown voltage of each device was used, consistent with the requirements of the Class E converter and adding a 20% safety margin.**

IPR2024-00706 EX. 2005

Device	V_{dss}	I_{d}	C_{g}	R_{g}	C_{ds0}	ψ	n	$r_{\mathrm{ds,on}}$
	V	A	pF	mΩ	pF	V		Ω
IXZ210N50L	500	10	857	1180	1970	0.184	0.421	1.00
DE150201N09A	200	15	1128	1064	2119	1.263	0.650	0.20
DE150102N02A	1000	2	673	1681	1314	1.775	0.756	3.20
IXFT21N50F	500	21	3190	56	4040	1.499	0.718	0.25
IXFT12N50F	500	12	2069	72	2335	1.075	0.635	0.40
ARF449A	450	9	1332	71	2381	0.129	0.514	0.80
ARF448B	450	15	2005	73	4683	0.151	0.542	0.40
ARF447	900	6	1975	80	4412	0.049	0.500	2.00

Table 4.1: **Measured and nominal parameters of the candidate MOSFETs for the high-power inverter example of Section 4.3.2. V_{ds} and I_{d} are nominal ratings. $r_{\mathrm{ds,on}}$ has greater relative uncertainty than many other parameters, and was increased by 1.8 times for simulations.**

(produced by IXYS) was chosen because it had the highest efficiency at manageable power, and was the least expensive switch. A switching frequency in the ISM band at 13.56 MHz was selected because the manageable heat dissipation and passive ratings anticipated for designs at this frequency.

4.3.2.2 Class E inverter

As a basis for evaluating the Class Φ inverter, a Class E converter was designed around the IXFT21N50F. A schematic — including parasitics — is shown in Fig. 4.19. The output-inductor value is the combination of the Class E resonant inductance and the L-match inductance required to match a 13 Ω source impedance into the 50 Ω coaxial load. The 13 Ω source impedance is the tank load required for Class E operation, and was computed for the desired tank Q, C_{ds}, and switching frequency as outlined in Section 4.1.1.2. Eight turns (2.3 cm winding length) of unserved 175/40 litz were wound on a plastic former with a 26 mm diameter for the tank/match inductor. This geometry was chosen to maximize Q (84 at 13.56 MHz) and limit the current density to under 500 A/cm^2. The input choke was also constructed as an air core solenoid, 21 turns of 18 gauge wire on the same plastic former used in the output tank. The gate capacitance was resonated with a lead-trimmed

IPR2024-00706 EX. 2005

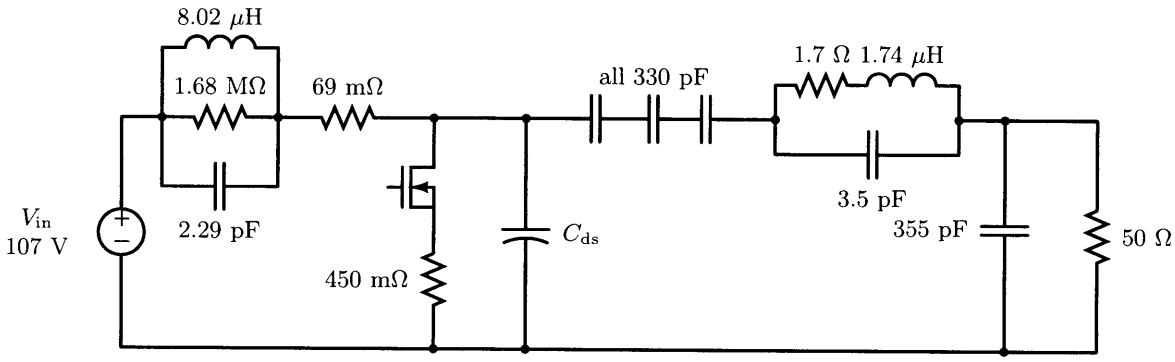

Figure 4.19: **Schematic (with parastics) of the Class E converter of Section 4.3.2.2.**

27 nH inductor, an air-core inductor of the Coilcraft Midi Spring family. This resonator had a peak impedance of 27 Ω at 13.56 MHz and nearly resistive phase as seen from the 50 Ω ac drive. Silver-mica chip capacitors were used in the output network, placed in series for higher standoff where necessary.

The 1 kW source (an HP 6015A DC power supply, 0-500 V/0-5 A) was set to 107 V and bypassed at the board with one 10000 pF and one 6800 pF silver-mica capacitor. The gate was driven by a 150 W Amplifier Research Class A power amplifier (Model 150A 100B, 10 kHz–100 MHz), with its gain set high enough that the switch transition could be controlled in the presence of drain-voltage feedback and harmonic distortion of the amplifier. High-voltage differential probes (two Tektronix P5205 100 MHz probes on a 500× attenuation setting) were used for both measurements. A Bird Series 5010 directional power sensor was placed between the load and converter, connected on either side with 2-foot lengths of RG-58 cable. The sensor was equipped with a Bird DPM-500H forward power sensor (500 W full-scale from 2-30 MHz) and a DPM-50H reflected sensor (50 W full-scale from 2-30 MHz), with readout provided by a Bird Model 500-EX digital power meter. The Load was a 50 Ω Bird Model 8401 Termaline coaxial resistor, rated at 600 W and resistive from DC to 3GHz (VSWR: DC to 1GHz = 1.1; 1 to 2.8GHz = 1.2; 2.8 to 3GHz = 1.3 maximum).

Measured drain- and load-voltage waveforms for the Class E converter are shown in Fig. 4.20 for V_{in} = 107 V. Input current, as measured by the HP 6015A supply, was 1.88 A, close to the DC value of 1.93 A measured by a Tektronix A6303 current probe with AM503B amplifier. The Bird meter read 163 W forward power, close to the 162.2 W computed from

IPR2024-00706 EX. 2005

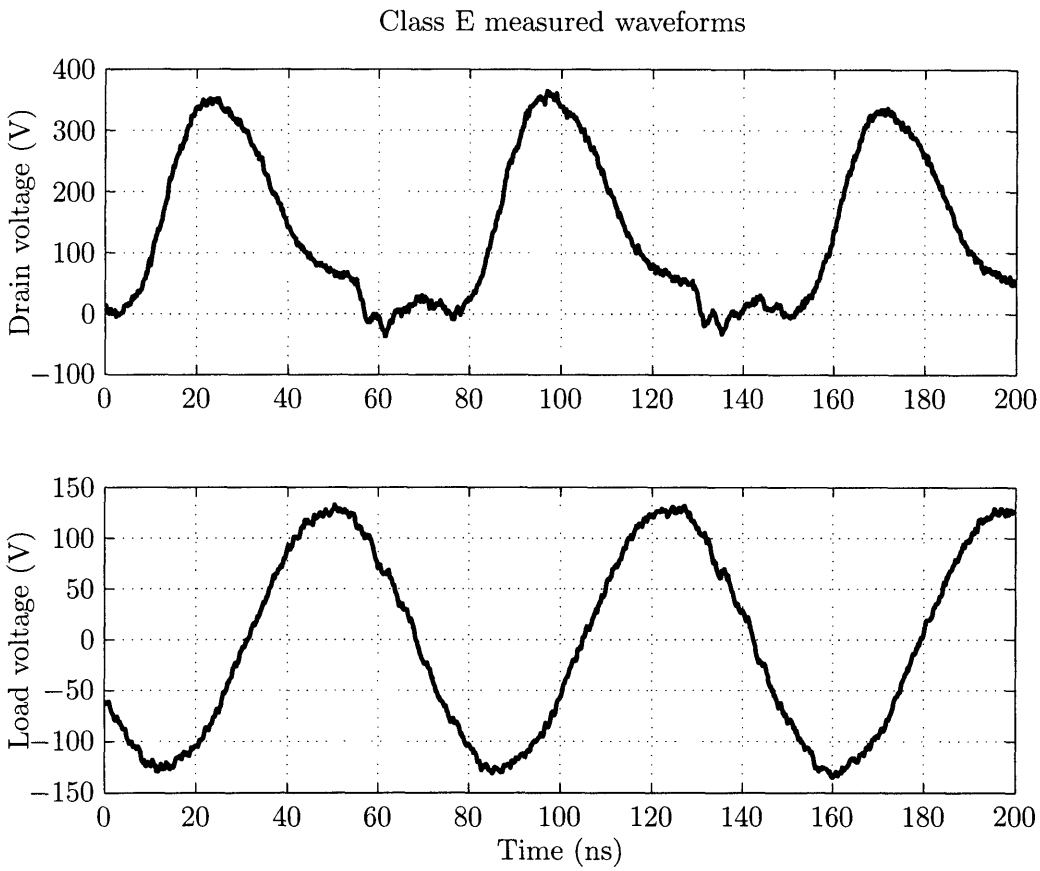

Figure 4.20: **Measured drain and load voltages for the Class E inverter in the high-power comparison of Section 4.3.2.2.**

the output-voltage measurement. The drain efficiency was around 81% (80.6% from voltage measurements, and 81% computed with the power meter). 85% efficiency was computed from a ideal-switching simulation of the schamtic of Fig. 4.19, taking no account of finite switch times. The resonant inductor was lossy, and became hot enough during converter operation to soften its former.

4.3.2.3 Distributed Class Φ implementation

To first demonstrate Class Φ operation at higher powers with little design effort, a prototype converter was constructed incorporating a transmission line rather than a multi-resonant line-simulating network. The converter schematic and components are shown in Fig. 4.21. The input line is a 135.5-inch section of RG-58/U, a quarter wavelength at 13.61 MHz. It is terminated at the dc bias input with 3 silver-mica snubber capacitors which are self-resonant

IPR2024-00706 EX. 2005

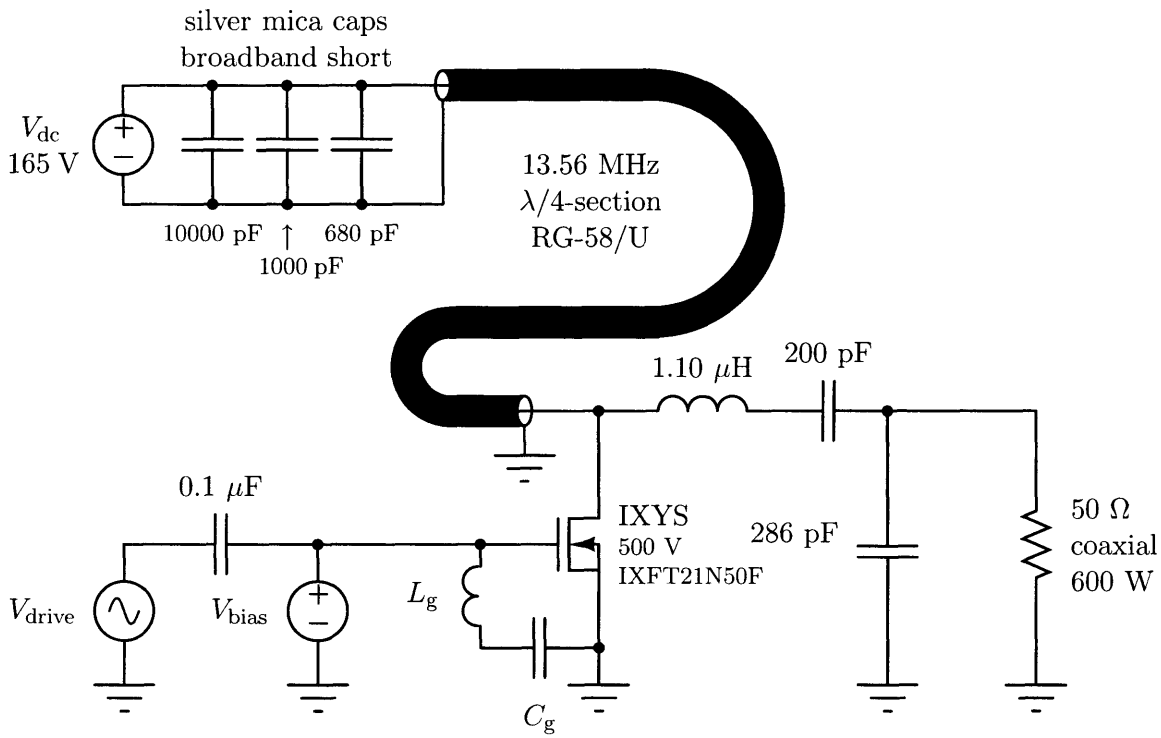

Figure 4.21: **Multi-resonant converter constructed with a length of RG-58/U coaxial line.**

near the switching fundamental and its fourth harmonic. Without this ac short, the line's boundary conditions are not enforced well enough to produce a square-wave voltage at the drain. The output network is an L-match into a 50 Ω coaxial power resistor, designed to provide 20 Ω seen from the source. The series element of this L-match (a 47 nH inductor) was again absorbed into the tank inductor.

The gate capacitance was resonated as before with a 27 nH inductor, this time in series with a 0.01 μF polypropylene blocking capacitor. This resonator had a peak impedance of 18 Ω and nearly resistive phase, as seen from the 50 Ω ac drive through a second 0.01 μF blocking capacitor. The dc voltage at the gate could be set with this arrangement to vary the switch on-time, as required for Class Φ ZVS conditions. A duty cycle of about 0.38 was enforced with this technique using a gate bias of −4.4 V.

Measured drain- and load-voltage waveforms for the RG-58 converter are shown in Fig. 4.22 for V_{in} = 165 V. The drain waveform shows the anticipated square-wave form, ringing up to around 320 V during the switch-off period. No power meter was available for this measurement, and the output power computed from the load-voltage measurement was

IPR2024-00706 EX. 2005

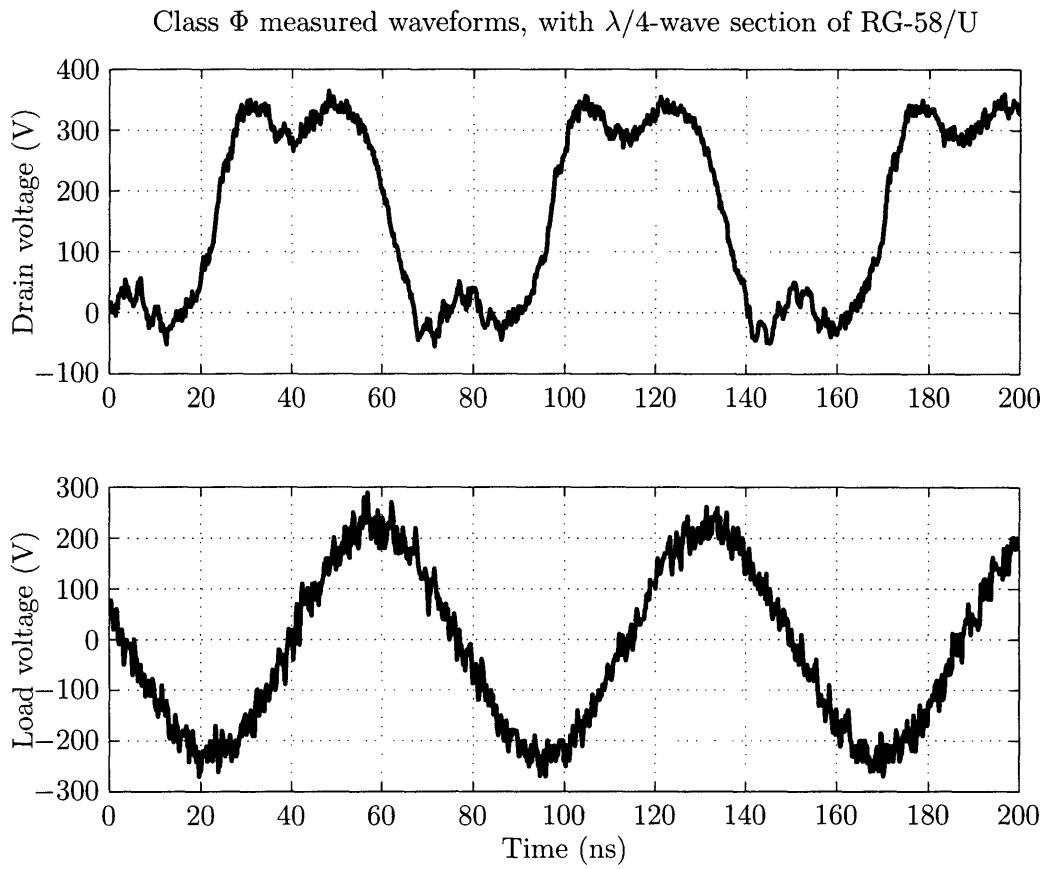

Figure 4.22: **Measured drain and load voltages for the distributed implementation (Fig. 4.21) of the inverter considered in Section 4.3.2.3.**

IPR2024-00706 EX. 2005

205.6 W. With the input source suppliying 2.91 A at 165 V, the computed drain efficiency is 88%. The resonant inductor ($5\frac{1}{2}$ turns of the same litz as in Section 4.3.2.2 wound on a glass former 27.4 mm in diameter) was again a major source of loss.

4.3.2.4 Integrated Class Φ implementation

A Class Φ converter with integrated air-core magnetics was designed to match the performance of the Class E of Section 4.3.2.2 with lower device stress. The multi-resonant choke was constructed into the thickness of a 4-layer PCB with 2 oz. copper on all layers (see Fig. 4.23). A 59 mil core was selected for the magnetic thickness dimension, with capacitors constructed across outer layers comprising 2 sheets of 2116 prepreg. The final laminate build was 83 mil, slightly more than anticipated because of an unexpectedly small prepreg compression. The inter-layer capacitances were smaller than designed, as a result, and the multi-resonant structure had a principle peak at 15.7 MHz rather than 13.56 MHz.

As in Figure 3.1, the multi-resonant toroid had an outer diameter of 2.5 inches and an inner diamter of 0.75 inches. The capacitors extended from each turn for a total diameter of 4.4 inches. Two turns of the gapped, 30-turn toroid were brought to the outer copper layers *after* the drain connection and left free of soldermask. These bare turns are magnetically coupled to the input network, providing an adjustable connection point to implement the inductance-cancellation scheme of Fig. 4.15a. The schematic of the complete converter with parastitcs is shown in Fig. 4.24, excluding details of the input bypassing (one each of four discrete silver mica values was used, 10000 pF, 6800 pF, 1000 pF, and 680 pF).

Measured drain- and load-voltage waveforms for the Class Φ converter with mult-resonant inductor are shown in Fig. 4.25 for $V_{\text{in}} = 102$ V. The drain waveform has a roughly square-wave form, ringing up to around 200 V during the switch-off period. Input current, as measured by the HP 6015A supply, was 2.11 A for an input power of 215 W. 178 W load power was computed from the output-voltage measurement, and the Bird meter read 163 W forward power.[15] The drain efficiency was 82.7% from voltage measurements, and 75.2% computed with the power meter. The resonant inductor was constructed as in Sec-

[15]The unexpectedly large fourth harmonic at the drain could have contributed to harmonic current into the load sufficient to explain this discrepancy. This fourth-harmonic distortion is a symptom of poor zero coincidence, as compared with the ideal transmission line.

IPR2024-00706 EX. 2005

tion 4.3.2.2 and was again very lossy, a likely target for efficiency improvement in subsequent designs. The multi-resonant structure, likewise, became warm during operation. The Q of its capacitor taps was around 50, and overall efficiency could be improved by higher quality dielectrics and higher-build copper in the planar structure.

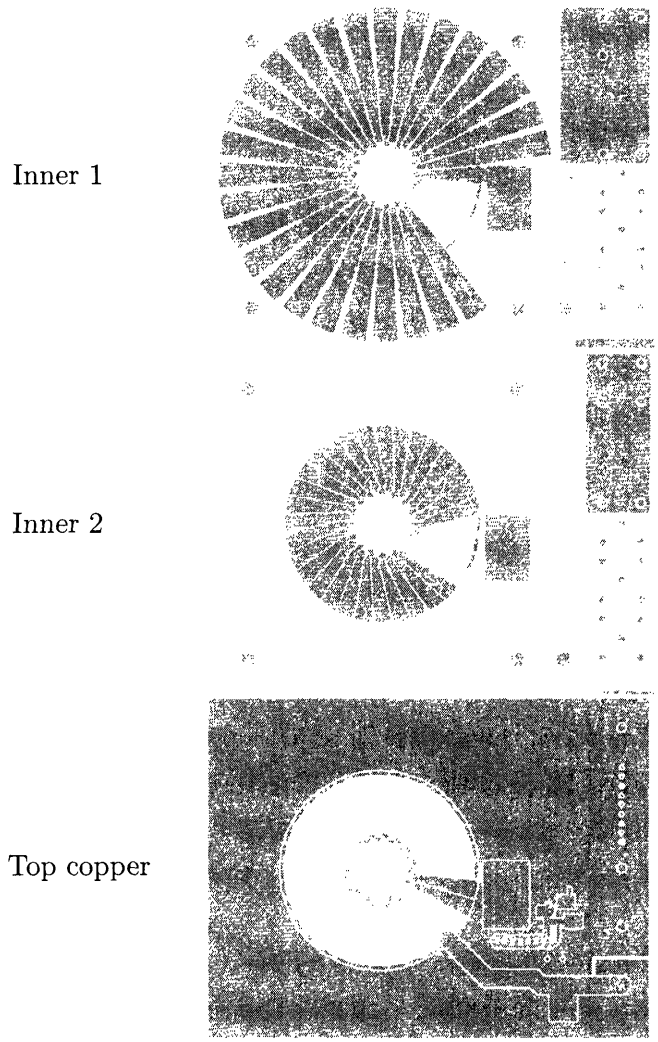

Figure 4.23: **Copper layers of the Class Φ converter with integrated 20 Ω multi-resonant structure.**

IPR2024-00706 EX. 2005

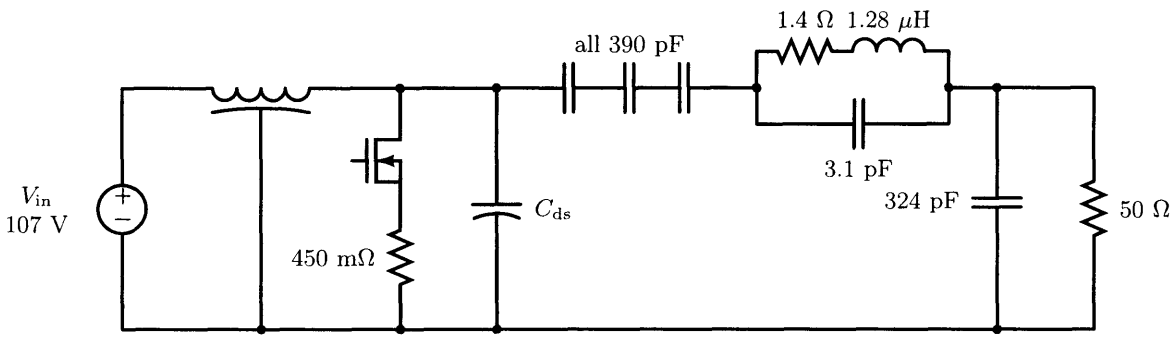

Figure 4.24: **Schematic (with parastics) of the Class Φ converter of Section 4.3.2.4.**

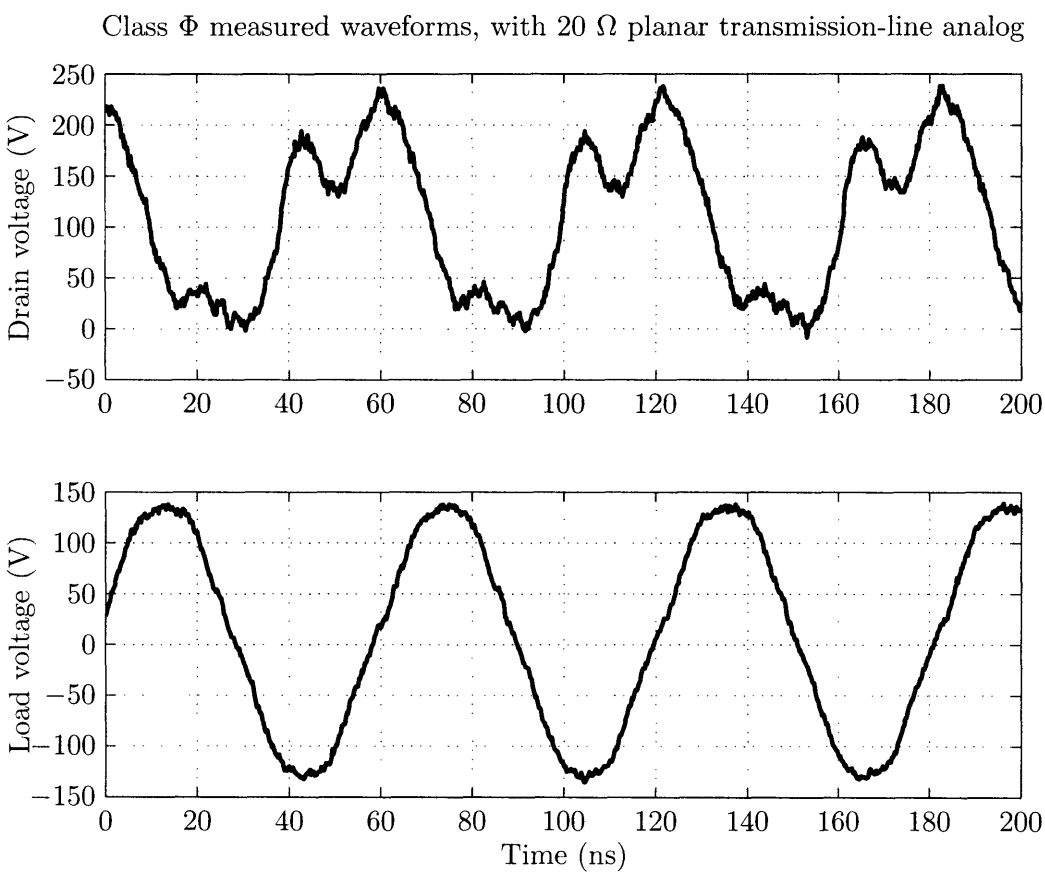

Figure 4.25: **Measured drain and load voltages for the lumped implementation (Fig. 4.21) of the inverter considered in Section 4.3.2.3. The transmission-line impedance was approximated with a planar, 20 Ω iterated LC network, cross-sections of which are shown in Fig. ??.**

IPR2024-00706 EX. 2005

Chapter 5

Fabrication

THE tapped magnetic structures of Chapter 3 were built in two forms, embedded into the thickness of a printed-circuit board or electroformed into epoxy molds on a silicon or pyrex substrate. The second means of construction was intended to demonstrate the possibilities wafer- or package-scale integration, in which multi-resonant structures can be constructed by in additive, post-processing step on finished wafers, or embedded with finished die in a package. The scales of the electroformed structured — millimeters rather than inches — could be suitable (by their impedance and resonant frequencies) for power conversion in the upper VHF and UHF.

Apart from the pyrex or silicon substrate, the PCB and wafer-scale implementations presented in this chapter are fundamentally similar from a materials-compatibility and adhesion standpoint. SU-8, the epoxy used as an electroforming mold in Section 5.2 is a Novolac resin with the same basic structure as the matrix materials in FR-4 core composite and many semiconductor packages, but with more epoxy functionality per molecule (see Fig. 5.1). Whereas in printed-circuit manufacture, an entire layup of patterned core and prepreg layers is bonded and drilled, wafer-level structures are "drilled" by a parallelized UV exposure of each epoxy coat individually. Both of these manufacturing methods rely on mask-based imaging of conductor layers, and repeatable lamination thicknesses (see Sections 5.1.2 and 5.2.1). So, though the critical frequencies and characteristic impedance of the networks we would like to build (*cf.* Fig. 3.1) shift with differential scaling among tap capacitances, for instance, or among the loop area of turns, *relative* alignment in the overall structure can still be good because with tight *ratiometric* control of features and uniform thicknesses. For applications in which poor absolute tolerance is unacceptable, a converter's switching frequency can be placed under closed-loop control to ensure that resonant alignment of multiple harmonics is always maintained [16, 18, 17, 19].

IPR2024-00706 EX. 2005

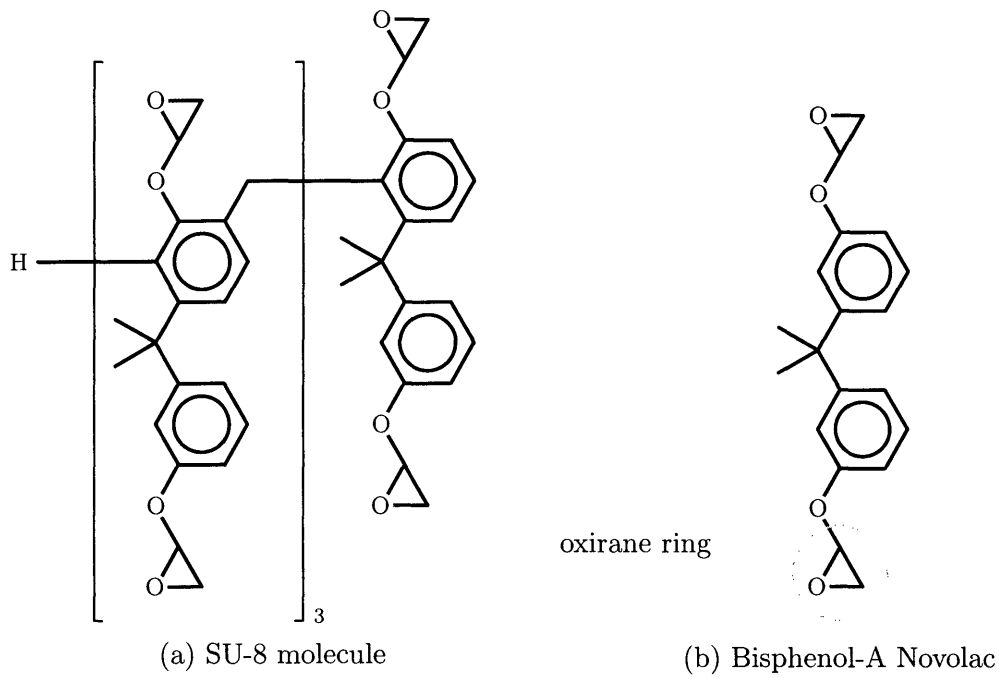

(a) SU-8 molecule (b) Bisphenol-A Novolac

Figure 5.1: **Compatibility of epoxy resins for fabrication at different scales: (a) SU-8, the epoxy resin used with a photo-active initiator in the wafer-level process described in Section 5.2 (b) Bisphenol-A Novolac resin used in the PWB industry for many epoxy-impregnated fiberglass laminates, including FR-4 cores (flame-retardant). The monomer is one-quarter of the SU-8 molecule. Prepreg layers often incorporate different uncured thermosetting resins, but are chemically compatible with Novolac formulations and have the same bisphenol base. "Epoxy functionality" refers to the number of oxirane rings on a resin monomer, highly stressed 3-element groups responsible for adhesion and polymerization.**

IPR2024-00706 EX. 2005

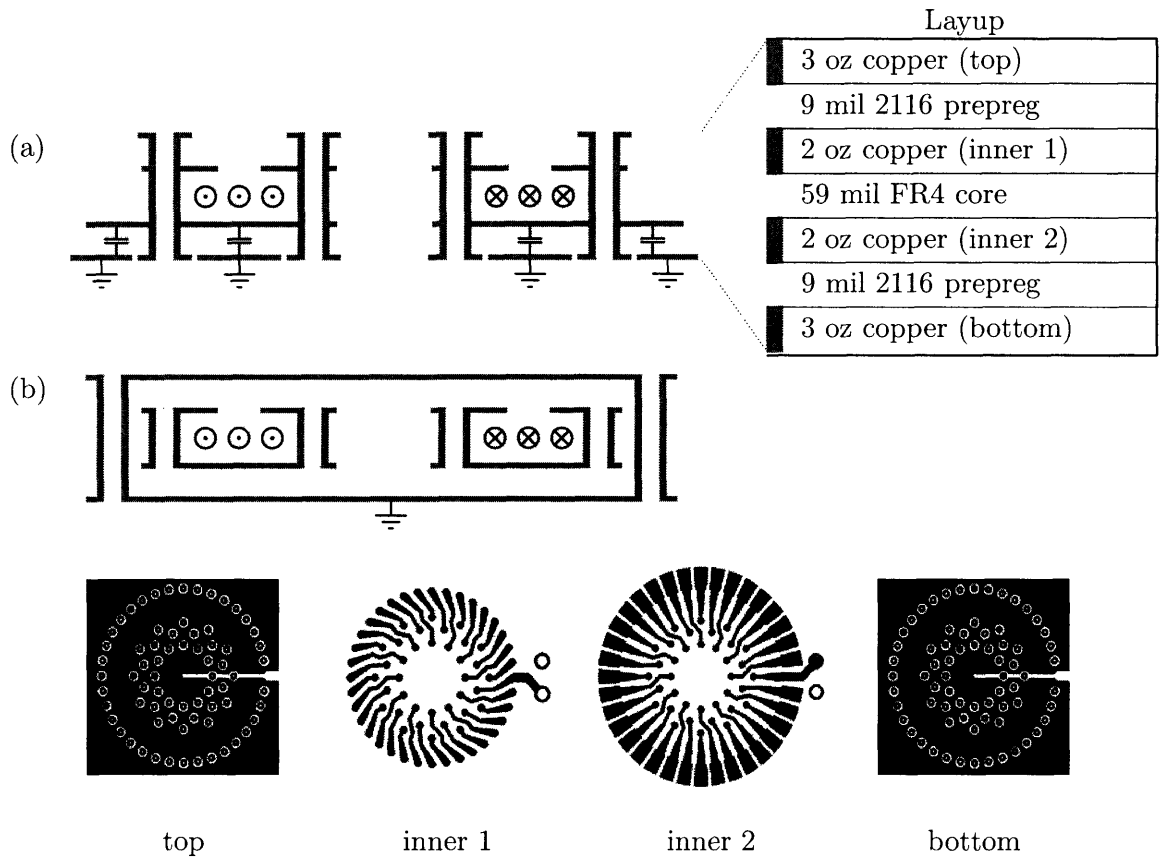

Figure 5.2: **(a) Cross-sectional view and layup for a 4-layer PCB used to manufacture low-power multi-resonant structures. The board in (b) incorporates blind vias for more complete shielding of the embedded air-core magnetics.**

5.1 Printed-Circuit Board Structures

A cross-section of a PCB device is shown in Fig. 5.2a, alongside mask views of inner and outer copper layers. The toroid turns in Fig. 5.2a make a radial traverse around the core on inner layers 1 and 2, so that the principal flux path lies within the board thickness. In this arrangement, outer copper layers can both shield the device from stray capacitance and tap the toroid in a distributed manner. For a high-volume process with blind vias, one might embed the toroid completely within the PCB, as in Fig. 5.2b, for superior shielding. The full-field problem of simultaneously designing the laminar winding and distributed capacitance is challenging, so many prototype devices had no ground plane directly over the toroid. By sacrificing shielding, such a design was partitioned so that section inductances

IPR2024-00706 EX. 2005

could be scaled independently of the loading capacitance per unit length along the structure (both distributed capacitance and tap capacitance). Toroids designed in this manner can be shielded by placing ground planes on the far side of removable boards, clamped over both faces of the toroid. Spaced 62 mil or more away from the magnetic structure, these ground floods minimally perturb designs analyzed on a lumped basis (see Section 3.4.4.2).

5.1.1 Layout

The layout of all PCB structures was scripted to generate geometries in terms of the desired signal-to-signal spacing, finished via size, and the thicknesses and permittivities of laminations. Appendix A.1 provides the relevant scripts, along with code to approximate the layout geometry for FastHenry inductance-matrix extraction. The inner vias for low-power structures were packed in a three-layer pattern comprising an inner dodecagon, squares, and equilateral triangles, each with edge lengths equal to a desired via-trace-via spacing d [43]. The circumradius of the base dodecagon for such a packing, expressed in terms of d, is

$$\text{circumradius} \qquad R = \frac{\sqrt{2}+\sqrt{6}}{2} \cdot d$$

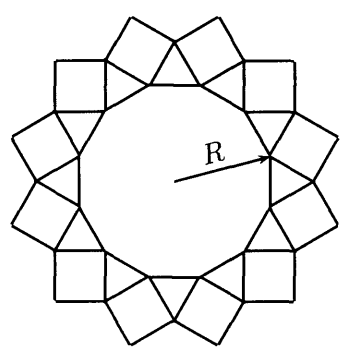

The high-current toroids used in Section 4.3.2 had a different packing scheme which placed at least 3 vias in series at each traverse of the board thickness (see Appendix A.1 for details). This arrangement was designed to decrease DC resistance and increase Q.

IPR2024-00706 EX. 2005

5.1.2 Estimation of inner-layer thickness

Designing multilayer boards with well-defined capacitances across inner layers is difficult because of the resin flow in prepreg layers encapsulates the underlying circuit during compression and curing. Especially when the inner copper build is a substantial fraction of prepreg thickness, the finished dielectric thickness depends on the prepreg itself (glass style, resin content, and resin flow when pressed) and the underlying copper pattern. One could resort to first-article construction methods or to expensive controlled-dielectric processes (normally reserved for high-volume rf and microwave boards with critical dielectric thicknesses), but one simple approximation is useful where no detailed guidelines or prototypes are available.

The contribution of underlying circuits to overall laminate-to-laminate spacing (the distance from from the top of one finished layer to the next) is approximated by the copper thickness multiplied by the circuit coverage (e.g., 0.30 for a pattern filling 30% of the layout area). Prepreg build over copper is obtained by subtracting the copper thickness, so that

$$\begin{aligned}\text{dielectric thickness} &= \text{prepreg nominal finished thickness} \\ &\quad - (1 - \text{coverage}) \times (\text{copper thickness})\end{aligned}$$

In a 4-layer board where this effect was not taken into account, for instance, a nominal 8.613-mil prepreg stack overlay a 2-ounce inner layer of copper (2.8 mil thickness). Assuming 30% coverage in this layer, the thickness overestimate was 22.6%, corresponding to capacitances higher than anticipated and an 11% decrease in resonant frequencies (a 9% decrease was observed). Note that this thickness-correction estimate is approximate because of uncertain copper coverage; manufacturers print calibration and venting patterns on the sides of production panels — along with other jobs — that affect finished thicknesses.

5.2 Wafer-level Structures

A batch microfabrication process suitable for constructing multi-resonant magnetic structures on the surface of integrated circuits or other substrates was also developed. The toroids depicted in Fig. 5.3 were constructed by electroformation, in which posts were elec-

IPR2024-00706 EX. 2005

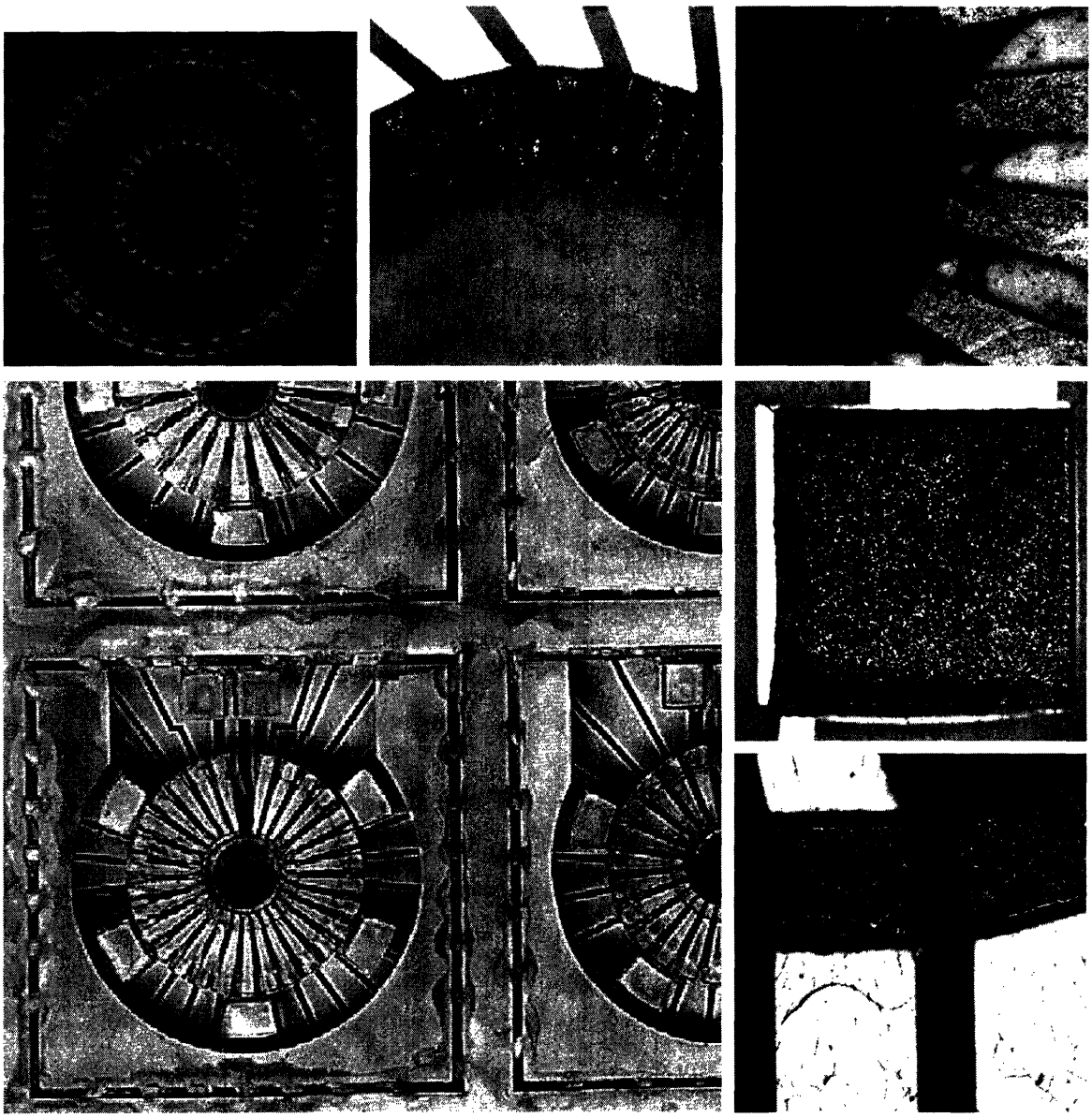

Figure 5.3: **Clockwise from lower left: (a) Die views of completed devices with 7.5 mm outer diameter and 3.3 mm inner diameter, (b) die view of lower layer and plating interconnect, with the beginnings of posts, (c) detail of inner posts, (d) detail of upper-level copper connecting to the top of electroformed posts, (e) detail of an input-port pad, (f) outer posts, shorted to demonstrate the effects of overplating in a region with thin epoxy build.**

IPR2024-00706 EX. 2005

troplated into a thick-film epoxy stencil, and connected by metal traces beneath the epoxy and in overlying patterns to form complete turns. Plating interconnects extend radially from the portion of the metal pattern incorporated into the toroid itself, and extend to die boundaries so that dicing isolates regions shorted during electroformation.

5.2.1 SU-8

The electroformation process centers around MicroChem's SU-8 2005, a negative-tone photosensitive epoxy formulation (MicroChem Corp,, Newton, Massachusetts). SU-8 was originally developed for the microelectronics industry to provide a high resolution negative resist for the fabrication of advanced semiconductor devices [44, 45]. SU-8 is supplied as a liquid consisting of an epoxy resin, a solvent (cyclopentanone for the 2000-series formulations, or gamma-butyrolactone for other families) and a photo-acid generator (PAG). The PAG is responsible for initiating the SU-8 polymerization by forming a strong acid when exposed to UV between 300 and 400 nm:

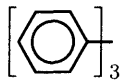

$$S^+A^- \text{ (PAG)} \implies H^+A^- \text{ (acid)} + \text{other products}$$

The SU-8 itself is nearly transparent at these wavelengths (the near UV), which allows thick structures with near-vertical side walls to be fabricated.[1] Because of the highly cross-linked matrix in the exposed SU-8 (which cures when heated above a critical temperature during post-exposure bake), it is thermally stable up to 200°C and chemically stable after development. Finally, its high solubility in a variety of organic solvents allows solutions with high solids contents to be formulated, so that substrates can be coated with a relatively thick film in a single spin.

SU-8 processing is a notorious "art," often requiring a great deal of experimentation to yield good results for a particular thickness and particular type of feature. Presented in sections 5.2.1.1 to 5.2.1.3 are those techniques — developed through experience, consultation with colleagues,[2] and dissatisfaction with the results of conventional processing [48, 49, 50, 51]— that are helpful for defining clean well features in films 500 μm or more in thickness.

[1] aspect ratios greater than 15 (for isolated sidewalls) can be achieved for films up to 100 μm thick in an optimized process [46].

[2] the advice of Mark Allen at Georgia Institute of Technology was especially helpful [47].

IPR2024-00706 EX. 2005

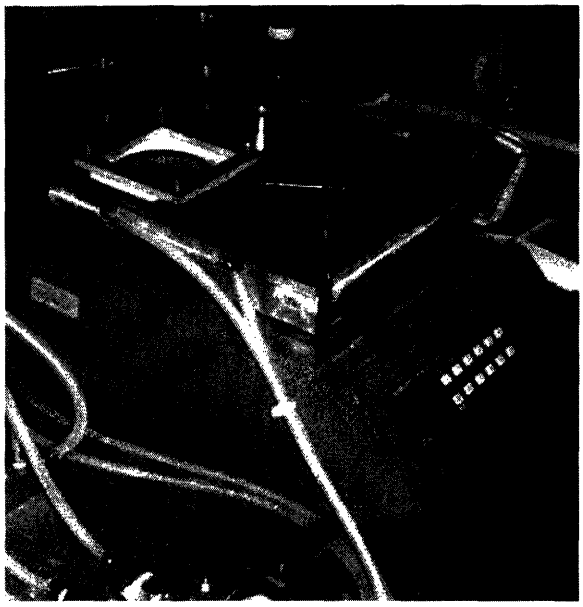

Figure 5.4: **LHS-720 Dataplate (Omega) levelled with a an adjustable tripod (one screw-adjustable foot of which is in the foreground). The hotplate was coated with a thin layer of heat sink compound and a tapped aluminum plate was placed on top. The plate has positions to hold four 4″ wafers and their O-ring molds, which are held in compression by aluminum clamps bolted at their corners into the tapped plate.**

5.2.1.1 Pour application

SU-8 2005 is a low-viscosity SU-8 formulation designed for spin-application of 5-8 μm-thick films, though more viscous members of MicroChem's SU-8 family can coat up to 450 μm in a single step. A substrate is normally coated using a conventional photoresist spinner, with film thickness controlled by the spin speed and the solids content of the epoxy solution. We abandoned spin application of thick films after extensive experimentation with SU-8 2150 and 2100 (MicroChem's most viscous epoxies). Even small axial misalignment in the coater chuck resulted in large variations in SU-8 thickness, especially in films applied at low RPM for a short spin time. Nonuniform epoxy thickness, complicated by the presence of bubbles throughout the viscous epoxy formulation, prevented electroformed posts from plating level to the tops of their molds simultaneously. Overlying interconnects failed to cover the resulting steps, and a single defect of this type could interrupt the conduction path around a toroid.

Films of lower-viscosity SU-8 2005, however, showed excellent thickness-uniformity when

IPR2024-00706 EX. 2005

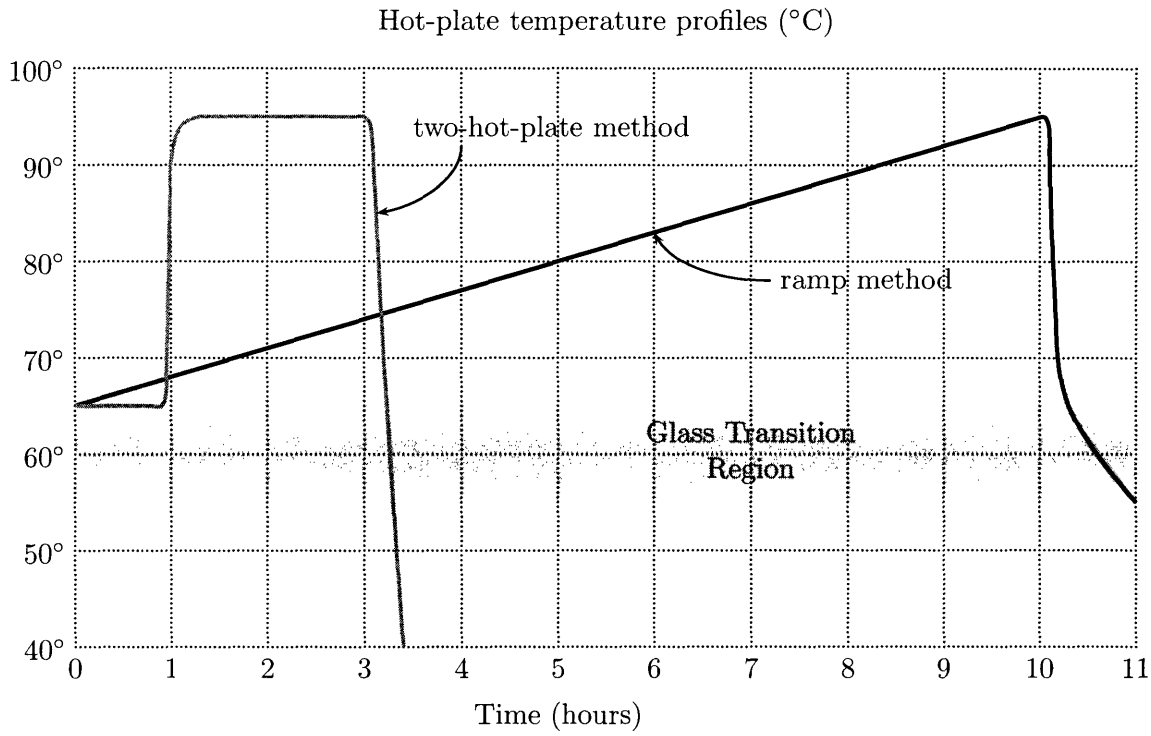

Figure 5.5: **Pre-bake temperature profiles, suitable for SU-8 films 450 μm to 1.2 mm thick. The ramp slope is 3°C per hour. The two-hot-plate method is recommended by the manufacturer for thinner SU-8 films ($<$ 450 μm). Process guidelines are available from the MicroChem website for SU-8 formulations 2–25, 2002–2025, 50–100, and 2035–2100 (`http://www.microchem.com`, last accessed May 22, 2005).**

poured, uniformity that was key to the making reliable electrical connections above the wafer plane. We metered volumes of SU-8 2005 of into molds on a meticulously levelled pre-bake hotplate (Fig. 5.4), confining the SU-8 on 4″ substrates with Double Seal Buna-N O-Rings (Standard Size AS-568A No. -340). The solid content of SU-8 2005 is 45% by mass, so assuming all the solvent is expelled during pre-bake, the final film thickness t is

$$t = \frac{V}{A} \cdot \frac{\rho_{\text{solvated}}}{\rho_{\text{solids}}}$$

where V is the metered volume over the area A, and $\rho_{\text{solvated}} = 995.2$ kg/m^3 is the density of the 2005 formulation and $\rho_{\text{solids}} = 1283.8$ kg/m^3 the density of SU-8 with no solvents. For example, 6 mL of SU-8 2005 in the O-ring mentioned above ($2\frac{3}{8}''$ ID) can be expected to yield a cured-film thickness of 518 μm.

The solvents are now driven out of the SU-8 film with a 3°C ramp from 65°C to 95°C

IPR2024-00706 EX. 2005

over 10 hours (Fig. 5.5). MicroChem suggests a two-hot-plate method for their thinner films which, when applied to thicknesses of 450 μm or greater did not drive out solvents uniformly. Even for bake times many hours longer than those shown for the two-temperature method in Fig. 5.5, films could slide and split during exposure. Cool down after pre-bake is possibly important for reducing stresses in the cross-linked epoxy. A slow ramp through the glass-transition region allows the film to accommodate internal stresses as it cools, and can be approximated by turning off the hotplate and relying on its thermal capacity for slow cool-down after the peak ramp temperature is reached.

5.2.1.2 Contrast Enhancement Lithography

The uniform, thick films made possible by the pouring method have tacky edge beads at the interface with the O-ring mold. This bead cannot be easily removed, mechanically or by solvents, and adheres to the mold, mask holders, and masks. When a wafer is separated from tooling for further processing, dried or exposed SU-8 is pulled or deformed, ruining the wafer in many cases. After pre-bake, a practical solution to this problem is to cut the mold ring in several places, pulling the pieces radially away from the epoxy. This technique minimizes buckling or stretching in the levelled film. During exposure, a sacrificial acetate sheet[3] can be placed over the SU-8 film to prevent adhesion to the aligner or mask. 3 mil acetate was used successfully in this regard, and can be carefully peeled off the underlying film after exposure, even if it tightly adheres at the edges. Leaving the dried SU-8 film in open air for at least 10–15 minutes before exposure reduces adhesion to the acetate protector.

The large separation between the SU-8 and mask introduced by a protecting sheet can limit the size and fidelity of patterned features because of light scattering and aerial-image effects. These problems are especially pronounced in well features, which are encroached by excess polymerization from the sidewalls. The mask features defining a well may be only 4 or 5 times larger than the separation of the mask itself, which — because it is a light-field mask — admits scattered UV from every direction.

[3]mylar and cellophane were also tested. The acetate was the thinnest available (3 mil) from a local art and craft supply.

IPR2024-00706 EX. 2005

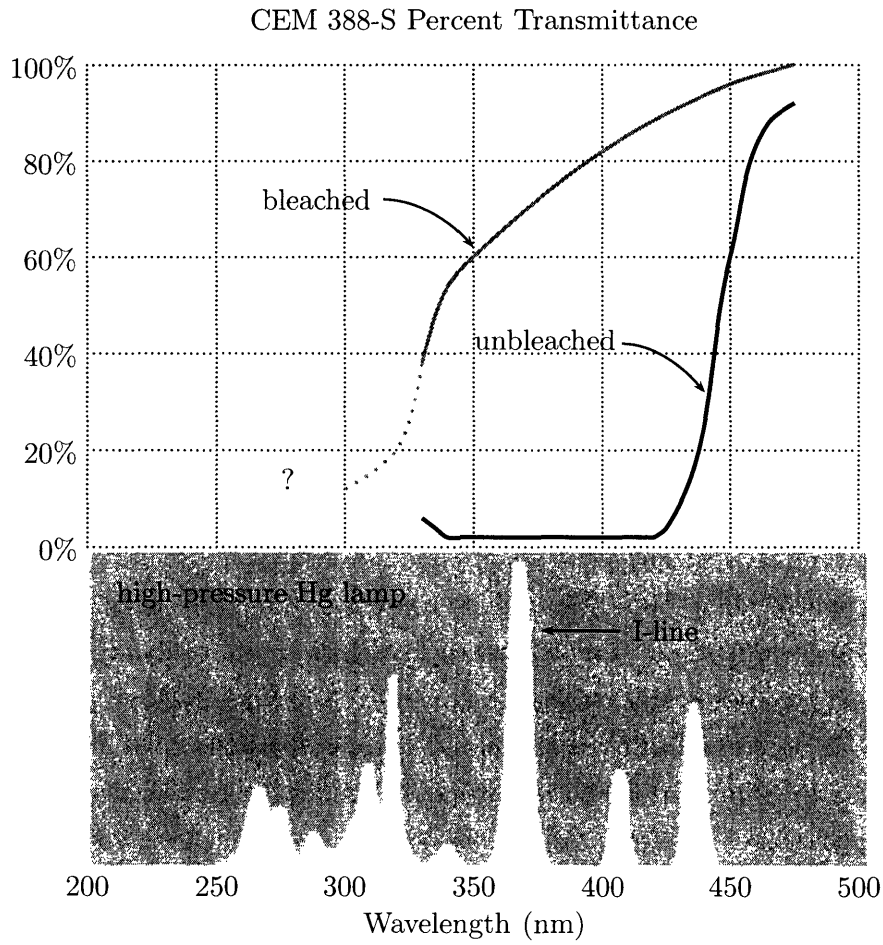

Figure 5.6: **Transmittance of CEM-388S Contrast Enhancement Material, produced by Shin-Etsu MicroSi, Inc. Both in the bleached and unbleached state, the CEM coat filters out many of the shorter wavelengths in broadband mercury-lamp exposure tools.**

IPR2024-00706 EX. 2005

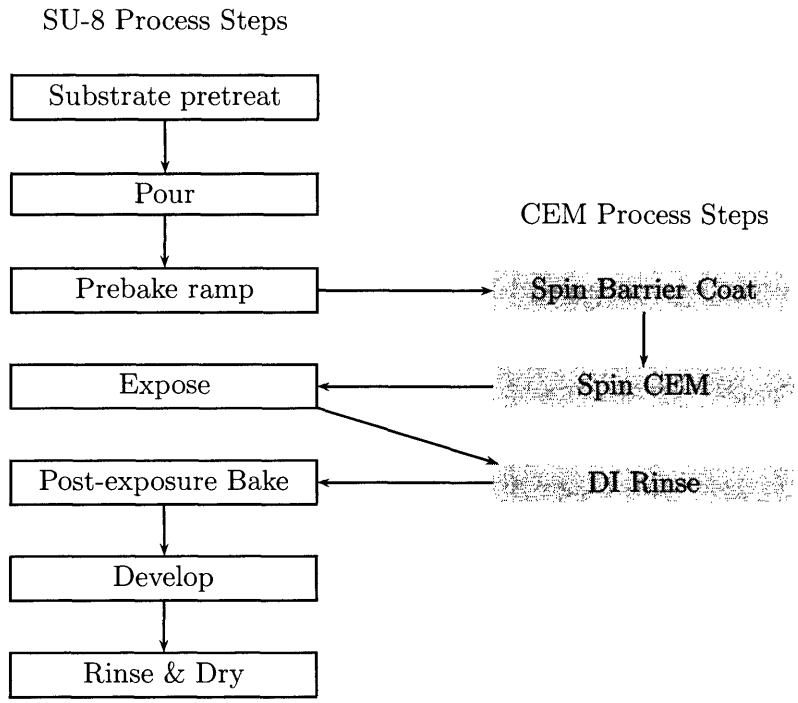

Figure 5.7: **Contrast Enhancement Material applied to SU-8 lithography**

CEM-388S, A Contrast Enhancement Material produced by ShinEtsu Micro-Si,[4] was applied as a top-coat for all SU-8 lithography to counteract the problems of exposing thick, tacky films. CEM is a photo-bleachable material, which is initially opaque to the exposure wavelengths, but becomes nearly transparent upon exposure (see Fig. 5.6). CEM is added to the basic SU-8 processing steps as shown in Fig. 5.7. A barrier coat (BC-7.5 is recommended for SU-8 by ShinEtsu) is first applied and spun dry over pre-baked SU-8, followed by the spin application of the CEM itself. Spin speeds were kept below 1 kRPM to minimize shear forces in the dried SU-8. After conventional exposure, the CEM and barrier coat are removed by a DI water pre-wet and the resist is developed in the ordinary manner (see Section 5.2.1.3, below).

Because of the presence of the bleachable material, the contrast of the illumination that reaches the photoresist is increased. Referring to Fig. 5.8, the aerial image during exposure bleaches regions of higher intensity (open areas of the mask) at a faster rate than the lower intensity regions (dark areas of the mask). By adjusting the bleaching dynamics so that the photospeeds of the CEM and resist layers are properly matched, it is possible to completely

[4]Shin-Etsu MicroSi, Inc., Phoenix, Arizona

IPR2024-00706 EX. 2005

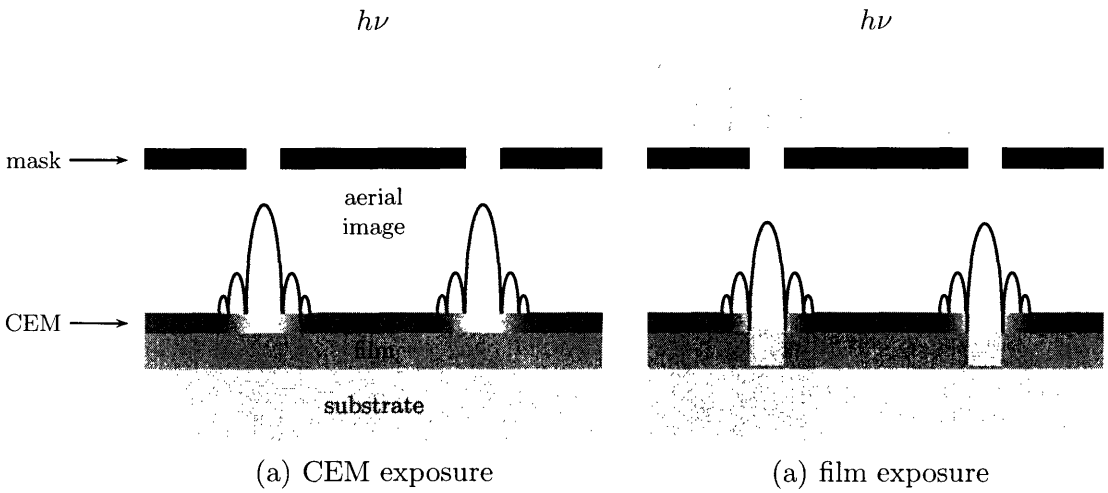

Figure 5.8: **Schematic representation of the effect of Contrast Enhancement Material on the exposure of an underlying film. With mask separation on the order of 50 μm — and on the same scale as mask features — the aerial image shows significant diffraction and scattering, as represented by the sinc-squared power lobes shown in the figures. The scattered light off the main lobe does not bleach the CEM coat enough to expose the underlying film, and the mask features are effectively reproduced by the conformal, removable CEM coat.**

expose the underlying photoresist in light areas before the CEM is bleached through in dark areas. During exposure, an in-situ "conformal contact mask" is in formed in the CEM layer, compensating for the large working distance in the exposure system.

The effect of CEM on a developed trench feature is seen in Fig. 5.9. The occlusion in Fig. 5.9a is polymerization in the topmost portion of the SU-8, called "T-topping." Scattered light for a large mask separation develops photo-acid beyond the borders of dark regions. This acid can diffuse and initiate polymerization sufficient to cover well and trench features as large as 50 μm, as depicted in Fig. 5.9a. This effect is particularly pronounced with broadband exposure tools (*cf.* the spectrum of Fig. 5.6) because of the high absorption of the photo-acid generator at wavelengths shorter than 350 nm. CEM helps in this regard also by acting as an I-line filter, attenuating higher UV frequencies as depicted by the transmittance curves of Fig. 5.6. The films of Fig. 5.9 were both exposed at a dose of 400 mJ/cm^2 in a Karl-Suss MJB-3 mask aligner with a 200W Hg lamp and 365/405 nm filters.

IPR2024-00706 EX. 2005

(a) T-topping with no CEM (b) With CEM

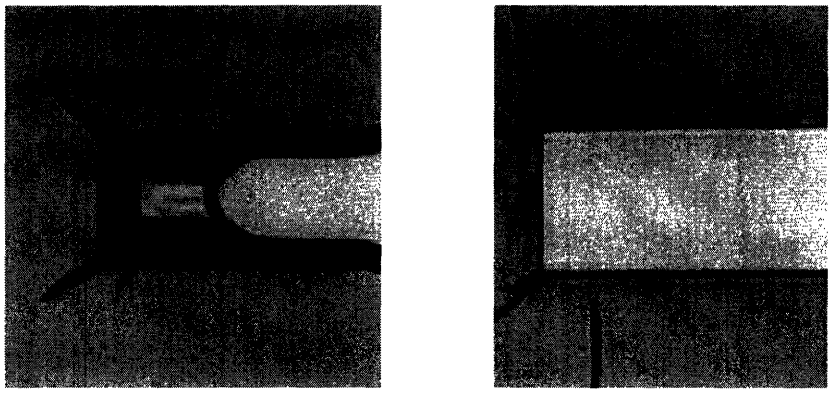

Figure 5.9: **Results from lithography of a 100 μm-thick film of SU-8 with Contrast Enhancement Material. The feature is the end of a trench 50 μm wide. Without CEM, the top of the feature in (a) is covered over with a thin layer of polymerized epoxy (the so-called "T-topping" effect). Photographs reproduced with the permission of Kurt Broderick.**

5.2.1.3 Thick-film development

The development of deep well features can be particularly troublesome, with no obvious means other than spray development for penetrating unexposed regions to remove the tacky, viscous SU-8. Exposure time and crosslinking density trade off with ease of development, and light-region epoxy that is well cured entails dark regions that will be more difficult to remove. Curing is rarely thorough immediately after the post-exposure bake, moreover, and a brute force approach to development — excessive development time, for instance — can swell and delaminate polymerized epoxy. One good solution is to not attempt full cross-linking at once, but expose with a moderate dose, followed by a normal post-exposure bake. E.g., for a 450 μm film, a dose of 3.18 J/cm^2 (measured at 365 nm), followed by a 31 minute, two-hot-plate post-exposure bake (6 minutes at 65°C and 25 minutes at 95°C) yields a film easily developed by alternating PGMEA and isopropanol rinses. The film can be flood exposed after initial development, and further cross-linked in a second bake. Cracking often appears after post-exposure bake because of insufficient exposure dose, so this method was a trade-off for a particular prebake profile and film thickness, determined by experimentation for a 500 μm film with the temperature ramp treatment of Fig. 5.5. Because cracking is caused by the shrinkage of the SU-8, film stresses around development time can be reduced by mask design. Features with short lengths, small areas, or appropriate fillets,

IPR2024-00706 EX. 2005

for instance, are better able than large features to accommodate internal stress without peeling or cracking.

Even after complete development, subsequent plating steps require that residual epoxy be removed from the underlying metal surface. Developed wafers were treated for 15 minutes in a Tegal Plasmod Photoresist Asher with O_2 plasma set to 50 W forward power at 350 mT. Oxygen plasma alone does not etch SU-8 significantly without fluorine radicals (SF_6 or CF_4), but is sufficient to remove epoxy residues in developed regions.

5.3 Electroplating

Copper was electrodeposited into plating-resist molds in Cubath-SC,[5] a commercial acid-copper bath. A $9 \times 9 \times 9''$ covered polypropylene tank from U.S. Plastics was leached for 8 hours according to the Enthone's guidelines, and filled with Cubath make-up. Phosphated copper anodes (0.04 to 0.06% P) in leached anode bags[6] were tried-in with a dummy cathode over a four hour period, and the recommended initial feed of additives was metered into the tank (SC-MD and 70/30 were added, always choosing the high volumes from the ranges gives in the instructions). The anode dimensions were 62×64 mm, with ridges on the front face for a total area of about 114 cm^2. Once the anode was coated with a black oxidized film, normal plating began, with a feed of 0.8 mL SC-MD and 0.2 mL 70/30 per ampere-hour administered every 5 hours.

A good cathode contact is crucial, and many wafers can be lost either by not making good contact to the cathode (and etching the seed layer in tens of seconds in the oxidizing bath) or by cracking fragile substrates with the cathode clip. A reliable method of making contact is to fold a small sheet of copper foil over itself in several plies. This malleable foil can be placed between the seed layer and teeth of a small alligator clip, which would otherwise make unpredictable point-contacts to the plating traces. A robust anode clip is necessary

[5]Manufactured by Enthone, Inc., a Cookson Electronics company. Cubath was chosen because of experience with an identical set-up in the Microfabrication Technology Laboratory [52]. We were not permitted to share the MTL bath with other users, whose wafers return from plating to the clean rooms, to reduce the risk of gold contamination. The Cubath series (bath make-up and additives) have since been replaced with another bright acid DC copper system, the CUPROSTAR ST Series.

[6]all anode supplies can be purchased from Kocour Company, Chicago, IL.

IPR2024-00706 EX. 2005

because of oxidation and dissolution at the anode; large copper clips were used here which would have cracked the cathode. The springs and lugs of cathode clips are not copper themselves, so these connectors should be replaced frequently before foreign metals corrode and shed chips into the tank.

An estimate of plating time can be made from the seed area, desired copper thickness, and plating-current density, keeping in mind that 2 Faradays of plating charge are necessary to deposit 1 mole of Copper atoms (reduced from Cu^{2+} ion in solution). Cubath SC is designed for 10–25 ASF throwing power,[7] so shifting to mks units, the plating current I can be determined from a mid-range value of current density and the seed area A

$$I = 17.5 \text{ ASF} \cdot \left(3.28 \frac{\text{foot}}{\text{m}}\right)^2 \cdot A$$

The plating time t for some desired copper thickness h is

$$t = \frac{96500 \text{ C}}{1 \text{ F}} \cdot I^{-1} \cdot \frac{2 \text{ F}}{1 \text{ mol Cu}} \cdot \frac{8920 \frac{\text{kg Cu}}{\text{m}^3}}{0.0635 \frac{\text{kg}}{\text{mol Cu}}} \cdot A \cdot h$$

Plated copper may not be dense in certain areas, and the seed area is especially difficult to predict in the presence of overlapping films and incomplete development, so this calculation is approximate. Enthone recommends a specific ratio of electrode areas (1.5:1 to 2:1 between between anode area and cathode area) which are not maintained for an immersed anode and a cathode with small plated features. As long as the current density at the cathode is controlled, this requirement is related to the long-term health of the anode. The area ratio was therefore ignored, with the caveat that the anode may need to be changed after fewer ampere-hours than its rated life.

5.4 Process flow

The complete process flow comprises three masks (see Appendix C) and three metal layers, and is outlined in Figs. 5.10-5.13. Fig. 5.10 details the deposition, patterning, and growth of the lowest copper layer. A Ti-Cu seed layer (150 Å titanium and 4000 Å cop-

[7]This is the PWB industry's expression for 10–25 amps-per-square-foot current density.

IPR2024-00706 EX. 2005

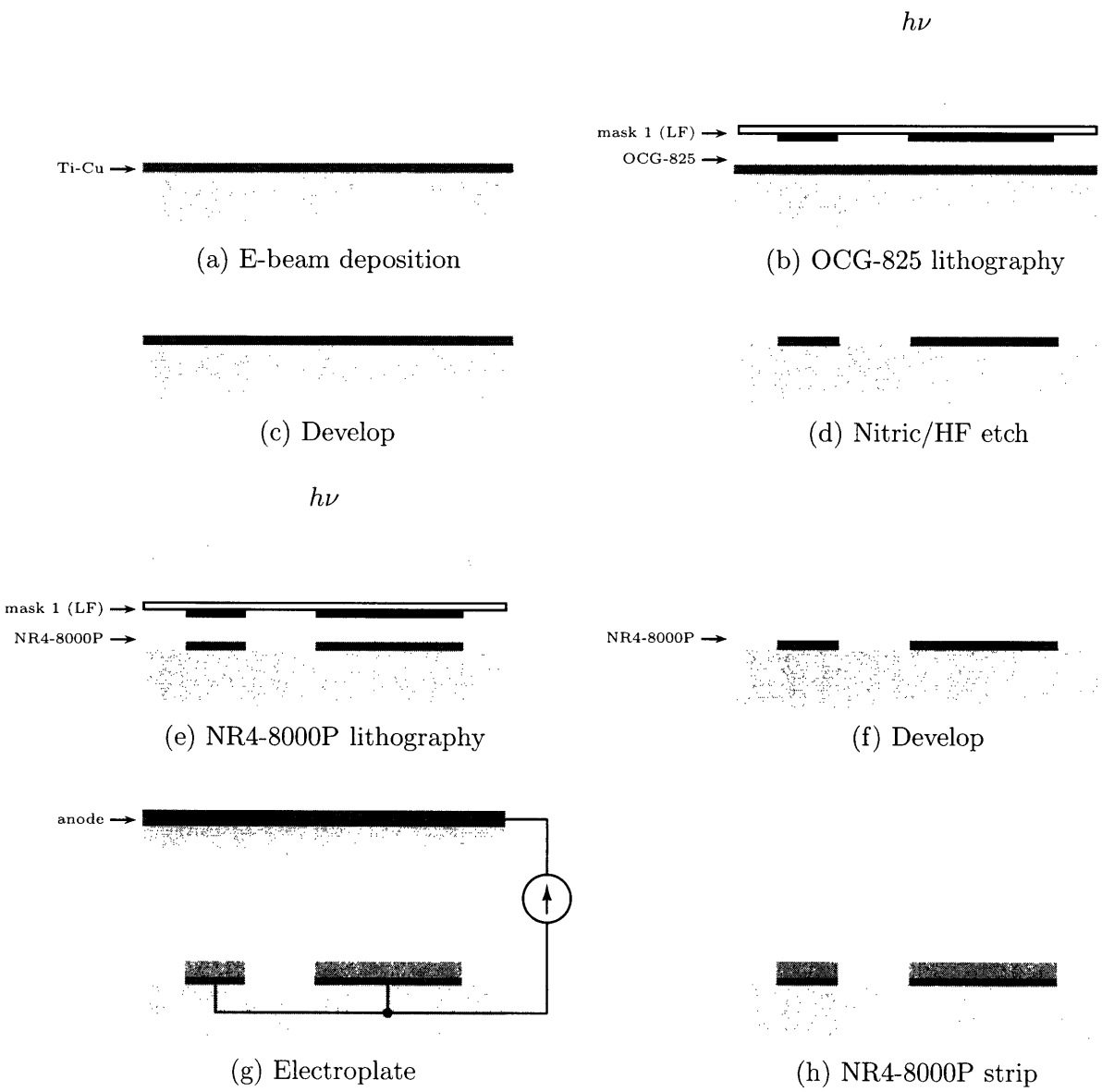

Figure 5.10: **Electroformation process with etched seed layer**

IPR2024-00706 EX. 2005

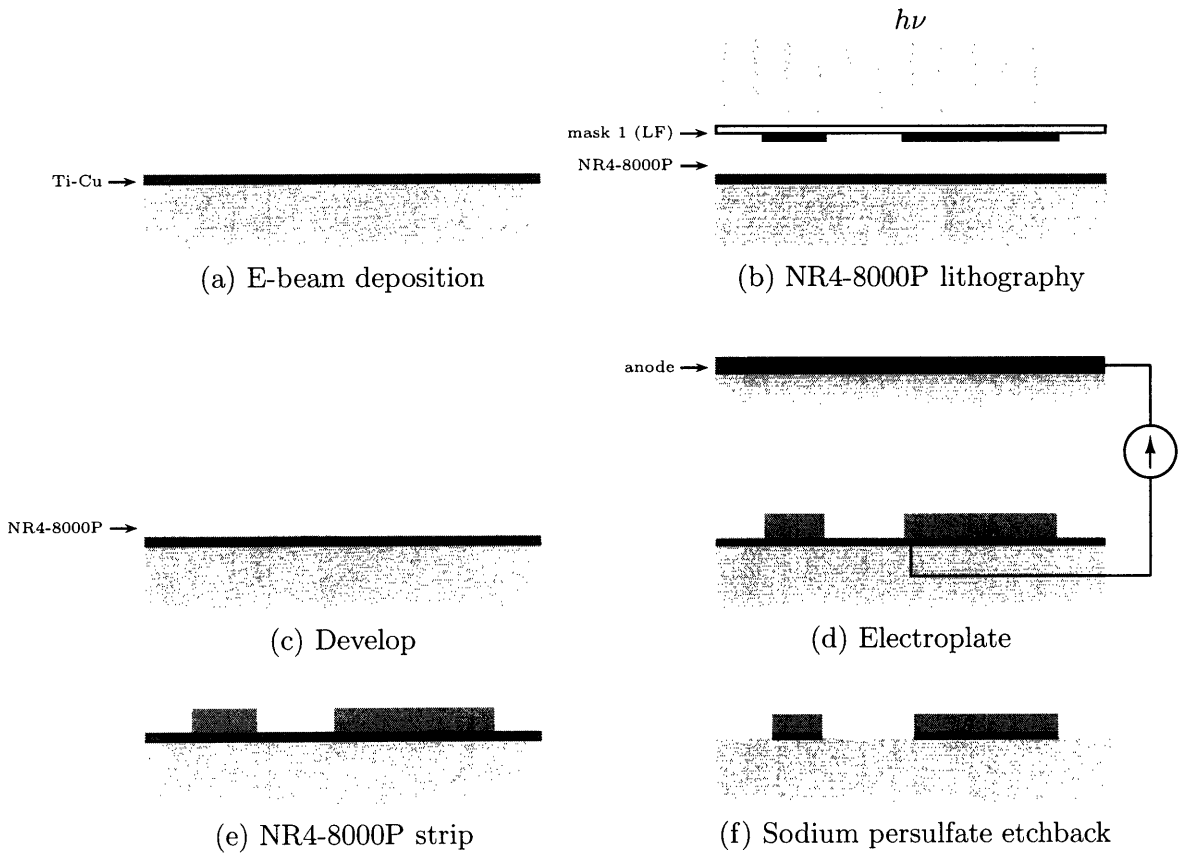

Figure 5.11: **Electroformation process with etchback**

IPR2024-00706 EX. 2005

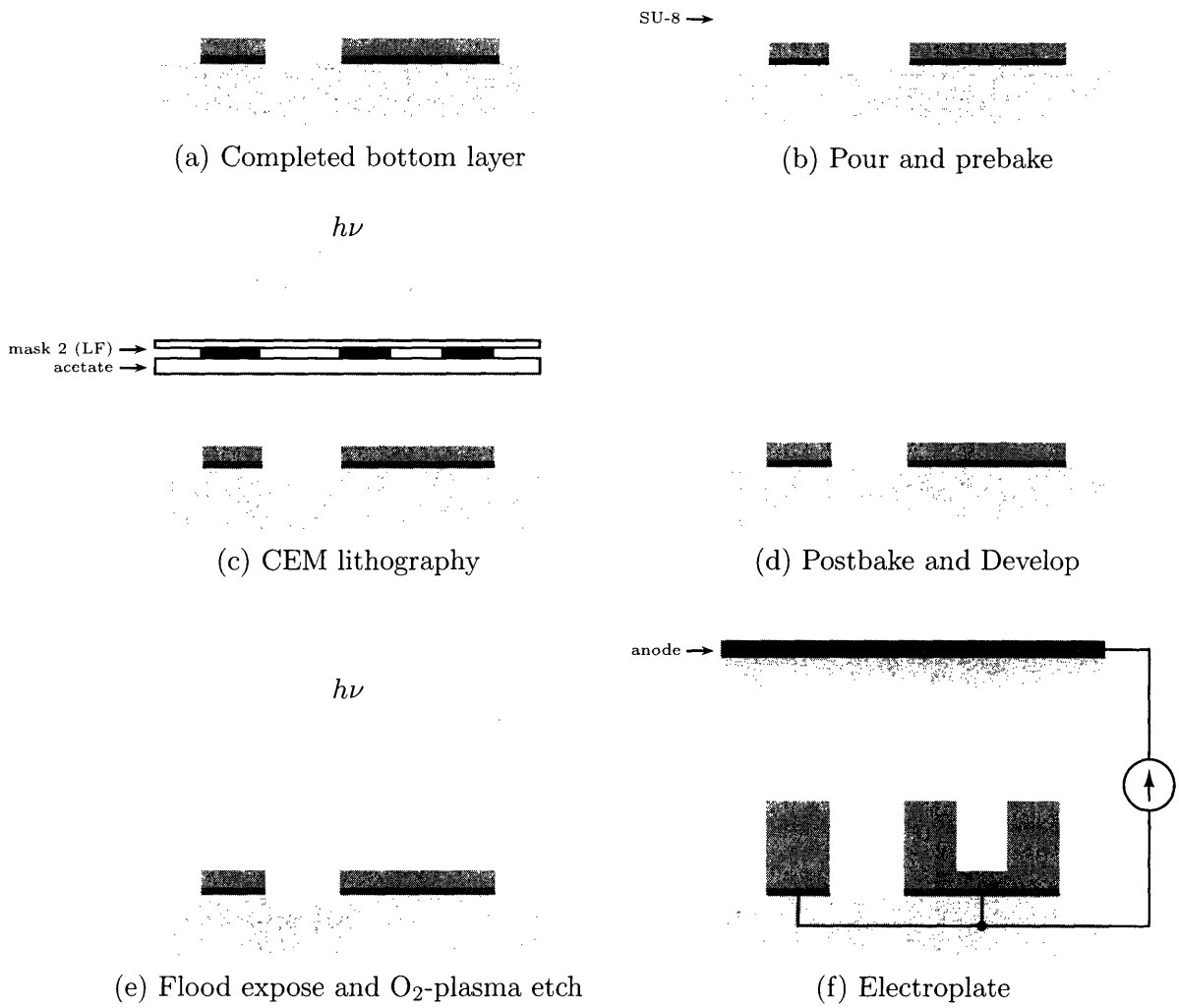

(a) Completed bottom layer

(b) Pour and prebake

(c) CEM lithography

(d) Postbake and Develop

(e) Flood expose and O_2-plasma etch

(f) Electroplate

Figure 5.12: **SU-8 process**

IPR2024-00706 EX. 2005

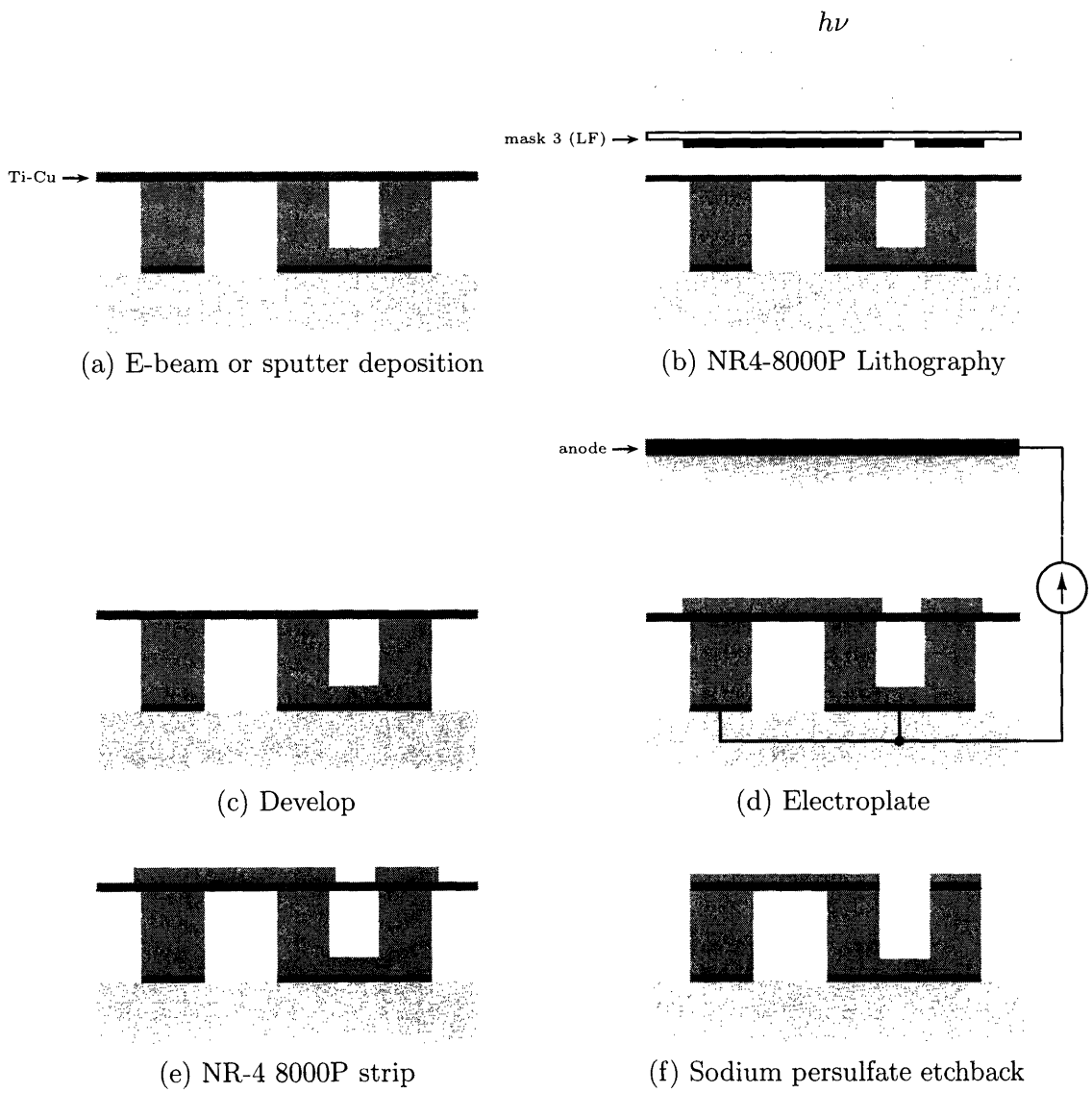

(a) E-beam or sputter deposition

(b) NR4-8000P Lithography

(c) Develop

(d) Electroplate

(e) NR-4 8000P strip

(f) Sodium persulfate etchback

Figure 5.13: **Top-layer interconnects**

IPR2024-00706 EX. 2005

per) is first evaporated as shown in Fig. 5.10a. The deposited titanium is important for adhesion of overlying films, and should not be *less* than 150 Å thick, though a thicker film is acceptable. Seed-layer lithography uses OCG-825-20 positive resist[8] at 2 μm thickness, prepared according to the manufacturer's directions. With no hardbake, this resist film will stand up to an Ti-Cu acid etch (Fig. 5.10d) of 60% DI water, 45% nitric acid, and 5% HF. After resist strip and drying, negative-tone lithography with a plating resist (Futurrex NR4-8000P[9]) and the same mask as above defines an electroforming mold with walls at the edges of the seed-layer pattern. Optimized processing steps for 20, 50, and 100 μm are provided by Futurrex for NR4-8000P, and a thickness can be selected based on the desired build of electroformed copper in subsequent steps (see Appendix C for further details). For quick alignment during experimentation with Pyrex substrates, the plating resist can be polymerized with back-side exposure, in which the Ti-Cu seed acts as a mask (the wafer chuck is protected with a with a sheet of acetate, in this case). Electrode current for mask 1 of Appendix C was 600 mA for 2.85×10^{-3} m^2 laid-out area, corresponding to 19.2 ASF and a 1 hour plating time for 27 μm copper build. The bottom copper layer routinely delaminated from the substrate around this plated thickness, remaining intact only in the region around the cathode contact.

By analogy to PCB manufacture [53], it would be simpler to electroform over an unpatterned seed (as shown in Fig. 5.11) and etch back seed and electroformed copper to leave the desired pattern intact. Gentle oxidizing agents like sodium persulfate and ferric chloride can remove seed copper in this case, but leave many small islands of titanium unetched after 20 or 30 minutes of activity. At this point, because of the higher etch rate for copper, thicker electroformed features can begin to etch away. Etch-back with dilute nitric acid, though faster, is likewise difficult to control because of the faster oxidation of copper. The imperfectly etched titanium does not short adjacent traces, but is an uncontrolled factor affecting adhesion of subsequent layers. The two-exposure method of Fig. 5.10 is therefore favored over the etch-back technique.

The thick-build mid-layer process is depicted schematically in Fig. 5.12, and defines the magnetic thickness dimension on the toroids of Fig. 5.3. This stage is a repetition of the electroformation process of the bottom layer, in which the ends of the radial toroid traces

[8]produced by Arch Chemicals, Norwalk, Connecticut; formerly Olin Microelectronic Materials, itself formerly Olin Ciba Geigy (OCG).

[9]Futurrex, Inc., Franklin, New Jersey

IPR2024-00706 EX. 2005

acts as seed layers for the posts which define the edges of toroid turns. For the mask set of Appendix C, 6 mL of SU-8 2005 was metered by pipette onto the wafer with the methods of Section 5.2.1.1, corresponding to 500 μm SU-8 thickness. After the prebake detailed in Fig. 5.5, the SU-8 was exposed with contrast-enhancement lithography (Section 5.2.1.2) with a dose of 3.18 J/cm^2 measured at 365 nm. After rinse, development, and ashing (see Fig. 5.7 and Section 5.2.1.3) high build posts were electroformed in a long plating step. Electrode current corresponding to the well areas defined by mask 2 of Appendix C was 125 mA for 6.36×10^{-4} m^2 total plating area, corresponding to 18.2 ASF and 19 hours plating time for 496 μm copper build.

After e-beam deposition of a second 4000 Å Ti-Cu seed, as shown in the top-level process of Fig. 5.13, crossbars are electroformed in a developed regions of 20 μm NR4-8000P. Unlike SU-8 — which is notoriously resistant to solvents, acids and bases — hard-baked NR4-8000P is readily removed by Futurrex remover RR4 (Fig. 5.13e). After stripping, a slow etch-back step in 0.5 M sodium persulfate clears unplated seed regions in several minutes (Fig. 5.13f), leaving plated copper dimensions nearly unchanged. Such a plate and etch-back step was necessary to improve metal step coverage over well edges; the NR4-8000P was never required, as an etch resist would be, to cover steps in order to protect underlying metal.

5.5 Results

The measured impedance magnitude of best-performing plated toroid, tapped with three 15 pF mica capacitors, is shown in Fig. 5.14. The structure had a 10 MHz Q of 9.8 and an inductance of 48 nH at the same frequency. Poor contacts in the top metal layer to the tops of electroformed posts are responsible for the low Q, which could be greatly improved by higher copper builds in the top layer.

Top-layer steps could also be suffering from joint-cracks of the type shown in Fig. 5.15a. Though the geometries are different in the case of protruding corners — cracking at recessed corners is shown in Fig. 5.15a — the cracking in either case could result from stress gradients in deposited copper between regions with low plating-current density and those with high current density. Periodic pulse-reverse plating is employed specifically to minimize

IPR2024-00706 EX. 2005

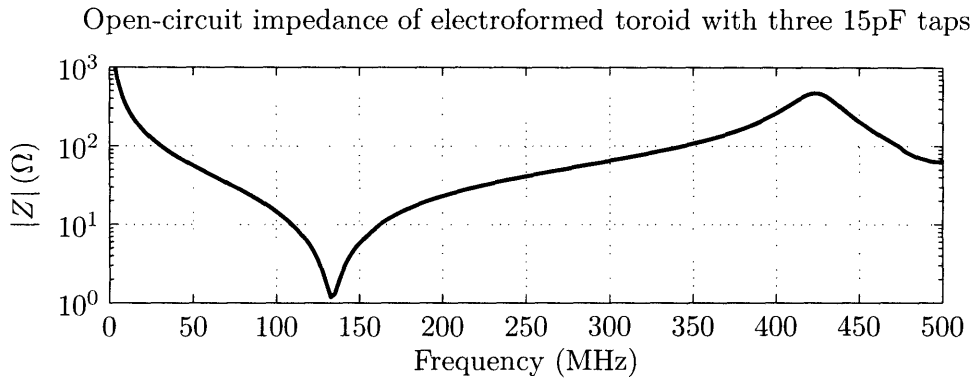

Figure 5.14: **Measured impedance magnitude of a wafer-level toroid. The structure had a 10 MHz Q of 9.8 and an inductance of 48 nH at the same frequency.**

(a) DC plating (b) Periodic pulse reverse plating

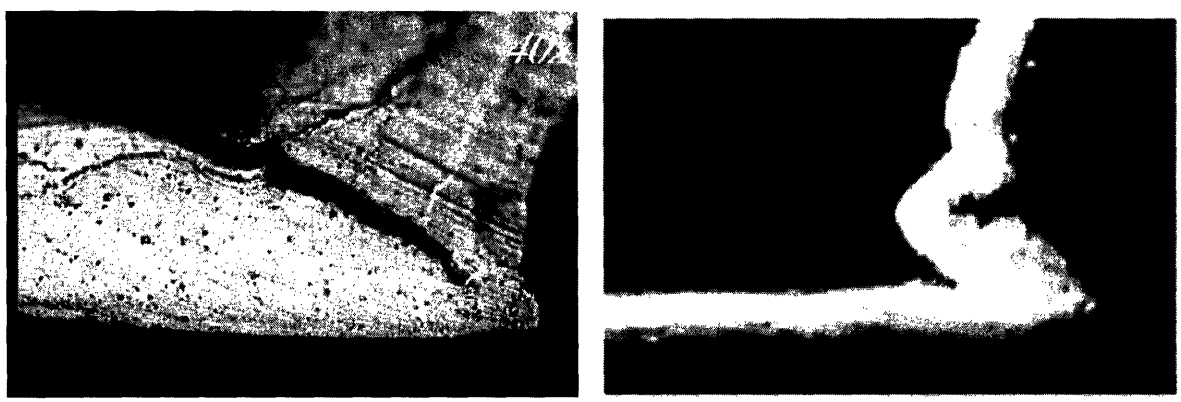

Figure 5.15: **Cracking in recessed corners with DC plating, and no cracking with periodic pulse-reverse plating. The inverter was a Dynatronix model DuPR 10-1-3, set for a 5 ms forward pulse at 0.0188 ASF and a 1 ms reverse pulse at 0.00313 ASF. Photos courtesy of Pádraig Cantillon-Murphy.**

differential stress across the copper surface. Though the Cubath additives are intended for dc systems as low-cost alternatives to pulse reversal, ac plating in the setup of Section 5.3 did remove visible cracking in recessed corners as shown in Fig. 5.15b.

IPR2024-00706 EX. 2005

Chapter 6

Summary and Conclusions

THIS thesis explores techniques for reducing the volume and values of passive components, techniques which are compatible with a shift to HF and VHF switching frequencies, air-core magnetics, and planar magnetic geometries. These techniques can be exploited to realize manufacturing advantages, increase converter efficiency, or increase power density for a roughly constant evolution of heat.

6.1 Thesis summary

Chapter 1 discusses the limits posed by passive elements to miniaturization of power electronics, and introduces a means of decreasing overall passive size by waveform storage or delay. In conventional converters, single-pole or "bulk" reactive elements develop impedances which isolate external circuitry from the switching action of the power stage. Impedance generated in this manner is fundamentally related to energy storage and size. Higher-order systems, whether second-order resonances or delays, take advantage of periodic switching to develop impedance extremes by energy *fidelity*. By storing and internally circulating periodic applied voltages or currents, a higher-order system can develop impedance extremes by decreasing the instantaneous work delivered through its terminals.

Chapter 2 considers second-order electrical networks and transmission lines as storage elements in the sense of Chapter 1. Foundations for later chapters are introduced here, including several lumped realizations of transmission-line impedances, and methods for comparing the size and critical-frequency alignment of such networks. The importance of frequency alignment of poles and zeros is considered with respect to waveform symmetries, symmetries which enable the soft-switching converter operation discussed in Chapter 4.

IPR2024-00706 EX. 2005

Chapter 3 treats in detail the critical-frequency alignment of a family of transmission-line analogs formed by tapping a planar inductor along its length with capacitors. Analytic and synthetic means of designing such structures are considered, corresponding to iterated networks and ladder structures with individually selected inductors and capacitors. For the iterated networks — the first type of artificial line — a relation between the critical frequencies of cascaded LC sections and the roots of Fibonacci polynomials is presented. This result is an analytic means of treating the transition between a distributed line and its lumped analogs, and appears to be new in the literature. The second type of line-simulating network, one with non-uniform placement of capacitive taps, is also treated in detail. These networks approximate the L and C values — computed by Cauer synthesis — for a *specified* driving-point reactance. Planar realizations of lumped-line inductances are explored, along with means of compensating for the mutual inductances introduced by this compact method of construction. The impedances of the different types of approximating networks are confirmed by experiment, and perturbations to the lumped analysis are considered, whether from distributed ground-shield capacitance or from end-to-end magnetic coupling in a toroid.

Chapter 4 applies the results of previous chapters to the design of a new, soft-switching RF inverter topology (the Class Φ) chosen to show the dramatic reduction in passive-component size possible with multi-resonant elements. The Class Φ is compared to the Class E inverter in an application taken from a cellular RF dc-to-dc converter topology. The natural soft-switching, square-wave action of the Class Φ contrasts favorably to the large peak stresses of the Class E. The Class Φ topology moreover replaces a large bulk inductance in the Class E with a much smaller value, and is superior from the standpoint of miniaturization and manufacturability.

Chapter 5 details a means of constructing planar multi-resonant structures at smaller scales than the experimental structures of Chapter 3. In an additive, low-temperature molding process compatible with batch-fabrication techniques, three layers of copper are electrodeposited to form a toroid in the thickness of a photo-imageable epoxy film. The scales and material compatibilities of this process make it a candidate for parallelizable manufacture of multi-resonant structures at a wafer or package level.

IPR2024-00706 EX. 2005

6.2 Thesis conclusions

Memory- or delay-based power electronics in general, and multi-resonant components in particular, are an effective means of reducing the values and bulk of passive components required to implement a power-conversion function. Multi-resonant passive networks enforce converter waveform symmetries that can be exploited to increase efficiency or output power with smaller reactive-component values, as seen in comparisons between the Class Φ and Class E inverters. By exploiting rather than fighting the parasitics which bound converter switching frequencies, transmission-line analogs encourage a shift to higher frequencies and nonpermeable cores. Air-core multi-resonant networks are moreover amenable to planar manufacturing methods, and have well-characterized impedance and critical frequencies. Iteration of network sections and Cauer synthesis can be used to design networks with pole-zero frequencies sufficiently coincident with switching harmonics to enforce square-wave symmetries in practice. Cauer synthesis and quasistatic inductance-matrix extraction, in particular, are precise enough to compensate for the frequency perturbations that arise from electrical parasitics and shielding. As a proximate goal, the components, converters, and manufacturing techniques presented in this thesis provide a viable means for *printing* all converter passives elements, including those normally considered too large for construction with laminate techniques. The Class Φ inverter is especially advantageous in this regard, as it contains no reactive blocking elements.

6.3 Future work

If the effort can be justified for a particular converter, iteration of the Cauer-synthesis and condensation method (see Sections 3.4.2 and 3.4.4.2) could lead to a completely embedded, shielded, line-simulating network in a single laminate layup. Successively designed experiments, complemented by full-field modelling, could accommodate distributed shield capacitance within a lumped framework to yield a compact multi-resonant structure. This process has already been attempted with more *ad hoc* layout choices, and viable designs with complete shielding — and no peculiarities such as pole or zero splitting — are known to exist. A second degree of freedom in the magnetics design, e.g., variable packing or variable width of turns, could provide the designer with a finely graduated selection of inductances

IPR2024-00706 EX. 2005

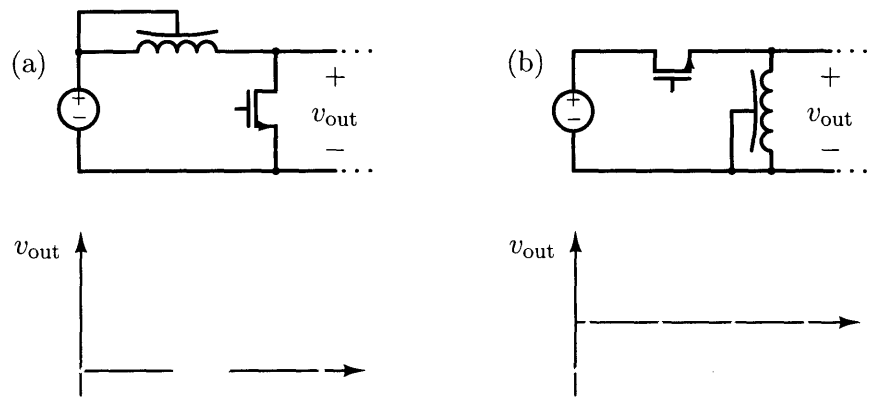

Figure 6.1: **Inverter networks with natural square-wave symmetries which incorporate multi-resonant networks (the inductors with proximate capacitor plate). These stages can form the core of several power converter topologies.**

with which to realize the Cauer-derived values. Because a detailed model of a particular inductance matrix would be required for this approach, the techniques outlined in Fig. 4.15 should be considered to increase efficiency or operating frequency.

The fabrication methods of Chapter 5 could be improved by a broader consideration materials and construction techniques. Epoxy-based electroformation, in the first place, should be considered alongside more conventional means of package assembly, including stamping and lead-frame assembly of the desired magnetic geometries. Magnetic materials — high-frequency ferrite composites, in particular — could be incorporated within laminar structures in two ways. Within the core of a planar toroid, permeable materials might alter the leakage inductances critical for transmission-line behavior, but could increase magnetic coupling between windings in multi-resonant transformers (see below). Thin ferrite layers *above* and *below* an air-core structure, in conjunction with conductive planes, could provide the low-loss shielding necessary for practical applications.

Beyond the Class E design considered in Chapter 4, many power-converter and amplifier topologies could benefit from reduced-value passive elements and the incorporation of multi-resonant structures. Indirect and direct switching cells with transmission elements, as depicted in Fig. 6.2, are inverter stages with natural square-wave symmetries, and form the core of many new converter topologies. Power amplifiers can also incorporate line-simulating networks in their inverter networks (as in the Class Φ) or in load networks. The Class F amplifier depicted in Fig. 6.3, for instance, often employs Foster reactance

IPR2024-00706 EX. 2005

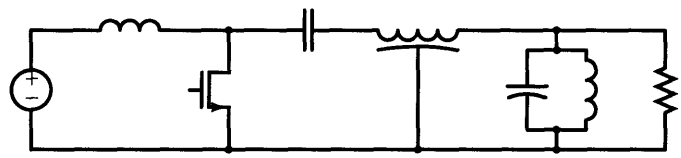

Figure 6.2: **Multi-resonant structures can be incorporated in load networks, as exemplified by the Class F power amplifier.**

networks to reduce the voltage stress on the switch (i.e., by developing impedance peaks at odd harmonics of a switching fundamental for square-wave symmetry at the drain, as in Fig. 4.5b). An integrated multi-resonant network could realize the desired impedance characteristic in a single structure with excellent tolerance.

Transformer windings, just like uncoupled self-inductances, can also impose symmetries on their terminal waveforms. Consider, for example, the push-pull converter of Fig. 6.3a, in which two switches are used to generate an ac square-wave output on the transformer secondary. Replacing the center-tapped transformer with a multi-resonant transformer having the appropriate dynamics allows one switch and a primary winding to be eliminated, as suggested by Fig. 6.3b. The natural modes of energy storage in the magnetizing impedance can ring magnetizing currents into the core that are a half-wave replica of those imposed by the switch. Note that the rectifier load is not necessary for application of such an isolated inverter stage; RF amplifiers, in particular, could benefit from the higher magnetizing impedance at discrete frequencies provided by a multi-resonant primary. Though the magnetics design for this case is more complicated than that of a tapped inductor — perhaps requiring permeable core material to transfer appreciable power — the analysis is probably tractable on the lumped basis of Chapter 3..

IPR2024-00706 EX. 2005

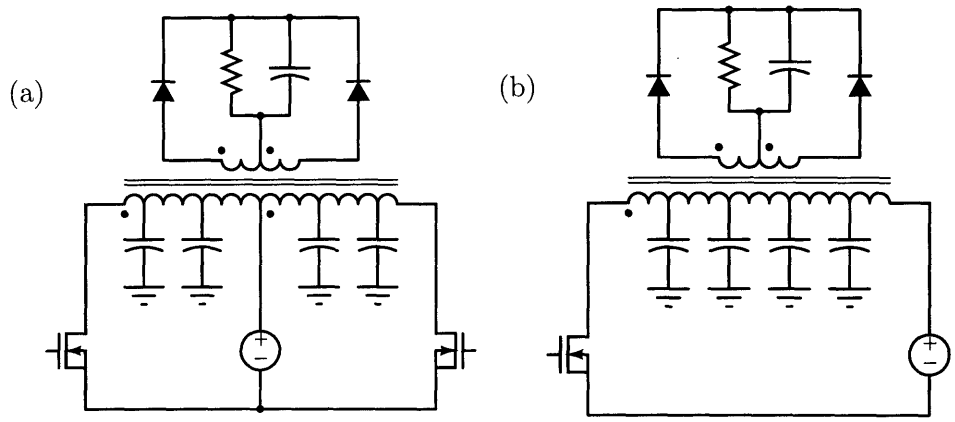

Figure 6.3: **A voltage-fed push-pull converter, illustrating an application of multi-resonant magnetizing reactance.**

Appendix A

Layout scripts

A.1 Eagle scripts

```
function [terminald,terminali,terminalo,outertapr]=eagletoroid(cx,cy,diameter,turns,taps,instructions,extensions,tapcaps,tapa

global eagle
global centerx
global centery
global viadiameter
global dds
global sss
global neck
global shieldside                                                    10
global shieldhole

fprintf(eagle,'Set Wire_Bend 2;\n');
fprintf(eagle,'\nChange Drill 24;\n');

extensionlength=361;
extensionwidth=20;
Cprime=202e-12/(1456*985-305*500);
Cprime=100e-12/getsinglecaparea(100e-12);
                                                                     20
polylinewidth1=viadiameter;
polylinewidth2=viadiameter; %polygon-side width for major radial traces and taps
extensions=extensions+polylinewidth2;

% Making the global copy below allows us to pass the centerpoint as an
% argument in the top-level call, but pass the centerpoint implicitly
% to underlying functions. We get a warning if we try to make the
% actual argument variables (cx and cy) global.
centerx=cx;
```


IPR2024-00706 EX. 2005

```
centery=cy;
id=250;

outertapr=0;
alpha=2*pi/(turns);
beta=pi/4-alpha/2;
gamma=pi/2-beta;

xbest=(neck/2+sss+viadiameter/2+dds*sin(gamma-alpha))/sin(alpha)-viadiameter/2;
id=2*(xbest*(sin(alpha)+tan(beta)*cos(alpha))/tan(beta)-sss/sin(beta)-dds/sqrt(2)-2*dds/sqrt(2)/tan(beta));

d2=sss/sin(beta);
d1=id/2+dds/sqrt(2)+2*dds/sqrt(2)/tan(beta);
d6=id/2+dds/sqrt(2)+dds/sqrt(2)/tan(beta);
x=tan(beta)*(d1+d2)/(sin(alpha)+tan(beta)*cos(alpha));
inr=d6+2*viadiameter;
outervias=floor(diameter/2*alpha/1.1/viadiameter);
outerviatheta=linspace(-(diameter/2*alpha/2-viadiameter/2-sss/2)*2/diameter,(diameter/2*alpha/2-viadiameter/2-sss/
outerviax=diameter/2*cos(outerviatheta);
outerviay=diameter/2*sin(outerviatheta);
inrtheta=(inr*alpha/2-viadiameter/2-sss/2)/inr;
inx=inr*cos(inrtheta);
iny=inr*sin(inrtheta);
xi=atan(diameter/2*sin(alpha)/(diameter/2-inr));
tapnodes=[];

turn=0;
tapindex=1;
stopflag=0;

for a=0:360/(turns/2):359,

 turn=turn+1;
 inlayer=0;

 if turn>turns-tickleturns-1
  fprintf(eagle,'\nLayer Top;\n');
  stopflag=1;
 else
  if findstr(instructions,'top')
   fprintf(eagle,'\nLayer Route2;\n');
   inlayer=1;
```


IPR2024-00706 EX. 2005

```
 else
  fprintf(eagle,'\nLayer Top;\n');
 end
end

% vias at input turn
if turn==turns-gapturns+1
 for i=1:length(outerviax),
  viaroteagle(a,outerviax(i),outerviay(i));
 end
 fprintf(eagle,'\nLayer Top;\n');
 wirerot(a,polylinewidth2,[outerviax],[outerviay]);
 fprintf(eagle,'\nLayer Bottom;\n');
 wirerot(a,polylinewidth2,[outerviax],[outerviay]);
 fprintf(eagle,'\nLayer Route2;\n');
 wirerot(a,polylinewidth2,[outerviax],[outerviay]);
 fprintf(eagle,'\nLayer Route15;\n');
 wirerot(a,polylinewidth2,[outerviax],[outerviay]);
 if inlayer>0
  fprintf(eagle,'\nLayer Route2;\n');
 else
  fprintf(eagle,'\nLayer Top;\n');
 end
end

%---------
if turn<turns-gapturns+1|turn>turns-tickleturns
 viaroteagle(a,id/2,0);
 viaroteagle(a,id/2+dds/sqrt(2),dds/sqrt(2));
 viaroteagle(a,id/2+dds/sqrt(2),-dds/sqrt(2));

 if turn>1|findstr('standalone',instructions)
  for i=1:length(outerviax),
   viaroteagle(a,outerviax(i),outerviay(i));
  end
 end
 fprintf(eagle,'\nLayer Top;\n');
 wirerot(a,polylinewidth2,[outerviax],[outerviay]);
 wirerot(a,polylinewidth1,[id/2+dds/sqrt(2) id/2 id/2+dds/sqrt(2)],[dds/sqrt(2) 0 -dds/sqrt(2)]);
 fprintf(eagle,'\nLayer Bottom;\n');
 wirerot(a,polylinewidth2,[outerviax],[outerviay]);
 wirerot(a,polylinewidth1,[id/2+dds/sqrt(2) id/2 id/2+dds/sqrt(2)],[dds/sqrt(2) 0 -dds/sqrt(2)]);
```


IPR2024-00706 EX. 2005

```
 fprintf(eagle,'\nLayer Route2;\n');
 wirerot(a,polylinewidth2,[outerviax],[outerviay]);
 wirerot(a,polylinewidth1,[id/2+dds/sqrt(2) id/2 id/2+dds/sqrt(2)],[dds/sqrt(2) 0 -dds/sqrt(2)]);
 fprintf(eagle,'\nLayer Route15;\n');
 wirerot(a,polylinewidth2,[outerviax],[outerviay]);
 wirerot(a,polylinewidth1,[id/2+dds/sqrt(2) id/2 id/2+dds/sqrt(2)],[dds/sqrt(2) 0 -dds/sqrt(2)]);
 if inlayer>0
  fprintf(eagle,'\nLayer Route2;\n');
 else
  fprintf(eagle,'\nLayer Top;\n');
 end
end
%----------

if findstr(instructions,'top'),

%------
 if turn<turns-gapturns+1|turn>turns-tickleturns;
  if stopflag==1
   fprintf(eagle,'\nLayer tStop;\n');
   wirerot(a,viadiameter*2,[d6 d6+viadiameter],[0 0])
   polyrot('1',a,polylinewidth1*2,[id/2 id/2+viadiameter/sqrt(2) d6 id/2+viadiameter/sqrt(2)],[0 viadiameter/sqrt(2) 0 -
   polyrot('1',a,polylinewidth1*2,[d6+viadiameter inx inx],[0 iny -iny]);
   polyrot('1',a,polylinewidth2*2,[inx inx outerviax],[iny -iny outerviay]);
   fprintf(eagle,'\nLayer Top;\n');
   wirerot(a,viadiameter,[d6 d6+viadiameter],[0 0])
   polyrotisolate('1',a,polylinewidth1,[id/2 id/2+viadiameter/sqrt(2) d6 id/2+viadiameter/sqrt(2)],[0 viadiameter/sqrt(2)
   polyrotisolate('1',a,polylinewidth1,[d6+viadiameter inx inx],[0 iny -iny]);
   polyrotisolate('1',a,polylinewidth2,[inx inx outerviax],[iny -iny outerviay]);
  else
   wirerot(a,viadiameter,[d6 d6+viadiameter],[0 0])
   polyrot('1',a,polylinewidth1,[id/2 id/2+viadiameter/sqrt(2) d6 id/2+viadiameter/sqrt(2)],[0 viadiameter/sqrt(2) 0 -v
   polyrot('1',a,polylinewidth1,[d6+viadiameter inx inx],[0 iny -iny]);
   polyrot('1',a,polylinewidth2,[inx inx outerviax],[iny -iny outerviay]);
   if find(taps==turn),
    wirerot(a,extensionwidth,[diameter/2 diameter/2+extensions(tapindex)],[0 0]);
    r1=diameter/2+extensions(tapindex)-polylinewidth2/2;
    r2=sqrt(2/taparc(tapindex)*tapcaps(tapindex)/Cprime+r1*r1)-polylinewidth2/2;
    if outertapr==0
     outertapr=r2;
    end
    r1=r1+polylinewidth2/2; % compensate for line thickness
```


IPR2024-00706 EX. 2005

```
    th=(taparc(tapindex)*mean([r2 r1])-polylinewidth2)/mean([r2 r1]);
    %th=taparc(tapindex);
    thv=linspace(-th/2,th/2,5);
    polyrot('1',a,polylinewidth1,[cos(thv)*r1 cos(thv)*r2],[sin(thv)*r1 sin(fliplr(thv))*r2]);
    tapindex=tapindex+1;
   end
  end

 end
%---------
end

turn=turn+1;

%vias at input turn
if turn==turns-gapturns+1
 for i=1:length(outerviax),
  viaroteagle(alpha*180/pi+a,outerviax(i),outerviay(i));
 end
 fprintf(eagle,'\nLayer Top;\n');
 wirerot(a,polylinewidth2,[outerviax],[outerviay]);
 fprintf(eagle,'\nLayer Bottom;\n');
 wirerot(a,polylinewidth2,[outerviax],[outerviay]);
 fprintf(eagle,'\nLayer Route2;\n');
 wirerot(a,polylinewidth2,[outerviax],[outerviay]);
 fprintf(eagle,'\nLayer Route15;\n');
 wirerot(a,polylinewidth2,[outerviax],[outerviay]);
 if inlayer>0
  fprintf(eagle,'\nLayer Route2;\n');
 else
  fprintf(eagle,'\nLayer Top;\n');
 end
end


%---------
if turn<turns-gapturns+1|turn>turns-tickleturns;

 for i=1:length(outerviax),
   viaroteagle(alpha*180/pi+a,outerviax(i),outerviay(i));
 end
```


IPR2024-00706 EX. 2005

```
 viaroteagle(alpha*180/pi+a,x+viadiameter/2,0)
 viaroteagle(alpha*180/pi+a,x+viadiameter/2+cos(gamma)*dds,sin(gamma)*dds);
 viaroteagle(alpha*180/pi+a,x+viadiameter/2+cos(gamma)*dds,-sin(gamma)*dds);

 fprintf(eagle,'\nLayer Top;\n');
 wirerot(a+alpha*180/pi,polylinewidth2,[outerviax],[outerviay]);
 wirerot(a+alpha*180/pi,polylinewidth1,[x+viadiameter/2+cos(gamma)*dds x+viadiameter/2 x+viadiameter/2+cos(gam
 fprintf(eagle,'\nLayer Bottom;\n');
 wirerot(a+alpha*180/pi,polylinewidth2,[outerviax],[outerviay]);
 wirerot(a+alpha*180/pi,polylinewidth1,[x+viadiameter/2+cos(gamma)*dds x+viadiameter/2 x+viadiameter/2+cos(gam
 fprintf(eagle,'\nLayer Route2;\n');
 wirerot(a+alpha*180/pi,polylinewidth2,[outerviax],[outerviay]);
 wirerot(a+alpha*180/pi,polylinewidth1,[x+viadiameter/2+cos(gamma)*dds x+viadiameter/2 x+viadiameter/2+cos(gam
 fprintf(eagle,'\nLayer Route15;\n');
 wirerot(a+alpha*180/pi,polylinewidth2,[outerviax],[outerviay]);
 wirerot(a+alpha*180/pi,polylinewidth1,[x+viadiameter/2+cos(gamma)*dds x+viadiameter/2 x+viadiameter/2+cos(gam
 if inlayer>0
  fprintf(eagle,'\nLayer Route2;\n');
 else
  fprintf(eagle,'\nLayer Route2;\n');
 end
end
%---------

if findstr(instructions,'top'),

%-------
 if turn<turns-gapturns+1|turn>turns-tickleturns
  if stopflag==1
   fprintf(eagle,'\nLayer tStop;\n');
    polyrot('1',alpha*180/pi+a,polylinewidth1*2,[x+viadiameter/2 x+viadiameter/2+cos(gamma)*dds inx inx x+viadian
    polyrot('1',alpha*180/pi+a,polylinewidth2*2,[inx inx outerviax],[iny -iny outerviay]);
   fprintf(eagle,'\nLayer Top;\n');
   polyrotisolate('1',alpha*180/pi+a,polylinewidth1,[x+viadiameter/2 x+viadiameter/2+cos(gamma)*dds inx inx x+viad
   polyrotisolate('1',alpha*180/pi+a,polylinewidth2,[inx inx outerviax],[iny -iny outerviay]);
  else
   polyrot('1',alpha*180/pi+a,polylinewidth1,[x+viadiameter/2 x+viadiameter/2+cos(gamma)*dds inx inx x+viadiamete
   polyrot('1',alpha*180/pi+a,polylinewidth2,[inx inx outerviax],[iny -iny outerviay]);

   if find(taps==turn),
    wirerot(a+alpha*180/pi,extensionwidth,[diameter/2 diameter/2+extensions(tapindex)],[0 0]);
    r1=diameter/2+extensions(tapindex)-polylinewidth2/2;
```


IPR2024-00706 EX. 2005

```
    r2=sqrt(2/taparc(tapindex)*tapcaps(tapindex)/Cprime+r1*r1)-polylinewidth2/2;
    if outertapr==0
     outertapr=r2;
    end
    r1=r1+polylinewidth2/2; % compensate for line thickness
    th=(taparc(tapindex)*mean([r2 r1])-polylinewidth2)/mean([r2 r1]);
    %th=taparc(tapindex);
    thv=linspace(-th/2,th/2,5);
    polyrot('1',a+alpha*180/pi,polylinewidth1,[cos(thv)*r1 cos(thv)*r2],[sin(thv)*r1 sin(fliplr(thv))*r2]);
    tapindex=tapindex+1;
   end
  end
 end
%--------
end

turn=turn-1;


if turn>turns-tickleturns-1
 fprintf(eagle,'\nLayer Bottom;\n');
 stopflag=1;
else
 if findstr(instructions,'bottom')
  fprintf(eagle,'\nLayer Route15;\n');
 else
  fprintf(eagle,'\nLayer Bottom;\n');
 end
end


%--------
if turn<turns-gapturns+1|turn>turns-tickleturns
  if stopflag==1
   fprintf(eagle,'\nLayer bStop;\n');
    wirerot(a,polylinewidth2*2,outerviax,outerviay);
    wirerot(a,polylinewidth1*2,[id/2+dds/sqrt(2) id/2 id/2+dds/sqrt(2)],[dds/sqrt(2) 0 -dds/sqrt(2)]);
   fprintf(eagle,'\nLayer Bottom;\n');
  end
  wirerot(a,polylinewidth2,outerviax,outerviay);
  wirerot(a,polylinewidth1,[id/2+dds/sqrt(2) id/2 id/2+dds/sqrt(2)],[dds/sqrt(2) 0 -dds/sqrt(2)]);
end
```


IPR2024-00706 EX. 2005

```
%————————

 if findstr(instructions,'bottom'),

%————————
  if turn<turns−gapturns+1|turn>turns−tickleturns
   if stopflag==1
    fprintf(eagle,'\nLayer bStop;\n');                                                    290
    polyrot('1',a,polylinewidth1*2,[id/2 id/2+viadiameter/sqrt(2) d6 id/2+viadiameter/sqrt(2)],[0 viadiameter/sqrt(2) 0 -
    polyrot('1',a,polylinewidth1*2,[d6+viadiameter inx inx],[0 iny −iny]);
    wirerot(a,viadiameter*2,[d6 d6+viadiameter],[0 0])
    ar=alpha;
    rotated=[cos(ar) −sin(ar);sin(ar) cos(ar)]*[outerviax;outerviay];
    xr=rotated(1,:);
    yr=rotated(2,:);
    polyrot('1',a,polylinewidth2*2,[inx inx xr],[iny −iny yr]);
    fprintf(eagle,'\nLayer Bottom;\n');
    polyrotisolate('1',a,polylinewidth1,[id/2 id/2+viadiameter/sqrt(2) d6 id/2+viadiameter/sqrt(2)],[0 viadiameter/sqrt(2)
    polyrotisolate('1',a,polylinewidth1,[d6+viadiameter inx inx],[0 iny −iny]);
    wirerot(a,viadiameter,[d6 d6+viadiameter],[0 0])
    polyrotisolate('1',a,polylinewidth2,[inx inx xr],[iny −iny yr]);
   else
    polyrot('1',a,polylinewidth1,[id/2 id/2+viadiameter/sqrt(2) d6 id/2+viadiameter/sqrt(2)],[0 viadiameter/sqrt(2) 0 −v
    polyrot('1',a,polylinewidth1,[d6+viadiameter inx inx],[0 iny −iny]);
    wirerot(a,viadiameter,[d6 d6+viadiameter],[0 0])
    ar=alpha;
    rotated=[cos(ar) −sin(ar);sin(ar) cos(ar)]*[outerviax;outerviay];
    xr=rotated(1,:);                                                                      310
    yr=rotated(2,:);
    polyrot('1',a,polylinewidth2,[inx inx xr],[iny −iny yr]);
   end
  end
%————————
 end
 turn=turn+1;

%————————
  if turn<turns−gapturns+1|turn>turns−tickleturns                                         320
   if stopflag==1
    fprintf(eagle,'\nLayer bStop;\n');
     wirerot(a+alpha*180/pi,polylinewidth2*2,outerviax,outerviay);
```


IPR2024-00706 EX. 2005

```
    wirerot(a+alpha*180/pi,polylinewidth1*2,[x+viadiameter/2+cos(gamma)*dds x+viadiameter/2 x+viadiameter/2+cos(
   fprintf(eagle,'\nLayer Bottom;\n');
  end
  wirerot(a+alpha*180/pi,polylinewidth2,outerviax,outerviay);
  wirerot(a+alpha*180/pi,polylinewidth1,[x+viadiameter/2+cos(gamma)*dds x+viadiameter/2 x+viadiameter/2+cos(gan
 end
%————————
%————————
 if turn<turns-gapturns+2|turn>turns-tickleturns
  if stopflag==1
   fprintf(eagle,'\nLayer bStop;\n');
    wirerot(a+2*alpha*180/pi,polylinewidth2*2,[outerviax],[outerviay]);
   fprintf(eagle,'\nLayer Bottom;\n');
  end
  wirerot(a+2*alpha*180/pi,polylinewidth2,[outerviax],[outerviay]);
 end
%————————

 if findstr(instructions,'bottom'),

%————————
 if turn<turns-gapturns+1|turn>turns-tickleturns
  if stopflag==1
   fprintf(eagle,'\nLayer bStop;\n');
   polyrot('1',alpha*180/pi+a,polylinewidth2*2,[inx inx xr],[iny -iny yr]);
   polyrot('1',alpha*180/pi+a,polylinewidth1*2,[x+viadiameter/2 x+viadiameter/2+cos(gamma)*dds inx inx x+viadiam
   fprintf(eagle,'\nLayer Bottom;\n');
   polyrotisolate('1',alpha*180/pi+a,polylinewidth2,[inx inx xr],[iny -iny yr]);
   polyrotisolate('1',alpha*180/pi+a,polylinewidth1,[x+viadiameter/2 x+viadiameter/2+cos(gamma)*dds inx inx x+viad
  else
   polyrot('1',alpha*180/pi+a,polylinewidth2,[inx inx xr],[iny -iny yr]);
   polyrot('1',alpha*180/pi+a,polylinewidth1,[x+viadiameter/2 x+viadiameter/2+cos(gamma)*dds inx inx x+viadiamete
  end
 end
%————————
 end

end

if findstr(instructions,'noground')
 if findstr(instructions,'standalone')&findstr(instructions,'top')
```


IPR2024-00706 EX. 2005

```
    fprintf(eagle,'\nLayer Top;\n');
   else
    fprintf(eagle,'\nLayer tRestrict;\n');
   end
   a=0;                                                                    370
   wirerot(a,polylinewidth2,[outerviax],[outerviay]);
   fprintf(eagle,'\nLayer tRestrict;\n');
   for a=(turns-gapturns+1)*360/turns:360/turns:(turns-tickleturns-1)*360/turns,
    wirerot(a,polylinewidth2,[outerviax],[outerviay]);
   end
   fprintf(eagle,'\nLayer bRestrict;\n');
   for a=(turns-gapturns+1)*360/turns:360/turns:(turns-tickleturns-1)*360/turns,
    wirerot(a,polylinewidth2,[outerviax],[outerviay]);
   end
else                                                                       380
   if isempty(findstr(instructions,'top'))
    fprintf(eagle,'\nLayer tRestrict;\n');
    wirerot(a,polylinewidth2,[outerviax],[outerviay]);
    fprintf(eagle,'\nLayer tRestrict;\n');
    for a=(turns-gapturns+1)*360/turns:360/turns:(turns-tickleturns-1)*360/turns,
     wirerot(a,polylinewidth2,[outerviax],[outerviay]);
    end
   end
   if isempty(findstr(instructions,'bottom'))
    fprintf(eagle,'\nLayer bRestrict;\n');                                 390
    for a=(turns-gapturns+1)*360/turns:360/turns:(turns-tickleturns-1)*360/turns,
     wirerot(a,polylinewidth2,[outerviax],[outerviay]);
    end
   end
end

% soldermask stop
halfwidthmrs=shieldside/2;
if outertapr>halfwidthmrs
 halfwidthmrs=outertapr;                                                   400
end
theta=linspace(0,2*pi,turns*4);
px=[];
py=[];
for m=1:length(theta),
 if theta(m)>=0.75*2*pi/turns & theta(m)<(turns-gapturns)*2*pi/turns|findstr('standalone',instructions)
  px=[px cos(theta(m))*(halfwidthmrs+viadiameter)];
```


IPR2024-00706 EX. 2005

```
  py=[py sin(theta(m))*(halfwidthmrs+viadiameter)];
 else
  px=[px cos(theta(m))*(diameter/2+viadiameter)];
  py=[py sin(theta(m))*(diameter/2+viadiameter)];
 end
end
fprintf(eagle,'\nLayer tStop;\n');
polyrot('2',0,polylinewidth1,[px],[py]);
fprintf(eagle,'\nLayer bStop;\n');
polyrot('2',0,polylinewidth1,[px],[py]);

%if findstr('standalone',instructions)
%theta=linspace(0,2*pi,turns*4);
%px=cos(theta)*(diameter/2+viadiameter);
%py=sin(theta)*(diameter/2+viadiameter);
%if isempty(findstr(instructions,'top'))
% fprintf(eagle,'\nLayer tStop;\n');
% polyrot('2',0,polylinewidth1,[px],[py]);
%end
%if isempty(findstr(instructions,'bottom'))
% fprintf(eagle,'\nLayer bStop;\n');
% polyrot('2',0,polylinewidth1,[px],[py]);
%end
%end

a=360/turns;
terminald=terminalrot(0*360/turns,diameter/2,0);
terminali=terminalrot((turns-gapturns)*360/turns,diameter/2,0);
terminalo=terminalrot((turns-tickleturns)*360/turns,diameter/2,0);


if findstr('standalone',instructions)
 outerterminalx=(4*viadiameter+diameter/2)*cos(fliplr(outerviatheta));
 outerterminaly=(4*viadiameter+diameter/2)*sin(fliplr(outerviatheta));
 if findstr('top',instructions)
  fprintf(eagle,'\nLayer Top;\n');
  polyrotisolate('1',0*360/turns,polylinewidth1,[outerviax outerterminalx],[outerviay outerterminaly])
  polyrotisolate('1',(turns-gapturns)*360/turns,polylinewidth1,[outerviax outerterminalx],[outerviay outerterminaly])
  fprintf(eagle,'\nLayer tStop;\n');
  polyrot('1',0*360/turns,polylinewidth1*2,[outerviax outerterminalx],[outerviay outerterminaly])
  polyrot('1',(turns-gapturns)*360/turns,polylinewidth1*2,[outerviax outerterminalx],[outerviay outerterminaly])
 end
```


IPR2024-00706 EX. 2005

```
 if findstr('bottom',instructions)
  fprintf(eagle,'\nLayer Bottom;\n');
   polyrotisolate('1',0*360/turns,polylinewidth1,[outerviax outerterminalx],[outerviay outerterminaly])
   polyrotisolate('1',(turns−gapturns)*360/turns,polylinewidth1,[outerviax outerterminalx],[outerviay outerterminaly])
   fprintf(eagle,'\nLayer bStop;\n');
   polyrot('1',0*360/turns,polylinewidth1*2,[outerviax outerterminalx],[outerviay outerterminaly])
   polyrot('1',(turns−gapturns)*360/turns,polylinewidth1*2,[outerviax outerterminalx],[outerviay outerterminaly])
 end
end

% 6-32 bolt free fit hole
% #25 drill    .1495"
fprintf(eagle,'\nChange Drill %i;\n',shieldhole);
fprintf(eagle,'Via ''GND'' 180 round (%-5.3f %-5.3f);\n',centerx+shieldside/2,centery+shieldside/2);
fprintf(eagle,'Via ''GND'' 350 square (%-5.3f %-5.3f);\n',centerx+shieldside/2,centery-shieldside/2);
fprintf(eagle,'Via ''GND'' 180 round (%-5.3f %-5.3f);\n',centerx-shieldside/2,centery+shieldside/2);
fprintf(eagle,'Via ''GND'' 180 round (%-5.3f %-5.3f);\n',centerx-shieldside/2,centery-shieldside/2);

fprintf(eagle,'\nChange Drill 24;\n');
```

```
% 4-layer PCB
% .062 Laminated Thickness
% Top      2 oz
%          8.613 mil
% Route2   2 oz
%          59 mil
% Route15  2 oz
%          8.613 mil
% Bottom   2 oz

% Finished prepreg thickness.
% 0.063 Laminated Thickness
% Quantity        Prepreg       Thickness
% 1 sheet         2116          0.003813"
% 2 sheets        2116          0.008613"

%     ///////////  H/H, 1/1 Foil ///////////
%              2 Sheets 2116 Prepreg
%     XXXXXXXXXXXXX .059 Core XXXXXXXXXXXXX
%              2 Sheets 2116 Prepreg
%     ///////////  H/H, 1/1 Foil ///////////
```


IPR2024-00706 EX. 2005

```
global eagle
global e0
global er
global erinner
global outerthick
global innerthick
global textlabelheight
global boardx                                                    30
global boardy
global boardz
global viadiameter
global dds          %drill-drill spacing
global sss          %signal-signal spacing
global neck         %smallest constriction in conductor
global shieldside
global shieldhole
global cornx
global corny                                                     40

shieldside=3500;
shieldhole=150;

viadiameter=40;     %mil
dds=viadiameter;
sss=20;
neck=viadiameter;

boardx=18500;     %mil                                           50
boardy=13000;     %mil

outercuthick=2*1.4; %mil
innercuthick=2*1.4;

outerthick=8.613;     %prepreg
innerthick=59; %core
boardz=innerthick;

% er=4.8 for outside layers and 3.5 for inside layers            60
e0=8.85e-12;
er=4.8;
erinner=3.5;
```


IPR2024-00706 EX. 2005

```
textlabelheight=70;

eagle = fopen('final.scr','w');
fprintf(eagle,'# File generated by finalboard.m, %s\n\n',date);
fprintf(eagle,'Grid mil 0.1 off;\nSet Wire_Bend 0;\n');
fprintf(eagle,'\nLayer Dimension;\nWire 0 (0 0) (%i %i) (0 0);\n',boardx,boardy);
%silkbox(0,0,boardx/2,boardy);
fprintf(eagle,'Set Wire_Bend 2;\n');

labelx=boardx-1600;
labely=600;
linespacing=100;
fprintf(eagle,'\nChange Size 70;\n');
fprintf(eagle,'Text ''%s'' (%-5.3f %-5.3f);\n','LEES @ MIT (C) 2004',labelx,labely-0*linespacing);
fprintf(eagle,'Text ''%s'' (%-5.3f %-5.3f);\n','Joshua Phinney',labelx,labely-1*linespacing);
fprintf(eagle,'Text ''%s'' (%-5.3f %-5.3f);\n','Prof. David Perreault',labelx,labely-2*linespacing);
fprintf(eagle,'Text ''%s'' (%-5.3f %-5.3f);\n','March 2004',labelx,labely-3*linespacing);


fprintf(eagle,'Change ISOLATE 20;\n');

% gap=4 designs
% 50 ohm
% tapL= 1.0e-07 * 0.0845 0.0946  0.0944   0.0996   0.1052   0.1079   0.1042
% Cph = 1.0e-10 * 0.2791 0.2846  0.2966   0.3178   0.3546   0.4256   0.6147
% design =  2    3    3    3    4    4    5   10

% 35 ohm
%tapL = 1.0e-08 * 0.4643   0.6406   0.6406   0.6406   0.7119   0.7973   0.8370   0.8309
%Cph = 1.0e-10 * 0.3376   0.3427   0.3536   0.3721   0.4018   0.4514   0.5448   0.7909
%design =  1    2    2    2    2    3    3    4    9

% 20 ohm
%tapL = 1.0e-08 *  0.1809   0.2303   0.2303   0.2303   0.2303   0.2303   0.2460   0.2667   0.1878
%Cph = 1.0e-09 * 0.0575 0.0582  0.0597   0.0621   0.0657   0.0714   0.0806   0.0977   0.1424
% design =  1    2    2    2    2    2    2    3    4    8

% 4-turn gap self inductances
%3.4302e-07 20 ohm
%6.3450e-07 35 ohm
%9.1658e-07 50 ohm
```


IPR2024-00706 EX. 2005

```
%##############################################################################
%##############################################################################
%##############################################################################
%##############################################################################
% LOWEST ROW 50 ohm iterated, 20 ohm cauer, no multires, shield

%-----------------------
mrdiameter=3000;
cornx=850;
corny=650;
fsw=13.56e6;
L=9.1658e-07;
C=1/(16*fsw*fsw*L);
Z0=sqrt(L/C);
[td,ti,to,outertapr]=eagletoroid(cornx+shieldside/2,corny+shieldside/2,mrdiameter,38,2:34,'topnoground',ones(1,34)*0,C/34*
fprintf(eagle,'\nLayer tPlace\n');
fprintf(eagle,'Text ''%s'' (%-5.3f %-5.3f);\n','50l',cornx+shieldhole,corny);
halfwidthmrs=shieldside/2+shieldhole/2+300;
if outertapr>halfwidthmrs
 halfwidthmrs=outertapr;
end
[capx,lengthCl]=loadnetwork(halfwidthmrs);
boardedge=capx+lengthCl+200;
bncsource=inputnetwork(ti,boardedge);
switchlayout(mrdiameter,boardedge,td)
floods(halfwidthmrs,boardedge)

%-----------------------
mrdiameter=2500;
cornx=boardedge+600;
corny=700;
tapL = 1.0e-08 * [ 0.1809  0.2303  0.2303  0.2303  0.2303  0.2303  0.2460  0.2667  0.1878];
Cph = 1.0e-09 * [ 0.0575 0.0582 0.0597  0.0621  0.0657  0.0714  0.0806  0.0977  0.1424];
design = [  1   2   2   2   2   2   2   3   4   8];
taps=cumsum(design);
taps=taps+1;
taps=taps(1:end-1);
tapL=tapL-1e-9;
extensions=tapL*(400/(10.8e-9-1.5e-9)); % linear approximation mils/H
tapangles=19*ones(1,length(Cph));
tapangles(1)=12;
```


IPR2024-00706 EX. 2005

```
tapangles(end-1)=25;
tapangles(end)=35;
tapangles=tapangles*pi/180;
[td,ti,to,outertapr]=eagletoroid(cornx+shieldside/2,corny+shieldside/2,mrdiameter,32,taps,'topbottomnoground',extensions,C
fprintf(eagle,'\nLayer tPlace\n');
fprintf(eagle,'Text ''%s'' (%-5.3f %-5.3f);\n','20C',cornx+shieldhole,corny);
% use last value
halfwidthmrs=halfwidthmrs+150;
%halfwidthmrs=shieldside/2+shieldhole/2;
%if outertapr>halfwidthmrs
% halfwidthmrs=outertapr;
%end
[capx,lengthCl]=loadnetwork(halfwidthmrs);
boardedge=capx+lengthCl;
bncsource=inputnetwork(ti,boardedge);
corny=corny-20;
switchlayout(mrdiameter,boardedge,td)
corny=corny+20;
floods(halfwidthmrs,boardedge)

%-----------------------
% no multiresonant structure: offset in x fools drawing subs
cornx=boardedge-2700;
oldcornx1=cornx;
corny=600;
halfwidthmrs=2000;
mrdiameter=2500;
[capx,lengthCl]=loadnetwork(halfwidthmrs);
boardedge=capx+lengthCl;
switchlayout(mrdiameter,boardedge,0)
floods(halfwidthmrs,boardedge,3000)

%-----------------------
cornx=boardedge+200;
corny=1450;
oldcornx2=cornx;
shield;

%##############################################################################
%##############################################################################
%##############################################################################
%##############################################################################
```


IPR2024-00706 EX. 2005

```
% MIDDLE ROW 50 ohm cauer, 20 ohm iterated, no multires, shield
%-------------------------------
mrdiameter=3000;
cornx=750;
corny=5050;
tapL= 1.0e-07 * [ 0.0845 0.0946  0.0944   0.0996   0.1052   0.1079   0.1042];
Cph = 1.0e-10 * [ 0.2791 0.2846  0.2966   0.3178   0.3546   0.4256   0.6147];
design = [  2    3    3    3    4    4    5    10];
taps=cumsum(design);
taps=taps+1;
taps=taps(1:end-1);
tapL=tapL-1e-9;
extensions=tapL*(400/(10.8e-9-1.5e-9)); % linear approximation mils/H
tapangles=19*ones(1,length(Cph));
tapangles(1)=12;
tapangles(end-1)=25;
tapangles(end)=35;
tapangles=tapangles*pi/180;
[td,ti,to,outertapr]=eagletoroid(cornx+shieldside/2,corny+shieldside/2,mrdiameter,38,taps,'topnoground',extensions,Cph,tap
fprintf(eagle,'\nLayer tPlace\n');
fprintf(eagle,'Text ''%s'' (%-5.3f %-5.3f);\n','50C',cornx+shieldhole,corny);
halfwidthmrs=shieldside/2+shieldhole/2;
if outertapr>halfwidthmrs
 halfwidthmrs=outertapr;
end
[capx,lengthCl]=loadnetwork(halfwidthmrs);
boardedge=capx+lengthCl+200;
bncsource=inputnetwork(ti,boardedge);
switchlayout(mrdiameter,boardedge,td)
floods(halfwidthmrs,boardedge)


%-------------------------------
mrdiameter=2500;
cornx=boardedge+530;
corny=5150;
fsw=13.56e6;
L=343e-9;
C=1/(16*fsw*fsw*L);
Z0=sqrt(L/C);
[td,ti,to,outertapr]=eagletoroid(cornx+shieldside/2,corny+shieldside/2,mrdiameter,32,2:28,'topbottomnoground',ones(1,28)*(
```

```
fprintf(eagle,'\nLayer tPlace\n');
fprintf(eagle,'Text ''%s'' (%-5.3f %-5.3f);\n','20I',cornx+shieldhole,corny);
halfwidthmrs=shieldside/2+shieldhole/2;
if outertapr>halfwidthmrs
 halfwidthmrs=outertapr;
end
[capx,lengthCl]=loadnetwork(halfwidthmrs);
boardedge=capx+lengthCl;
bncsource=inputnetwork(ti,boardedge);
switchlayout(mrdiameter,boardedge,td)
floods(halfwidthmrs,boardedge)


%-----------------------
% no multiresonant structure: offset in x fools drawing subs
cornx=oldcornx1;
%corny=500;
halfwidthmrs=2000;
mrdiameter=2500;
[capx,lengthCl]=loadnetwork(halfwidthmrs);
boardedge=capx+lengthCl;
switchlayout(mrdiameter,boardedge,0)
floods(halfwidthmrs,boardedge,3000)

%-----------------------
cornx=oldcornx2;
corny=5250;
shield;

%##############################################################################
%##############################################################################
%##############################################################################
%##############################################################################
% TOP ROW 50 ohm bottom w/ no shield, 50 ohm bottom with shield, 20 ohm shielded, shield

%-----------------------
mrdiameter=3000;
cornx=350;
corny=9300;
[td,ti,to,outertapr]=eagletoroid(cornx+shieldside/2,corny+shieldside/2,mrdiameter,38,2:34,'bottomnogroundstandalone',one
fprintf(eagle,'\nLayer tPlace\n');
fprintf(eagle,'Text ''%s'' (%-5.3f %-5.3f);\n','50B',cornx+shieldhole,corny);
```


IPR2024-00706 EX. 2005

```
halfwidthmrs=shieldside/2+shieldhole/2;
if outertapr>halfwidthmrs
 halfwidthmrs=outertapr;
end
boardedge=2*halfwidthmrs+cornx−shieldhole/2;
floods(halfwidthmrs,boardedge)

%————————————————————
mrdiameter=3000;
cornx=boardedge+200;
corny=9300;
[td,ti,to,outertapr]=eagletoroid(cornx+shieldside/2,corny+shieldside/2,mrdiameter,38,2:34,'topstandalone',ones(1,34)*0,0/3
fprintf(eagle,'\nLayer tPlace\n');
fprintf(eagle,'Text ''%s'' (%-5.3f %-5.3f);\n','50TS',cornx+shieldhole,corny);
halfwidthmrs=shieldside/2+shieldhole/2;
if outertapr>halfwidthmrs
 halfwidthmrs=outertapr;
end
boardedge=2*halfwidthmrs+cornx−shieldhole/2;
floods(halfwidthmrs,boardedge)

%————————————————————
mrdiameter=2500;
cornx=boardedge+200;
corny=9300;
C=0;
[td,ti,to,outertapr]=eagletoroid(cornx+shieldside/2,corny+shieldside/2,mrdiameter,32,2:28,'topbottom',ones(1,28)*0,C/28*o
fprintf(eagle,'\nLayer tPlace\n');
fprintf(eagle,'Text ''%s'' (%-5.3f %-5.3f);\n','20S',cornx+shieldhole,corny);
halfwidthmrs=shieldside/2+shieldhole/2;
if outertapr>halfwidthmrs
 halfwidthmrs=outertapr;
end
[capx,lengthCl]=loadnetwork(halfwidthmrs);
boardedge=capx+lengthCl;
bncsource=inputnetwork(ti,boardedge);
switchlayout(mrdiameter,boardedge,td)
floods(halfwidthmrs,boardedge)

%————————————————————
mrdiameter=3000;
cornx=boardedge+200;
```

```
corny=9300;
[td,ti,to,outertapr]=eagletoroid(cornx+shieldside/2,corny+shieldside/2,mrdiameter,38,2:34,'bottomstandalone',ones(1,34)*0,
fprintf(eagle,'\nLayer tPlace\n');
fprintf(eagle,'Text ''%s'' (%-5.3f %-5.3f);\n','50BS',cornx+shieldhole,corny);
halfwidthmrs=shieldside/2+shieldhole/2;
if outertapr>halfwidthmrs
 halfwidthmrs=outertapr;
end
boardedge=2*halfwidthmrs+cornx−shieldhole/2;
floods(halfwidthmrs,boardedge)


fprintf(eagle,'\nGrid Last;\nWindow Fit;\n');


fclose(eagle);
```

A.2 FastHenry model scripts

```
function makehenry(diameter,turns,henryname);

global henry
global viadiameter
global henrynode
global henryedge
global boardz
global dds
global sss
global neck
global sectionsperwedge
global skind
global viafilaments
global wirewidthfilaments
global wireheightfilaments

extensionlength=361;
extensionwidth=20;

id=250;
```


IPR2024-00706 EX. 2005

```
henry = fopen([henryname '.inp'],'w');
fprintf(henry,'* File generated by makehenry.m, %s\n\n.Units mils\n.default sigma=1473.2\n',date);
fprintf(henry,'\n\n* Skin effect defaults\n.default nwinc=3 nhinc=3\n');
henrynode=1;
henryedge=1;

alpha=2*pi/(turns);
beta=pi/4-alpha/2;
gamma=pi/2-beta;

xbest=(neck/2+sss+viadiameter/2+dds*sin(gamma-alpha))/sin(alpha)-viadiameter/2;
id=2*(xbest*(sin(alpha)+tan(beta)*cos(alpha))/tan(beta)-sss/sin(beta)-dds/sqrt(2)-2*dds/sqrt(2)/tan(beta));

d2=sss/sin(beta);
d1=id/2+dds/sqrt(2)+2*dds/sqrt(2)/tan(beta);
d6=id/2+dds/sqrt(2)+dds/sqrt(2)/tan(beta);
x=tan(beta)*(d1+d2)/(sin(alpha)+tan(beta)*cos(alpha));
inr=d6+2*viadiameter;
outervias=floor(diameter/2*alpha/1.1/viadiameter);
outerviatheta=linspace(-(diameter/2*alpha/2-viadiameter/2-sss/2)*2/diameter,(diameter/2*alpha/2-viadiameter/2-sss/:
outerviax=diameter/2*cos(outerviatheta);
outerviay=diameter/2*sin(outerviatheta);
inrtheta=(inr*alpha/2-viadiameter/2-sss/2)/inr;
inx=inr*cos(inrtheta);
iny=inr*sin(inrtheta);
xi=atan(diameter/2*sin(alpha)/(diameter/2-inr));
tapnodes=[];

for a=0:360/(turns/2):359, %don't take off any turns

viarothenry(a,id/2+dds/sqrt(2),0,dds*2)
noderothenry(a,d6,0,0);
edgehenry(henrynode-1,henrynode-3,viadiameter,1.4);
nodestore=henrynode-1;
noderothenry(a,d6,0,boardz);
edgehenry(henrynode-1,henrynode-3,viadiameter,1.4);
noderothenry(a,d6+viadiameter,0,boardz);
edgehenry(henrynode-2,henrynode-1,neck,1.4)
wedgerot(a,sectionsperwedge,inr,0,boardz,diameter/2,0,boardz,iny*2+viadiameter,outerviay(end)*2+viadiameter,1.4);
%noderothenry(a,diameter/2+extensionlength,0,boardz);
%edgehenry(henrynode-2,henrynode-1,extensionwidth,1.4)
```

```
tapnodes=[tapnodes henrynode-1];
if a>0,
 viarothenryindex(a,nodestore6,henrynode-1,outerviay(end)*2+viadiameter)
else
 terminalnode1=henrynode-1;
end
edgehenry(henrynode-sectionsperwedge-2,henrynode-sectionsperwedge-1,0.5*(neck+iny*2+viadiameter),1.4);
noderothenry(a,d6+viadiameter,0,0);
edgehenry(nodestore,henrynode-1,neck,1.4)
wedgerot(a,sectionsperwedge,inr,0,0,diameter/2*cos(alpha),diameter/2*sin(alpha),0,iny*2+viadiameter,outerviay(end)*2+via
edgehenry(henrynode-sectionsperwedge-2,henrynode-sectionsperwedge-1,0.5*(neck+iny*2+viadiameter),1.4);
nodestore2=henrynode-1;

viarothenry(alpha*180/pi+a,x+viadiameter/2+cos(gamma)*dds,0,2*dds*sin(gamma))
nodestore3=henrynode-1;
wedgerot(alpha*180/pi+a,sectionsperwedge,inr,0,boardz,diameter/2,0,boardz,iny*2+viadiameter,outerviay(end)*2+viadiamet
tapnodes=[tapnodes henrynode-1];
viarothenryindex(alpha*180/pi+a,nodestore2,henrynode-1,outerviay(end)*2+viadiameter)
edgehenry(nodestore3+1,nodestore3,viadiameter,1.4);
nodestore5=henrynode-1;
wedgerot(alpha*180/pi+a,sectionsperwedge,inr,0,0,diameter/2*cos(alpha),diameter/2*sin(alpha),0,cos(xi)*(iny*2+viadiamet
nodestore6=henrynode-1;
edgehenry(nodestore5+1,nodestore3-1,viadiameter,1.4);

end


fprintf(henry,'\n\n* Define the ports\n');
%for i=1:length(tapnodes),
%fprintf(henry,'.external N%i N%i\n',tapnodes(i),henrynode-1);
for i=1:length(tapnodes)-1,
fprintf(henry,'.external N%i N%i\n',tapnodes(i),tapnodes(i+1));
end
fprintf(henry,'.external N%i N%i\n',tapnodes(i+1),henrynode-1);

fprintf(henry,'\n\n* frequency range\n');
fprintf(henry,'.freq fmin=13.56e6 fmax=13.56e6 ndec=1\n');
%fprintf(henry,'.freq fmin=0.1592 fmax=0.1592 ndec=1\n');
fprintf(henry,'* The end\n.end\n');

fclose(henry);
```

```
eval(['!fasthenry -f simple ' henryname '.inp'])
!zbuf zbuffile
eval(['!mv zbuffile.ps ' henryname '.ps'])
!rm zbuffile
!rm zbuffile_shadings
```

A.3 Cauer synthesis scripts

```
% only good for series inductor and terminating inductorM̂
M̂
function [Z,L,C]=cauersynth3(z,p,k)M̂
M̂
flarge=max([z p])*1e6;M̂
M̂
Z=oldsynthesizereactance(p,z,k);M̂
M̂
for i=1:length(p)M̂
    L(i)=getslope(Z,flarge);M̂
    Y=synthesizereactance(Z);M̂
    C(i)=getslope(Y,flarge);M̂
    Z=synthesizereactance(Y);M̂
endM̂
M̂
[num den]=tfdata(Z,'v');M̂
L(i+1)=1/den(end);M̂
M̂
Z=tf([L(end) 1],1);M̂
M̂
for i=length(C):-1:1;M̂
    Z=parz(Z,tf(1,[C(i) 0]));M̂
    Z=Z+tf([L(i) 0],1); M̂
endM̂
M̂
M̂
M̂
M̂
```


IPR2024-00706 EX. 2005

```
function Z=synthesizereactance(p,z,k)M̂
M̂
den=1;M̂
num=1;M̂
M̂
for i=1:length(p),M̂
    if p(i)==0M̂
        den=conv(den,[1 0]);M̂
    elseM̂
        den=conv(den,[1 0 p(i)*p(i)]);M̂
    endM̂
endM̂
M̂
for i=1:length(z),M̂
    if z(i)==0M̂
        num=conv(num,[1 0]);M̂
    elseM̂
        num=conv(num,[1 0 z(i)*z(i)]);M̂
    endM̂
endM̂
M̂
Z=k*tf(num,den);M̂
```

```
function Y=synthesizereactance(Z)M̂
M̂
[num,den]=tfdata(Z,'v');M̂
[r,p,k]=residue(num,den);M̂
resid=0;M̂
for i=1:2:length(r),M̂
    if i==length(r)M̂
        resid=resid+tf(r(i),[1 0]);M̂
    elseM̂
        resid=resid+tf([2*r(i) 0],[1 0 imag(p(i))^2]);M̂
    endM̂
endM̂
Y=1/resid;M̂
```

```
addpath '/home/jphinney/work/cauer'
```


IPR2024-00706 EX. 2005

```
[h,Z]=getz('final20ohm.mat');
Lfirst=14e-9; %target value of inductor at drain node
taps=9;       %number of capacitor taps

%[h,Z]=getz('final35ohm.mat');
%Lfirst=30e-9; %target value of inductor at drain node
%taps=8;       %number of capacitor taps

%[h,Z]=getz('final50ohm.mat');
%Lfirst=47e-9; %target value of inductor at drain node
%taps=7;       %number of capacitor taps

L=imag(Z)/13.56e6/2/pi;
dimL=length(diag(L));
gap=4;

m=dimL/2;
if mod(m,2)==1,
 Lbig=L(m,m);
 n=m+1;
 Lsmall=L(n,n);
else
 n=m;
 m=m+1;
 Lbig=L(m,m);
 Lsmall=L(n,n);
end

Msmall=[L(n,n+1:end) transpose(L(1:n-1,n))];
Mbig=[L(m,m+1:end) transpose(L(1:m-1,m))];

% these mutual functions are so similar for the 32-44 turn toroid cases
% that we could just use one function M=Mbig=Msmall
%plot(Msmall)
%hold on
%plot(Mbig)
%hold off

% generate lumped multiresonant model

% cauersynth3 yields a network with end inductances
```


IPR2024-00706 EX. 2005

```
% i.e., zeros at 0 and highest critical frequency.
% For simulation, we'll add a large cap in series with
% the inductor farthest from the switch

% work in normalized frequency/impedance

z=0:2:taps*2;
p=z+1;
p=p(1:length(p)-1);
k=1;            %L(1)=1 for this choice of k

[Z,Lph,Cph]=cauersynth3(z,p,k);

Lph=fliplr(Lph);
Cph=fliplr(Cph);

% Lph(end) Cph(end) next to switch
% Lph(1) Cph(1) next to input source
% vectors flipped so that state numbering increases from Vin->drain

% frequency response of normalized network can be evaluated
% (denormalized network gives errors)
Qph=60;       %Q of inductors in multiresonant network at f=fsw
fsw=1/2/pi;
Rph=fsw*2*pi*Lph/Qph;
Znorm=tf([Lph(1) Rph(1)],1);

for i=1:length(Cph),
    Znorm=parz(Znorm,tf(1,[Cph(i) 0]));
    Znorm=Znorm+tf([Lph(i+1) Rph(i+1)],1);
end
[Zinmag,Zinphase,normw]=bode(Znorm);
Zinmag=squeeze(Zinmag);
Zinphase=squeeze(Zinphase);
fsw=13.56e6;
a=Lfirst/Lph(end)*2*pi*fsw;
w=normw*fsw*2*pi;
Zinmag=Zinmag*a;
%figure(1)
%semilogy(w,Zinmag)

% denormalize network
```


IPR2024-00706 EX. 2005

```
%
Lph=Lph/fsw/2/pi;
Cph=Cph/fsw/2/pi;
                                                                    90
a=Lfirst/Lph(end);
Lph=Lph*a;
Cph=Cph/a;
Rph=fsw*2*pi*Lph/Qph;

Z=tf([Lph(1) Rph(1)],1);

for i=1:length(Cph),
    Z=parz(Z,tf(1,[Cph(i) 0]));
    Z=Z+tf([Lph(i+1) Rph(i+1)],1);                                  100
end

Lph=fliplr(Lph);
Cph=fliplr(Cph);
turn=1;
design=[];
Lapprox=[];
Ldesign=zeros(taps+1,dimL-gap);
for section=1:taps+1,
  Lavail=availableinductors(turn,Lbig,Mbig,Lsmall,Msmall);          110
  for m=1:length(Lavail),
     if section>1
        Lavail(m)=Lavail(m)+mutual(turn,lastturns,m,Lbig,Mbig,Lsmall,Msmall);
     end
     % guess the contribution of the next section to this self-inductance
     Lavail(m)=Lavail(m)+mutual(turn,m,m,Lbig,Mbig,Lsmall,Msmall);
  end
  lastturns=max(find(Lph(section)>Lavail));
  Lapprox=[Lapprox Lavail(lastturns)];
  if isempty(lastturns)                                             120
     lastturns=1;
  end
  design=[design lastturns];
  Ldesign(section,1:length(Lavail))=Lavail;
  turn=turn+lastturns;
  if turn>=dimL-gap & section<taps+1
    disp('turns exceeded!');
    break
```


IPR2024-00706 EX. 2005

```
  end
end

turn=1;
L=zeros(1,length(design));
tapL=zeros(1,length(design)-1);
for m=1:length(design),
  L(m)=selfinductance(turn,design(m),Lbig,Mbig,Lsmall,Msmall);
  if m>1
     tapL(m-1)=mutual(turn,design(m-1),design(m),Lbig,Mbig,Lsmall,Msmall);
     L(m-1)=L(m-1)+tapL(m-1);
     L(m)=L(m)+tapL(m-1);
  end
  turn=turn+design(m);
end
```

A.4 simulation scripts

```
function [Pin,Pout]=classphsim(fsw,duty,Vin,P,Lph,Cph,Rph,Rload,Lload,Cload,Cds,rdsonnom)

linewidth=2;
mygrey=[1 1 1]*0.7;
% state-space hack for voltage source
Chuge=1;  %Farads!
taps=length(Cph);
Qph=Lph(1)*fsw*2*pi/Rph(1);

tstep=1/fsw/2/100;
Tsw=1/fsw;

% record
tv=[];
iswv=[];
vdv=[];
xv=[];

ILin=P/Vin;

% input network, switch on
```


IPR2024-00706 EX. 2005

```
nph=1+length(Lph)+length(Cph);


%                    -1/Chuge
%                     1/C1  -1/C1
%                            1/C2  -1/C2
% 1/L1 -1/L1         -R1/L1
%       1/L2  -1/L2          -R2/L2
%              1/L3                  -R3/L3

Cquad=diag(1./[Chuge Cph])*(-eye(nph/2)+[zeros(1,nph/2);eye(nph/2-1) zeros(nph/2-1,1)]);
Lquad=diag(1./Lph)*(eye(nph/2)+[zeros(nph/2-1,1) -eye(nph/2-1);zeros(1,nph/2)]);
Rquad=-diag(1./Lph)*diag(Rph);
Rquad(end,end)=Rquad(end,end)-rdsonnom/Lph(end);

Ain=[zeros(nph/2) Cquad;Lquad Rquad];

Bin=zeros(nph,1);
Cin=eye(nph);
Din=zeros(nph,1);

switchonin=ss(Ain,Bin,Cin,Din);

% output network, switch on

n=2;

Aout=[0 -1/Cload;
1/Lload -Rload/Lload-rdsonnom/Lload];

Bout=zeros(n,1);
Cout=eye(n);
Dout=zeros(n,1);

switchonout=ss(Aout,Bout,Cout,Dout);

% entire converter, switch off
% x1   v Cout
% x2   i Lout
% x3   v Cds
% x4   v Cin
```


IPR2024-00706 EX. 2005

```
% xend i Lph(end) (inductor closest to drain in the input network)

n=3+nph;

A=[Aout [0;1/Lload] zeros(2,nph);
0 -1/Cds 0 zeros(1,nph-1) 1/Cds;
zeros(nph,2) [zeros(nph-1,1);-1/Lph(end)] Ain;];

B=zeros(n,1);
C=eye(n);
D=zeros(n,1);

switchoff=ss(A,B,C,D);

y=[0 0 0 zeros(1,nph/2) ones(1,nph/2)*ILin];

switchcycles=50;

for i=1:switchcycles,

%t=linspace(0,Tsw*duty);%bad for later power calculations (variable time step)
t=tstep:tstep:(Tsw*duty);

x0=y(end,1:2);
y1=initial(switchonout,x0,t);
x0=[Vin y(end,5:end)];
y2=initial(switchonin,x0,t);

if isempty(tv)
 tv=t;
else
 tv=[tv t+tv(end)];
end
iswv=[iswv; y2(:,end)-y1(:,2)];
%xv=[xv; y1 zeros(length(t),1) y2];
xv=[xv; y1 (y2(:,end)-y1(:,2))*rdsonnom y2];

%t=linspace(0,Tsw*(1-duty));%bad for later power calculations (variable time step)
t=tstep:tstep:(Tsw*(1-duty));

x0=[y1(end,1:end) 0 y2(end,1:end)];
y=initial(switchoff,x0,t);
```


IPR2024-00706 EX. 2005

```
tv=[tv t+tv(end)];
iswv=[iswv; zeros(length(t),1)];
xv=[xv; y];
                                                                    110
end

Pinv=xv(:,4).*xv(:,4+nph/2); %Chuge voltage times input inductor current
Poutv=xv(:,2).^2*Rload;

cyclepoints=1/fsw/tstep
%halfcyclepoints=length(t);

Pin=mean(Pinv(cyclepoints*10:end));
Pout=mean(Poutv(cyclepoints*19:end));                               120

Poutcyclemean=zeros(length(Poutv),1);
Pincyclemean=zeros(length(Poutv),1);
for i=1:cyclepoints,
  Poutcyclemean=Poutcyclemean+Poutv(1:cyclepoints*switchcycles);
  Poutv=[0; Poutv];
  Pincyclemean=Pincyclemean+Pinv(1:cyclepoints*switchcycles);
  Pinv=[0; Pinv];
end
Poutv=Poutv(cyclepoints+1:end);                                     130
Poutcyclemean=Poutcyclemean/cyclepoints;
Pinv=Pinv(cyclepoints+1:end);
Pincyclemean=Pincyclemean/cyclepoints;

figure(1)

orient tall
tstart=length(tv)-cyclepoints*5;
%tstart=1
                                                                    140
tv=tv(tstart:end)*1e9;
tv=tv-tv(1);

plots=4;
 subplot(plots,1,2)
h=plot(tv,xv(tstart:end,3),'k-');
set(h,'linewidth',linewidth);
```


IPR2024-00706 EX. 2005

```
set(gca,'xlim',[tv(1) tv(end)]);
psfraglabel(gca,'noxlabel')

subplot(plots,1,3)
h2=plot(tv,xv(tstart:end,end)-xv(tstart:end,2));
hold on
h1=plot(tv,iswv(tstart:end),'k-');
set(h1,'linewidth',linewidth);
set(h2,'color',mygrey);
set(h2,'linewidth',linewidth);
hold off
set(gca,'xlim',[tv(1) tv(end)]);
psfraglabel(gca,'noxlabel','notitle','ylabel2')

subplot(plots,1,4)
h2=plot(tv,xv(tstart:end,2),'k-');
hold on
h1=plot(tv,xv(tstart:end,end),'k-');
set(h1,'linewidth',linewidth);
set(h2,'color',mygrey);
set(h2,'linewidth',linewidth);
hold off
set(gca,'xlim',[tv(1) tv(end)]);
set(gca,'ylim',[-20 20]);
psfraglabel(gca,'ylabel3','notitle')

print -depsc ../Figures/classphsim
```


IPR2024-00706 EX. 2005

Appendix B

Pulse-reverse current source

See next page

IPR2024-00706 EX. 2005

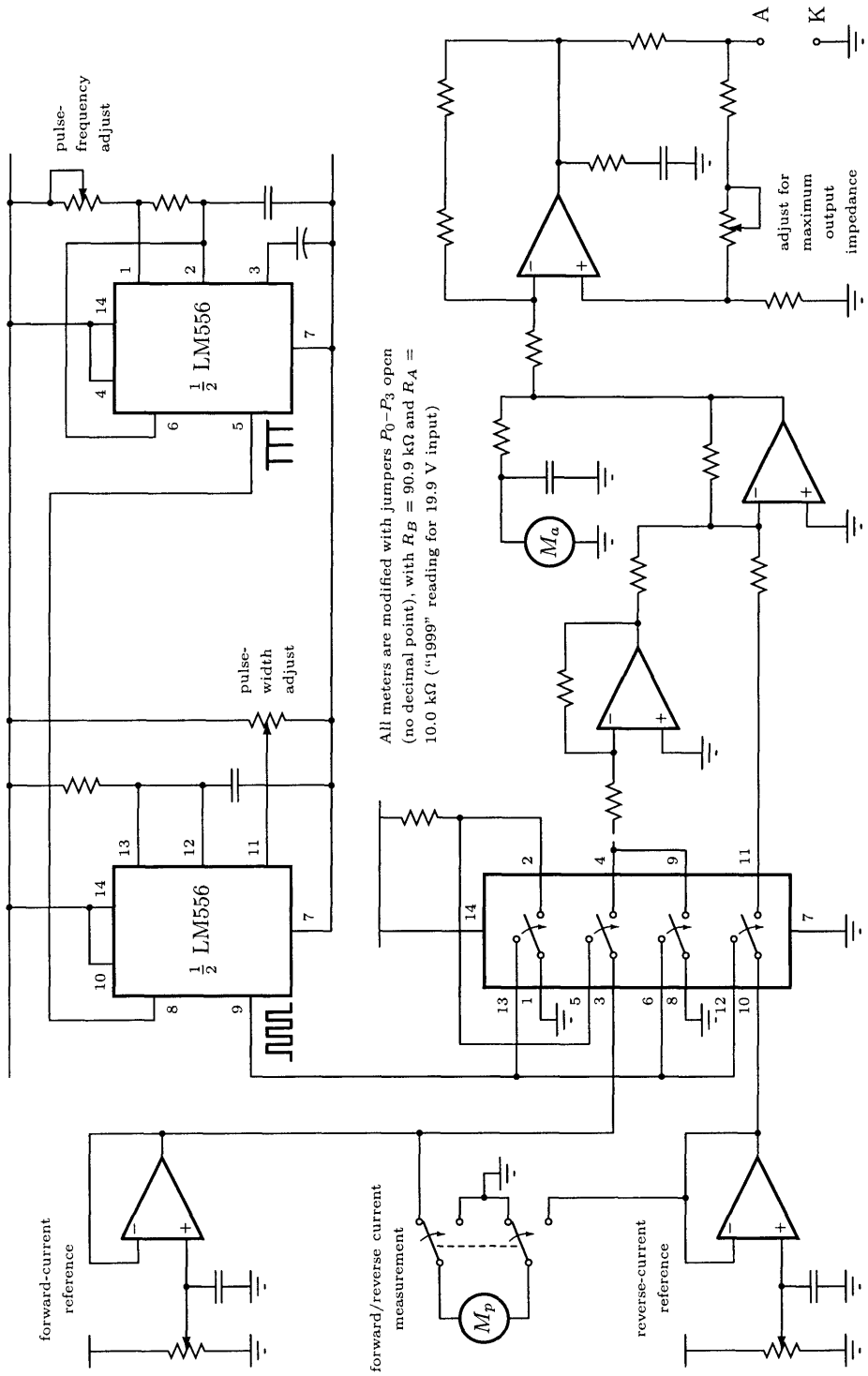

IPR2024-00706 EX. 2005

Appendix C

Lithography Masks

Mask 1 (Bottom layer)

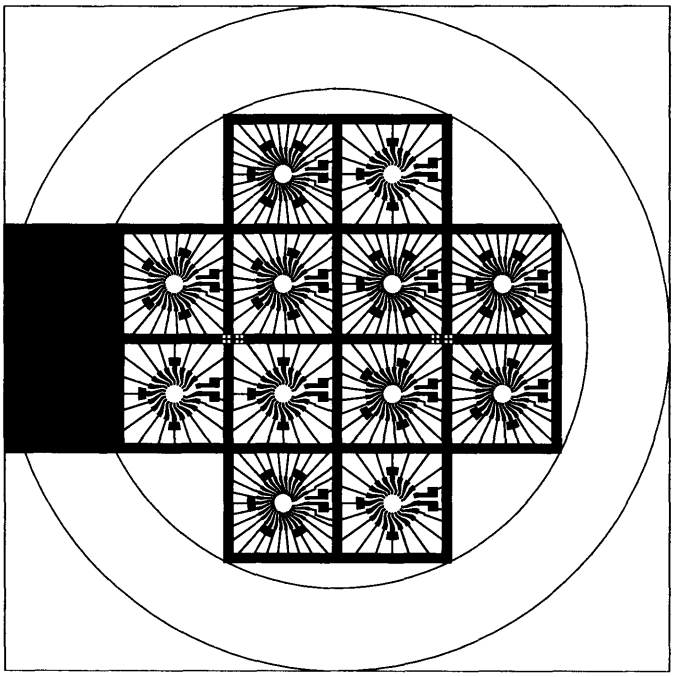

IPR2024-00706 EX. 2005

Mask 2 (Middle layer)

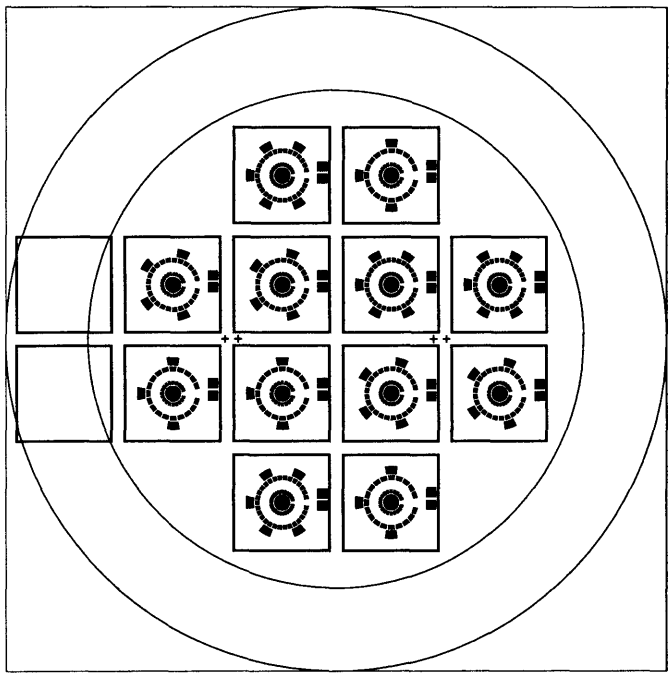

Mask 3 (Top layer)

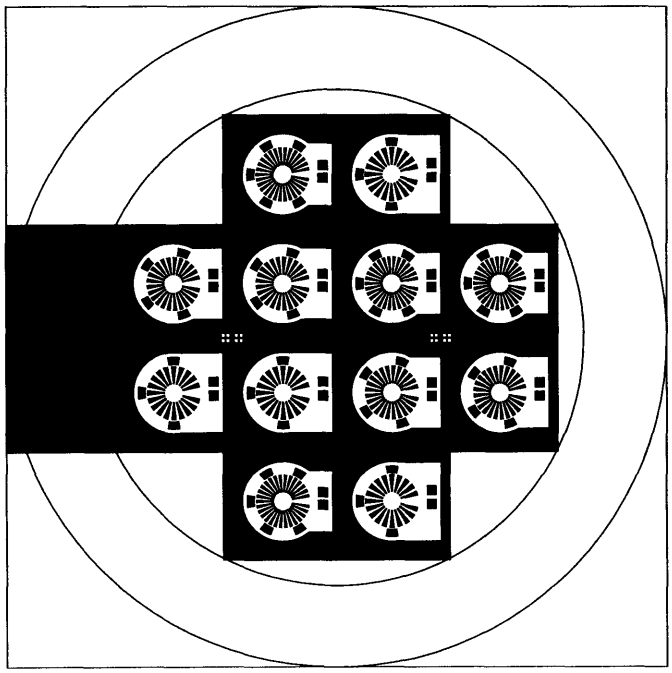

IPR2024-00706 EX. 2005

Bibliography

[1] E. Waffenschmidt, "Design and application of thin, planar magnetic components for embedded passives integrated circuits," in *36th Annual Power Electronics Specialists Conference Proceedings*, vol. 6, pp. 4546–4552, June 2004.

[2] E. Waffenschmidt and J. Ferreira, "Embedded passives integrated circuits for power converters," in *33th Annual Power Electronics Specialists Conference Proceedings*, vol. 1, pp. 12–17, June 2002.

[3] R. Erickson and D. Maksimović, *Fundamentals of Power Electronics.* Norwell, Massachusetts: Kluwer Academic Publishers, 2nd ed., 2001.

[4] M. Thompson, *High Temperature Superconducting Magnetic Suspension for Maglev.* Ph.D. thesis, Dept. of Electrical and Computer Engineering, Massachusetts Institute of Technology, 1997.

[5] F. Grover, *Inductance Calculations.* New York: Dover, 1946.

[6] L. Daniel, C. Sullivan, and S. Sanders, "Design of microfabricated inductors," *IEEE Trans. Power Electron.*, vol. 14, pp. 709–723, July 1999.

[7] C. Sullivan and S. Sanders, "Design of microfabricated transformers and inductors for high-frequency power conversion," *IEEE Trans. Power Electron.*, vol. 11, pp. 228–238, March 1996.

[8] J. Y. Park, L. K. Lagorce, and M. G. Allen, "Ferrite-based integrated planar inductors and transformers fabricated at low temperature," *IEEE Transactions on Magnetics*, vol. 33, no. 5, pp. 3322–3325, 1997.

[9] W. Bowman, J. Balicki, F. Dickens, R. Honeycutt, W. Nitz, W. Strauss, W. Suiter, and N. Zeisse, "A resonant dc-to-dc converter operating at 22 megahertz," in *Third Annual Applied Power Electronics Conference Proceedings*, pp. 3–11, 1988.

[10] K. Watanabe, S. Takeishi, I. Norigoe, and R. Hiramatsu, "Self running converter utilizing partial resonance," in 10th *International Telecommunications Energy Conference Proceedings*, pp. 186–193, 1988.

[11] D. Perreault, *Design and Evaluation of Cellular Power Converter Architectures.* Ph.D. Thesis, Dept. of Electrical and Computer Engineering and Comp. Science, Massachusetts Institute of Technology, 1997.

IPR2024-00706 EX. 2005

[12] E. Landsman, "A unifying derivation of switching dc-dc converter topologies," *IEEE Power Electronics Specialists Conference Record*, pp. 239–243, 1979.

[13] J. Kassakian, M. Schlecht, and G. Verghese, *Principles of Power Electronics.* New York: Addison-Wesley, 1991.

[14] L. L. Beranek, *Acoustics.* New York: American Institute of Physics and the Acoustical Society of America, 1986.

[15] T. Hueter and R. Bolt, *Sonics: Techniques for the use of sound and unltrasound in engineering and science.* New York: John Wiley & Sons, 1955.

[16] J. Phinney, *Filters with Active Tuning for Power Applications.* S.M. thesis, Dept. of Electrical Engineering and Comp. Science, Massachusetts Institute of Technology, Laboratory for Electromagnetic and Electronic Systems, 2001.

[17] J. Phinney and D. Perreault, "Filters with active tuning for power electronics," *IEEE Trans. Power Electron.*, vol. 18, pp. 636–647, March 2003.

[18] J. Phinney and D. Perreault, "Filters with active tuning for power electronics," *IEEE Power Electronics Specialists Conference*, pp. 363–370, June 2001.

[19] R. Balog and P. Krein, "Automatic tuning of coupled inductor filters," *IEEE Power Electronics Specialists Conference*, vol. 2, pp. 591 –596, June 2002.

[20] S. Tang, S. Hui, and H.-H. Chung, "Coreless planar printed-circuit-board (PCB) transformers — a fundamental concept for signal and energy transfer," *IEEE Transactions on Power Electronics*, vol. 15, pp. 931–941, September 2000.

[21] D. Lymar, T. Neugebauer, and D. Perreault, "Coupled-magnetic filters with adaptive inductance cancellation," *IEEE Power Electronics Specialists Conference*, 2005.

[22] R. Heartz and H. Buelteman, "The application of perpendicularly superposed magnetic fields," *AIEE Transactions*, vol. 74, pp. 655–660, November 1955.

[23] H. McCreary, "The magnetic cross valve," *AIEE Transactions*, vol. 70, no. 2, pp. 1868–1875, 1951.

[24] F. Beck and J. Kelly, "Magnetization in perpendicularly superposed direct and alternating fields," *Journal of Applied Physics*, vol. 19, pp. 551–562, June 1948.

[25] D. Pozar, *Microwave Engineering.* New York: John Wiley & Sons, 2nd ed., 1998.

[26] E. Guillemin, *Synthesis of passive networks: theory of methods appropriate to the realization and approximation problems.* New York: John Wiley & Sons, 1957.

[27] E. Guillemin, *Introductory Circuit Theory.* New York: John Wiley & Sons, 1953.

[28] E. Guillemin, *The Mathematics of Circuit Anlysis.* New York: John Wiley & Sons, 1949.

IPR2024-00706 EX. 2005

[29] W. Everitt and G. Anner, *Communication Engineering.* New York: McGraw-Hill, 3nd ed., 1956.

[30] T. Lee, *Design of CMOS Radio-Frequency Integrated Circuits.* Cambridge, United Kingdom: Cambridge University Press, 1998.

[31] E. Guillemin, *Communication Networks, Volume II: the Classical Theory of Long Lines, Filters and Related Networks.* New York: John Wiley & Sons, 1935.

[32] unknown, "Polynomials from pascal's triangle," `http://www.mathpages.com/home/kmath304.htm`, site accessed as of April 28, 2005.

[33] M. Kamon, M. Tsuk, and J.White, "Fasthenry, a multipole-accelerated preconditioned iterative methods for three-dimensional potential problems," in *Proceedings of the* 30th *Design Automation Conference*, June 1993, FastHenry is freely available for academic or commercial use; documentation and code can be downloaded from `http://www.fastfieldsolvers.com/`, last accessed May 9, 2005.

[34] T. Neugebauer, J. Phinney, and D. Perreault, "Filters and components with inductance cancellation," *Industry Applications Conference.* 37th *IAS Annual Meeting.*, vol. 2, pp. 939–947, October 2002.

[35] T. Neugebauer and D. Perreault, "Filters with inductance cancellation using printed circuit board transformers," *IEEE Trans. Power Electron.*, vol. 19, May 2004.

[36] J. Rivas, R. Wahby, J. Shafran, and D. Perreault, "New architectures for radio-frequency dc/dc power conversion," in *35*th *Annual Power Electronics Specialists Conference Proceedings*, pp. 4074–4084, June 2004.

[37] Y. Han, O. Leitermann, D. Jackson, J. Rivas, D.J., and Perreault, "Resistance compression networks for resonant power conversion," in *36*th *Annual Power Electronics Specialists Conference Proceedings*, June 2005.

[38] N. Sokal and A. Sokal, "Class E — a new class of high-efficiency tuned single-ended switching power amplifiers," *IEEE Journal of Sold-State Circuits*, vol. SC-10, pp. 168–176, June 1975.

[39] N. Sokal, "Class-E RF power amplifiers," *QEX*, pp. 9–20, Jan/Feb 2001.

[40] V. Tyler, "A new high-efficiency high-power amplifier," *The Marconi Review*, vol. 21, pp. 96–109, Fall 1958.

[41] M. Albulet, *RF Power Amplifiers.* Atlanta: Noble, 2001.

[42] J. R. Warren III, *Cell-Modulated Resonant dc/dc Power Converter.* M.Eng. Thesis, Dept. of Electrical and Computer Engineering and Comp. Science, Massachusetts Institute of Technology, 2005.

[43] P. Murgatroyd, "The optimal form of coreless inductors," *IEEE Transactions on Magnetics*, vol. 25, pp. 2670–2677, May 1989.

IPR2024-00706 EX. 2005

[44] J. Shaw, J. Gelorme, N. Labianca, W. Conley, and S. Holmes, "Negative photoresists for optical lithography," *IBM J. Res. Develop.*, vol. 41, pp. 81–93, January/March 1997.

[45] J. Gelorme and R.J. Cox, S.A.R., "Photoresist composition and printed circuit boards and packages made therewith." United States Patent 4,882,245, Nov. 21 1989.

[46] R. Ruhman, K. Pfeiffer, M. Falenski, F. Reuther, R. Engelke, and G. Gruetzner, "SU-8 — a high-performance material for MEMS applications," *MSTnews*, vol. 41, pp. 45–46, January 2002.

[47] J.-W. Park, J. Y. Park, Y.-H. Joung, and M. G. Allen, "Fabrication of high current and low profile micromachined inductor with laminated ni/fe core," *IEEE Transactions on Components and Packaging Technologies*, vol. 25, pp. 106–111, March 2002.

[48] M. Despont, H. Lorenz, N. Fahrni, J. Brugger, P. Renaud, and P. Vettiger, "High-aspect-ratio, ultrathick, negative-tone near-UV photoresist for MEMS applications," *IEEE Tenth Annual International Workshop on Micro Electro Mechanical Systems, (MEMS '97)*, pp. 518–522, 1997.

[49] M. C. Peterman, P. Huie, D. Bloom, and H. A. Fishman, "Building thick photoresist structures from the bottom up," *Journal of Micromechanics and Microengineering*, vol. 13, pp. 380–382, January 2003.

[50] R. Feng and R. J. Farris, "Influence of processing conditions on the thermal and mechanical properties of SU8 (*sic.*) negative photoresist coatings," *Journal of Micromechanics and Microengineering*, vol. 13, pp. 80–88, 2003.

[51] B. Eyre, J. Blosie, and D. Wiberg, "Taguchi optimization for the processing of Epon SU-8 resist," *IEEE Eleventh Annual International Workshop on Micro Electro Mechanical Systems*, pp. 218–222, 1998.

[52] J. Wu, *A High Aspect-Ratio Silicon Substrate-Via Technology and Applications.* S.M. Thesis, Dept. of Electrical and Computer Engineering and Comp. Science, Massachusetts Institute of Technology, 2000.

[53] G. Wheeler, *The Design of Electronic Equipment.* New York: Prentice-Hall, 1972.

IPR2024-00706 EX. 2005